9-7

CONTRACTOR REPORT

SAND94– 2019
Unlimited Release
UC–707

Extensions to the Integral Line-Beam Method for Gamma-Ray Skyshine Analyses

J. K. Shultis, R. E. Faw
Department of Nuclear Engineering
Kansas State University
Manhattan, Kansas 55606

Prepared by
Sandia National Laboratories
Albuquerque, New Mexico 87185 and Livermore, California 94550
for the United States Department of Energy
under Contract DE-AC04-94AL85000

Printed August 1995

Issued by Sandia National Laboratories, operated for the United States Department of Energy by Sandia Corporation.

Available to DOE and DOE contractors from
Office of Scientific and Technical Information
PO Box 62
Oak Ridge, TN 37831

Prices available from (615) 576-8401, FTS 626-8401

Available to the public from
National Technical Information Service
US Department of Commerce
5285 Port Royal RD
Springfield, VA 22161

NTIS price codes
Printed copy: A08
Microfiche copy: A01

SAND94-2019
Unlimited Release
Printed August 1995

Distribution
Category UC-707

Extensions to the Integral Line-Beam Method for Gamma-Ray Skyshine Analyses

J. K. Shultis and R. E. Faw,
Department of Nuclear Engineering
Kansas State University
Manhattan, Kansas 55606

Sandia Contract No. 78-5706

Abstract

A computationally simple method for estimating gamma-ray skyshine dose rates has been developed on the basis of the line-beam response function. Both Monte Carlo and point-kernel calculations that account for both annihilation and bremsstrahlung were used in the generation of line beam response functions (LBRF) for gamma-ray energies between 10 and 100 MeV. The LBRF is approximated by a three-parameter formula. By combining results with those obtained in an earlier study for gamma energies below 10 MeV, LBRF values are readily and accurately evaluated for source energies between 0.02 and 100 MeV, for source-to-detector distances between 1 and 3000 m, and beam angles as great as 180 degrees. Tables of the parameters for the approximate LBRF are presented.

The new response functions are then applied to three simple skyshine geometries, an open silo geometry, an infinite wall, and a rectangular four-wall building. Results are compared to those of previous calculations and to benchmark measurements. A new approach is introduced to account for overhead shielding of the skyshine source and compared to the simplistic exponential-attenuation method used in earlier studies. The effect of the air-ground interface, usually neglected in gamma skyshine studies, is also examined and an empirical correction factor is introduced. Finally, a revised code based on the improved LBRF approximations and the treatment of the overhead shielding is presented, and results shown for several benchmark problems.

Contents

Preface

In 1986, at the urging of Charles Negin of Grove Engineering Inc., we began the development of the integral line-beam method for skyshine analysis. The improvement of existing approximations to the line beam response function, a key component of this simplified method, was a priority so that the method could be extended to greater source-to-detector distances and to accommodate a greater range of photon energies. Under the encouragement of Hong-Nian and Ted Simmons of Sandia National Laboratory this work has continued. This support and enthusiasm for the project are gratefully acknowledged and are responsible in large part for the evolution of this method into a even more practical tool for routine gamma skyshine analysis.

This report summarizes the present state of the integral line-beam method as applied to bared and shielded gamma-ray skyshine sources. Results present here allow the method to be applied with more accuracy over wider energy and source-to-detector ranges than was previously possible.

The success of this project depended on the cooperative efforts of many of our students who, at various times over the past ten years, have contributed to many aspects of this skyshine problem. In particular, Murray Roseberry, Darin George, and Michael Bassett, contributed to the early developed of the method. During this present project, Xiaohong Deng, Ronald Brockhoff, Faisal Kahn, and Mark Stedry performed many of the calculations reported here. To these students we extend our thanks, and we hope that their work on this project will contribute to their successful professional careers.

JKS and REF
Kansas State University
June, 1994.

Chapter 1

Introduction

1.1 Skyshine

The term skyshine generally refers to radiation that originates from a fixed source and scatters in the atmosphere before reaching a point of interest (detector) near the ground. Skyshine is important when sufficient shielding between the source and detector prevents any significant radiation from reaching the detector directly through the shield material.

Skyshine dose calculations have been used widely in the design of nuclear facilities such as nuclear power plants, spent-fuel storage areas, and research laboratories. In these facilities, radiation sources are generally well shielded against radiation emitted horizontally. However, there is usually far less shielding provided against radiation emitted upward through the roofs of these facilities. Radiation escaping through the roofs interacts in the air and returns to earth exposing people both near and far from the facilities.

Elementary ray-analysis techniques coupled with buildup-factor concepts have been applied very successfully to treat the direct dose arising from gamma photons that travel directly from the source to the detector [Ch84]. In skyshine problems, however, ray-analysis techniques fail, and the radiation protection analyst has to resort to specialized and generally computationally intensive techniques. The large computational expense inherent in multi-dimensional transport calculations precludes the use of these techniques for routine or preliminary design analyses. Thus, approximate techniques have been developed for the skyshine problem to reduce the computational effort. In this study, one such approximate technique is refined and its range of applicability extended.

1.2 Previous Skyshine Studies

In previous skyshine studies, a variety of methods has been used, including radiation transport methods, single-scattering methods, and response-function methods. The Monte Carlo method was the first radiation transport method applied to the skyshine problem. Lynch et al. [Ly58], using a customized Monte Carlo code, computed the air dose as a function of distance from point monodirectional sources emitting photons at different angles from the source-detector axis. General purpose Monte Carlo codes such as OGRE [Pe65], COHORT [So75], and MORSE [Em75] have been applied to skyshine calculations [An87]. All of these codes are based on an exact transport description of a particular skyshine problem and normally require a multidimensional geometry and multigroup energy formulation, and, hence, a large computational effort.

The discrete-ordinate technique, another method based on transport theory, has also been used in skyshine analyses [Gi90]. The codes DOT [My73] and ANISN [En67] are representatives of general-purpose transport codes which also have been used for skyshine calculations. To avoid troublesome ray effects inherent in these multidimensional calculations involving a severely anisotropic source, fine angular meshes and first or second scattered source formulations must be used. Also, as with general purpose Monte Carlo codes, large computational efforts are required and the usefulness of these codes for preliminary or routine skyshine calculations is limited.

An elementary single-scatter approximation method for calculating skyshine doses was proposed by Trubey [Tr61]. This single-scatter technique ignores both the contributions of multiply-scattered gamma photons as well as the attenuation and the buildup of photons in the air. It is successful for near-field calculations, when the detector is near the source, involving bare skyshine sources, but it is not as suitable for shielded sources or for far-field calculations, when the detector is far from the source. Based on Trubey's work, Kitazume [Ki68] modified the single-scatter approximation by incorporating exponential attenuation and a Taylor-type buildup factor. The inclusion of exponential attenuation for both uncollided photons and scattered photons and the consideration of secondary radiation buildup allows this single-scatter method to be applied to more complicated skyshine geometries and at distances farther from the source. Other applications of the single-scatter method to various gamma-ray skyshine problems include the work of Roseberry [Ro80], Roseberry and Shultis [Ro82], Chou et al. [Ch83], and George [Ge88]. Also general-purpose single-scatter codes such as QAD [Pr74] and G3 [Ma73] have been used for skyshine calculations.

An alternative simplified approach for skyshine analyses is the use of a skyshine line-beam response function (LBRF) that gives the skyshine dose arising from a monodirectional and monoenergetic beam of gamma radiation directed into the atmosphere. Lynch et al. [Ly58] computed by Monte Carlo techniques the air dose caused by multiply-scattered gamma photons initially emitted in a monoenergetic beam into an infinite air medium at angles up to 180 degrees from the source-detector axis. The

LBRF could then be used as the basis for obtaining the skyshine dose for an arbitrary source by simply decomposing the actual source into a sum of beam components.

Radiation Research Associates (RRA) carried out more extensive Monte Carlo calculations for obtaining the LBRF and implemented the LBRF method in the SKYSHINE series of codes [Pr76, La79, La88]. These codes were originally designed to evaluate the effects of structure geometry upon the skyshine dose rate at detector positions outside a building housing energetic gamma-ray sources. The structure geometry allowed by the SKYSHINE codes can include a rectangular structure with four walls, a roof, and a floor. Each of the containment surfaces may be subdivided into a maximum of nine different subsections, each with different composition or thickness. A Monte Carlo sampling technique is used by SKYSHINE to determine from which surface radiation is emitted and with what energy. After a correction for attenuation as the beam penetrates the structure, the contribution to the skyshine dose made by the transmitted beam is then calculated with the LBRF.

To reduce further the computational effort, and yet improve the accuracy of the LBRF calculational method, Shultis and Faw [Sh87, Sh91, Sh92] developed a different method to obtain the LBRF. The skyshine dose rate at a detector arising from a monodirectional, monoenergetic photon beam was calculated by the point-kernel technique accounting for gamma-photon attenuation, secondary photons, and pair production in the scattered radiation field. These LBRF calculations, for fixed energy and emission angle, were then approximated by an empirical formula whose parameters were determined by least-square fitting a three-parameter formula to calculated values of the LBRF. The resulting LBRF was a function of source photon energy, source-to-detector distance, and photon emission angle. To make the approximate LBRF continuous in both energy and angle, a linear interpolation scheme was introduced. The skyshine dose from a given photon source was then obtained by numerically integrating the LBRF over all emission directions and energies allowed by the skyshine source. This integral LBRF method with revised LBRF data has been incorporated in the microcomputer code MICROSKYSHINE [Gr87].

Compared to the original LBRF approximation used by the SKYSHINE series of codes, the LBRF obtained by Shultis and Faw had three important improvements. First, the SKYSHINE approximation of the LBRF yielded good agreement with benchmark calculations over source-to-detector distances to 1500 m. Calculated skyshine dose rates at beyond this limit, however, not only were overestimated but also did not decrease as rapidly with increasing distance as did other benchmark calculations. The new LBRF approximation is suitable for a greater source-to-detector range, namely to 2500 m. Second, the photon energy and beam angle are treated in a multigroup formulation in the SKYSHINE method [La88]. This multigroup treatment of the energy and angular variables occasionally produces random variations (a few percent) in the calculated doses when one of the geometry parameters is altered only slightly. Such random variations make sensitivity studies difficult since rather large parameter changes must be used to obtain a meaningful change in the skyshine dose. Shultis and Faw introduced an energy and angular interpolation scheme to make the LBRF con-

tinuous in these variables. The new continuous LBRF greatly improves the precision of skyshine calculations so that sensitivity studies can be more easily performed. The new LBRF also eliminates the stochastic variations observed in the original LBRF caused by the fits to Monte Carlo data which themselves contained statistical errors. Third, unlike the SKYSHINE method which uses a Monte Carlo technique to account for different source emission directions, MICROSKYSHINE calculates the skyshine dose by integrating (numerically) the line-beam response function over all directions allowed by the problem geometry. Consequently, it is relatively easy to analyze simple skyshine geometries, such as a bare source in an open cylindrical silo or behind an infinitely-wide wall.

For a skyshine problem with shielding over the source, exponential attenuation has been employed in estimates of the skyshine dose caused by all gamma photons (uncollided and scattered) passing through the source shield [Sh91]. The integral LBRF method has been also incorporated into a composite method to treat the silo collimation with shielding over the source. This composite method [Ke82, Ba89] uses an accurate one-dimensional transport code to compute the energy and angular distribution of photons escaping from the source shield. Then a modified integral LBRF method treats the emergent photons as an effective bare skyshine source in calculations of the skyshine dose at the detector location.

1.3 Summary of the Integral Line-Beam Method

The LBRF $\Re(d, E, \phi)$ gives the air kerma (rad per photon) at a distance d from a point source emitting photons of energy E into an infinite air medium at an angle ϕ relative to the source-detector axis. The skyshine dose rate $R(d)$ arising from a bare, collimated point source which emits $S(E, \mathbf{\Omega})\, dE\, d\Omega$ photons per unit time with energies in dE about E into directions $d\Omega$ about $\mathbf{\Omega}$ is found by integrating the LBRF over all source energies and over all photon emission directions allowed by the source collimation, namely [Sh91]

$$R(d) = \int_0^\infty dE' \int_{\mathbf{\Omega}_s} d\Omega\, S(E', \mathbf{\Omega}) \Re(d, E', \phi(\mathbf{\Omega})). \tag{1.1}$$

Here $\mathbf{\Omega}_s$ represents those directions in which radiation can stream directly from the source into the atmosphere. Implicit in this approach is the assumption that the ground can be treated as an infinite air medium. This assumption has proven to be quite reasonable for most gamma skyshine problems.

For a shielded skyshine problem, the energy and angular distribution of photons leaving the shield can be treated as a bare, polyenergetic, anisotropic, point source, and the skyshine dose at a detector location can be calculated by Eq. (1.1). The composite method for a shielded source uses this approach [Ba89]. In this method, a one-dimensional transport model is used to calculate first the energy and angular distributions of photons leaving the source shield. Then the skyshine dose is calculated for the escaping photons by using the integral LBRF method.

When the source energy distribution is represented by a multigroup approximation, the multigroup source spectrum can be incorporated in Eq. (1.1) as

$$R(d) = \sum_{g=1}^{G} \int_{\Omega_s} d\Omega\, S(E_g, \Omega) \Re(d, E_g, \phi(\Omega)). \tag{1.2}$$

The above results are based on two implicit approximations. First, the walls of the source collimation are assumed to be "black", i.e., any photons that hit the walls are assumed to be absorbed. This assumption allows one to neglect the dose contribution at the detector of photons that penetrate the source containment walls or that scattered from the walls before escaping into the atmosphere. Second, the source containment structure is assumed to have a negligible perturbation on the skyshine radiation field; i.e., once photons enter the atmosphere, they do not interact again with the source structure. With this assumption, the calculation of the energy and angular distribution of source photons penetrating any overhead source shield or escaping from the containment structure becomes independent of the subsequent transport of the photons through the air to the detector. In most far-field skyshine calculations, the source and its containment have a negligible effect on the transport of the photons through the air once the photons have left the source structure [Ba89]. However, for near-field calculations, as will be seen, this second assumption is not always true.

If the point source is isotropic and monoenergetic, emitting S_p photons of energy E per unit time, the energy and angular distribution of the source can be represented as

$$S(E', \Omega) = \frac{S_p}{4\pi} \delta(E' - E). \tag{1.3}$$

Then, in terms of a spherical-polar coordinate system with the source at the origin and the polar axis directed vertically upwards, Eq. (1.1) reduces to

$$R(d) = \frac{S_p}{4\pi} \int_0^{2\pi} d\psi \int_{\omega_{min}}^{\omega_{max}} d\omega\, \Re(d, E, \phi), \tag{1.4}$$

where ω is the cosine of the polar angle θ, and the azimuthal angle ψ is defined with respect to the projection on the horizontal plane of the source-to-detector axis. Here ω_{min} and ω_{max} define the permissible range of the cosine of polar angles for photon emission allowed by the source collimation. Generally, these limits are functions of the azimuthal angle ψ.

The above formulation can be used to calculate the skyshine dose rate for any point skyshine source. For some simple skyshine geometries, explicit expressions for the limits ω_{min} and ω_{max} can be obtained (see Ch. 4). In any case, the integral in Eq. (1.1) or (1.4) can be evaluated readily using standard numerical integration techniques.

1.3.1 Approximation of the LBRF

An analytical approximation of the LBRF is used to evaluate efficiently the integral in Eq. (1.1) or (1.4). As originally proposed for the SKYSHINE code [Pr74, La79] and later confirmed by Shultis et al. [Sh92], the LBRF may be accurately approximated by the following three-parameter function:

$$\Re(x, E, \phi) \equiv E\mathcal{F} \simeq E\kappa(\rho/\rho_o)^2[x(\rho/\rho_o)]^b \mathrm{e}^{a-cx(\rho/\rho_o)}. \tag{1.5}$$

Here ρ is the air density in the same units as the reference density $\rho_o = 0.001225$ g/cm^3. When E is measured in MeV and x in meters, the constant κ is equal to $(1.602\times10^{-6}$ erg/MeV$)/$ $[(100$ erg/g·cGy$)(1225$ g/m$^3)] = 1.308\times10^{-11}$ cGy·m^3/MeV. The parameters a, b and c, which depend on the photon energy E and the emission angle ϕ, are determined by fitting Eq. (1.5) to calculated values of the LBRF.

Several compilations of the parameters a, b and c are available [La88, Sh91, Sh92] for different energy and direction (E and ϕ) grids. Indeed, one of the prime objectives of the present study is to obtain a set of fit parameters that allow the integral line-beam method to be used at lower and higher energies or for smaller and greater source-to-detector distances than was previously possible.

Interpolation of Fitted LBRF

The fit parameters a, b and c in Eq. (1.5) are tabulated at discrete energies $E_i, i = 1, \ldots, I$ and at discrete emission directions $\phi_j, j = 1, \ldots, J$. In earlier applications of the integral line-beam method, for example in the SKYSHINE codes [La79, La88], the approximate LBRF was also restricted to these discrete energies and directions. However, to evaluate numerically the integrals in Eqs. (1.1) or (1.4), it has been found [Sh91] that much better results can be obtained if the approximate LBRF is made continuous in both E and ϕ.

A double interpolation scheme is proposed to make the approximate line-beam response function continuous in both energy and angle [Sh91, Sh92]. The approximate LBRF is first linearly interpolated in energy to yield the response at the energy E of interest. If $E_i \le E \le E_{i+1}$ then the approximating function $\mathcal{F}$ at the two bracketing discrete energies are reconstituted from the fitting parameters in Eq. (1.5) and $\mathcal{F}(E, x, \phi_j)$ is then obtained by linear interpolation as

$$\mathcal{F}(x, E, \phi_j) = \mathcal{F}_{i+1,j}\frac{E_i - E}{E_i - E_{i+1}} + \mathcal{F}_{i,j}\frac{E - E_{i+1}}{E_i - E_{i+1}}, \tag{1.6}$$

where

$$\mathcal{F}_{i,j} \equiv \mathcal{F}(x, E_i, \phi_j). \tag{1.7}$$

Once the energy interpolation has been performed for at the two bracketing angles, an interpolation in the beam direction ϕ is performed. For $\phi_j \le \phi \le \phi_{j+1}$

$$\mathcal{F}(x, E, \phi) = \mathcal{F}(x, E, \phi_j) + [\mathcal{F}(x, E, \phi_{j+1}) - \mathcal{F}(x, E, \phi_j)]\frac{\phi - \phi_j}{\phi_{j+1} - \phi_j}. \tag{1.8}$$

Here is assumed that $0 < \phi_1 < \phi_2 < \ldots < \phi_J < 180$ degrees. For beam directions in the two end intervals, a linear extrapolation procedure is used, namely, for $\phi_{J-1} \leq \phi \leq \phi_J$ degrees,

$$\mathcal{F}(x, E, \phi) = \mathcal{F}(x, E, \phi_J) + [\mathcal{F}(x, E, \phi_J) - \mathcal{F}(x, E, \phi_{J-1})] \frac{\phi - \phi_J}{\phi_J - \phi_{J-1}}, \tag{1.9}$$

and for $0 \leq \phi \leq \phi_1$ degrees

$$\mathcal{F}(x, E, \phi) = \mathcal{F}(x, E, \phi_1) + [\mathcal{F}(x, E, \phi_2) - \mathcal{F}(x, E, \phi_1)] \frac{\phi - \phi_1}{\phi_2 - \phi_1}. \tag{1.10}$$

With this double interpolation scheme, the approximating function of Eq. (1.5) is made completely continuous in angle ϕ and energy E. Unlike the original LBRF [La79] which was represented as histograms in both energy and angle, the new approximating LBRF proposed here varies smoothly with small changes in the arguments of the LBRF. However, it should be noted that, while this continuity feature increases the precision of a skyshine calculations, it does require more computational effort and has little effect on the accuracy of the skyshine doses [Sh87, Sh92].

1.3.2 Azimuthally Symmetric Skyshine Sources

In many skyshine problems, the gamma-ray emission from a source into the atmosphere is azimuthally symmetric about a vertical axis. For such cases, the integral line-beam method for estimating the skyshine dose can be further simplified by introducing a *conical beam response function* (CBRF). This function, denoted by $\Re_c(x, E, \theta, h)$, gives the skyshine dose per source photon at a distance x and an elevation h from a point source that emits photons of energy E uniformly in azimuth at an angle θ to the vertical axis. Thus, if an azimuthally symmetric skyshine source has an angular and energy distribution, i.e., $S(E, \mathbf{\Omega}) = S(E, \theta)$, the skyshine dose at the detector is given by

$$R(d) = \int_0^\infty dE \int_0^{\theta_{max}} d\theta \, \sin\theta \, S(E, \theta) \, \Re_c(x, e, \theta, h). \tag{1.11}$$

From a comparison of this result to the integral line-beam result of Eq. (1.1), it is seen that Eq. (1.11) requires the numerical evaluation of only a double integral, one less than required for Eq. (1.1).

Evaluation of the CBRF From the LBRF

For an infinite air medium, the conical-beam response function $\Re_c(x, E, \theta, h)$ generally depends on four independent variables: the photon energy E, the polar source angle θ, the horizontal source-to-detector distance x, and the elevation of the detector with

respect to the source h. From a comparison of Eq. (1.1) to Eq. (1.11), it is seen that the conical-beam response function can be obtained from the line-beam response function $\Re(x, E, \phi)$ by integrating the latter over all azimuthal angles, namely,

$$\Re_c(x, E, \theta, h) = \int_0^{2\pi} d\psi \, \Re(E, \phi(\theta, \psi, h), x). \tag{1.12}$$

For the special case in which the source and detector are at the same elevation (i.e., $h = 0$), the conical beam response function has only three independent variables. This simplified CBRF is easily obtained by integrating the LBRF over all azimuthal source angles ψ to give

$$\Re_c(x, E, \theta) = \int_0^{2\pi} d\psi \, \Re(x, E, \phi(\theta, \psi)). \tag{1.13}$$

This integral over ψ is readily performed by any standard numerical integration method such as Gaussian quadrature, using the approximate LBRF of Eq. (1.5) to evaluate the integrand. The resulting values of the CBRF can then be approximated in the same manner as was used for the line-beam response function. Eq. (1.5) was found to produce a good approximation to values calculated from Eq. (1.13) and tabulations of the fitting coefficients a, b and c for different photon energies and conical angles have been produced [De91, Sh92].

1.4 Outline of Study

Although the integral LBRF method has produced results in good agreement with other more elaborate calculations as well as with benchmark experimental data [Sh87, Ba89], its accuracy can still be improved, especially for sources of lower and higher energies and for near-field skyshine calculations. For example, the MICROSKYSHINE code is limited to skyshine problems with source energies from 0.1 to 10 MeV, and for the range 0.1 to 1 MeV the LBRF energy dependence is sparsely represented. Also the MICROSKYSHINE code is suitable only for far-field calculations, namely for source-to-detector distances greater than about 50 m. In this study, several aspects of the integral line-beam method are refined. Specifically, the LBRF is improved (1) to treat more accurately low-energy skyshine sources in the range 0.02 to 1 MeV, (2) to permit calculations for high energy sources in the range 10 to 100 MeV, and (3) to allow both near-field and far-field skyshine calculations.

In Chapter 2, a point-kernel procedure for obtaining the skyshine dose arising from a monodirectional photon beam is presented. The point kernel model for the LBRF is improved over an earlier model [Sh91] by introducing a new approximation for the differential scattering cross section and by adopting new gamma-ray interaction data. Approximate methods for the inclusion of bremsstrahlung production and for positron transport in the air prior to annihilation are also proposed.

In Chapter 3, Monte Carlo calculations of the LBRF, performed with the MCNP code, are presented and used both to verify the accuracy of the point kernel model and to generate reference values. As will be seen, the point-kernel model, gives excellent values for the LBRF for source energies below 15 MeV. However, at higher energies and for small beam angles, the point kernel model underpredicts the LBRF because of the approximate way in which the model accounts for the angular distribution of the bremsstrahlung. For energies above 15 MeV, the MCNP values of the LBRF are thus recommended as the basis for obtaining a revised approximate LBRF.

In Chapter 4, the approximation of the LBRF by empirical formulas is considered, and a data base is developed to allow ready evaluation of the LBRF as a continuous function of source energy, emission direction and source-to-detector distance. Both the traditional 3-parameter and a new 4-parameter approximation of the LBRF are developed for use in the integral line-beam method.

The integral line-beam skyshine method based on the new approximations to the LBRF is applied in Chapter 5 to simple skyshine geometries. The skyshine dose rate is obtained by numerically integrating the LBRF over all emission directions allowed by the source collimation in these geometries. Three simple collimation geometries are treated by this integral LBRF method, namely, the open silo, the infinite wall, and an open rectangular four-wall building. Comparisons of results with previous skyshine benchmarks and calculations are also presented.

In Chapter 6, the integral line-beam method is applied to skyshine sources with overhead horizontal shields. A hybrid method is developed in which the radiation transport through the shield is treated by a specialized Monte Carlo procedure, and the subsequent air-transport of escaping photons is treated with the integral line-beam method. This hybrid method is compared to the simple exponential attenuation approach used in earlier integral line-beam studies.

Finally in Chapter 7, results are shown for the effect of the air-ground interface. Inherent in the integral line-beam method is the assumption that the ground interface can be approximated by an infinite medium of air. It is shown that near the source, the ground acts as a reflector and enhances the skyshine dose while far from the source the ground acts as an absorber and depresses the skyshine dose. Approximate correction factors are developed to modify the infinite-air LBRF to account for the presence of the ground interface.

Chapter 2

Point-Kernel Model for the Line-Beam Response Function

The detector response caused by the photons emitted from any source can be divided conceptually into two components. The first component is the direct dose arising from gamma photons that travel directly from the source to the detector without interaction. The second dose component is due to photons that scatter one or more times before reaching the detector. Skyshine refers to this second dose component caused by the reflection in the air of photons emitted from a ground source back to a target near the ground.

The integral line-beam skyshine method developed by Shultis and Faw [Fa87, Sh91] was based on the availability of a line-beam response function (LBRF). The LBRF $\Re(x, E, \phi, \ldots)$ is the air kerma (rad) at a distance x away from a point source that emits a single photon of energy E into atmosphere at an angle ϕ from the source-to-detector axis. Both the source and detector are located at or above the ground surface. An exact calculation of the LBRF would consider the effects of the air-ground interface on the skyshine radiation field. In this case the LBRF would also be a function of the source and detector coordinates as well as the source energy and emission direction. The LBRF would even be different for different ground compositions. Clearly it would be very difficult to evaluate and use such a complicated response function.

To obtain an analytical formula for the LBRF that is just a function of E, x, and ϕ, the effect of the air-ground interface must be neglected. Since the average Z number for most soils is reasonably close to that of air, the small contribution to the LBRF made by photons reflected from the ground would be nearly the same as that reflected by a half-space of air.[1] With this approximation, the LBRF $\Re(x, E, \phi)$ can be obtained by considering a beam of photons emitted into an infinite air medium.

[1]The greater soil density will cause photons that cross the interface and subsequently scatter back into the atmosphere to do so at geometrically different positions than in the infinite air case. However, this change in the interface-reflected dose is usually negligible. Quantification of the ground interface effect is presented in Chapter 7.

Several techniques have been used to calculate the skyshine dose at the detector arising from a monodirectional gamma-photon beam. The Monte Carlo method was first used by RRA to obtain the LBRF [La79]. This method, however, is computational expensive, particularly for large source-to-detector distances. Discrete-ordinates transport methods have also been attempted [Gi89], but since the skyshine problem is inherently multi-dimensional, this method is also computational expensive. Moreover, the so-called ray effects aggravated by the severe anisotropy of the skyshine source limited the accuracy of the multi-dimensional discrete-ordinates approach. As an alternative, the point kernel technique can be employed to evaluate the skyshine dose at the detector [Fa87, Sh91]. It is this latter approach that is used for the most part in this study.

2.1 Point-Kernel Calculation of the LBRF

Consider a point monoenergetic and monodirectional photon source in an infinite homogeneous air medium, as shown in Fig. 2.1. The source emits I_o photons per unit time of energy E in a direction ϕ from the axis between the source and a point isotropic detector that is a distance x from the source. Four types of secondary photons produced by interactions of the beam photons are mainly responsible for the skyshine dose at the detector: (1) photons that are Compton scattered by the atomic electrons in the air, (2) 0.511-MeV annihilation photons that arise from pair production in the air, (3) fluorescent photons produced by photoelectric interactions, and (4) bremsstrahlung photons produced by secondary electrons. These four skyshine components are discussed in the following sections.

2.1.1 Compton Scattering Component

Compton scattering refers to the elastic scattering of a photon by an atomic electron. Consider a source photon that travels a distance y along the emission direction, and, while traveling a further differential distance dy, is Compton scattered (see Fig. 2.1). After the scattering interaction, the photon has energy E' and moves at an angle θ_s measured from its initial direction. The scattered photon energy E' is given by the Compton relation [Ch84]

$$E' = \frac{E}{1 + (E/m_e c^2)(1 - \cos\theta_s)}. \tag{2.1}$$

The scattering angle can be found by

$$\theta_s = \cos^{-1}[(x^2 - r^2 - y^2)/2ry], \tag{2.2}$$

where $r^2 = y^2 + x^2 - 2yx\cos\phi$. Here x is the source-to-detector distance and r is the distance between the photon scattering point dy and the detector.

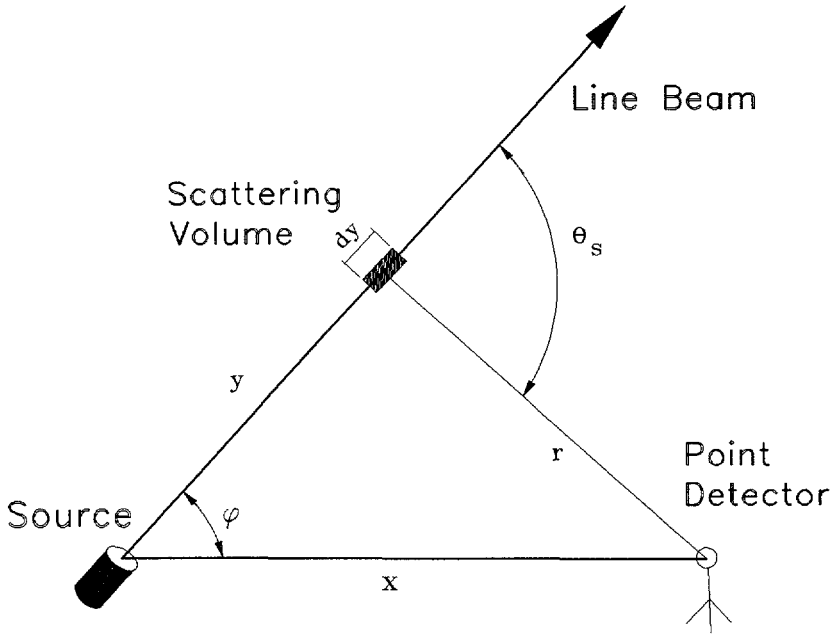

Figure 2.1. Geometry used for calculating the line-beam response function. Source and detector are in an infinite homogeneous air medium.

The probability a source photon reaches a distance y along the beam without interaction is $\exp(-\mu y)$; and the probability that this photon, while traveling a further distance dy, is scattered through an angle θ_s into a unit solid angle about θ_s is

$$Z\,N\,{}_e\sigma_s(E,\theta_s)\,\exp(-\mu y)\,dy,$$

where N is the atomic density of the air, Z is the average number of electrons per atom ($= 7.225$ for air), μ is the total linear interaction coefficient for photons of energy E, and ${}_e\sigma_s(E,\theta_s)$ is the microscopic differential scattering cross section per electron for photons of energy E being scattered into a unit solid angle about a scattering angle θ_s. For photons scattered by an unbound (free) electron, the microscopic differential scattering cross section is given by the Klein-Nishina formula [Ch84]

$${}_e\sigma_{KN}(E,\theta_s) = \frac{1}{2}\,r_e^2\,p^2\,[1 + p^2 - p(1-\cos^2\theta_s)]. \tag{2.3}$$

where $p \equiv E'/E$, and r_e is the classical electron radius (equals to 2.818×10^{-15} m).

In a previous study by Shultis and Faw [Sh91], the Klein-Nishina formula was used to approximate the actual differential scattering cross section for all photon energies considered (0.1 to 10 MeV). In general, however, photons are scattered by bound electrons, and binding effects become especially important for low energy photons. However, it is very difficult to calculate the differential scattering cross section accounting for electron binding effects, and tabulated values of photon scattering cross sections that include binding effects are not readily available.

An approximate way to correct for electron binding effects is to assume that the differential scattering cross section ${}_e\sigma_s(E,\theta_s)$ is proportional to the Klein-Nishina (free electron) differential scattering cross section ${}_e\sigma_{KN}(E,\theta_s)$ and normalized to give the correct total scattering cross section, namely

$$ {}_e\sigma_s(E,\theta_s) \simeq {}_e\sigma_s(E)\frac{{}_e\sigma_{KN}(E,\theta_s)}{{}_e\sigma_{KN}(E)}. \tag{2.4} $$

This approximation for ${}_e\sigma_s(E,\theta_s)$, when integrated over all scattering angles, yields the correct bound-electron total scattering cross section ${}_e\sigma_s(E)$. Here ${}_e\sigma_{KN}(E)$ is the total incoherent Klein-Nishina scattering cross section from a free electron given by [Ch84]

$$ \begin{aligned} {}_e\sigma_{KN}(E) &= 2\pi \int_{-1}^{1} d(\cos\theta_s)\, {}_e\sigma_{KN}(E,\theta_s) \\ &= \pi r_e^2 \lambda \left[(1-2\lambda-2\lambda^2)\ln\left(1+\frac{2}{\lambda}\right) + \frac{2(1+9\lambda+8\lambda^2+2\lambda^3)}{(\lambda+2)^2} \right], \end{aligned} \tag{2.5} $$

where $\lambda = m_e c^2/E$ or $\lambda = 0.511/E$ with E expressed in units of MeV.

In this study values for the total cross section for scattering from bound electrons, ${}_e\sigma_s(E)$, were taken from the DLC-139 library of photon interaction coefficients developed at the Ontario Cancer Institute [Dl88]. A comparison of the microscopic differential scattering cross section ${}_e\sigma_s(E,\theta_s)$ obtained by the approximate procedure of Eq. (2.4) to ${}_e\sigma_{KN}(E,\theta_s)$ evaluated from the Klein-Nishina formula of Eq. (2.3) is shown in Fig. 2.1.1 for three scattering angles. This plot shows the relative importance, in air, of electron binding effects on low energy photon scattering. At photon energies above 0.2 MeV, the approximation of Eq. (2.4) gives nearly same results as the Klein-Nishina formula. However in the low energy range (less than 0.2 MeV), the difference between Eq. (2.4) and Eq. (2.3) increases with decreasing photon energy. Note also that the difference is larger for small scattering angles than that for large scattering angles.

To express the angular distribution of Compton scattered photons scattered from the source beam, the function f_{KN} is defined as

$$ \frac{1}{2\pi} f_{KN}(E,\theta_s) \equiv \frac{{}_e\sigma_{KN}(E,\theta_s)}{{}_e\sigma_{KN}(E)}. \tag{2.6} $$

Thus the probability a photon is scattered in dy into an unit solid angle about θ_s can be rewritten as

$$ \frac{1}{2\pi} Z\, N\, {}_e\sigma_s(E)\, f_{KN}(E,\theta_s)\, \exp(-\mu y)\, dy, $$

If the photons scattered from dy are treated as a point source, their contribution to the dose rate at the detector can be estimated from point kernel theory as

$$ \dot{D}_s = \frac{I_o}{2\pi} N \int_0^\infty dy\, \frac{e^{-\mu y}}{r^2} Z\, {}_e\sigma_s(E)\, f_{KN}(E,\theta_s) B(E',\mu' r) \mathcal{R}(E')\, e^{-\mu' r}, \tag{2.7} $$

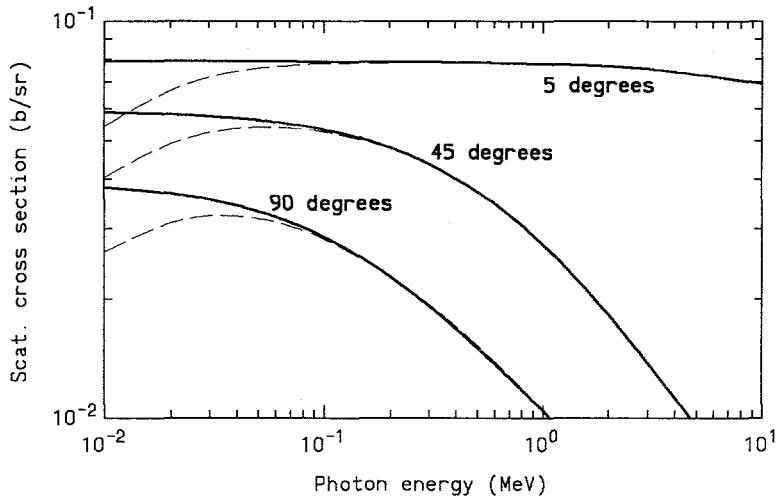

Figure 2.2. Variation with energy of the differential scattering cross section as given by the Klein-Nishina formula (solid lines) and by the approximation (dashed lines) of Eq. (2.4) that accounts for electron binding effects.

where the total linear interaction coefficient at the scattered energy E' is denoted by μ', and $B(E', \mu' r)$ is an appropriate infinite-medium buildup factor. The detector response function $\mathcal{R}(E)$ is taken here as the air absorbed dose per unit fluence of photons with energy E, and is given by [Ch84]

$$\mathcal{R}(E) = 1.602 \times 10^{-8}\, E\, (\mu_{tr}/\rho). \tag{2.8}$$

where (μ_{tr}/ρ) is the mass energy transfer coefficient for air in units of cm^2 per gram, E is in units of MeV, and $\mathcal{R}(E)$ is in units of rad cm^2.

2.1.2 Annihilation Radiation Component

If a photon has an energy greater than $2m_e c^2$ (= 1.02 MeV), the photon can be completely absorbed and in its place a positron-electron pair formed. The ultimate fate of the positron is annihilation with an electron of the air, generally after slowing to practically zero kinetic energy. The annihilation process results in the creation of two photons moving in opposite directions, each with energy of $E_a = m_e c^2$ (= 0.511 MeV). The angular distribution of the annihilation photons is usually assumed to be isotropic. In this section, for simplicity of model development, it is also assumed that the positron travels a negligible distance before annihilation.

The probability a source photon, after traveling a distance y along the beam, will undergo pair production in dy and produce an annihilation photon traveling in a unit solid angle directed towards the detector is

$$\frac{1}{2\pi}\, N\, \sigma_{pp}(E)\, \exp(-\mu y)\, dy,$$

where $\sigma_{pp}(E)$ is the microscopic pair-production cross section (per atom) for the incident photon of energy E. Thus, based on point kernel theory, the contribution of the annihilation photons produced along the beam to the skyshine dose at the detector is

$$\dot{D}_{pp} = \frac{I_o}{2\pi} N \int_0^\infty dy \, \frac{e^{-\mu y}}{r^2} \, \sigma_{pp}(E) B(E_a, \mu_a r) \mathcal{R}(E_a) \, e^{-\mu_a r}, \tag{2.9}$$

in which $\mu_a \equiv \mu(E_a)$ is the total linear interaction coefficient for annihilation photons.

The above result is valid only if positron transport effects can be neglected. This is a reasonable assumption for source photons below about 10 MeV and can be argued plausibly as follows. The maximum kinetic energy of a positron created by a 10 MeV photon is about 9 MeV ($E_{e^+}^{max} = E_\gamma - 2m_e c^2$). The range for this a positron is about 40 meters in air. For this worst case, if the detector is located several hundreds or thousands of meters away from the source, this 40 meters is still a negligible value. But if the detector is located near the source, the skyshine dose will tend to be overestimated if the positron travel distance is neglected. Even for near-field skyshine calculations, the effect of positron transport is minor for photon energies less than 10 MeV. Positrons produced by 10 MeV photons have an average initial kinetic energy of 4.5 MeV for which the range in air is 20 meters. Also, only 20 percent of 10-MeV photons will produce electron-positron pairs when interacting with air.

However, for higher energy source photons above 10 MeV positron transport between creation and annihilation sites becomes increasingly important, and neglect of positron transport can no longer be justified. In Section 2.2, refined models are proposed to correct the above result for positron travel prior to annihilation.

2.1.3 Fluorescence Component

In the photoelectric effect, a photon interacts with an entire atom, resulting in the emission of a photoelectron, usually from the K-shell of the atom. As the electron-shell vacancy left by the photoelectron is filled by an electron from an outer shell, either a fluorescence photon or an Auger electron will be emitted with an energy equal to the potential energy change of the electronic transition. The probability of photon emission during this transition is given by the fluorescence yield ω.

To account for fluorescence photons in the calculation of the skyshine dose rate, it is assumed that (1) every photoelectric interaction produces a K-shell vacancy so that all fluorescence photons have the K_α energy; (2) only fluorescence in oxygen and nitrogen is important; and (3) the fluorescence photons are emitted isotropically; Thus the number of fluorescence photons produced by a source photon in dy that are traveling in a unit solid angle directed towards the detector is

$$\frac{I_o}{4\pi} \sum_i N \, \sigma_{ph}^i(E) \, \omega_K^i \, \exp(-\mu y) \, dy,$$

where, for element i, ω_K^i is the fluorescent yield per K-shell vacancy ($\simeq 0.005$), E_K^i is the energy of the fluorescence photon, and $\sigma_{ph}^i(E)$ denotes the photoelectric effect

cross section for energy E. For air, only oxygen and nitrogen need to be considered in the summation in the above expression. For these elements, the energy of fluorescence photons is assumed equal to the K_α edge energy ($E_{K_\alpha} = 0.525$ keV for oxygen, and $E_{K_\alpha} = 0.392$ keV for nitrogen).

Thus the contribution to the skyshine dose rate at the detector is estimated as

$$\dot{D}_{ph} = \frac{I_o}{4\pi} N \int_0^\infty dy \, \frac{e^{-\mu y}}{r^2} \sum_i \sigma_{ph}^i(E) \, \omega_K^i B(E_K^i, \mu_K r) \mathcal{R}(E_K^i) \, e^{-\mu_K r}. \tag{2.10}$$

2.1.4 Bremsstrahlung Component

Source photons of sufficiently high energy produce energetic secondary electrons positrons that in turn generate bremsstrahlung as they move through the air. The angular distributions of both secondary electrons and the resulting bremsstrahlung are very complex. Bremsstrahlung emission becomes increasingly anisotropic in the forward direction as the photon energy increases. A rigorous treatment of the bremsstrahlung component requires coupled photon/electron transport calculations, calculations that are generally very computationally expensive. Moreover, even state-of-the-art Monte Carlo codes which purport to treat bremsstrahlung do so with inherent simplifications, e.g., one bremsstrahlung photon per electron or straight-ahead bremsstrahlung emission.

Because of the severe anisotropy in bremsstrahlung production in the energy regime for which bremsstrahlung is important, point kernel techniques based on isotropic point-source buildup factors are poorly suited to treat this source of radiation. Nevertheless, approximations can be introduced to allow the contribution of the bremsstrahlung to the skyshine dose to be estimated with the relatively simple point kernel techniques used in this study. Deng [De91] considered a low energy approximation in which the angular distribution of secondary electrons produced by Compton scattering and pair production can be assumed isotropic. But for those source-photon energies that lead to significant bremsstrahlung production, this assumption of isotropy is invalid. In this section, an alternative point kernel formulation that accounts for the severe anisotropy of bremsstrahlung emission at high energies is proposed.

Secondary electrons produced by Compton scattering and pair production from high energy gamma rays move almost directly along the original photon direction. Similarly, the bremsstrahlung photons produced by the more energetic of these secondary electrons, i.e., those that produce the important bremsstrahlung, are emitted very close to the original travel direction of the initial electron. One may thus assume that all bremsstrahlung from the secondary electrons produced by interactions of the *original* high-energy source photons continues to move along the source-beam direction. Subsequently, the bremsstrahlung, with most photons much less energetic than the source photons, is removed from the beam by Compton scattering or pair production interactions, thus producing a response in the skyshine detector.

With this straight-ahead approximation, the photon beam intensity in Fig. 2.1 should be augmented to include not only the original uncollided source photon intensity $I_o(y)$ but also the intensity of bremsstrahlung produced by secondary electrons released in source-photon interactions. Let $I_b(y, E_b)\, dE_b$ denote the intensity at a distance y along the beam of bremsstrahlung photons with energies in dE_b about E_b produced indirectly as a result of the interactions of the uncollided source photons. This bremsstrahlung component is given by

$$\frac{\partial I_b(y, E_b)}{\partial y} = -\mu(E_b) I_b(y, E_b) + S_b(y, E_b), \tag{2.11}$$

where $S_b(y, E_b)$ is the rate at which bremsstrahlung photons within unit energy about E_b are introduced into the beam. If the distances the secondary electrons move along the beam are neglected,[2] then this source equals the rate at which bremsstrahlung is produced by Compton recoil electrons and the electron-positron pairs at the location in the beam where the electrons are produced, i.e.,

$$S_b(y, E_b) = N \int_0^E dT\, I_o(y) \left\{ Z_e \sigma_s(E, T) f_b(T, E_b) + \sigma_{pp}(E, T)[f_b(T, E_b) + f_b(E - 2m_e c^2 - T, E_b)] \right\} \tag{2.12}$$

$$\equiv \hat{S}_b(E_b) I_o(y). \tag{2.13}$$

Here ${}_e\sigma_s(E, T)$ is the differential electron production cross sections for Compton scattering (per electron), $\sigma_{pp}(E, T)$ is the differential electron production cross section for pair production (the accompanying positron is emitted with energy $E - 2m_e c^2 - T$), and $f_b(T, E_b)\, dE_b$ is the number of bremsstrahlung photons with energies in dE_b about E_b ultimately produced by an electron of initial energy T.

The uncollided intensity of source photons (all with energy E) along the beam is

$$I_o(y) = I_o\, e^{-\mu(E) y}, \tag{2.14}$$

With this result, the solution of Eq. (2.11), subject to the initial condition $I_b(0) = 0$, is

$$I_b(y, E_b) = \begin{cases} \hat{S}_b(E_b) I_o \left[e^{-\mu y} - e^{-\mu_b y} \right] / (\mu_b - \mu), & \mu \neq \mu_b \\ y \hat{S}_b(E_b) I_o\, e^{-\mu_b y}, & \mu = \mu_b. \end{cases} \tag{2.15}$$

where $\mu \equiv \mu(E)$ and $\mu_b \equiv \mu(E_b)$.

The detector response caused by the removed beam bremsstrahlung (from Compton scattering, pair production and photoelectric interactions) is obtained in the same manner used to obtain the detector response for source photons removed from the

[2] Although secondary electrons from high-energy gamma rays can travel large distances in air (see Section 2.1.2), the more energetic and hence more important bremsstrahlung will be produced near the point where the energetic electron is produced. Thus the neglect of electron travel is somewhat justified.

beam. Replacement of $I_o\, e^{-\mu y}$ by the bremsstrahlung intensity $I_b(y, E_b)$ in Eqs. (2.7), (2.9), and (2.10) and integration over all bremsstrahlung energies yield

$$\dot{D}_b = \frac{N}{2\pi}\int_0^{T_{max}} dE_b \int_0^{\infty} dy\, \frac{I_b(y,E_b)}{r^2}[Z_e\sigma_s(E_b) f_{KN}(E_b,\theta_s) B(E',\mu' r)\mathcal{R}(E') e^{-\mu' r}$$
$$+ \sigma_{pp}(E_b) B(E_a,\mu_a r)\mathcal{R}(E_a) e^{-\mu_a r}$$
$$+ 2\sum_i \sigma^i_{ph}(E_b)\,\omega^i_K B(E^i_K,\mu_K r)\mathcal{R}(E^i_K) e^{-\mu_K r}], \qquad (2.16)$$

where the primed variables represent values at the scattered photon energy after Compton scattering from energy E_b through and angle θ_s. For Compton scattering the maximum energy of the recoil electron is $T_{max} = 2E/(2 + m_e c^2/E)$, while for pair production the maximum electron/positron energy is $T_{max} = E - 2m_e c^2$.

Other Approximations

To evaluate $I_b(y, E_b)$, the energy distribution of the bremsstrahlung radiation along the beam, $\hat{S}_b(E_b)$, must be evaluated from Eq. (2.13). To evaluate this expression, the distributions ${}_e\sigma_s(E,T)$, $\sigma_{pp}(E,T)$ and $f_b(T,E_b)$ must be known. Rigorous expressions for these distributions are very complex, and since the present straight-ahead treatment of the bremsstrahlung is itself approximate, the following approximations are used for these distributions.

For Compton recoil electrons, it is assumed that ${}_e\sigma_s(E,T) \simeq {}_e\sigma_{KN}(E,T)$, where the Klein-Nishina recoil electron cross section is given by [Ch84]

$${}_e\sigma_{KN}(E,T) = \frac{\pi r_e^2 \lambda^2}{m_e c^2}\left[(1-\lambda\tau) + \frac{1}{1-\lambda\tau} + \frac{(\lambda^2\tau)(\lambda^2\tau + 2\lambda\tau - 2)}{(1+\lambda\tau)^2}\right], \qquad (2.17)$$

where $\tau \simeq T/m_e c^2$ and $\lambda \simeq m_e c^2/E$.

There is no simple formula for $\sigma_{pp}(E,T)$, and for the purposes of this model, it is assumed that the energy distribution of the electron or positron is uniformly distributed over the permissible energy range, i.e.,

$$\sigma_{pp}(E,T) = \frac{\sigma_{pp}(E)}{E - 2m_e c^2}. \qquad (2.18)$$

One simple approximation that describes the high-energy portion of the *thick-target yield* $f_b(T,E_b)$ is given by the Kramer formula [Kr23]

$$f_b(T,E_b) = 2kZ\left(\frac{T}{E_b} - 1\right), \qquad E_b < T, \qquad (2.19)$$

where $k \simeq 0.0007$ MeV^{-1}. Another approximation which holds to somewhat lower bremsstrahlung energies is [Wy52]

$$f_b(T,E_b) = \mathcal{C}\left[4\left(\frac{T}{E_b} - 1\right) + 3\ln(E_b/T)\right], \qquad E_b < T \qquad (2.20)$$

where $\mathcal{C}$ is an empirical constant sometimes taken as $Z/4000$ MeV^{-1}. However, better agreement with more exact calculations can be achieved by expressing $\mathcal{C}$ in terms of the $Y(T)$, the fraction of the incident electron's kinetic energy that is subsequently emitted as bremsstrahlung. Integration of Eq. (2.20) yields

$$Y(T) = \frac{1}{T}\int_0^T dE\, E f_b(T,E) = \frac{13}{16}\mathcal{C}T, \tag{2.21}$$

This result can be used to express the normalization constant $\mathcal{C}$ in terms of $Y(T)$, namely $\mathcal{C} = 16Y(T)/(13T)$. With this choice for $\mathcal{C}$, the approximation of Eq. (2.20) agrees quite well with the thick-target bremsstrahlung spectrum calculated by much more elaborate methods such as the continuous slowing down model (see Fig. 2.3).

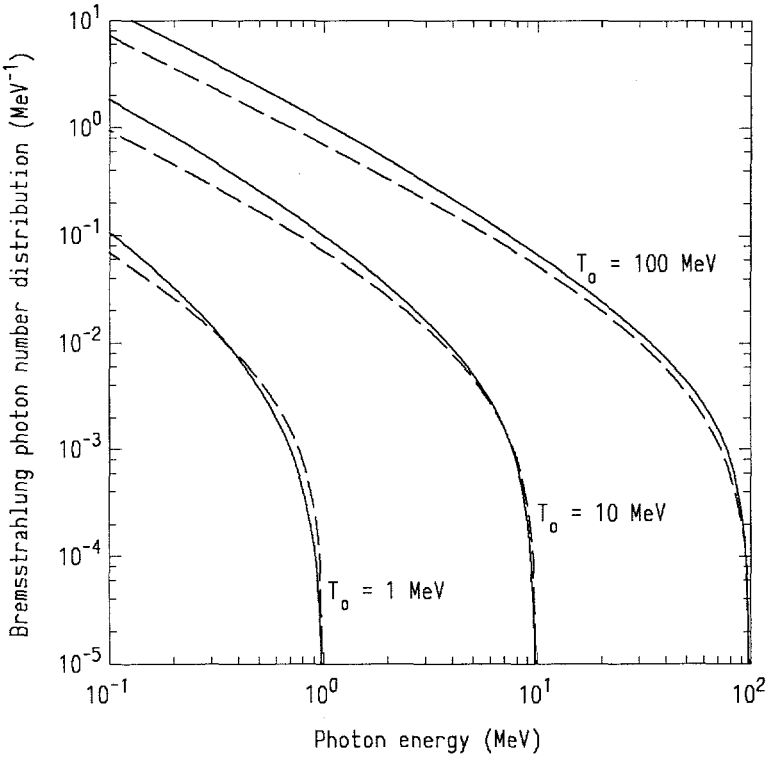

Figure 2.3. The distribution of bremsstrahlung photons, $f_b(T_o, E)$, produced by monoenergetic electron beams (energy T_o) incident on a thick nitrogen target. The solid lines are calculations based on the continuous slowing down approximation (CSDA) and the dashed lines are based on the Wyard approximation of Eq. (2.20).

2.1.5 Total Dose at the Detector

The total skyshine dose rate at the detector location is the sum of the four individual components developed in the previous sections. However, for the source photon

energies of interest in this study, i.e., > 0.02 MeV, the fluorescence component can be neglected.

In Fig. 2.4, the mean-free-path length ($\Lambda = \mu^{-1}$) of a photon in air at standard density as a function of the photon energy. Fluorescence photons from photoelectric interactions in air are all below 10 keV in energy and have a mean-free-path length of less than a few centimeters. Consequently, fluorescence from the skyshine radiation field can be completely ignored.

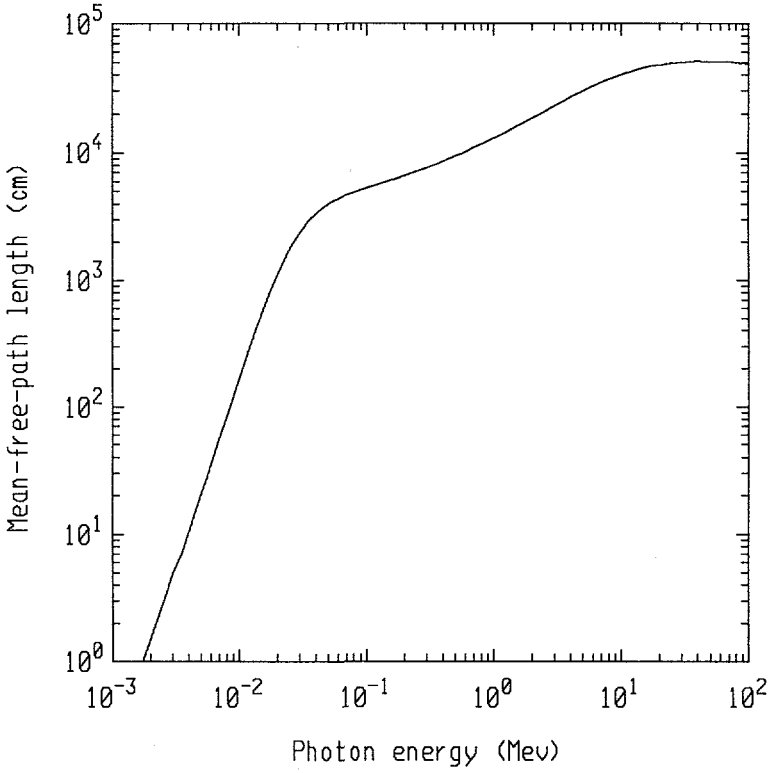

Figure 2.4. Variation with energy of the mean-free-path length in air at standard temperature and pressure. Data are from the DLC/139 photon library [Dl88].

Thus the LBRF $\Re(x, E, \phi)$ for source photon energies of less than about 15 MeV can be reduced to two components, those for the Compton scattered photons, annihilation photons, and bremsstrahlung. Thus adding Eqs. (2.7), (2.9), and (2.16) and setting the source intensity I_o unit emission rate give the LBRF in the form

$$\Re(x, E, \phi) = \frac{N}{2\pi} \int_0^\infty dy \, \frac{e^{-\mu y}}{r^2} [Z_e \sigma_s(E) f_{KN}(E, \theta_s) B(E', \mu' r) \Re(E') e^{-\mu' r} + \sigma_{pp}(E) B(E_a, \mu_a r) \Re(E_a) e^{-\mu_a r}] + \Re_b(x, E, \phi), \qquad (2.22)$$

where the bremsstrahlung component (neglecting fluorescence) is

$$\Re_b(x,E,\phi) = \frac{N}{2\pi}\int_0^{T_{max}} dE_b \int_0^{\infty} dy\, \frac{I_b(y,E_b)}{r^2}[Z_e\sigma_s(E_b)f_{KN}(E_b,\theta_s)B(E',\mu' r)\times$$

$$\Re(E')e^{-\mu' r} + \sigma_{pp}(E_b)B(E_a,\mu_a r)K(E_a)e^{-\mu_a r}]. \qquad (2.23)$$

Inherent in this expression for the LBRF is the inclusion of an appropriate buildup factor to account for the buildup of secondary photons between the location dy on the beam where source photons are removed from the beam and the detector. Annihilation photons are emitted isotropically near dy; however, Compton scattered photons are removed from dy in a preferentially forward direction. Nevertheless, the assumption of isotropic photon removal does not appear to introduce any serious error for the energy range being considered [Sh91]. Thus the buildup factor selected for use in Eq. (2.24) is that for the air-kerma for a point isotropic source in an infinite air medium.

To simplify the numerical evaluation of Eq. (2.22), distances are re-expressed in terms of mean-free-path lengths. The change of variables $\hat{y} \equiv \mu y$, $r' \equiv \mu' r$, $r'' \equiv \mu_a r$, and $R \equiv \mu r$, recasts the line-beam response function as

$$\Re(E,x,\phi) = \frac{1}{2\pi}\rho^2(\mu/\rho)\int_0^{\infty} d\hat{y}\,\frac{e^{-\hat{y}}}{R^2}[(\mu/\rho)_s f_{KN}(E,\theta_s)B(E',r')\Re(E')e^{-r'}$$

$$+(\mu/\rho)_{pp}(E)B(E_a,r'')\Re(E_a)e^{-r''}] + \Re_b(x,E,\phi), \qquad (2.24)$$

where (μ/ρ), $(\mu/\rho)_s$, and $(\mu/\rho)_{pp}$ are the total mass interaction coefficient, mass incoherent Klein-Nishina scattering coefficient, and mass pair-production interaction coefficient in air for photons of energy E, respectively. Here ρ is the mass density of air which was taken as 0.001225 g cm^{-3} for the calculations in this study.

The bremsstrahlung component can similarly be written in dimensionless form with the change of variables $\hat{y} \equiv \mu(E_b)y \equiv \mu_b y$, $r' \equiv \mu' r$, $r'' \equiv \mu_a r$, and $R \equiv \mu(E_b)r$. The result is

$$\Re_b(x,E,\phi) = \frac{1}{2\pi}\rho^2(\mu_b/\rho)\int_0^{T_{max}} dE_b \int_0^{\infty} dy\,\frac{\hat{I}_b(\hat{y},E_b)}{R^2}[Z_e\sigma_s(E_b)f_{KN}(E_b,\theta_s)\times$$

$$B(E',\mu' r)\Re(E')e^{-r'} + (\mu_{pp}(E_b)/\rho)B(E_a,r'')\Re(E_a)e^{-r''}]. \qquad (2.25)$$

where the renormalized bremsstrahlung beam intensity $\hat{I}(\hat{y},E_b)$ is

$$\hat{I}_b(\hat{y},E_b) = \begin{cases} \hat{S}_b(E_b)\left[e^{-\hat{y}(\mu/\mu_b)} - e^{-\hat{y}}\right]/(\mu_b-\mu), & \mu \neq \mu_b, \\ \hat{y}\hat{S}_b(E_b)\,e^{-\hat{y}}/\mu_b, & \mu = \mu_b. \end{cases} \qquad (2.26)$$

The bremsstrahlung component in the above results can be neglected for source photons below about 10 MeV. Since the radiative energy loss of secondary electrons

or positrons is proportional to EZ^2, bremsstrahlung production is most important for electrons with high energies in absorber materials of large atomic number Z. The ratio of the radiative energy loss to collisional and ionization energy loss is approximately $EZ/700$ with energy in MeV [Kn89]. For a 10 MeV electron in air, only 10 percent of its initial energy is lost as bremsstrahlung. Moreover, for a typical secondary electron with a few MeV of energy, the average energy of resulting bremsstrahlung emission is relatively low and normally reabsorbed close to its point of origin.

2.2 Correction for Positron Transport

In the point kernel formulation of the line-beam response function all secondary annihilation photons are assumed to be produced at the point where the positron-electron pair are created. However, the range of positrons produced by high-energy photons can be appreciable, and the distance travelled by the positron while slowing down before annihilation should be taken into consideration. For example, a 50-MeV electron has a CSDA range of 162 m in air at STP, while a 100-MeV positron can travel 262 m before annihilation.

In this section, two simplified methods are proposed for incorporating positron transport effects into the point kernel calculation of the LBRF. These two models are then applied to the positrons created directly by the source photons and then to positrons created by secondary bremsstrahlung that is also moving along the source beam.

2.2.1 General Formulation

Consider a monodirectional beam of photons at an angle ϕ with respect to the source-detector axis, as in Fig. 2.1. At any distance y along the beam, let $I(y, E)\,dE$ be the number of photons with energies in dE about E.

The number of positrons created in dy' about y' through pair-production interactions caused by the beam photons is

$$\left\{ \int_{E_{min}}^{E_{max}} dE\, \mu_{pp}(E)\, I(y', E) \right\} dy',$$

where $E_{min} = 2m_e c^2$ is the minimum photon energy that can cause pair production and E_{max} is the maximum photon energy in the photon beam.

Now make the key assumption that the positrons are emitted in the same direction as the photon beam. This assumption is reasonable since positron emission in pair production is highly forward peaked at high energies. Further, let $P_{\beta+}(E, z)\,dz$ be the probability that a positron created by a photon of energy E will travel a distance z (crow-flight) and undergo annihilation in dz about z. With this distribution, the

number of annihilation photons $N_a(y)$ produced per unit distance along the beam at $y = y' + z$ can be expressed as

$$N_a(y) = 2 \int_{E_{min}}^{E_{max}} dE\, \mu_{pp}(E) \int_0^y dy'\, I(y', E) P_{\beta+}(E, y - y') \tag{2.27}$$

$$= 2 \int_{E_{min}}^{E_{max}} dE\, \mu_{pp}(E) \int_0^y dz\, I(y - z, E) P_{\beta+}(E, z). \tag{2.28}$$

With the above source of annihilation photons, which are emitted isotropically along the beam, the standard point kernel technique can be used to estimated the dose rate D_a at the detector caused by these annihilation photons. Explicitly, one has

$$D_a(x) = \mathcal{R}(E_a) \int_0^\infty dy\, \frac{N_a(y)}{4\pi r^2}\, e^{-\mu_a r} B(E_a, \mu_a r), \tag{2.29}$$

where $\mathcal{R}(E_a)$ is the detector response function for photons of energy E_a, $\mu_a \equiv \mu(E_a)$ is the total attenuation coefficient for annihilation photons, $r = \sqrt{x^2 + y^2 - 2xy\cos\phi}$ the distance from the positron annihilation site on the beam to the detector, and $B(E_a, \mu_a r)$ the dose buildup factor.

2.2.2 Approximation of the Positron Travel Distribution

In order to evaluate Eq. (2.27) or (2.28), it is first necessary to obtain an explicit expression for $P_{\beta+}(E, z)$. This distribution can be expressed in terms of a related distribution $F(E, E_{\beta+})$ that is the probability a photon of energy E will, upon undergoing a pair-production interaction, produce a positron with an energy in unit differential energy about $E_{\beta+}$. The crow-flight distance z that a positron, with initial energy $E_{\beta+}$, travels before annihilation is taken here as the CSDA range $\Lambda(E_{\beta+})$. The inverse relation is denoted by

$$E_{\beta+} = \Lambda^{-1}(z). \tag{2.30}$$

For corresponding dz and $dE_{\beta+}$ intervals

$$P_{\beta+}(E, z)\, dz = F(E, E_{\beta+})\, dE_{\beta+}. \tag{2.31}$$

From this relation one then obtains

$$P_{\beta+}(E, z) = F(E, \Lambda^{-1}(z)) \frac{dE_{\beta+}}{dz}$$

$$= F(E, \Lambda^{-1}(z)) \frac{d\Lambda^{-1}(z)}{dz}. \tag{2.32}$$

Unfortunately, the distribution F, and consequently $P_{\beta+}$, is quite complex. Two highly simplified approximations are introduced here for $P_{\beta+}$ that allow Eq. (2.28) to be evaluated analytically.

Model 1 ("Mid-Range Model"): In this model, it is assumed that the positron travel distance z is the range corresponding to the average positron energy. Explicitly

$$P_{\beta+}(E,z) = \delta(z - \bar{\Lambda}(E)), \tag{2.33}$$

where $\bar{\Lambda}(E) \equiv \Lambda([E - 2m_e c^2]/2)$, i.e., the range of a positron with one-half of the kinetic energy of the positron-electron pair.

Model 2 ("Uniform-Travel Model"): In this approximation, the range of the positron is assumed to be uniformly distributed between zero and the maximum range a positron could have. Explicitly,

$$P_{\beta+}(E,z) = \begin{cases} 1/\Lambda(E - 2m_e c^2), & \text{if } 0 < z < \Lambda(E - 2m_e c^2), \\ 0, & \text{otherwise.} \end{cases} \tag{2.34}$$

2.2.3 Application to Monoenergetic Source Photons

The intensity of monoenergetic source photons with energy E_o along the beam is simply

$$I(E,y) = I_o\, e^{-\mu_o y}\, \delta(E - E_o) \tag{2.35}$$

where $\mu_o \equiv \mu(E_o)$, the total attenuation coefficient for source photons in air.

Model 1: Substitution of Eq. (2.35) into Eq. (2.27) gives

$$N_a(y) = \begin{cases} 2\mu_{pp}(E_o) I_o e^{-\mu_o(y - \bar{\Lambda}_o)}, & \text{if } y > \bar{\Lambda}_o, \\ 0, & \text{if } y < \bar{\Lambda}_o, \end{cases} \tag{2.36}$$

where $\bar{\Lambda}_o \equiv \bar{\Lambda}(E_o) = \Lambda([E_o - 2m_e c^2]/2)$. Substitution of this result into Eq. (2.29) then yields the following detector dose rate

$$D_a^o(x) = \mathcal{R}(E_a) \int_{\bar{\Lambda}_o}^{\infty} dy\, \frac{\mu_{pp}(E_o) I_o e^{-\mu_o(y - \bar{\Lambda}_o)}}{2\pi r^2}\, e^{-\mu_a r} B(E_a, \mu_a r), \tag{2.37}$$

or equivalently

$$D_a^o(x) = \mathcal{R}(E_a) \int_0^{\infty} dy'\, \frac{\mu_{pp}(E_o) I_o e^{-\mu_o y'}}{2\pi r'^2}\, e^{-\mu_a r'} B(E_a, \mu_a r'), \tag{2.38}$$

where $r' = \sqrt{(y' + \bar{\Lambda}_o)^2 + x^2 - 2x(y' + \bar{\Lambda}_o)\cos\phi}$.

This result has the same form as that used in the previous study [Sh92] for which no account was taken of positron travel, the only difference being that the beam distance y' is now replaced by $y' + \bar{\Lambda}_o$. Consequently, the positron travel correction of Model 1 is easily incorporated into the existing point kernel program for calculating the LBRF.

Model 2: Substitution of Eq. (2.36) into Eq. (2.28) gives

$$N_a(y) = \frac{2\mu_{pp}(E_o)I_o}{\mu_o\Lambda_o}\, e^{-\mu_o y}[e^{\mu_o\zeta_o(y)} - 1], \tag{2.39}$$

where $\zeta_o(y) = \min[y, \Lambda_o]$ and $\Lambda_o = \Lambda(E_o - 2m_ec^2)$. Substitution of this result into Eq. (2.29) then yields

$$D_a^o(x) = \frac{\mathcal{R}(E_a)\mu_{pp}(E_o)I_o}{2\pi\Lambda_o\mu_o}\int_0^\infty dy \frac{e^{-\mu_o y}}{r^2}[e^{\mu_o\zeta_o(y)} - 1]e^{-\mu_a r}B(E_a, \mu_a r). \tag{2.40}$$

2.2.4 Application to Bremsstrahlung Photons

As the source photons travel along the beam, they produce secondary electrons which, in turn, produce bremsstrahlung photons. If it is assumed that these secondary bremsstrahlung photons are (1) produced at the site of the secondary electron production and (2) that the bremsstrahlung is peaked in the forward direction so that the bremsstrahlung photons can be assumed to travel along the beam direction, then the intensity of bremsstrahlung photons along the beam is given by Eq. (2.15), namely

$$I_b(y, E_b) = \begin{cases} S_b(E_b)I_o[e^{-\mu_o y} - e^{-\mu_b y}]/[\mu_b - \mu_o], & \mu_b \neq \mu_o, \\ S_b(E_b)I_o e^{-\mu_o y}y, & \mu_b = \mu_,o \end{cases} \tag{2.41}$$

where $\mu_b \equiv \mu(E_b)$ and $\hat{S}_b(E_b)$ is the energy spectrum of bremsstrahlung photons ("thick-target spectrum") produced by secondary electrons which in turn were produced by source photons of energy E_o. The maximum energy of the bremsstrahlung spectrum is $E_b^{max} = E_o - 2m_ec^2$, and only those bremsstrahlung photons above $2m_ec^2$ can cause pair production.

Model 1: Substitution of Eqs. (2.33) and (2.41) into Eq. (2.28) gives

$$N_a(y) = \begin{cases} 2\int_{2m_ec^2}^{E_b^{max}} dE_b\, \mu_{pp}(E_b)I_b(y - \bar{\Lambda}_b), & \text{if } y > \bar{\Lambda}_b, \\ 0, & \text{if } y < \bar{\Lambda}_b, \end{cases} \tag{2.42}$$

where $\bar{\Lambda}_b \equiv \bar{\Lambda}(E_b) = \Lambda([E_b - 2m_ec^2]/2)$. With this result, Eq. (2.29) becomes

$$D_a^b(x) = \mathcal{R}(E_a)\int_{2m_ec^2}^{E_b^{max}} dE_b\, \mu_{pp}(E_b)\int_{\bar{\Lambda}_b}^\infty dy\, \frac{I_b(y - \bar{\Lambda}_b, E_b)}{2\pi r^2}\, e^{-\mu_a r}B(E_a, \mu_a r), \tag{2.43}$$

or equivalently

$$D_a^b(x) = \mathcal{R}(E_a)\int_{2m_ec^2}^{E_b^{max}} dE_b\, \mu_{pp}(E_b)\int_0^\infty dy'\, \frac{I_b(y', E_b)}{2\pi r'^2}\, e^{-\mu_a r'}B(E_a, \mu_a r'), \tag{2.44}$$

where $r' = \sqrt{(y' + \bar{\Lambda}_b)^2 + x^2 - 2x(y' + \bar{\Lambda}_b)\cos\phi}$.

Again, Model 1 yields a result of the same form as the uncorrected annihilation dose rate with y' simply replaced by $y' + \bar{\Lambda}_b$ and it thus easily incorporated into the existing LBRF program.

Model 2: Substitution of Eq. (2.272) into Eq. (2.28) yields

$$N_a^b(y) = 2I_o \int_{2m_ec^2}^{E_b^{max}} dE_b \frac{\mu_{pp}(E_b)S_b(E_b)}{(\mu_b - \mu_o)\Lambda(E_b)} \left\{ \frac{e^{-\mu_o y}}{\mu_o}[e^{\mu_o \zeta_b} - 1] - \frac{e^{-\mu_b y}}{\mu_b}[e^{\mu_b \zeta_b} - 1] \right\}, \tag{2.45}$$

where $\zeta_b = \min[y, \Lambda(E_b)]$. For those energies E_b such that $\mu_b = \mu_o$ the integrand in the above equation reduces to

$$\frac{\mu_{pp}(E_b)S_b(E_b)}{\mu_o \Lambda(E_b)} \left\{ e^{\mu_o \zeta_b} - 1 \right\}.$$

Finally, substitution of this result into Eq. (2.29) gives the contribution to the detector dose rate from bremsstrahlung produced annihilation photons as

$$D_a^b(x) = \mathcal{R}(E_a) \int_{2m_ec^2}^{E_b^{max}} dE_b \frac{\mu_{pp}(E_b)S_b(E_b)}{\Lambda(E_b)} \int_0^\infty dy \, \frac{I_b(y)}{2\pi r^2} \, e^{-\mu_a r} B(E_a, \mu_a r), \tag{2.46}$$

where

$$I_b(y) = \begin{cases} I_o \left\{ \frac{e^{-\mu_o y}}{\mu_o}[e^{\mu_o \zeta_b} - 1] - \frac{e^{-\mu_b y}}{\mu_b}[e^{\mu_b \zeta_b} - 1] \right\} / (\mu_b - \mu_o), & \text{if } \mu_b \neq \mu_o, \\ I_o \, e^{-\mu_o y} y [e^{\mu_o \zeta_b} - 1]/\mu_o, & \text{if } \mu_b = \mu_o. \end{cases} \tag{2.47}$$

2.3 Approximation of Needed Nuclear Data

To evaluate numerically the above models for the LBRF, many gamma interaction data for air are needed. Specifically, interaction coefficients, buildup factors, and positron ranges are needed for a wide range of energies. Many of these data are available in tabulated form; others such as buildup factors above 15 MeV are not available and had to be calculated for this project.

To avoid extensive sets of tabulated data and various energy interpolation techniques, it is possible to fit multi-parameter functions to the tabulated values of the needed nuclear data and to use these approximating functions whenever values of the data are needed. In this section, such empirical approximations to the needed air data are presented.

2.3.1 Interaction Coefficients

Gamma-ray interaction coefficient data for air were taken from references [Tr89, Cu80], and the tabulated data were fit to a wide variety of multi-parameter formulas

with the program TABLECURVE [Ja90]. Air was assumed to have the composition (by weight fraction): carbon (0.00014), nitrogen (0.75519), oxygen (0.23179) and argon (0.01288). The following formula was found to give excellent approximations for most of the mass interaction coefficients in air over the energy range 0.01 MeV to 100 MeV.

$$\mu_j(E)/\rho = 10^{f_j(\log_{10}(E))} \tag{2.48}$$

where the function $f_j(x)$ is

$$f_j(x) = \frac{a_0 + a_1 x + a_2 x^2 + a_3 x^3 + a_4 x^4 + a_5 x^5}{1 + b_1 x + b_2 x^2 + b_3 x^3 + b_4 x^4 + b_5 x^5}. \tag{2.49}$$

Here the subscript j denotes the type of interaction.

In these approximations the positron energy is in units of MeV and the mass interaction coefficients $\mu_j(E)/\rho$ in cm^2/g. The empirical coefficients a_n and b_n for the fits are given in Table 2.1.

Table 2.1. Parameters of Eq. (2.49) for the approximation of various mass interaction coefficients in air over the energy range 0.01 to 100 MeV.

	μ_{ph}	μ_{incoh}	$\mu_{tot-coh}$	μ_{tot}	μ_{en}
a_0	−5.411953857	−1.197066383	−1.197570951	−1.197148390	−1.558534822
a_1	−4.757725614	−0.949999366	−1.287939042	−1.255239241	−0.656955552
a_2	−6.099164835	−0.827908760	−0.478620029	−0.462805586	+0.337975295
a_3	−3.195266607	−0.544433391	−0.187140386	−0.183781928	−0.028192013
a_4	−0.561096127	−0.215300329	−0.159402680	−0.152173001	−0.479570878
a_5	−0.214401838	−0.032556304	−0.054576238	−0.052578736	−0.220448317
b_1	+0.499549111	+0.384881199	+0.668221483	+0.640028823	+0.303486701
b_2	+1.125996521	+0.429221785	+0.044919259	+0.043998833	−0.389069276
b_3	+0.209836111	+0.228570328	+0.116185742	+0.115072083	+0.084709952
b_4	+0.121207584	+0.036489965	+0.135682591	+0.130827016	+0.337659150
b_5	+0.003724012	−0.001333414	+0.026786314	+0.025457364	+0.077213621
%Err					
av	0.113	0.022	0.082	0.077	< 0.1
max	1.214	0.091	0.642	0.499	< 1

The interaction coefficient for pair production was fit over the range 1.022 MeV to 100 MeV with the formula

$$\mu_{pp}(E)/\rho = \sum_{n=0}^{10} a_n x^n \tag{2.50}$$

where $x = \log_{10}(E)$. The coefficients a_n are given in Table 2.2 below. Above 2 MeV this approximation has an average absolute deviation from the tabulated data of 0.062% with a maximum deviation of 0.44%. Between 1.022 and 1.5 MeV this approximation is poor; however, μ_{pp} is negligibly small in this energy region.

Table 2.2. Parameters in Eq. (2.50) for the approximation of the pair-production mass interaction coefficient over the range 0.01 to 100 MeV.

a_0	+5.228865308E-06	a_6	+0.000266593
a_1	−0.000448964	a_7	+0.000676182
a_2	+0.005342360	a_8	−0.000378873
a_3	+0.001886103	a_9	+4.607691079E-05
a_4	−0.001164943	a_{10}	+4.537544864E-06
a_5	−0.001169877		

2.3.2 Positron CSDA Range in Air

To correct the LBRF for positron transport by the methods proposed in Section 2.2, it is first necessary to be able to evaluate the positron range $\Lambda(E)$ in air. In this study the positron range was taken as the CSDA range which is tabulated in [IC82]. To avoid interpolation of the tabulated data, the following fit to the tabulated data was obtained:

$$\rho\Lambda(E) = 10^{\lambda(\log_{10}(E))} \tag{2.51}$$

where the function $\lambda(x)$ is

$$\lambda(x) = \frac{a_1 + a_2x + a_3x^2 + a_4x^3 + a_5x^4}{1 + b_1x + b_2x^2 + b_3x^3 + b_4x^4 + b_5x^5}. \tag{2.52}$$

The empirical coefficients a_i and b_i for the fit range $0.01 \leq E \leq 100$ MeV are given in Table 2.3

Table 2.3. Fit parameters for the Eq. (2.52) approximation of the CSDA positron range in air over the energy range 0.01 to 100 MeV.

i	a_i	b_i
1	−0.30573759	−0.00763379
2	+1.23660309	+0.35065179
3	−0.39492659	−0.06292815
4	+0.51295052	−0.00300923
5	−0.12342656	−0.00106880

In this approximation the positron energy is in units of MeV and the mass range $\rho\Lambda$ in g/cm^2. The maximum deviation between this approximation and the tabulated data is 0.038%.

2.4 Radiation Yield in Air

To calculate the thick target yield of bremsstrahlung produced by electrons in air using the Wyard approximation of Eq. (2.20), it is necessary to first evaluate the empirical constant C. This constant can be expressed in terms of the radiation yield $Y(T)$, the fraction of an electron's initial kinetic energy T that is emitted as photons as it thermalizes in an infinite air medium. Explicitly, $C = 16Y(T)/(13T)$.

The radiation yield $Y(T)$ for nitrogen can be approximated as

$$Y(T) = 10^{y(\log_{10}(E))} \tag{2.53}$$

where the function $y(x)$ is

$$y(x) = \frac{a_1 + a_2 x + a_3 x^2 + a_4 x^3}{1 + b_1 x + b_2 x^2 + b_3 x^3}. \tag{2.54}$$

By fitting the above expressions to yield data from [IC82], the empirical coefficients a_i and b_i for the fit range $0.01 \leq E \leq 100$ MeV were determined and are given in Table 2.4. The radiation yield for air can then be evaluated by multiplying Eq. (2.53) by the ratio of the average atomic number for air (7.225) to that for nitrogen (7).

Table 2.4. Parameters in Eq. (2.54) for the approximation of the thick-target radiation yield in nitrogen for electrons whose initial energy is in the range 0.01 to 100 MeV.

a_1	-2.396006067	b_1	-0.397306727
a_2	$+1.838708507$	b_2	$+0.336262525$
a_3	-0.994388033	b_3	$+0.018521651$
a_4	$+0.227334919$		

2.4.1 Buildup Factors

In the numerical evaluation of the LBRF, infinite medium buildup factors for the absorbed dose in air for a point isotropic source are needed.

For low energies ($E < 15$ MeV), the buildup factor $B(E, \mu r)$ in the integrand of Eq. (2.22) was taken to be the infinite medium exposure (air-kerma) buildup factor as approximated by the geometric progression (GP) model [Ha86] for a point isotropic source in air. This buildup-factor approximation is expressed as

$$B(E, \mu x) = \begin{cases} 1 + (b-1)\frac{(K^{\mu x}-1)}{(K-1)} & K \neq 1 \\ 1 + (b-1)\mu x & K = 1 \end{cases}, \tag{2.55}$$

where μx is the source-to-detector distance in mean-free-path lengths, b is the value of the buildup at 1 mean free path, and K is the multiplication per mean free path length and is approximated by

$$K(\mu x) = c(\mu x)^a + d\left[\frac{\tanh(\mu x/\xi - 2) - \tanh(-2)}{1 - \tanh(-2)}\right]$$

$$= c(\mu x)^a + d\left[1 - \frac{1 + \exp(4)}{\exp(2\mu x/\xi) + \exp(4)}\right]. \qquad (2.56)$$

The parameters a, b, c, d, and ξ, for this buildup factor approximation were taken from a revision of the QAD code [Rs86] and have recently been approved as a new buildup-factor standard [An91]. The values of these parameters vary with the photon energy, the shielding material, and the type of detector response. Parameters for the exposure (kerma) buildup factor in air are presented in Table 2.5.

At high energies ($E > 15$ MeV), no buildup factor data were available. Consequently it was necessary to compute the needed buildup factors in this energy range. The GP buildup factor approximation was then fit to these calculated values. Thus it was possible to use Eq. (2.55) over the full energy range 0.02 MeV to 100 MeV that was of interest in this study. In the section below, details of the buildup factor computations for the 10 to 100 MeV energy range are summarize. More complete information is provided in [Fa93].

2.4.2 Calculation of High-Energy Buildup Factors

Method of Calculation

The EGS4 code [Ne85] employed in these calculations made use of the PRESTA method [Bi86] for subdivision of the electron path length. Photons were tracked from source energy E_o to cutoff energy $E_{cut} = 10$ keV. Secondary electrons were tracked until their energies fell below 1 MeV. The only variance-reduction technique applied was exponential transformation of the photon path length. Electron and photon cross sections were generated using the PEGS4 code [Ne85]. Ordinarily, in determining the pair-production cross section, the PEGS4 code interpolates in tabulated values [St67] for energies less than 50 MeV and calculates cross sections for higher energies. For this work, the code was modified to use tabulated values for all photon energies. Atomic composition of air was as prescribed by ANS-6.4.3 [An91], namely 75.519% nitrogen by weight, 23.179% oxygen, 1.288% argon, and 0.014% carbon. Air density was taken as 0.0012 g cm^{-3}. In calculation of the absorbed dose in air, mass energy transfer and absorption coefficients, μ_{tr}/ρ and μ_{en}/ρ, were taken from the DLC-139 data library.[Rs88, Pl75, Jo80]

In the calculations, electrons and photons were tracked to distances r equivalent to as many as $\mu(E_o)r = 40$ mean free paths radially from the source, measured at

Table 2.5. Coefficients for the geometric progression form of the buildup-factor correlation for low energy photons in air. The "Max. Dev." is the maximum absolute deviation between the GP approximation and the buildup factors to which the GP approximation was fit over the range 0 to 40 mean free path lengths. From [An91]

Energy (MeV)	a	b	c	d	ξ	Max. Dev.
0.015	0.2167	1.17648	0.40953	−0.12538	12.46546	0.83%
0.020	0.1893	1.41631	0.47543	−0.10996	13.17036	1.34%
0.030	0.1143	2.30165	0.67197	−0.06318	12.74985	1.81%
0.040	0.0008	3.39496	1.04034	−0.01072	12.09683	0.65%
0.050	−0.0718	4.32342	1.38544	0.02813	13.21649	1.05%
0.060	−0.1169	4.81537	1.66130	0.05295	13.40168	1.90%
0.080	−0.1583	4.93526	1.97885	0.07171	13.63476	2.50%
0.100	−0.1799	4.56104	2.15575	0.07797	12.58171	2.27%
0.150	−0.1727	3.89109	2.14568	0.06853	14.31641	2.02%
0.200	−0.1746	3.34907	2.13884	0.06974	14.05719	2.11%
0.300	−0.1595	2.88692	1.98686	0.06177	13.99073	2.01%
0.400	−0.1449	2.63845	1.85412	0.05647	14.13847	1.87%
0.500	−0.1333	2.48289	1.75191	0.05304	13.90710	1.76%
0.600	−0.1212	2.36534	1.66164	0.04769	14.02672	1.52%
0.800	−0.1050	2.19612	1.54101	0.04362	13.78023	1.53%
1.000	−0.0898	2.09339	1.44260	0.03762	13.68232	1.25%
1.500	−0.0613	1.93203	1.27950	0.02723	13.48698	0.87%
2.000	−0.0444	1.82827	1.18906	0.02184	12.70825	0.95%
3.000	−0.0159	1.70545	1.06508	0.00737	11.71059	0.46%
4.000	0.0059	1.62521	0.98381	−0.00580	14.74790	0.32%
5.000	0.0207	1.56255	0.93337	−0.01492	12.94014	0.47%
6.000	0.0291	1.50882	0.90463	−0.02496	14.72248	0.74%
8.000	0.0415	1.42594	0.86792	−0.02660	11.81421	0.65%
10.00	0.0440	1.36386	0.85769	−0.02925	13.51159	0.81%
15.00	0.0533	1.26857	0.83193	−0.03967	14.08234	0.89%

the photon-source energy. However, buildup factors are reported for mean free paths only from 0 to 20. Mass interaction coefficients used in the EGS4 code are listed in Table 2.6. Photon energies and directions were extracted when photons crossed surfaces at selected values of r. From these data, the energy spectra of secondary-photon fluences, $\Phi_s(E,r)$, normalized to one source photon, were determined implicitly and absorbed-dose buildup factors were computed as

$$B(E_o,r) = 1 + \frac{1}{\Phi_o(r)E_o\mu_{en}(E_o)/\rho}\int_{E_{cut}}^{E_o} dE\ \Phi_s(E,r)E\mu_{en}(E)/\rho, \qquad (2.57)$$

where $\Phi_o(r)$ is the fluence of uncollided particles, namely, $e^{-\mu(E_o)r}/4\pi r^2$.

Table 2.6. Mass interaction coefficients used in the EGS4 calculations.

E_o (MeV)	$\mu(E_o)/\rho$ (cm^2/g)	$\mu_{tr}(E_o)/\rho$ (cm^2/g)	$\mu_{en}(E_o)/\rho$ (cm^2/g)
10	0.0204	0.0151	0.0145
15	0.0180	0.0142	0.0134
20	0.0170	0.0142	0.0132
30	0.0162	0.0143	0.0129
40	0.0160	0.0145	0.0127
50	0.0161	0.0149	0.0127
60	0.0162	0.0151	0.0125
70	0.0163	0.0154	0.0124
80	0.0165	0.0156	0.0123
90	0.0166	0.0159	0.0122
100	0.0168	0.0162	0.0122

Buildup Factor Results

Buildup factors for 10-MeV photons are examined in Fig. 2.5 and compared with results of moments method calculations [An91, Ch80]. The upper set of data (squares) are absorbed dose buildup factors computed using Eq. (2.57), which, in both numerator and denominator, uses the energy absorption coefficient μ_{en}, as is appropriate when the fluence energy spectrum $\Phi_s(E)$ accounts for bremsstrahlung. The moments method calculations are for air kerma. In order to make a comparison, in one set of EGS4 calculations (results shown as diamonds), production of bremsstrahlung was suppressed as was the displacement during slowing down of the positron created in pair production. This forced annihilation photons to be produced at the point of the pair-production interaction, an assumption inherent in the moments method. For that set of calculations, the air kerma buildup factor was computed using a variant of Eq. (2.57) in which μ_{en} was replaced by the energy transfer (kerma) coefficient μ_{tr}, as is appropriate when the fluence energy spectrum $\Phi_s(E)$ does not account for bremsstrahlung. The excellent agreement between the air kerma buildup factors provides validation of the use of the EGS4 code.

The fact that the absorbed dose buildup factor, say B_{en}, exceeds the air kerma buildup factor, say B_{tr}, is expected. For high energy source photons, secondary charged particles are produced preferentially in the forward direction, and their energy is subsequently deposited in the medium relatively farther from the source. Thus, within about a mean free path of the source, the total kerma $D_{tr}(E_o, r)$, which is proportional to $B_{tr}(E_o, r)\mu_{tr}(E_o)\Phi_o(r)$, exceeds the absorbed dose $D_{en}(r)$, which is proportional to $B_{en}(E_o, r)\mu_{en}(E_o)\Phi_o(r)$. However, farther from the source, the absorbed dose exceeds the kerma as energetic secondaries produced near the source deposit their energies. The minimum value of the ratio D_{en}/D_{tr} occurs as $r \rightarrow 0$ (where the Bs approach unity) and equals $\mu_{en}(E_o)/\mu_{tr}(E_o)$. The ratio of the two

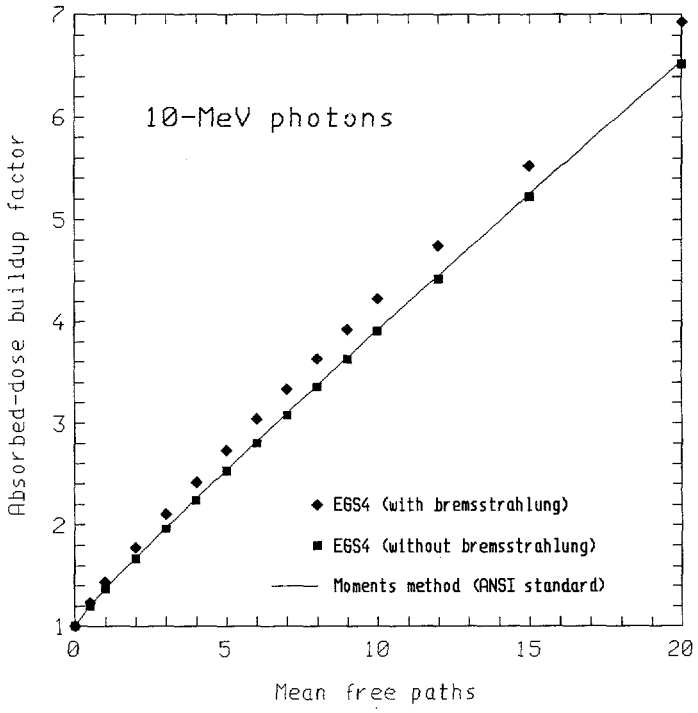

Figure 2.5. Comparison of the buildup factors for 10-MeV photons calculated using the Monte Carlo and moments methods.

buildup factors is simply

$$\frac{B_{en}(E_o,r)}{B_{tr}(E_o,r)} = \frac{D_{en}(r)}{D_{tr}(r)}\frac{\mu_{tr}(E_o)}{\mu_{en}(E_o)} \geq \left[\frac{D_{en}(r)}{D_{tr}(r)}\right]_{min}\left[\frac{\mu_{tr}(E_o)}{\mu_{en}(E_o)}\right] = 1. \qquad (2.58)$$

For source photons below a few MeV in energy, bremsstrahlung and positron-transport effects are negligible and electronic equilibrium is closely approximated, except very near the source. Consequently, the absorbed-dose and kerma buildup factors may be used interchangeably. This is explicitly done in the "exposure" buildup factors reported in Standard ANSI/ANS-6.4.3 [An91], which are actually B_{tr} values. However, when the total absorbed dose is calculated for energies above a few MeV, it important that B_{en} be used and that the absorbed dose from uncollided photons be calculated using the energy absorption coefficient μ_{en}/ρ.

Absorbed-dose buildup factors computed from photon fluences by Eq. (2.57) are presented in Table 2.7. Uncertainties, computed as the standard deviation of the mean value for ten trials, are less than 1% for 15 or fewer mean free paths and 3% for 20 mean free paths.

Table 2.7. Absorbed-dose buildup factors for photons in air computed from photon fluences calculated using the EGS4 Monte Carlo code for coupled electron and photon transport.

mean free paths	Photon Energy (MeV)										
	10	15	20	30	40	50	60	70	80	90	100
0.5	1.24	1.20	1.18	1.16	1.16	1.16	1.16	1.16	1.16	1.17	1.17
1	1.44	1.36	1.33	1.30	1.30	1.31	1.33	1.34	1.36	1.38	1.40
2	1.78	1.64	1.57	1.53	1.53	1.57	1.62	1.67	1.73	1.79	1.85
3	2.11	1.89	1.78	1.72	1.74	1.81	1.89	1.99	2.09	2.20	2.31
4	2.42	2.13	1.99	1.91	1.95	2.05	2.16	2.31	2.46	2.62	2.81
5	2.74	2.37	2.19	2.10	2.15	2.28	2.44	2.63	2.85	3.07	3.34
6	3.04	2.60	2.39	2.29	2.35	2.51	2.72	2.97	3.26	3.55	3.90
7	3.33	2.83	2.59	2.47	2.55	2.76	3.01	3.31	3.70	4.07	4.51
8	3.63	3.05	2.78	2.68	2.77	2.99	3.29	3.68	4.14	4.66	5.17
9	3.92	3.27	2.97	2.83	2.96	3.22	3.60	4.06	4.61	5.23	5.87
10	4.22	3.51	3.14	3.04	3.16	3.48	3.93	4.46	5.14	5.89	6.73
12	4.75	4.00	3.56	3.38	3.60	4.01	4.58	5.33	6.31	7.27	8.53
15	5.53	4.64	4.10	4.00	4.23	4.82	5.69	6.72	8.20	9.82	11.80
20	6.92	5.77	5.11	4.89	5.12	6.49	7.59	9.60	12.48	15.24	20.20

GP Buildup Factor Correlations

The data in Table 2.7 have been used to generate parameters for three commonly used buildup-factor correlations in terms of the mean-free-path distance between the source and detector $x = \mu(E_o)r$ [Fa93]. In particular, this study uses the resulting fit to the GP buildup factor approximation, Eq. (2.55). The correlation coefficients are presented in Table 2.8. The resulting geometric progression correlation had a maximum error of less than 1%, save for the highest energies for which the maximum deviation between the data and correlation slightly exceeds 1%.

Unlike previous tabulations of GP coefficients [Ha86] that were determined by a multistep fit procedure so that they varied smoothly with photon energy, the present coefficients were obtained by a simultaneous five-parameter minimization fit of the GP formula to the calculated buildup factor data. Since coefficients do not always vary continuously with energy, as can be seen from inspection of Table 2.8. Thus, when applying any correlation in determination of the buildup factor for arbitrary photon energy and source-to-detector distance, one should interpolate among buildup factors calculated for tabulated energies, not among coefficients for the correlation.

Table 2.8. Coefficients for the geometric progression form of the buildup-factor correlation for photons in air.

Energy (MeV)	a	b	c	d	ξ	Max. Dev.
10	0.091229	1.43245	0.76969	−0.05815	6.23291	0.32%
15	0.107053	1.36147	0.72474	−0.06088	7.78164	0.39%
20	0.101951	1.32233	0.72250	−0.04453	8.05175	0.48%
30	0.078499	1.28715	0.77095	−0.06878	13.22408	0.68%
40	0.088896	1.29297	0.76542	−0.06847	9.38404	0.31%
50	0.058493	1.30223	0.83687	−0.00767	6.23426	0.37%
60	0.046676	1.31855	0.88327	−0.04043	12.67235	0.56%
70	0.006063	1.33520	0.98051	0.02702	5.35244	0.65%
80	−0.007779	1.35151	1.04327	0.03035	5.83653	0.92%
90	−0.029070	1.37007	1.11056	0.04685	5.45224	1.05%
100	−0.046403	1.38530	1.18551	0.06058	6.36943	1.19%

2.4.3 Evaluation of the Buildup Factor in Air

The numerical evaluation of the integrals in the LBRF formulation of Eqs. (2.24) and (2.25), requires that the air buildup factor $B(E, z)$ be known for energies E between 0.02 and 100 MeV and for all penetration distances $z \equiv \mu(E)z$. In this study, the dose (kerma) buildup factor in air was based on the GP formulation of Eq. (2.55), and interpolation and extrapolation procedures were used to obtain values of B at any energy and for distances beyond those for which the GP approximation was made.

First the buildup factor $B(E, z)$ is evaluated at three adjacent energies E_{j-1}, E_j and E_{j+1} for which the GP parameters are tabulated where the selected tabulated energies are such that $E_{j-1} < E \leq E_j < E_{j+1}$.[3] Then from the logarithms of buildup factors evaluated at these three adjacent energies, a quadratic (parabolic) interpolation procedure is used to estimate the value of $B(E, z)$.

To evaluate $B(E_j, z)$ the GP approximation of Eq. (2.55) is used. For $E_j < 10$ MeV, $B(E_j, z)$ is based on parameters in Table 2.5 which are valid for penetration distances up to 40 mean free paths (mfp). For distances beyond 40 mfp, an extrapolation scheme implemented in the DANIEL program [Rs87] and the QAD program [Sa90] is employed. This scheme extrapolates the GP K parameter of Eq. (2.56) from its values at 35 and 40 mpf. This extrapolated value of K is then used in the GP formula to evaluate the buildup factor at distances beyond 40 mfp.

For $E_j \geq 10$ MeV, the GP parameters of Table 2.8 are used. These parameters are valid up to penetration distances of 20 mfp, beyond 20 mfp, a linear extrapolation of $B(E_j, z)$ is used based on values at 15 and 20 mfp.

[3] If E is between the two highest tabulated energies (i.e., between 90 and 100 MeV), then E_{j+1} is replaced by $E_{j-2} = 80$ MeV.

To avoid estimating buildup factors at excessive penetration distances, for which the above extrapolation procedures would give meaningless results, the buildup factor is limited to a maximum distance of 60 mfp. For greater penetration distances, the 60 mfp value is used. While this limiting value is incorrect, the contribution of beam scattering at such extreme distances is negligible in the numerical evaluation of the LBRF integral along the beam — see Eq. (2.24). The value of the LBRF is determined by scattering from the source beam along portions of the beam that are much closer to the detector.

The air buildup factor calculated by the above procedure is illustrated in Fig. 2.6. Also shown on this plot are tabulated buildup factor values which are in excellent agreement with the GP approximated values. To be noted are the exceptionally large values which occur around 0.1 MeV and which require quadratic-logarithmic interpolation to obtain reasonable interpolated values. The *attenuation factor* $A(E,z)$, defined by

$$A(E,z) = B(E,z)e^{-\mu(E)z}, \tag{2.59}$$

has been suggested as a preferable function for interpolation in energy, but as seen from Fig. 2.7 this function exhibits even larger variation below 0.1 MeV.

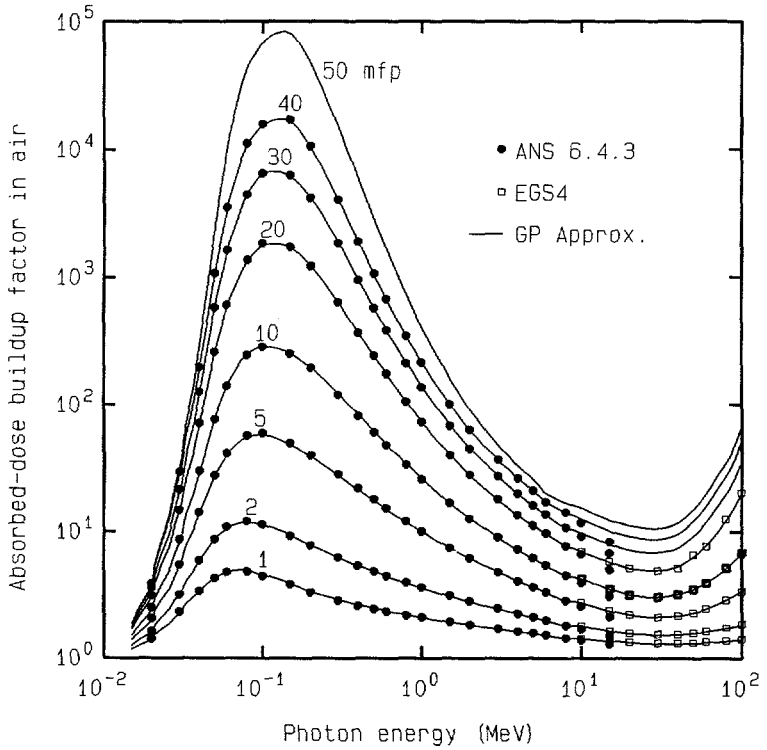

Figure 2.6. The absorbed-dose buildup factor for a point isotropic source in an infinite air medium. The solid circles are air-kerma values reported in [An91] and the hollow squares are absorbed-dose values [Fa93] calculated by EGS4. The curves are values calculated with the GP approximation.

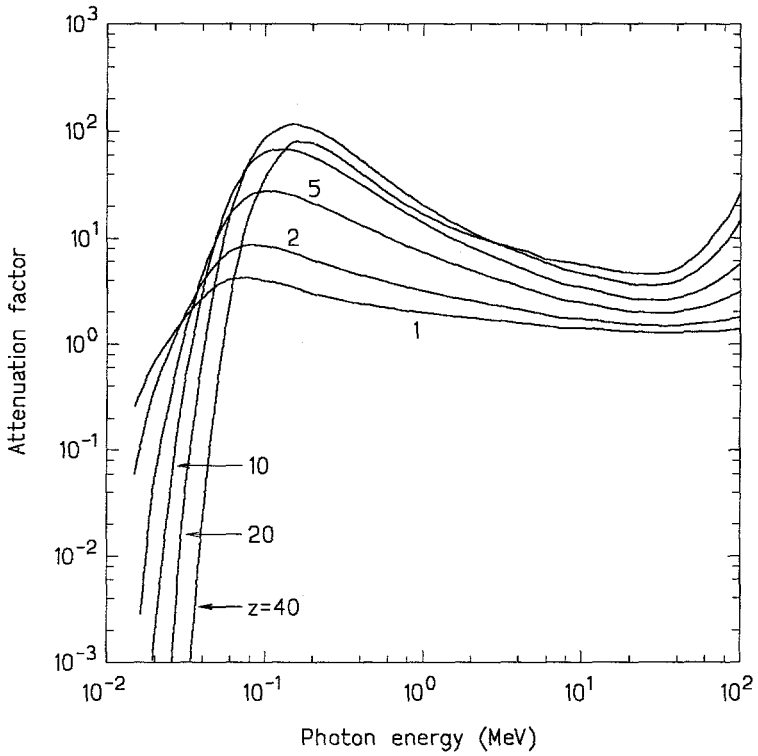

Figure 2.7. The absorbed-dose attenuation factor for a point isotropic source in an infinite air medium.

2.5 Numerical Evaluation of the LBRF

To evaluate the LBRF given by Eqs. (2.24) and (2.25), it is necessary to evaluate the integrals numerically. The integrands can be accurately evaluated using the data approximations described in the previous sections. In this section, the numerical methods used to evaluate the various LBRF integrals are summarized.

2.5.1 Integration Along the Beam

In the absence of bremsstrahlung, the LBRF of Eq. (2.24) can be written as

$$\Re(E, x, \phi) = \int_0^\infty d\hat{y}\, f(\hat{y}, x, E, \phi) \tag{2.60}$$

where the integrand $f(\hat{y}, x, E, \phi)$ is given by

$$f(\hat{y}, x, E, \phi) = \frac{e^{-\hat{y}}}{R^2}[(\mu/\rho)_s f_{KN}(E, \theta_s) B(E', r')\Re(E')\, e^{-r'} + (\mu/\rho)_{pp} B(E_a, r'')\Re(E_a) e^{-r''}], \tag{2.61}$$

where $\hat{y}$ is measured in units of mfp from the source along the beam direction. This positive integrand varies by many orders of magnitude over the effective integration range and not always in a monotonic manner.

The variation of the integrand with $\hat{y}$ and the source-to-detector distance x is shown in Fig. 2.8 for 2 MeV photons at an emission angle of 5 degrees. It is seen that the maximum value and the minimum value of the integrand differ by about 6 orders of magnitude over the range in which $\hat{y}$ changes from 0.05 to 1 mfp and the source-to-detector distance changes from 1 to 200 m. In this plot, there is a sharp ridge which is particularly pronounced at small source-to-detector distances and small $\hat{y}$ values. The accurate numerical integration over this ridge presents a challenge.

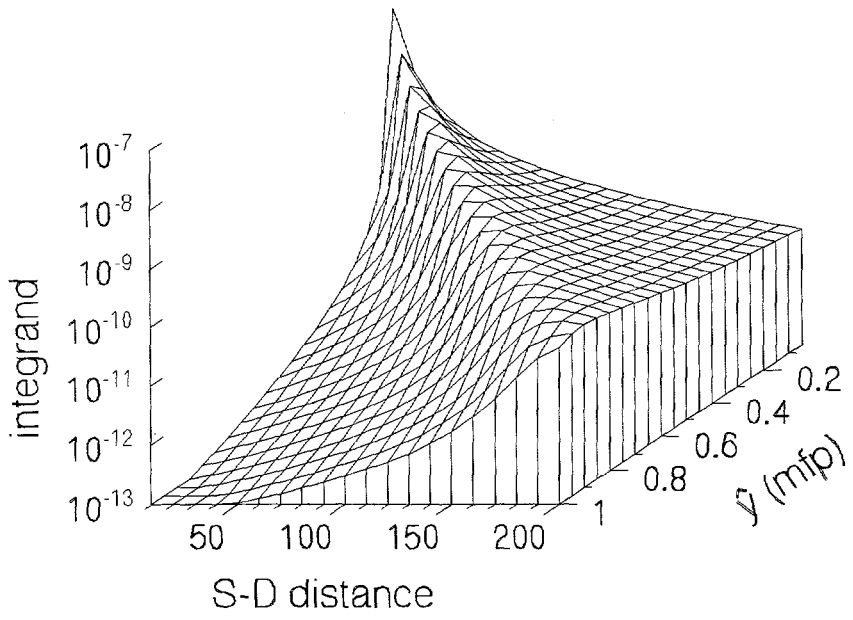

Figure 2.8. Variation of the integrand in Eq. (2.61) with the source-to-detector distance and the distance $\hat{y}$ along the beam for 2-MeV photons with a beam angle of 45 degrees.

Figure 2.9 shows the integrand as a function of $\hat{y}$ and emission angle ϕ for photons of energy 2 MeV and a source-to-detector distance of 100 m. In this case, the integrand varies smoothly over most of the $\hat{y}$ and ϕ range except in a small region about $\phi = 0.5$ degrees and $\hat{y} = 0.05$ where the integrand again exhibits a sharp peak. Numerical integration over this peak must be performed carefully to obtain accurate results.

Both examples have two common features: first, the integrand can change by many orders of magnitude and, second, there may be a sharp ridge for forward emission angles near the source. The ridge in the integrand shown in Figs. 2.8 and 2.9 is mainly caused by the $1/R^2$ term in Eq. (2.61). The value of $1/R^2$ has a maximum for that point on the beam that is closest to the detector, i.e., where y, x, and r in Fig. 2.1 form a right-angle triangle (i.e., $\hat{y}_{max} = x\cos\phi$ and $r_{min} = x\sin\phi$). The peak

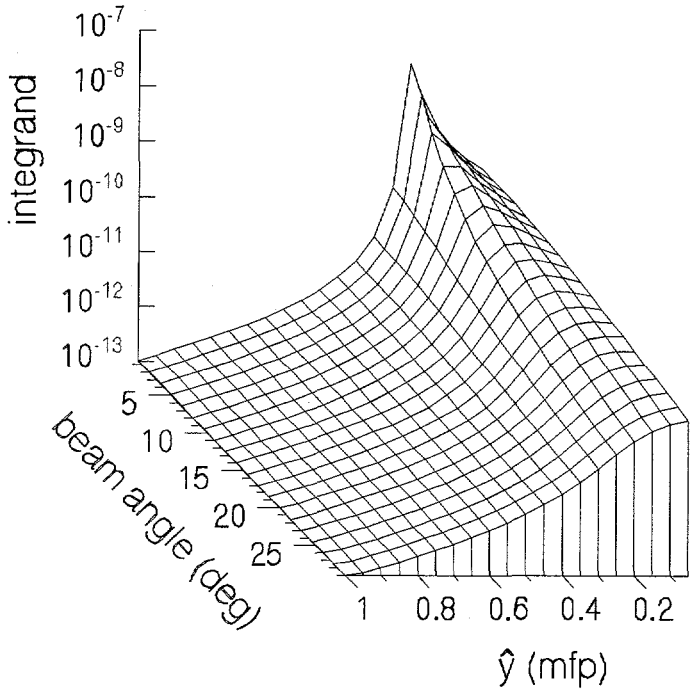

Figure 2.9. Variation of the integrand in Eq. (2.61) with the beam emission angle and the distance $\hat{y}$ along the beam for 2-MeV photons at a source-to-detector distance of 100 m.

in $f(\hat{y}, E, x, \phi)$ is most pronounced for small angles and disappears if ϕ is larger than 30 degrees. The sharpness of the peak in Figs. 2.8 and 2.9 and the large variation of the integrand make numerical evaluation of Eq. (2.60) difficult.

Several numerical quadrature schemes were investigated for evaluating Eq. (2.60) [Sh92]. The most accurate and robust method is one which breaks the integration along the beam into a sum of integrals over J contiguous subintervals, i.e.,

$$\Re(E, x, \phi) = \int_0^\infty d\hat{y}\, f(\hat{y}, x, E, \phi) \simeq \sum_{j=1}^{J} \int_{\hat{y}_{j-1}}^{\hat{y}_j} d\hat{y}\, f(\hat{y}, x, E, \phi), \qquad (2.62)$$

where $\hat{y}_j \equiv j\delta\hat{y}$ and $\delta\hat{y}$ is some appropriate subinterval width such as 0.5 or 1 mfp. The integral over each subinterval is then performed by using an adaptive 8-point Gauss-Legendre algorithm with automatic interval bisection. A subroutine from the SANDIA Mathematics Library [Ha78], called GAUS8, was used for this adaptive integration. This routine uses relative/absolute error control and a computed maximum refinement level when the integration limits and are close together so as to achieve any user-specified accuracy.

The number of subintegrals J needed to evaluate the LBRF is generally fairly small since the integrand $f(\hat{y}, x, E, \phi)$ falls off rapidly to negligible values after the first few mean-free-path lengths from the source, i.e., for $\hat{y} > 5$ mfp. In evaluating

Eq. (2.62), the number of subintegrals J was determined by either of the following two conditions: (1) the ratio of the integral from a subinterval to the cumulative integral from all proceeding subintervals is less than some user-prescribed value, say 10^{-4}, or (2) the ratio of the integral from one subinterval to that from the preceding subinterval is smaller than some user-prescribed value, say 10^{-2}. Generally, criterion (1) was preferred.

2.5.2 Evaluation of the Bremsstrahlung Spectrum

The evaluation of the bremsstrahlung spectrum $\hat{S}_b(E_b)$ defined by Eqs (2.12) and (2.13) requires an integration over recoil electron energies, namely

$$\hat{S}_b(E_b) = N \int_0^E dT \; \{Z_e \sigma_s(E,T) f_b(T,E_b) + \sigma_{pp}(E,T)[f_b(T,E_b) + f_b(E - 2m_e c^2 - T, E_b)]\Big\}. \qquad (2.63)$$

The thick target yield $f_b(T, E_b)$ was taken as the Wyard's approximation of Eq. (2.20). The integral over all recoil energies was then performed using the adaptive Gauss-Legendre subroutine GAUS8 [Ha78].

2.5.3 Integration over the Bremsstrahlung Spectrum

The evaluation of the bremsstrahlung component of the LBRF, Eq. (2.25), or of the bremsstrahlung-induced pair production component, Eq. (2.44) or Eq. (2.46), requires evaluation of double integrals of the form

$$\int_{E_{min}}^{E_{max}} dE_b \int_0^\infty d\hat{y} \; g(E_b, \hat{y}, x, E, \phi).$$

The inner integral along the beam was evaluated using the adaptive Gauss-Legendre method described above. To avoid excessive evaluation of the inner integral, the outer integral was evaluated using fixed quadrature ordinates between E_{min} and E_{max}. Since the integrand in the above expression is proportional to the bremsstrahlung spectrum $\hat{S}_b(E_b)$ which is highly peaked towards the low energies, the integration over E_b was split into two integrals, one from E_{min} to E_{mid} and one from E_{mid} to E_{max}. For each subintegral, fixed-point Gauss-Legendre numerical quadrature or order 4, 8 or 16 was used. Typically, the energy E_{mid} dividing the integration range was chosen by experience to obtain the best estimate of the bremsstrahlung contribution.

Chapter 3

Monte Carlo Evaluation of the LBRF

Although the single-scatter point-kernel model for the LBRF has previously been verified for photon energies between 0.1 and 10 MeV [Sh87, Sh91, Sh92], there are no benchmark experimental or calculated data for high energy skyshine. Thus in this study, the LBRF was also calculated by Monte Carlo techniques to obtain results against which the point kernel model could be compared as well as serve as an independent method whose results could be used in deriving approximations to the LBRF.

In this study the Monte Carlo code MCNP [Br93] was used to calculate the LBRF. This code, which can perform neutron, photon, and coupled neutron-photon, and electron transport calculations in general three-dimensional geometry, has been widely tested against benchmark problems[Wh91] and even against a benchmark skyshine experiment[Ol93]. Such comparisons have shown that MCNP can produce very accurate results for photon transport problems. From these and many other comparisons, MCNP has become widely accepted and was thought to be an excellent tool for this study to investigate the LBRF at high energies and to assess the accuracy of the point kernel model of the LBRF.

3.1 Using MCNP for the LBRF Problem

A rigorous description of high energy photon transport requires a detailed treatment of all secondary photons and electrons. Moreover, at energies above 10 MeV, the concept of doses and electronic equilibrium near such a beam of high energy photons must be analyzed carefully. In this section, the modeling of the LBRF by MCNP is described. Additional details may be found in [Br94].

3.1.1 The LBRF Geometry

The spatial distribution of doses around a photon beam in an infinite air medium exhibits a cylindrical symmetry about the beam. Thus, the point photon source was located at the origin of a cylindrical coordinate system with the source beam oriented vertically upward along the positive z-axis. The LBRF $\mathcal{R}(x, E, \phi)$ then is the dose per source photon at distance x from the origin along a conical surface making an angle ϕ with respect to the positive z-axis (see Fig. 3.1). The radiation field is the same at all points at distance x along the surface of this cone (i.e., on the circle formed by the intersection of a horizontal plane with the cone).

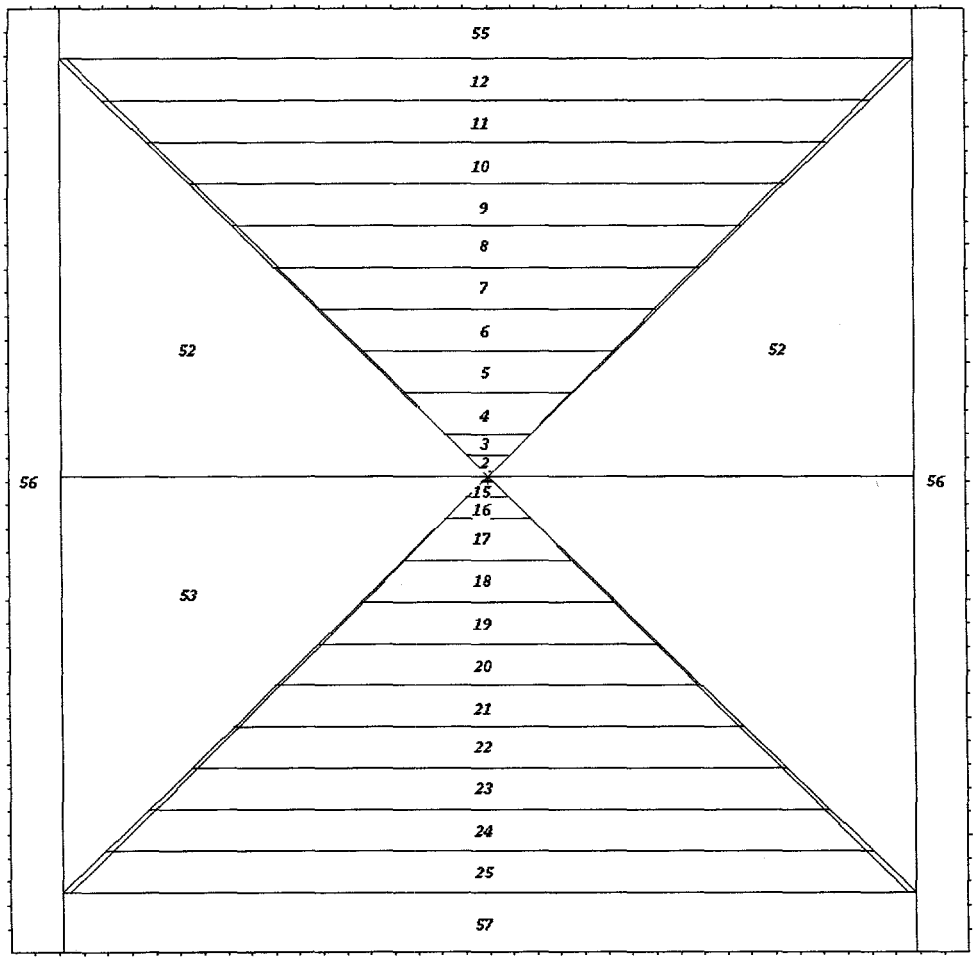

Figure 3.1. The MCNP cylindrical geometry used to model the LBRF. The monoenergetic source is at the origin (at the apex of the cones) and the photon beam is directed upward along the conical axis. All cells contain air, and the volumes formed by the horizontal planes and the nearly concentric conical surfaces are the detector volumes used.

Rather than use a point or ring detector, which are poorly suited for deep penetration problems, the photon flux density was estimated by a volumetric track-length detector. These ring-like volumetric detectors were defined by the intersection of horizontal planes with two concentric cones, both of which have their vertices at the origin but which have slightly different conical angles ($\phi \pm \Delta\phi$) as shown in Fig. 3.1. To simulate the infinite air medium, cell 55 in Fig. 3.1 extends radially outward 5 mean-free-path lengths while cells 56 and 57 are 10 mean-free-path lengths in thickness. The point monodirectional source, nominally at the origin, was placed 1 cm above the origin in cell 1 since a source cannot be placed on a surface in MCNP .

The air used in the MCNP simulation was that specified by ANSI-6.4.3[An91], namely 75.519% nitrogen, 23.179% oxygen, 1.288% argon, and 0.0014% carbon by weight. The air density was taken as 0.0012 g cm^{-1}.

3.1.2 The Transport Physics

With two exceptions, the full coupled photon/electron physics afforded by MCNP were used. Specifically, photons could produce electrons, coherent photon scattering was implemented, bremsstrahlung was produced by electrons, the full Bethe-Heitler Born approximation was used for bremsstrahlung angular distributions, expected-value straggling for electron energy loss was used, and all photon-induced secondary electrons were considered. The only simplification used was the neglect of electron-induced X rays and knock-on electrons. These two simplifications reduced significantly the computational effort while introducing little error in the calculated results for the high energy source photons considered in this study. An example LBRF calculated with and without these two simplifying assumptions is shown in Fig. 3.2, and the simplifications are seen to have negligible effect.

3.1.3 Choice of Tally

The average energy-integrated photon flux density in a cell was estimated using MCNP's "f4 tally" which computes the average path length per unit volume of the cell, i.e.,

$$\frac{1}{V}\int_V \int_E \Phi(\vec{r}, E)\, dE\, dV = \frac{1}{V}\langle W_i T_i \rangle \simeq \frac{1}{N}\sum_{i=1}^{N} \frac{W_i T_i}{V} \tag{3.1}$$

where W_i is the i-th photon's weight, T_i the track length of the photon in the cell, V the cell volume, and N is the number of photons that enter the cell. The above average can also include a response function $\mathcal{R}(E)$ so that the volumetric-averaged response in the cell is

$$R \equiv \frac{1}{V}\int_V \int_E \Phi(\vec{r}, E)\mathcal{R}(E)\, dE\, dV = \frac{1}{V}\langle W_i T_i \mathcal{R}(E_i) \rangle \simeq \frac{1}{N}\sum_{i=1}^{N} \frac{W_i T_i \mathcal{R}(E_i)}{V} \tag{3.2}$$

where E_i is the energy of the i-th photon entering the cell.

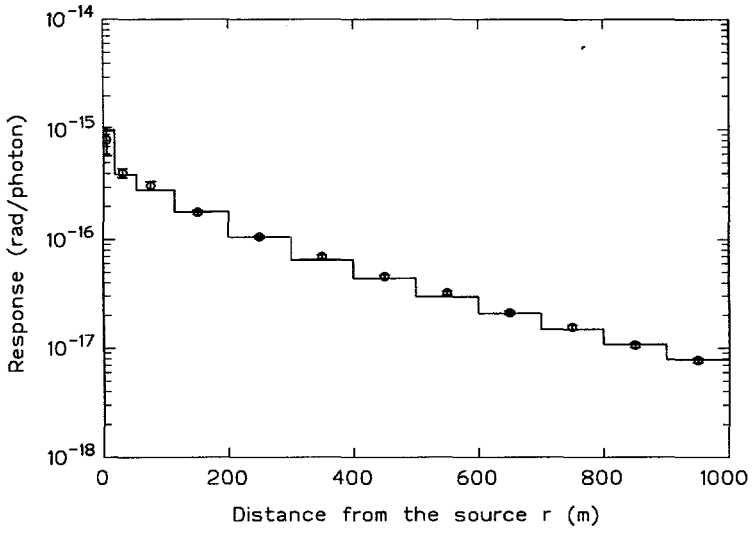

Figure 3.2. An MCNP calculated LBRF (100 MeV and a beam angle of 2 degrees) using the full physics treatment (points) with that produced by neglecting electron-induced X rays and knock-on electrons (histogram).

In the MCNP simulation of the LBRF, all secondary photons produced from Compton scattering, annihilation interactions, fluorescence emission, and bremsstrahlung emission are included in the photon flux density $\Phi(\vec{r}, E)$. Thus under the assumption of *electronic equilibrium*, the average air absorbed dose in a cell can be obtained by using a response function based on the mass energy absorption coefficient for air (μ_{en}/ρ), i.e.,

$$\mathcal{R}(E) = 1.602 \times 10^{-8}\, E \left(\frac{\mu_{en}}{\rho}\right), \tag{3.3}$$

where E is the photon energy in MeV, and $\mathcal{R}(E)$ has units of rad cm^2 if (μ_{en}/ρ) is in units of cm^2/g [Ch84].

The MCNP code allow provides a "flagged f8 tally" which estimates the energy deposition in a cell by both photons and electrons that enter the cell. This particular tally must be used carefully, since it can give misleading results especially if variance reduction techniques are used in the simulation [Br93]. For the LBRF problem, it is important to use variance reduction techniques, particularly for beams emitted in the backward directions. Nonetheless, the f8 tally does provide a mechanism to estimate absorbed doses in air under conditions in which electronic equilibrium does not exist. For 100 MeV photons near the source, previous studies [Fa93] have revealed significant deviations from electronic equilibrium.

Point Isotropic Source Example

To verify the proper operation of MCNP and to test its ability to treat high energy photon transport problems, the absorbed dose distribution arising from a 100 MeV point isotropic source in infinite air was calculated. In modeling this problem, spherical shells concentric to the source were used as cells in which the average absorbed doses were to be calculated. Also for this problem the f2 surface flux tally was used in place of the f4 tally because of its greater efficiency in this problem. The f2 tally is just a special case of the f4 track length per unit volume tally as the thickness of the f4 volume goes to zero.

The results obtained are shown in Fig. 3.3. Also shown are three values obtained from the buildup factors of Table 2.7 calculated from

$$R(r) = \frac{\mathcal{R}(E)e^{-\mu(E)r}B(E,\mu(E)r)}{4\pi r^2}. \tag{3.4}$$

From these results it is seen the true dose profile (f8 tally with electron transport) near the source is considerably less than that predicted from the photon flux and the assumption of electronic equilibrium (f2 tally), while at large distances from the source the actual dose is greater than that predicted from the f2 tally. The neglect of electron transport causes the f8 tally to overpredict the dose since electrons then deposit their energy where they are created, i.e., nearer the source.

In this problem the f2 tally is dominated by the uncollided photons moving radially outward from the source, thereby accounting for the exponential trend of the f2 results. The dose profile due only to secondary photons is shown in Fig. 3.4 along with values inferred from the buildup factors and obtained using Eq. (3.4), but with B replaced by $B - 1$. Notice that near the source where there is not electronic equilibrium, the dose inferred from the scattered flux density is far less than the true absorbed dose (shown on the previous figure).

LBRF Examples

The difference between using the f4 and f8 tallies to calculate the LBRF is shown in Figs. 3.5 and 3.6 for 100 MeV photons. For the 2-degree case of Fig. 3.5, the f8 tally is seen to give much greater estimates of the absorbed dose than the f4 tally. In this case the source photons along the beam produce energetic secondary electrons that travel mostly along the beam. These electrons then produce secondary bremsstrahlung that also mostly travel along the beam direction, which in turn produce cascades of low energy electrons. Near the beam, as in this 2-degree case, there will not be electronic equilibrium, and the f8 photon-electron absorbed dose, dominated by low energy electrons, will appear much higher than that predicted by the f4 tally of Eq. (3.2). Most of the f8 dose is no doubt due to relatively low energy electrons, which, if a human subject were present, would contribute primarily to skin dose. For the 45-degree case of Fig. 3.6, the detector volumes are removed from the strong divergence along the beam axis, and the f4 and f8 tallies are seen to agree much more closely.

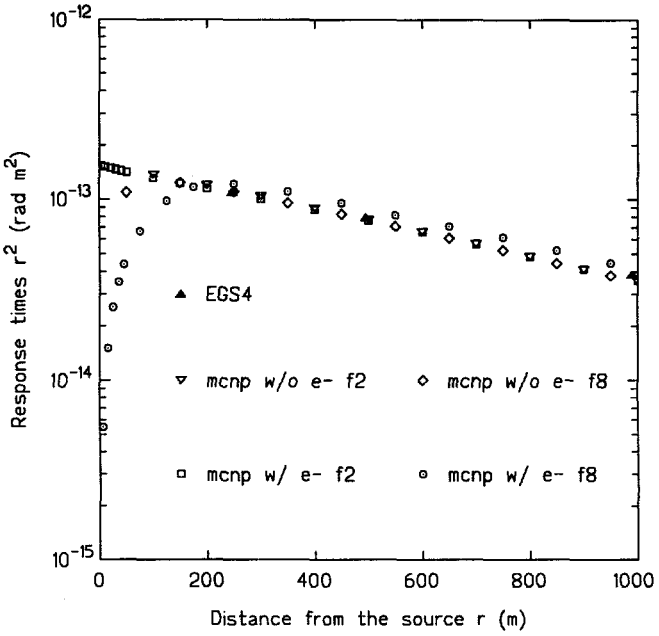

Figure 3.3. Total absorbed dose as a function of distance from a 100 MeV point isotropic source. The f2 tally results use Eq. (3.3) to convert the flux density to a dose, and the f8 tally results are actual energy absorptions converted to dose units. The `w/ e-` and `w/o e-` designation indicate electron transport was or was not used. The solid triangles are values inferred from buildup factors calculated with the EGS4 code.

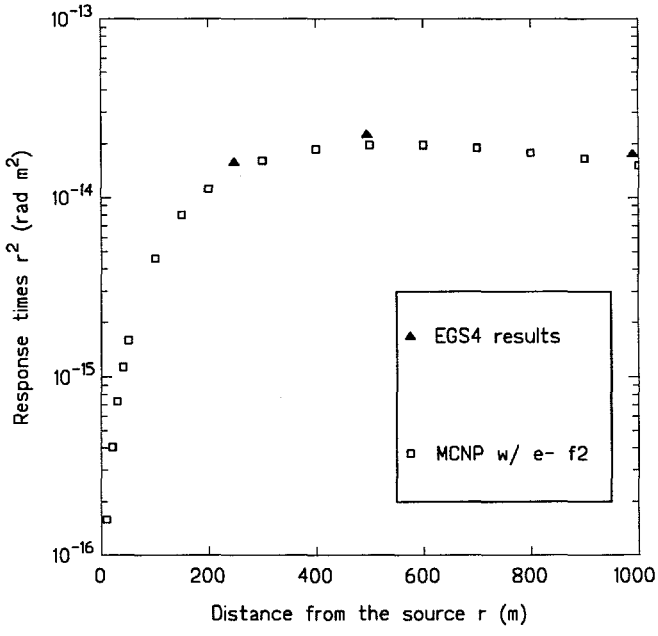

Figure 3.4. Absorbed dose from secondary photons as a function of distance from a 100 MeV point isotropic source. The f2 tally results use Eq. (3.3) to convert the flux density to a dose and employed coupled electron/photon transport. The solid triangles are values inferred from buildup factors calculated using the EGS4 code.

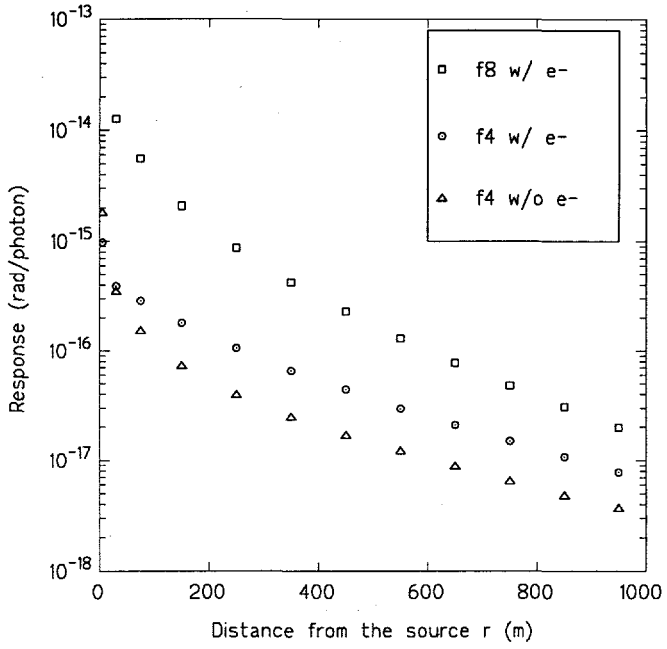

Figure 3.5. The MCNP calculated LBRF for 100 MeV photons emitted at 2 degrees using the f4 (circles) and f8 (squares) tallies. Also shown are f4 tally results (triangles) when electron transport was omitted.

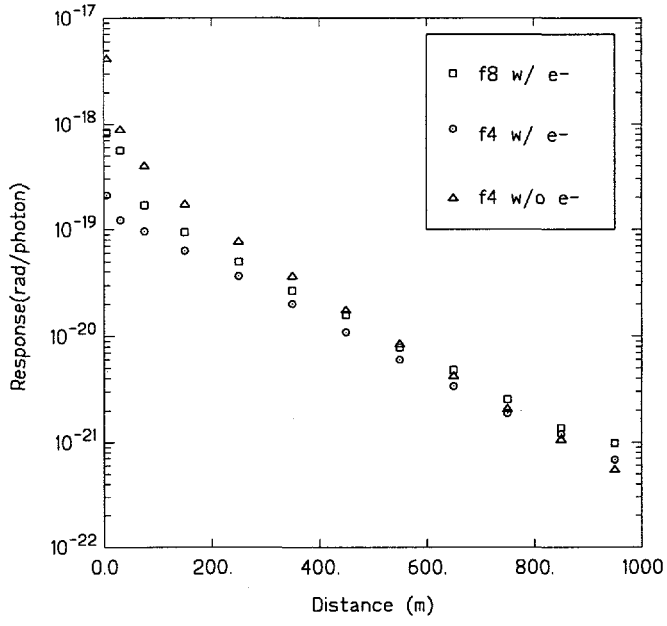

Figure 3.6. The MCNP calculated LBRF for 100 MeV photons emitted at 45 degrees using the f4 (circles) and f8 (squares) tallies. Also shown are f4 tally results (triangles) when electron transport was omitted.

Also shown in Figs. 3.5 and 3.6 are f4 tally results obtained when electron transport was omitted in the MCNP calculations. As would be expected, the effect of electron transport is to reduce the dose very near the source by allowing energetic secondary electrons to travel along the beam before producing secondary annihilation or bremsstrahlung photons. From the large differences in the f4 tallies with and without electron transport, it is clearly important to use the MCNP electron transport option for high energy photon sources.

Interpretation of LBRF Doses

As is apparent, for photon energies much in excess of 10 MeV and line beams passing near detector locations, lack of electronic equilibrium makes interpretation and application of dose tallies very uncertain. Both the f4 and f8 tallies are possible point functions that might be useful in characterizing the skyshine radiation field but both are for air dose, the f8 tally for the true absorbed dose and the f4 tally for what we might call the *equilibrium air dose* — the absorbed dose that would be experienced were secondary electrons in equilibrium with the photons. Which tally best serves to characterize the radiation risk to human subjects? It would seem that the f8 tally is the poorer choice. The tally includes local energy deposition in air due to electrons and positrons as well as photons. The electrons and positrons, contributing the bulk of the air dose, would contribute much of the shallow dose to the skin and eye lens but not the deep dose in the body. By contrast, the photon flux f4 tally estimates the dose strictly from the photon field, a dose that generally will be more penetrating. In Table 3.1 the response function of Eq. (3.3) is compared to two deep-dose phantom response functions for high energy photons. It is seen from this table that the point dose estimate based on Eq. (3.3) tracks quite well with the phantom deep dose.

Table 3.1. Comparison of response functions.

	Response function $\mathcal{R}(E)$, Gy cm^2 x 10^{10}		
	Eq. (3.3)	Slab Phantom[a]	Sphere Phantom[b]
E(MeV)	$\mathcal{R}_{D_{air}}$	$\mathcal{R}_{H_{I,d}}$	$\mathcal{R}_{H_{I,d}}$
1.0	0.0445	–	0.0531
10.	0.232	0.243	0.234
20.	0.423	0.416	0.403
30.	0.620	0.577	–
40.	0.814	0.732	–
50.	1.02	0.925	0.873
100.	1.95	1.53	1.46

[a]Maximum absorbed dose in a 30-cm thick slab phantom [Ic87]
[b]Maximum absorbed dose in a 30-cm diameter sphere phantom [Sa94]

In this study, it was decided that the more penetrating deep dose was of primary concern in evaluating the skyshine field. Thus in the subsequent evaluation of the

LBRF, the f4 tally, with Eqs. (3.2) and (3.3), is used exclusively. Only for very energetic source beams that pass near the volume of interest will this dose estimate be significantly underpredictive, and then primarily from the neglect of the shallow dose.

3.1.4 Energy Spectrum of the Skyshine

In Fig. 3.7, the energy spectrum of LBRF dose contribution made by the photons is shown at various distances from the source of 100 MeV emitted at an angle of 2° to the source-detector axis. These spectra were generated using the f4 tally with modified to bin each photons according to its energy. The spectra exhibit a continuous nature that becomes increasingly soften as the source-to-detector distance increases. Also evident in this figure at the annihilation photon peak at 0.51 MeV and its first slowing down discontinuity at 0.17 MeV (corresponding to the maximum change in the Compton wavelength of $\lambda_a + 2$ that an annihilation photon with wavelength $\lambda_a = m_e c^2 / E_a = 1$ can have in a single scatter. Also notice that the very low energy part of the spectrum decreases with increasing distance as photoelectric interactions preferentially remove the low energy photons.

3.1.5 Importance Sampling

Early experience with MCNP indicated that if skyshine doses far from the LBRF source are to be obtained, it would be necessary to use some of the variance reduction and biasing options available in this code. It was decided to use the powerful "weight windows" biasing technique which has many advantages over the simpler geometry splitting or importance sampling methods (also available in MCNP)[Br93]. The basic idea of weight windows is to first specify appropriate upper and lower weight bounds for each cell. Then if a particle entering into (or interacting in) a cell has a weight below the lower weight bound, Russian roulette is used either to increase the particle weight until it lies within the weight bounds or to terminate the particle. If the entering or interacting particle has a weight above the upper weight bound, the particle is split such that all split particles lie within the cell's weight bounds.

The establishment of weight bounds (in space and energy) is generally complex. Fortunately MCNP has a weight window generator that estimates appropriate weight windows for each cell. Thus by using multiple runs of MCNP , it is possible to obtain near optimal weight windows for a particular problem. For difficult problems, such as the LBRF emitted in the backwards direction (i.e., at angles greater that 90°), it was very important to accurate determine the weight windows to avoid instabilities in the results. Even with weight windows it was computationally prohibitive to calculate many of the LBRF for distances greater than 1000 m from the source. Thus in this phase of the study, the MCNP calculations of the LBRF were restricted to a maximum distance of 1000 m.

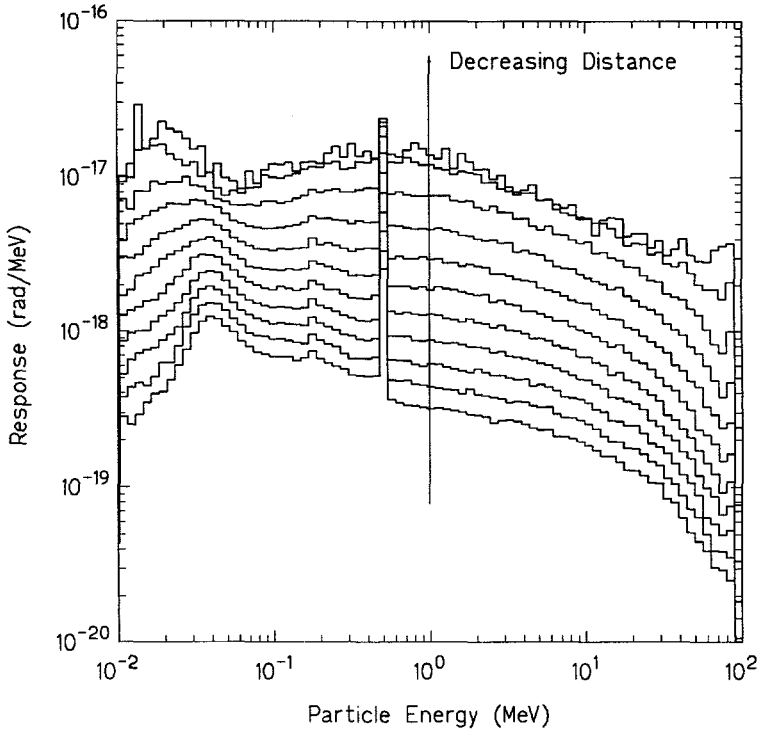

Figure 3.7. The MCNP calculated dose energy spectrum of photons contributing to the LBRF for a 100 MeV source emitting at 2 degrees from the source detector axis. Spectra are shown for distances of 30, 75, 150, 250, 350, 450, 550, 650, 750, 850, and 950 meters from the source.

3.2 Electron Transport Correction for the Point-Kernel LBRF Model

In the development of the point kernel model of the LBRF, two methods were proposed for correcting for the transport of energetic secondary electrons and positrons (see Section 2.2). To decide which of these two methods is the best, MCNP calculated LBRF using full electron transport were compared to results obtained with the point kernel model. The effect of positron/electron transport is most evident near the source and becomes increasingly important as the source energy increases. An example comparison is shown in Fig. 3.8.

The travel correction has the most importance for those positrons created near the source by the source photons causing pair production interactions. These energetic positrons travel primarily in the beam direction, and, if their transport is neglected, their subsequent annihilation will produce annihilation photons closer to the source than actually occurs thereby causing the skyshine dose near the source to be larger

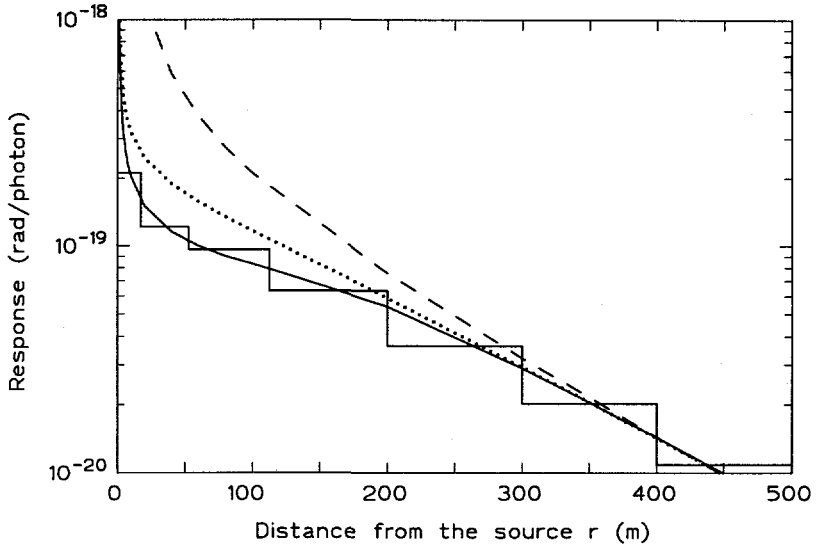

Figure 3.8. The MCNP calculated LBRF (histogram) for a 100 MeV beam emitted at 45 degrees to the source-detector axis. The smooth lines represent results obtained from the point kernel model of the LBRF using various electron/positron travel correction approximations. The dashed line is for no travel correction, the dotted line is for the "uniform travel" correction method, and the solid line is for the "mid-range" model.

than it should be. Fig. 3.8 clearly shows that near-field skyshine analyses, neglect of positron travel can significantly overpredict the dose.

From fig. 3.8 and other comparisons, it was found the mid-range correction method gives better agreement to MCNP results near the source. However, far from the source, both correction methods give almost the same results as those obtained without any correction. Finally, for source energies below 10 MeV, no electron/positron travel correction appears to be necessary. In all subsequently reported calculations using the point kernel LBRF model, the mid-range method is used.

3.3 Comparison of MCNP and Point-Kernel Results

To assess the capabilities of the point kernel LBRF model, MCNP LBRF were performed for a grid of energies between 0.01 and 100 MeV and for grid of beam angles between 1.5 and 175 degrees. These computed LBRF values were then compared to corresponding values obtained from the point kernel model. Because of the computationally intensive nature of the MCNP calculations, the MCNP evaluations were

limited to source-to-detector distances less than 1000 m. The point kernel model, by contrast, can be used to estimate skyshine dose at distances several times this limit.

Representative examples of these LBRF comparisons are shown in Figs. 3.9 to 3.16. Detailed tables of all the MCNP results are available in [Br94]. From these comparisons it is seen that the point kernel model agrees well with the MCNP at all beam angles for energies below about 20 MeV. For higher energies the point kernel model, while giving good agreement in the backward directions, tends to increasingly underpredict the skyshine dose as the energy increases and the beam angle decreases. Clearly, for high-energy, forward-directed beams, the straight-ahead approximation used in the point kernel model to account for bremsstrahlung is too severe and approximation.

The primary purpose of this study was to produce simple approximations for the LBRF over as large a source-to-detector range as possible. From these comparisons it is evident than point kernel calculations can be used for source energies less than 20 MeV. However, for higher-energy sources it was decided to use the MCNP results as the basis of approximating the LBRF. These approximations are discussed in the next chapter.

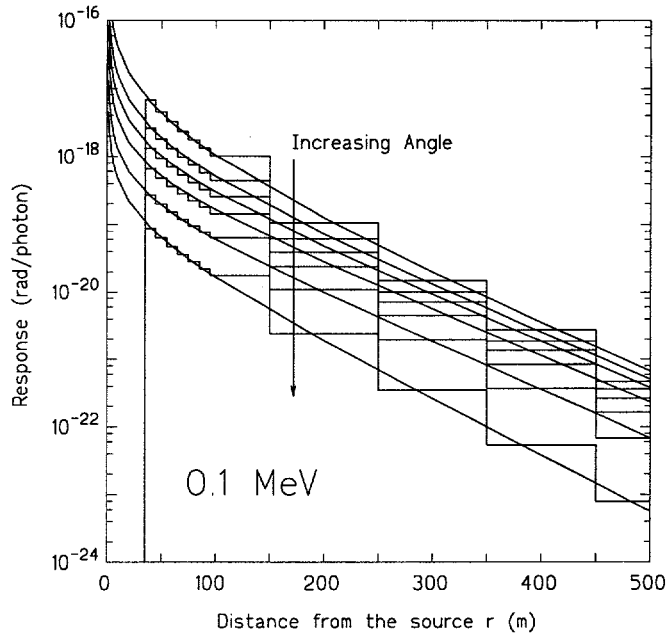

Figure 3.9. Comparison of the single-scatter point-kernel LBRF (smooth lines) to MCNP calculations (histograms) for 0.1 MeV photons. The six LBRF angles are 2, 5, 10, 20, 45, and 150 degrees.

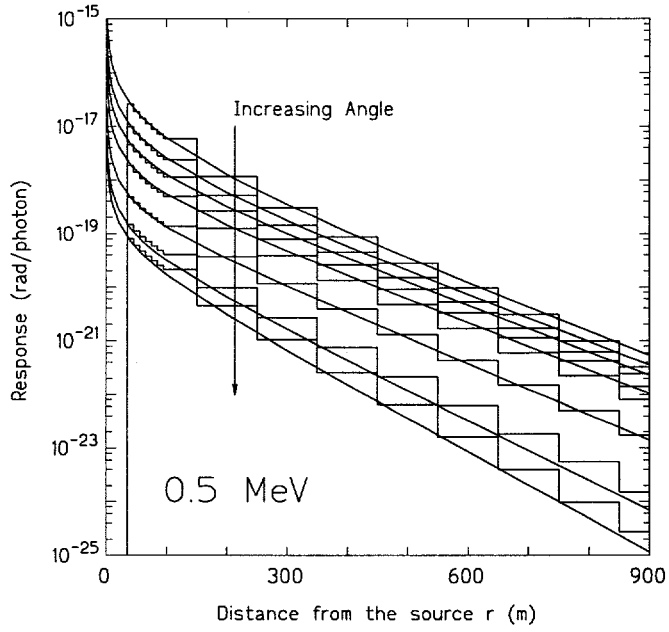

Figure 3.10. Comparison of the single-scatter point-kernel LBRF (smooth lines) to MCNP calculations (histograms) for 0.5 MeV photons. The seven LBRF angles are 2, 5, 10, 20, 45, 90, and 150 degrees.

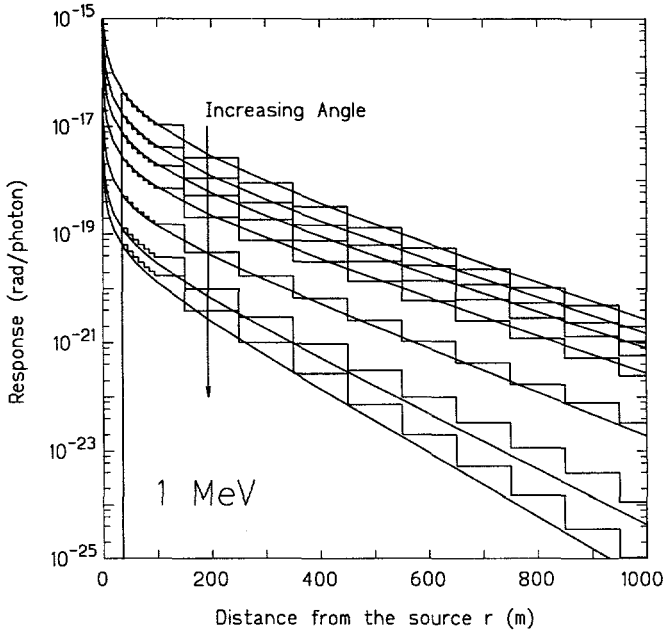

Figure 3.11. Comparison of the single-scatter point-kernel LBRF (smooth lines) to MCNP calculations (histograms) for 1 MeV photons. The seven LBRF angles are 2, 5, 10, 20, 45, 90, and 150 degrees.

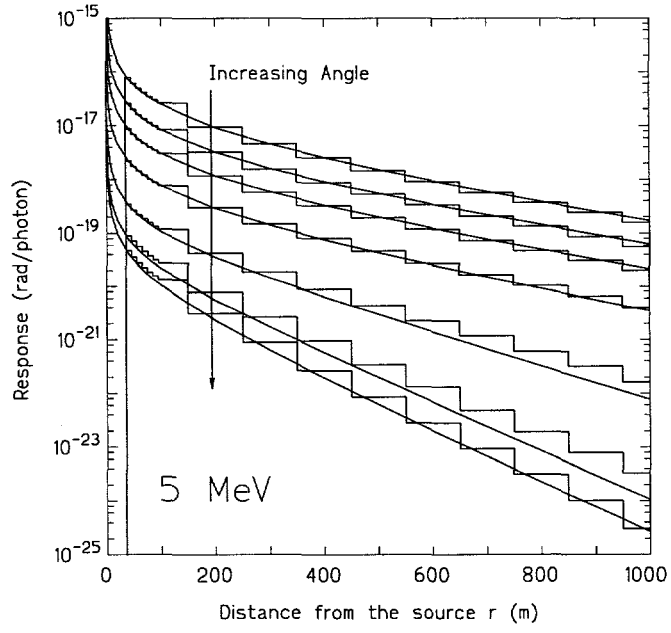

Figure 3.12. Comparison of the single-scatter point-kernel LBRF (smooth lines) to MCNP calculations (histograms) for 5 MeV photons. The seven LBRF angles are 2, 5, 10, 20, 45, 90, and 150 degrees.

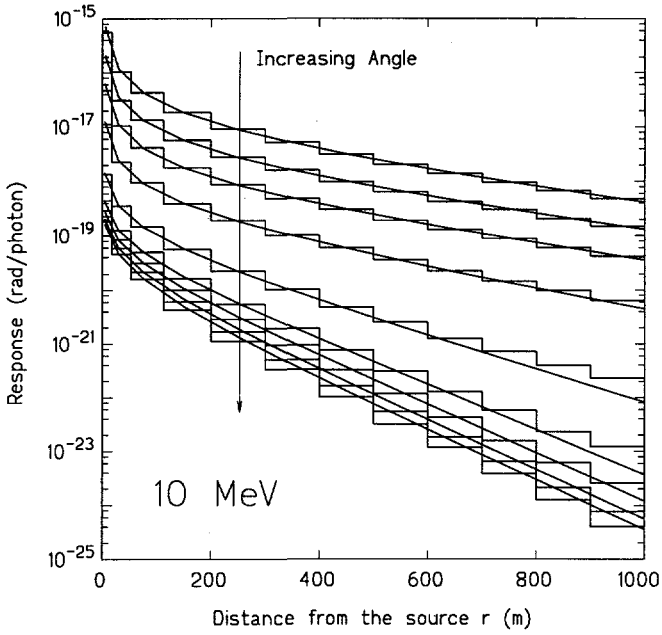

Figure 3.13. Comparison of the single-scatter point-kernel LBRF (smooth lines) to MCNP calculations (histograms) for 10 MeV photons. The nine LBRF angles are 2, 5, 10, 20, 45, 75, 95, 120, and 150 degrees.

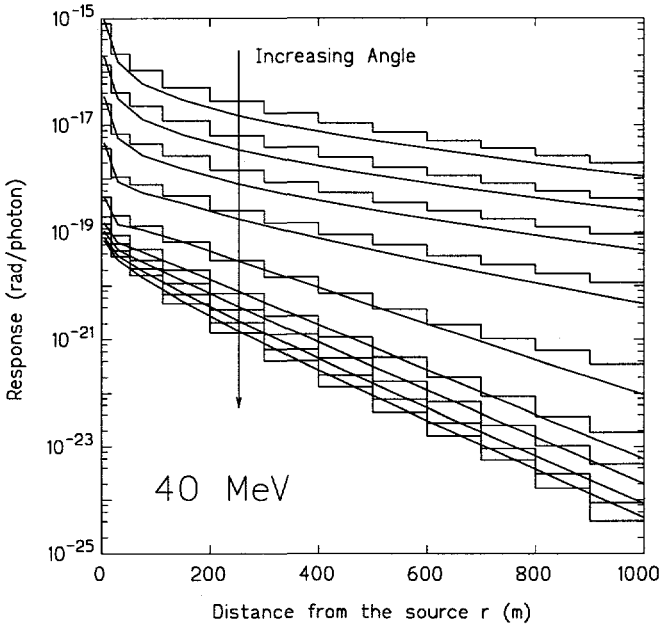

Figure 3.14. Comparison of the single-scatter point-kernel LBRF (smooth lines) to MCNP calculations (histograms) for 40 MeV photons. The nine LBRF angles are 2, 5, 10, 20, 45, 75, 95, 120, and 150 degrees.

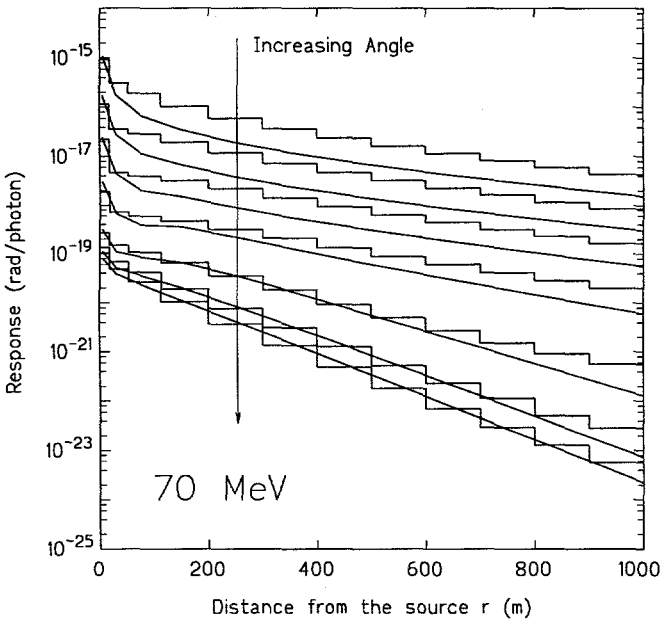

Figure 3.15. Comparison of the single-scatter point-kernel LBRF (smooth lines) to MCNP calculations (histograms) for 70 MeV photons. The seven LBRF angles are 2, 5, 10, 20, 45, 75, and 95 degrees.

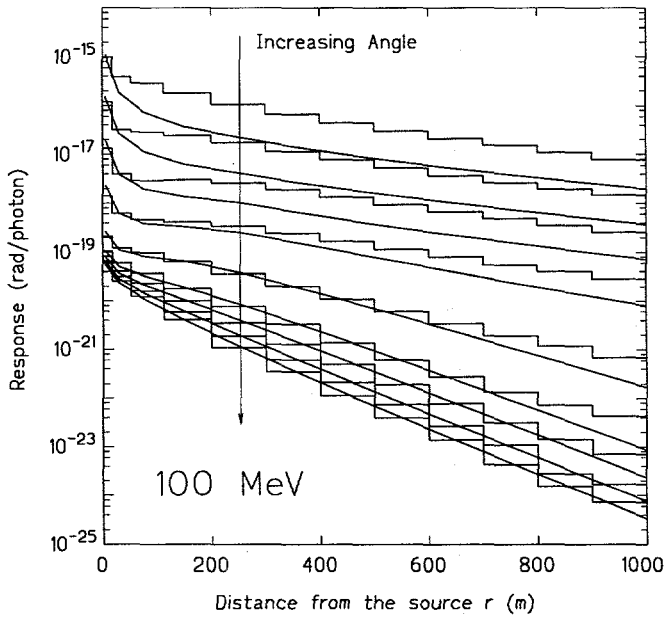

Figure 3.16. Comparison of the single-scatter point-kernel LBRF (smooth lines) to MCNP calculations (histograms) for 100 MeV photons. The nine LBRF angles are 2, 5, 10, 20, 45, 75, 95, 120, and 150 degrees.

Chapter 4

Approximation of the LBRF

Compared to Monte Carlo techniques, calculating the line-beam response function (LBRF) by the point kernel technique (discussed in the previous chapter) is considerably expensive computationally. However, for routine skyshine analyses and calculations, even the point kernel method is prohibitively expensive, and an approximate procedure is needed to reduce the computational effort even further.

It has been found that the LBRF $\Re(x, E, \phi)$ can be approximated by an appropriate empirical formula with a few adjustable parameters. The first approximate LBRF was obtained by Radiation Research Associates (RRA) by fitting an empirical formula with three adjustable parameters to results obtained by Monte Carlo skyshine calculations. This approximate function then formed the basis of the SKYSHINE series of codes [Pr76, La79].

Shultis and Faw [Sh87] later fitted the three-parameter RRA formula to point kernel LBRF results for use in the MICROSKYSHINE code [Gr87]. A set of revised parameters was obtained by least-squares fitting the approximating formula to point kernel results. An interpolation and an extrapolation scheme were also introduced to make the approximate LBRF continuous in both energy and emission angle. The resulting data set of fitting parameters used by MICROSKYSHINE could treat skyshine sources with energies from 0.1 MeV to 10 MeV and source-to-detector distances from 30 to 2500 m.

The omission of energies below 0.1 MeV and the relatively coarse energy mesh used between 0.1 and 1 MeV is generally satisfactory for far-field skyshine calculations since low energy source photons usually are of minor importance. However, for near-field calculations with low-energy sources, there is a need for an improved approximate LBRF to treat energies below 1 MeV. Recently, Shultis et al. [Sh92] revised the energy grid for lower energy photons and obtained approximations for the LBRF valid for the energy range 0.02 MeV to 10 MeV.

In this study, the energy range is extended above 10 MeV and a new approximation for the LBRF is proposed for source energies between 10 and 100 MeV and which is

valid for source-to-detector distances from 100 to 1000 m. Additionally, two refined LBRF approximations are given for source energies between 0.02 and 15 MeV and for source-to-detector distances between 1 and 3000 m.

4.1 Approximating the LBRF

It is possible to approximate the LBRF defined by Eqs. (2.24) and (2.25), and modified for positron migration by the methods of Section 2.2, by a number of simple approximate functions with a few adjustable parameters. To separate explicitly the principal energy dependence of the response function, the LBRF is approximated as

$$\Re(x, E, \phi) \simeq E\kappa F(x, a, b, c, \ldots). \tag{4.1}$$

The fitting parameters a, b, c, ... of the approximating function F are functions of the source photon energy E and the beam emission angle ϕ. The beam response $\Re$ has units of rad per photon, E has units of MeV per photon and x has units of meters. The function $F(x, a, b, c, \ldots)$ is the fraction of the source photon energy absorbed per m^3 of air. The conversion factor κ thus has units of rad absorbed dose per MeV/m^3 energy absorption in air at the reference air density for the calculations.

4.1.1 Estimation of Fit Parameters

Once a particular approximating function $F(x, a, b, c, \ldots)$ is chosen (see the following subsection), the values of the parameters $a, b, c, \ldots$ can be obtained for a given beam energy and direction by fitting the approximating function to values of the LBRF evaluated at a set of discrete source-to-detector distances $x_m, m = 1, \ldots, M$, i.e., to $\Re(x_m, E, \phi)/(\kappa E) \equiv \Re_m/(\kappa E)$. In this study, the reference LBRF values $\Re_m$ were calculated from the point kernel model of Chapter 2 for $E < 10$ MeV or by MCNP for $E > 10$ MeV.

To fit an approximating function $F(x, a, b, c, \ldots)$ to LBRF data $\Re_m/(\kappa E)$, some criterion must be specified *a priori* for adjusting the parameters $a, b, c, \ldots$ so as to obtain close agreement between the approximation and the LBRF data. In this study the following three criteria were investigated.

Least Squares Fit to Logarithm of LBRF

The LBRF $\Re(x, E, \phi)$ is strongly affected by the source-to-detector distance and the skyshine dose may vary by many orders of magnitude when x varies by a few hundred meters. Thus, it is preferable to obtain the parameters $a, b, c, \ldots$ by fitting, not F, but rather its logarithm to the logarithm of the LBRF. With this method, the LBRF

is approximated by choosing values of the fitting parameters $a, b, c, \ldots$ such that

$$\ln F(x, a, b, c, \ldots) \simeq \ln[\Re(x, E, \phi)/(\kappa E)]. \tag{4.2}$$

For a fixed source energy E and beam emission angle ϕ, the least squares estimations of $a, b, c, \ldots$ are those parameter values which minimize

$$S_1(a, b, c, \ldots) \equiv \sum_{m=1}^{M} [\ln F(x, a, b, c, \ldots) - \ln(\Re_m/\kappa E)]^2, \tag{4.3}$$

Minimize Maximum Fractional Deviation

A widely used criterion for fitting approximations to a set of data is to choose the fitting parameters so as to minimize the maximum absolute deviation between the fit and the data. Because the LBRF varies so widely over the source-to-detector range of 1 to 3000 m, the fractional or relative difference is used. Thus $a, b, c, \ldots$ are chosen so that

$$S_2(a, b, c, \ldots) \equiv \max_m \left| 1 - \frac{(\kappa E) F(x_m, a, b, c, \ldots)}{\Re_m} \right| \tag{4.4}$$

is minimized.

Minimize Average of Fractional Deviations

A modification of the above criterion is to minimize the sum of the absolute fractional differences between the approximating function and the LBRF. This is equivalent to minimizing the average of the absolute fractional deviations between the data and the fitting function. In this method, fit parameters $a, b, c, \ldots$ are chosen to minimize the following function.

$$S_3(a, b, c, \ldots) \equiv \sum_{m=1}^{M} \left| 1 - \frac{(\kappa E) F(x_m, a, b, c, \ldots)}{\Re_m} \right|. \tag{4.5}$$

For all three of these fitting criteria, the minimization of the objective function $S_i(a, b, c, \ldots)$ is readily accomplished using the simplex procedure [Pr92].

4.1.2 Reference Values of the LBRF

Before obtaining an approximation for the LBRF, it is first necessary to obtain reference values $\Re_m$ of the LBRF at different distances from the source for each beam energy and direction for which an approximate LBRF is desired. Because the point kernel model of the LBRF was found to be sufficiently accurate for photon energies below 15 MeV, it was used to generate the reference LBRF values. For higher energies MCNP was used to generate the necessary reference values.

For the low-energy point-kernel calculations, the LBRF was evaluated at the 28 distances x_m, at the 15 discrete energies E_i, and at the 20 discrete beam directions ϕ_j (see Table 4.1). For the MCNP calculations above 15 MeV, spatial cells centered about the following 12 source-to-detector distances were used: 5, 30, 75, 150, 250, 350, 450, 550, 650, 750, 850, and 950 m. The discrete energies E_i selected were 10, 20, 40, 70 and 100 MeV, and the 17 discrete beam angles ϕ_j that were used are listed in Table 4.2. The MCNP reference LBRF values used to obtain an approximate LBRF for high energy photons have been tabulated by Brockhoff [Br94].

Table 4.1. Source-to-detector distances x_m (meters), photon energies E_i, and beam angles ϕ_j used in the point kernel LBRF reference calculations for photon energies below 15 MeV.

Source-to-detector distances x_m (m):

m	x_m	m	x_m	m	x_m	m	x_m	m	x_m
1	1	7	20	13	300	19	1000	25	2250
2	2	8	40	14	400	20	1200	26	2500
3	4	9	60	15	500	21	1400	27	2750
4	6	10	80	16	600	22	1600	28	3000
5	8	11	100	17	700	23	1800		
6	10	12	200	18	800	24	2000		

Beam energies E_i (MeV):

i	E_i	i	E_i	i	E_i	i	E_i	i	E_i
1	0.02	4	0.06	7	0.20	10	1.0	13	7.0
2	0.03	5	0.08	8	0.40	11	2.0	14	10.0
3	0.04	6	0.10	9	0.70	12	4.0	15	15.0

Beam angles ϕ_j (degrees):

j	ϕ_j	j	ϕ_j	j	ϕ_j	j	ϕ_j	j	ϕ_j
1	0.5	5	6.0	9	25.0	13	65.0	17	110.0
2	1.5	6	8.5	10	35.0	14	75.0	18	130.0
3	2.5	7	12.5	11	45.0	15	85.0	19	150.0
4	4.0	8	17.5	12	55.0	16	95.0	20	170.0

4.1.3 Selection of the Approximating Function

Many formulas can be used for fitting function F to approximate the LBRF. One of the initial purposes of this study was to seek alternate fitting formulas for the LBRF to that previously used. To find alternate fitting formulas, the microcomputer program TABLECURVE [Ja90] was used. This program fits a given set of (x, y) data to many hundred fitting formulas and produces statistical information about each fit. It then ranks the different fits in decreasing order of the goodness of the fit as determined by the r^2 correlation coefficient. The program also allows one to see the

Table 4.2. The discrete beam directions ϕ_j (degrees), with respect to the source-detector axis, used for deriving reference LBRF values for energies above 15 MeV.

j	ϕ_j	j	ϕ_j	j	ϕ_j	j	ϕ_j	j	ϕ_j
1	2.0	5	10.0	9	45.0	13	95.0	17	150.0
2	3.5	6	15.0	10	60.0	14	105.0		
3	5.0	7	20.0	11	75.0	15	120.0		
4	7.5	8	30.0	12	85.0	16	135.0		

estimated confidence bands around the fit, the residuals, and, most importantly, how the fit behaves outside the x-range of the data. An example of the rankings of the first 76 formulas used by TABLECURVE for a typical LBRF fit is shown in Table 4.3.

To approximate the LBRF, one seeks a simple formula (i.e., one with only a few parameters) that not only gives a good fit over the data range but one that also behaves reasonably when extrapolated past the last datum. TABLECURVE was used to fit representative LBRF point kernel data for low and high photon energies and for small and large beam angles. Based on a balance between a good fit to the data, simplicity of the fitting formula, and proper asymptotic behavior at large x, those formulas with more than four parameters were not considered.

The best fitting formula with four adjustable parameters was found to be

$$\ln[F(x,a,b,c,d)] = a + b\,x + c\,\ln x + d\,x^2, \tag{4.6}$$

the best among the three-parameter formulas was

$$\ln[F(x,a,b,c)] = a + b\,\ln x - c\,x, \tag{4.7}$$

and the best among the two-parameter formulas was

$$\ln[F(x,a,b)] = a + b\sqrt{x}. \tag{4.8}$$

The parameters in these formulas are still functions of the photon energy E and emission angle ϕ. Interestingly, formula (4.7) is the same approximating function used by RRA to represent the original line-beam response function [Pr76, La88].

Recently, a new version of TABLECURVE (version 3.0) was released that increased the number of formulas for approximating the input data to several thousand. In particular, the number of three parameter formulas was increased from 27 to 630 different formulas. Representative LBRF point kernel data have recently been analyzed by this new version of the program. Again Eq. (4.7) was found to be either the best or second best of the three parameter formulas. One formula which yielded a slightly better fit for high energy sources was considerably worse at low energy. Thus Eq. (4.7), originally introduced with little justification, now appears to be a very astute choice.

Table 4.3. The equations used by TABLECURVE [Ja90] to fit the LBRF. The r^2 values are for fitting to point kernel LBRF results for 3.5 MeV photon at an emission angle of 45 degrees and for source-to-detector distances from 1 to 3000 meters.

Rank	r^2	Equation
1	0.999986784	y=(a+bx+cln(x)+dx2)
2	0.999983793	y=(a+bx+cln(x)+dexp(-x))
3	0.999981885	y=(a+bx+cln(x)+d/x2)
4	0.999977734	y=(a+bx+cln(x)+dsqrt(x))
5	0.999966853	y=(a+bx+cln(x)+d/x)
6	0.999965859	y=(a+bx+cln(x)+dx3)
7	0.999965568	y=(a+bx+cln(x))
8	0.999886711	y=(a+cx+ex2+gx3+ix4+kx5)/(1+bx+dx2+fx3+hx4+jx5
9	0.999824100	y=(a+cx+ex2+gx3+ix4)/(1+bx+dx2+fx3+hx4+jx5)
10	0.999788045	y=(a+cx+ex2+gx3+ix4)/(1+bx+dx2+fx3+hx4)
11	0.999758396	y=(a+cx+ex2+gx3)/(1+bx+dx2+fx3+hx4)
12	0.999571195	y=(a+cx+ex2+gx3)/(1+bx+dx2+fx3)
13	0.999477716	y=(a+bx+c/x+dsqrt(x))
14	0.999059623	y=(a+bx+csqrt(x)+dexp(-x))
15	0.999058343	y=(a+bx+cx2+dx3+ex4+fx5+gx6+hx7+ix8+jx9+kx10)
16	0.998914975	y=(a+bx+csqrt(x)+d/x2)
17	0.998684487	y=(a+bx+cx2+dx3+ex4+fx5+gx6+hx7+ix8+jx9)
18	0.998599909	y=(a+cx+ex2)/(1+bx+dx2+fx3)
19	0.998308829	y=(a+bx+csqrt(x)+dx2)
20	0.998139449	y=(a+bsqrt(x)+cx2)
21	0.998125158	y=(a+bx+cx2+dx3+ex4+fx5+gx6+hx7+ix8)
22	0.997949142	y=(a+bx+csqrt(x)+dx3)
23	0.997704006	y=1/((a+cx+ex2)/(1+bx+dx2))
24	0.997381553	y=(a+bx+c/x+dexp(-x))
25	0.997356687	y=(a+bx+cx2+dx3+ex4+fx5+gx6+hx7)
26	0.997087051	y=(a+bx+csqrt(x))
27	0.997050439	y=(a+bx+c/x+dx2)
28	0.996812046	y=((a+cx+ex2)/(1+bx+dx2))
29	0.996605050	y=(a+bx+cx2+dx3+ex4+fx5+gx6)
30	0.996376560	y=1/((a+cx)/(1+bx+dx2))
31	0.996206689	y=(a+bx+c/x+d/x2)
32	0.996078913	y=(a+bx+c/x+dx3)
33	0.995831741	y=(a+bx+cx2+dx3+ex4+fx5)
34	0.995798418	y=(a+bsqrt(x)+cx3)
35	0.995354403	y=(a+bx+cx2+dexp(-x))
36	0.994988939	y=(a+bx+cx2+d/x2)

Table 4.3. (cont.):

Rank	r^2	Equation
37	0.994663233	y=(a+bx+cx2+dx3+ex4)
38	0.993993224	y=(a+bx+cx3+dexp(-x))
39	0.993583705	y=(a+bx+c/x2+dx3)
40	0.992857540	y=(a+bx+cx2+dx3)
41	0.992823326	y=(a+bx+c/x)
42	0.991416880	y=((a+cx)/(1+bx+dx2))
43	0.989948137	y=(a+bx+c/x2+dexp(-x))
44	0.989783884	y=(a+bx+cx2)
45	0.989560417	y=(a+bx+cexp(-x))
46	0.989030837	y=(a+bx+c/x2)
47	0.987628576	y=(a+bx+cx3)
48	0.987524653	y=1/((a+cx)/(1+bx))
49	0.986630980	y=((a+cx)/(1+bx))
50	0.980963339	y=(a+bx)
51	0.980326577	y=(a+bln(x)+csqrt(x))
52	0.976763918	y=(a+bln(x)+cx2)
53	0.972450550	y=1/(a+bx+cx2+dx3+ex4)
54	0.968988761	y=1/(a+bx+cx2+dx3)
55	0.968086424	y=(a+b/x+csqrt(x))
56	0.967276292	y=(a+bsqrt(x)+cexp(-x))
57	0.967254806	y=(a+bsqrt(x)+c/x2)
58	0.966964866	y=(a+bsqrt(x))
59	0.961787417	y=1/(a+bsqrt(x))
60	0.945617104	y=(a+bln(x)+cx3)
61	0.930547347	y=(a+bx2+cx3)
62	0.910399712	y=1/(a+bx+cx2)
63	0.881016930	y=(a+b/x+cx2)
64	0.862562487	y=(a+bx2+cexp(-x))
65	0.860796660	y=(a+bx2+c/x2)
66	0.852790865	y=1/(a+bln(x))
67	0.831747013	y=(a+bx2)
68	0.812584302	y=1/(a+bx)
69	0.782989034	y=(a+b/x+cx3)
70	0.763944860	y=(a+bln(x)+c/x)
71	0.756049099	y=(a+bx3+cexp(-x))
72	0.753688193	y=(a+b/x2+cx3)
73	0.737016402	y=(a+wn(x)+cexp(-x))
74	0.732439718	y=(a+bln(x)+c/x2)
75	0.714115818	y=(a+bx3)
76	0.685126772	y=(a+bln(x))

The residual between a fitting formula and the LBRF of Eq. (2.24), for a fixed source energy E and emission angle ϕ, is defined as

$$R(x) = \ln F(x) - \ln[\Re(E, x, \phi)/\kappa E]. \tag{4.9}$$

An illustration of the residuals obtained with the three fitting formulas, Eqs. (4.6) to (4.8), for 3.5 MeV photons at an emission angle of 2.5 degrees is given in Fig. 4.1. Obviously, the two parameter formula should not be used for this fitting because of its large residuals both near and far from the source. While the four-parameter formula looks a little bit better than the three parameter formula, the three-parameter formula is still reasonably accurate over the full 1 to 3000 m source-to-detector range. Based on a balance between the goodness of the fitting and the computational effort, the three-parameter formula of Eq. (4.7) is a good choice.

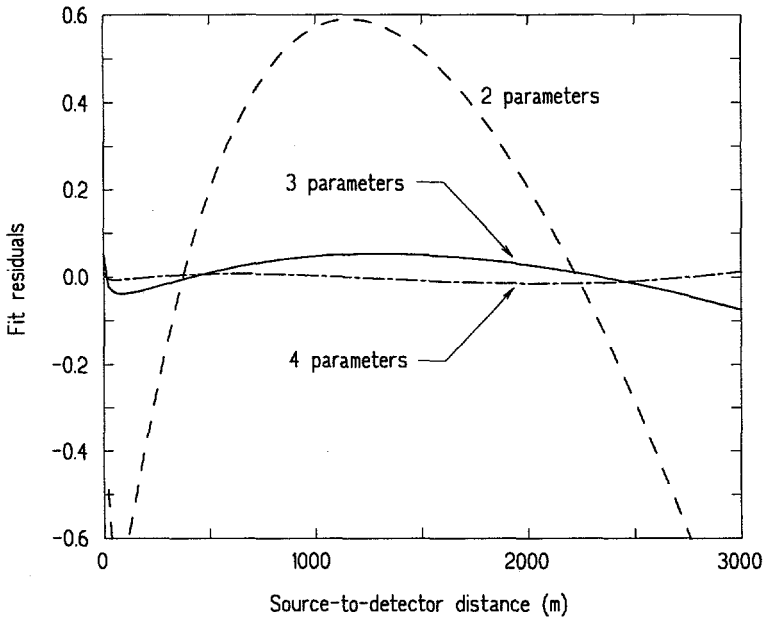

Figure 4.1. Residuals for the three approximating formulas Eqs. (4.6)-(4.8) for the LBRF at a photon energy of 2 MeV and for a beam angle of 45 degrees.

Recently, another four-parameter approximating function has been proposed for the LBRF, namely [Ha94]

$$\ln[F(x, a, b, c, d)] = a + b \ln x - cx - dx \ln x \tag{4.10}$$

This fitting formula was found to be superior to that of Eq. (4.6) for energies less than a few MeV. However, for energies above 10 MeV, it does not approximate the LBRF as well as Eq. (4.6). Consequently, for the low-energy approximation to the LBRF this formula, along with Eq. (4.7), was fitted to the reference LBRF values for beam energies below 10 MeV.

4.2 Improved LBRF Approximations

4.2.1 A Three-Parameter Approximation

From the experience gained with TABLECURVE, it was apparent that the three-parameter formula of Eq. (4.7) to approximate the LBRF is a good choice. Therefore, Eq. (4.1) can be expressed as

$$\begin{aligned} \Re(x, E, \phi) &\simeq \kappa E \exp[\ln F(x, a, b, c)] \\ &\simeq \kappa E x^b \exp[a - c\,x]. \end{aligned} \tag{4.11}$$

In this section the results of fitting the this three-parameter formula to the reference LBRF values are presented.

The fitting parameters a, b, and c were determined in this study for 20 discrete energies E_i and for 20 or 17 (depending on the energy region) discrete beam angles ϕ_j (see Tables 4.1) and 4.2. Compared to LBRF energies used in previous studies [La88, Sh91], this energy set has three new features. The first is that, while the original energy had a lower limit of 100 keV, the new energy range is extended down to 20 keV. The second is that there are more energies in the lower energy range than in the higher, since the skyshine dose rate varies much more rapidly with energy in the lower energy range. The third is that the upper energy range has been extended from 10 MeV to 100 MeV. The angular structure used for energies below 15 MeV, listed in Table 4.1, is the same as that used in earlier studies [La88, Sh91].

For each discrete beam energy and angle, the parameters, a, b, and c of Eq. (4.11), were found by minimizing one of the objective functions $S_i(a, b, c)$, $i = 1, 2, 3$ for source-to-detector distances x_m from some minimum distance (1 m for the point kernel data or 100 m for the MCNP data) to a maximum range x_M . The maximum range was taken to be 3000 m or the distance x_M at which $\Re_M$ becomes less than some prescribed value, e.g., 10^{-30} rads per photon. Although greater fit ranges can be achieved than those limited by the 10^{-30} rads per photon criterion, the point kernel reference values used in such a fit would be unreliable since the point kernel model would make use of buildup-factor approximations beyond their range of applicability.

The variation of x_M with energy E is shown in Fig. 4.2 for the three emission angles of 1.5, 45, and 150 degrees. As would be expected, the x_M range increases with increasing energy and with decreasing emission angle. For smaller emission angles, x_M increases faster than for larger emission angles. The approximate LBRF of Eq. (4.11) for low energy photons in the backward directions has a maximum fit range considerably less than the 3000 m desired. Nevertheless, this approximation may still be applied in most skyshine analyses for distances greater than x_M since the extremely small and uncertain doses from such low-energy and backward moving beam components are negligible compared to the much higher doses caused by higher energy or forward directed source photons.

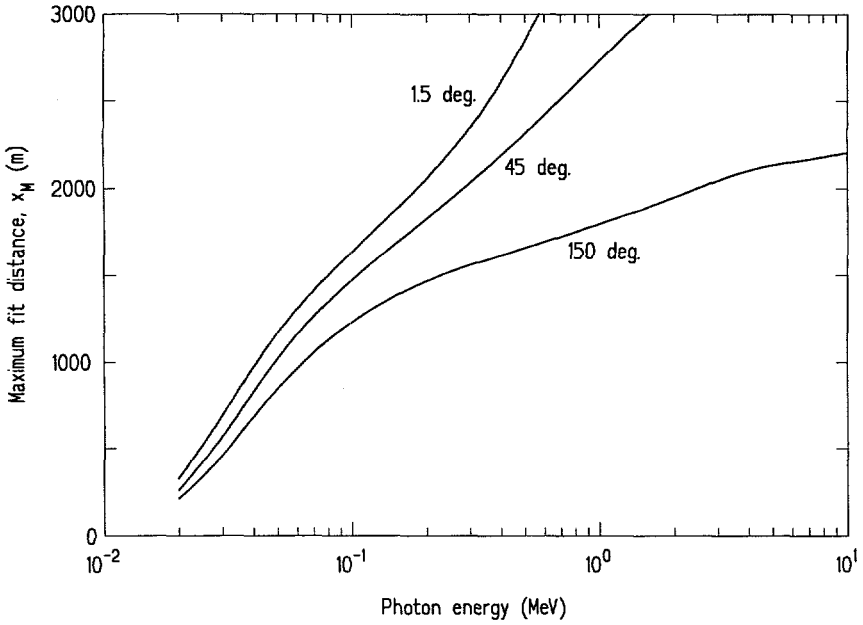

Figure 4.2. Variation of the maximum range x_M (m)used in the fit of the LBRF with photon energy. For source-to-detector distances greater than x_M (m), the LBRF was less than 10^{-30} rad/photon.

Values of the approximation parameters a, b and c depend on the fitting criterion used, i.e., which of the objective functions S_i of Eqs. (4.3) to (4.5) is to be minimized. Several measures of the goodness of the approximating fit can be used such as the average absolute deviation, the maximum deviation, or the mean squared deviation between the fit and the reference values. A plot is shown in Fig. 4.3 of the resulting maximum versus average fit deviations for the least squares (S_1) and the minimization of the maximum deviation (S_2) or MMD criteria for the low-energy (< 15 MeV) fits made to the 300 different beam energies and angles of Table 4.1. Although both fitting criteria produce the same range of average deviations, the S_2 criterion produces, as would be expected, smaller maximum deviations between the fits and the reference values. The deviations produced by the S_3 criterion (not shown in Fig. 4.3) are very similar to those for the S_1 criterion except than several fits produced average deviations considerably greater than those for the S_1 fits. From these results it was decided to use the MMD (S_2) criterion to obtain the approximation parameters for the 3-parameter approximation of the LBRF.

The results obtained for the fitting parameters a, b, and c, are presented in Appendix A, together with the quantifications of the absolute deviations of the fit to the reference values.

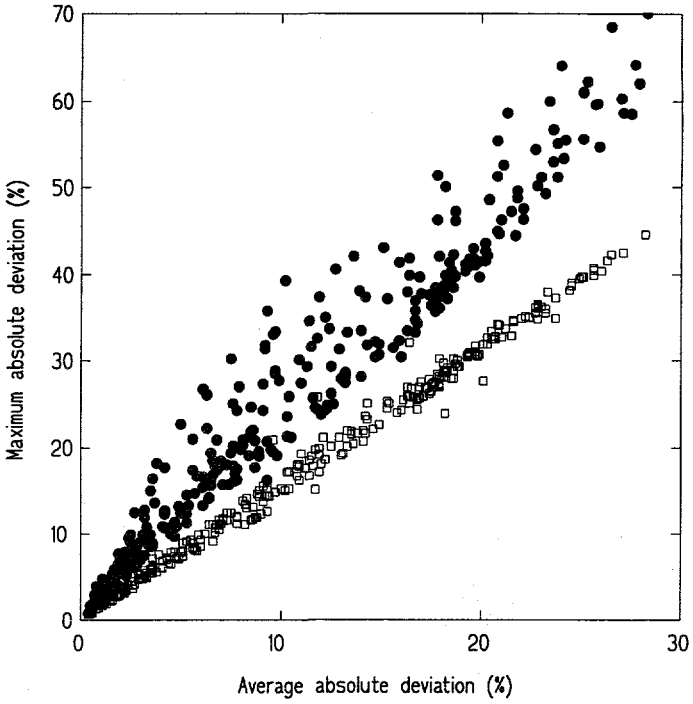

Figure 4.3. Fit deviations produced by fitting the 3-parameter formula Eq. (4.11) to the 300 sets of energy-angle reference LBRF data calculated from the point kernel LBRF model for 15 MeV and below. Shown are results obtained by the least-squares method (circles) and by the MMD method (open squares).

4.2.2 A Four-Parameter Approximation

The four-parameter function of Eq. (4.10) can also be used to approximate the LBRF as

$$\Re(x, E, \phi) \simeq \kappa E x^{(}b - dx)e^{a-cx}. \tag{4.12}$$

This function was fitted to the 300 sets of point kernel reference LBRF data for photon energies of 15 MeV or less. In Fig. 4.4 the average and maximum deviations between the fit and the reference data are shown for the 280 fits for energies of 10 MeV or less. From a comparison of this figure to Fig. 4.3, it is apparent that the four-parameter function represents the LBRF data much better than does the three-parameter approximation. Indeed, if the 10 MeV case were also excluded from Fig. 4.4 there would be only three points with average deviations above 7%. Again the S_2 fit is seen to produce results with slightly lower maximum deviations than does the least-squares S_1 fit. For this reason the S_2 fit was used to obtain the fitting parameters a, b, c, and d tabulated in Appendix B.

Because the fitting errors produced with the four-parameter approximation were

comparable to those produced with the three-parameter formula, no four-parameter fits are reported for energies above 15 MeV.

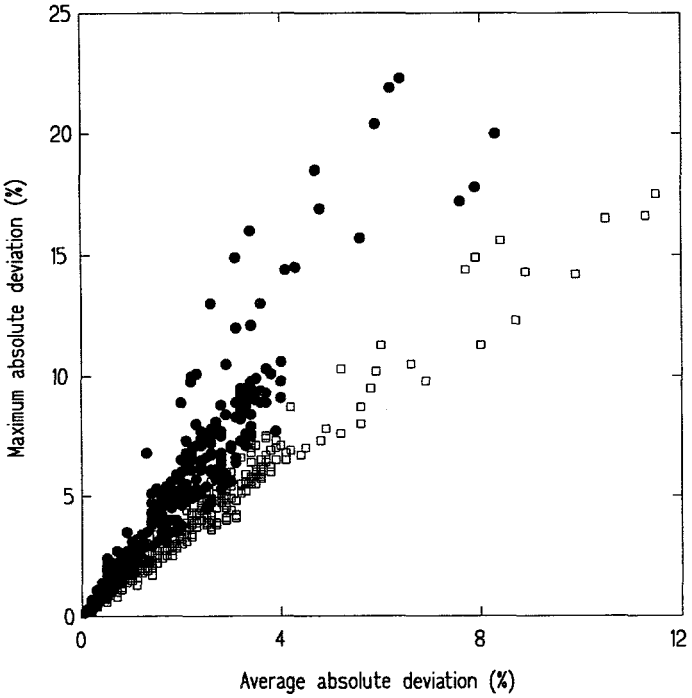

Figure 4.4. Fit deviations produced by fitting the 4-parameter formula Eq. (4.12) to the 280 sets of energy-angle reference LBRF data calculated from the point kernel LBRF model for 10 MeV and below. Shown are results obtained by the least-squares method (circles) and by the MMD method (open squares).

4.3 Correction for Different Air Densities

For an infinite homogeneous medium of density ρ with a point source of arbitrary energy and angular distribution at the origin, the dose distribution $D_\rho(\mathbf{r})$ can rigorously be related the dose distribution $D_{\rho_o}(\mathbf{r})$ for the same problem but with the medium's density changed to ρ_o. Specifically, Zerby [Ze56] showed

$$D_\rho(\mathbf{r}) = \frac{\rho^2}{\rho_o^2} D_{\rho_o}(\rho\mathbf{r}/\rho_o). \tag{4.13}$$

This general result can be immediately applied to the LBRF.

The calculations of $\Re$ and its approximation of Eq. (4.11) were all made with a reference mass density $\rho_o = 0.0012$ g/cm^3. Skyshine problems often involve atmospheres at different densities. With the density scaling property of Eq. (4.13), the

3-parameter approximate LBRF for air with density ρ becomes

$$\Re(x, E, \phi) = \kappa E(\rho/\rho_o)^2[x(\rho/\rho_o)]^b e^{(a-cx\rho/\rho_o)}. \tag{4.14}$$

The fitting parameters a, b, and c are the same as those obtained at the reference density ρ_o and depend only on the source energy E and the beam angle ϕ.

The 4-parameter LBRF approximation of Eq. (4.12) can be corrected similarly for atmospheric density, namely

$$\Re(x, E, \phi) = \kappa E(\rho/\rho_o)^2[x(\rho/\rho_o)]^{(b-dx\rho/\rho_o)} e^{(a-cx\rho/\rho_o)}. \tag{4.15}$$

An example of this density scaling result is shown in Fig. 4.5 which shows MCNP calculated values of the LBRF in an infinite air medium of density $\rho_o = 0.0012$ g cm^{-3} (open squares) and then corrected to a density of $\rho = 0.00135$ g cm^{-3} by Eq. (4.13). Also shown in the figure by the solid squares are values directly calculated by MCNP for an air density of $\rho = 0.00135$ g cm^{-3}. Clearly, the two sets of results are in excellent agreement.

If the medium is not homogeneous, then Eq. (4.13) does not rigorously apply. However, because soil has very similar photon cross sections as those of air, one might expect that the scaling property used in Eqs. (4.14) and (4.15) might be excellent approximations of the effect of changes in the air density. In Fig. 4.6, MCNP calculations similar to those shown Fig. 4.5 are shown except in these calculations there was an air-ground interface present. The good agreement between the density corrected values and the calculated values verifies that density scaling can also be used for skyshine problems with an air-ground interface. Further effects of the air-ground interface are presented in Chapter 7.

4.4 Interpolation of Fitted Response Function

A double interpolation scheme was used in this study to make the approximate line-beam response function continuous in both energy and angle [Sh91]. The approximate LBRF is first linearly interpolated in energy to yield the response at the energy E of interest. If $E_i \leq E \leq E_{i+1}$ then the approximating function $\mathcal{F} \equiv \Re/E$ at the two bracketing discrete energies are reconstituted from the fitting parameters in Eq. (4.11) or (4.12) and $\mathcal{F}(E, x, \phi_j)$ is then obtained by linear interpolation as

$$\mathcal{F}(x, E, \phi_j) = \mathcal{F}_{i+1,j} \frac{E_i - E}{E_i - E_{i+1}} + \mathcal{F}_{i,j} \frac{E - E_{i+1}}{E_i - E_{i+1}}, \tag{4.16}$$

where

$$\mathcal{F}_{i,j} \equiv \mathcal{F}(x, E_i, \phi_j). \tag{4.17}$$

Once the energy interpolation has been performed at the two bracketing angles, an interpolation in the beam direction ϕ is performed. In earlier work [Sh87, Sh92]

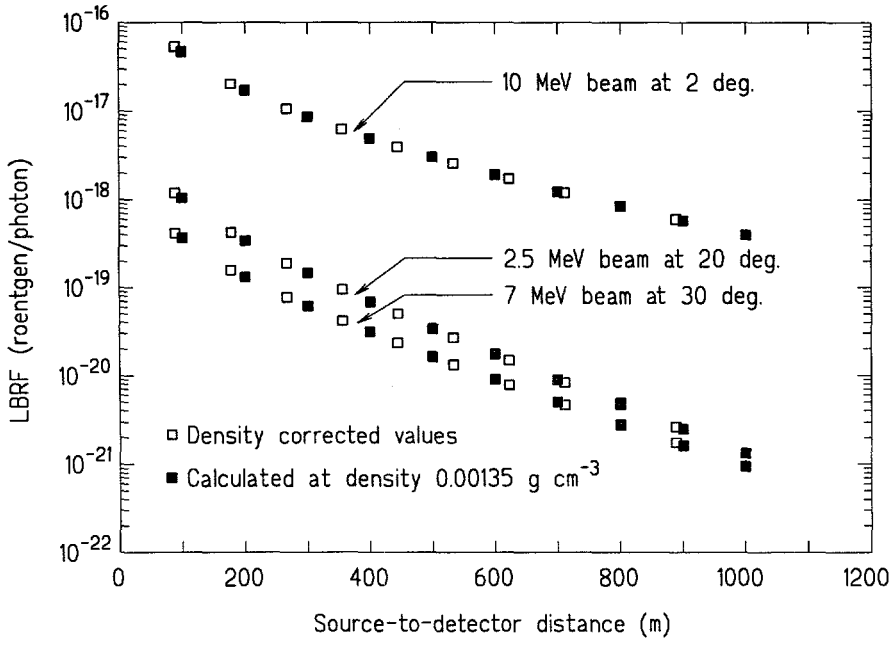

Figure 4.5. MCNP calculated values of the LBRF in an infinite air medium. The open squares are values calculated with a density $\rho_o = 0.0012$ g cm^{-3} and then corrected to a density of $\rho = 0.00135$ g cm^{-3} by Eq. (4.13). The solid squares are values directly calculated by MCNP for an air density of $\rho = 0.00135$ g cm^{-3}.

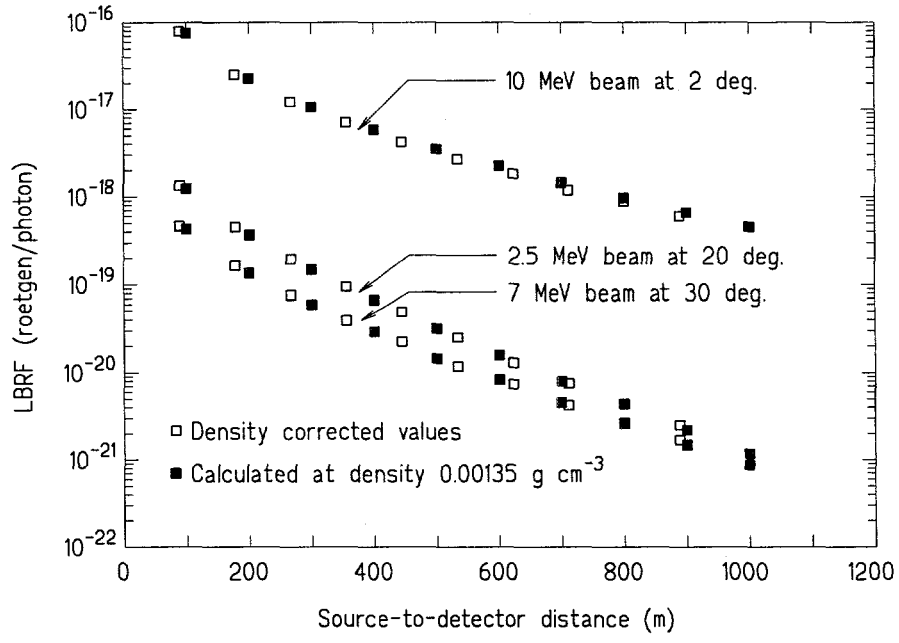

Figure 4.6. MCNP calculated values of the LBRF with a ground interface present. The open squares are values calculated with a density $\rho_o = 0.0012$ g cm^{-3} and then corrected to a density of $\rho = 0.00135$ g cm^{-3} by Eq. (4.13). The solid squares are values directly calculated by MCNP for an air density of $\rho = 0.00135$ g cm^{-3}.

this angular interpolation employed linear interpolation between $\mathcal{F}(x, E, \phi_{j+1})$ and $\mathcal{F}(x, E, \phi_j)$. However, at large distances, it was found that these two bracketing values could vary by more than an order of magnitude and that such linear interpolation could produce quite inaccurate results. Much better results are obtained by using a logarithmic interpolation scheme. Thus, with $\mathcal{G} \equiv \ln \mathcal{F}$, one obtains for $\phi_j \leq \phi \leq \phi_{j+1}$

$$\mathcal{G}(x, E, \phi) = \mathcal{G}(x, E, \phi_j) + [\mathcal{G}(x, E, \phi_{j+1}) - \mathcal{G}(x, E, \phi_j)] \frac{\phi - \phi_j}{\phi_{j+1} - \phi_j}. \tag{4.18}$$

For beam directions in the two end intervals, a logarithmic linear extrapolation procedure is used, namely, for $\phi_J \equiv \max\{\phi_j\} \leq \phi \leq 180$ degrees,

$$\mathcal{G}(x, E, \phi) = \mathcal{G}(x, E, \phi_J) + [\mathcal{G}(x, E, \phi_J) - \mathcal{G}(x, E, \phi_{J-1})] \frac{\phi - \phi_J}{\phi_J - \phi_{J-1}}. \tag{4.19}$$

and for $0 \leq \phi \leq \phi_1 \equiv \min\{\phi_j\}$ degrees

$$\mathcal{G}(x, E, \phi) = \mathcal{G}(x, E, \phi_1) + [\mathcal{G}(x, E, \phi_2) - \mathcal{G}(x, E, \phi_1)] \frac{\phi - \phi_1}{\phi_2 - \phi_1}. \tag{4.20}$$

Finally, the desired LBRF is obtained as

$$\Re(x, E, \phi) \simeq E \exp[\mathcal{G}(x, E, \phi)] \tag{4.21}$$

With this double interpolation scheme, the approximate LBRF of Eq. (4.11) or (4.12) is made completely continuous in angle ϕ and energy E. Unlike the original LBRF [La79] which was represented as histograms in both energy and angle, the new approximating LBRF proposed here varies smoothly with small changes in the arguments of the LBRF. However, it should be noted that, while this continuity feature increases the precision of a skyshine calculations, it does require more computational effort and has little effect on the accuracy of the skyshine doses [Sh87].

4.5 Examples of the Approximate LBRF

Both a three-parameter and a four-parameter approximation for the LBRF has been developed, the former applicable over the entire energy range studied (0.02 to 100 MeV) and the latter applicable only to energies less than 15 MeV. The parameters for the three-parameter approximate LBRF of Eq. (4.14) are tabulated in Appendix A, and those for the four-parameter approximation given by Eq. (4.15) are listed in Appendix B. Before examples of skyshine calculations are presented in the next chapter, examples of the LBRF and its approximations are given here.

4.5.1 Comparison of Point-Kernel and Approximate LBRF

Example comparisons of the approximate line-beam response functions, Eqs. (4.14) and (4.15), to the point kernel model of Eq. (2.24) are shown in Figs. 4.7 through 4.11. The data points in these figures are calculated with the point kernel LBRF

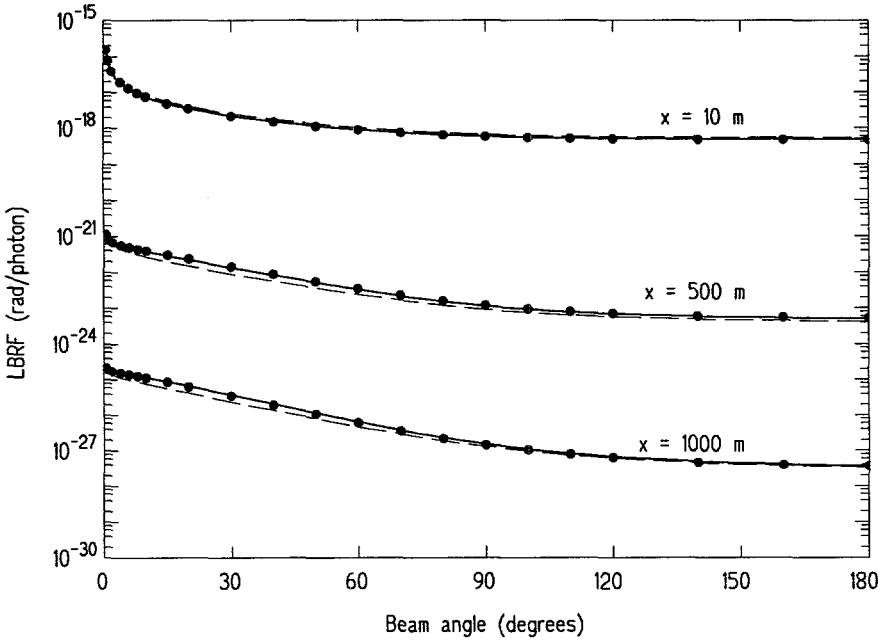

Figure 4.7. Comparison of the point kernel LBRF (dots) with the three-parameter (dashed lines) and four-parameter (solid lines) LBRF approximations for 100 keV photons at different source-to-detector distances.

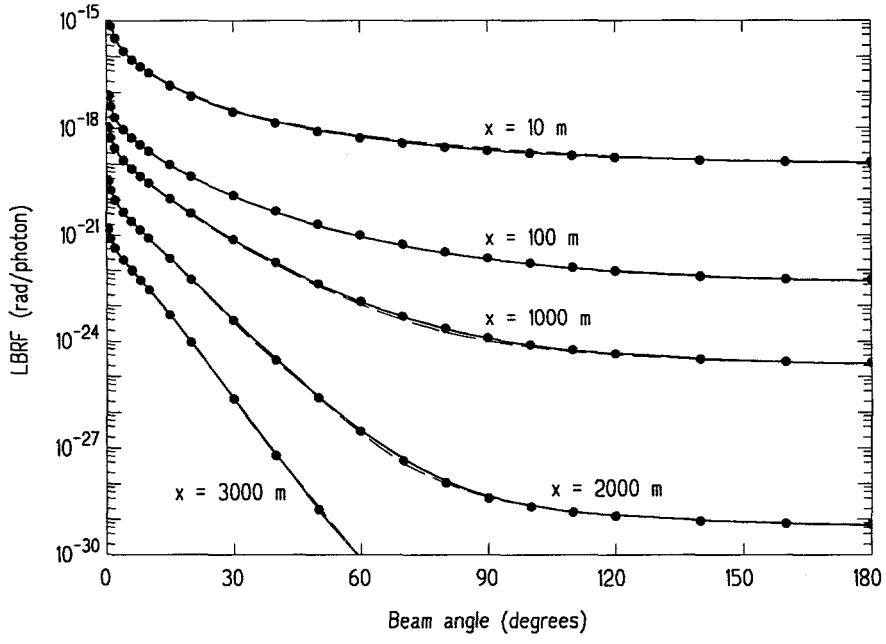

Figure 4.8. Comparison of the point kernel LBRF (dots) with the three-parameter (dashed lines) and four-parameter (solid lines) LBRF approximations for 7 MeV photons at different source-to-detector distances.

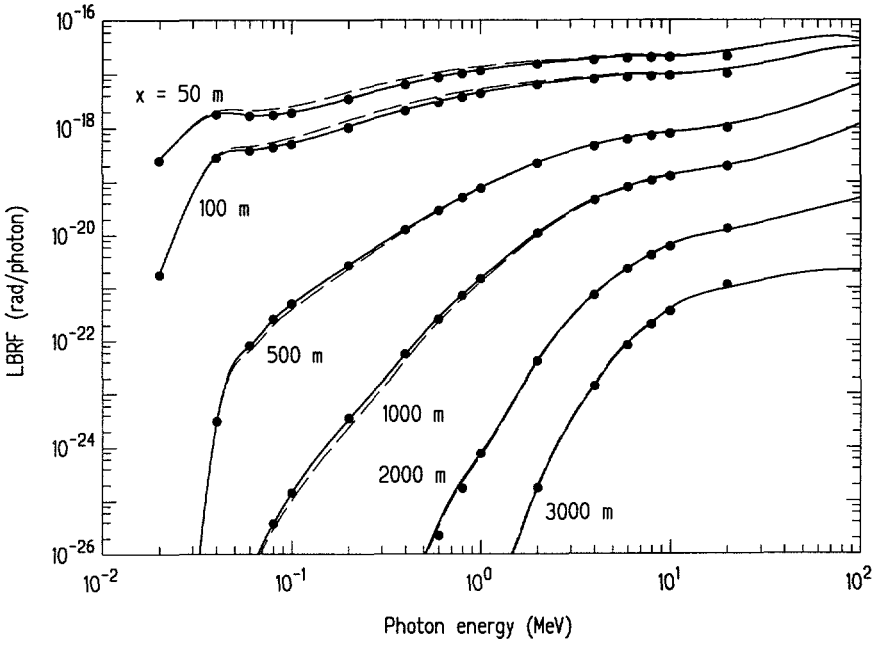

Figure 4.9. Comparison at different source-to-detector distances of the point kernel LBRF (dots) with the three-parameter (dashed lines) and four-parameter (solid lines) LBRF approximations for a beam angle of 5 degrees.

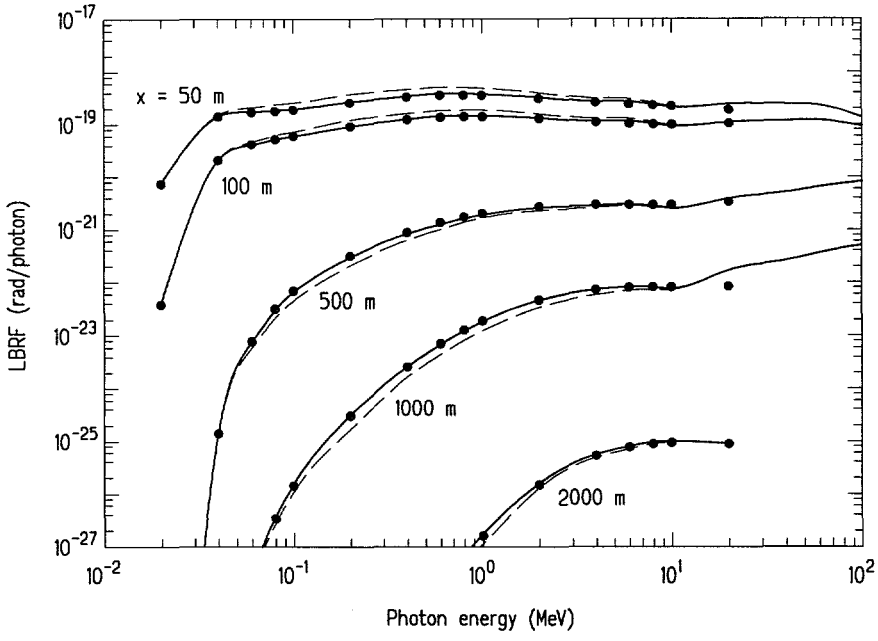

Figure 4.10. Comparison at different source-to-detector distances of the point kernel LBRF (dots) with the three-parameter (dashed lines) and four-parameter (solid lines) LBRF approximations for a beam angle of 45 degrees.

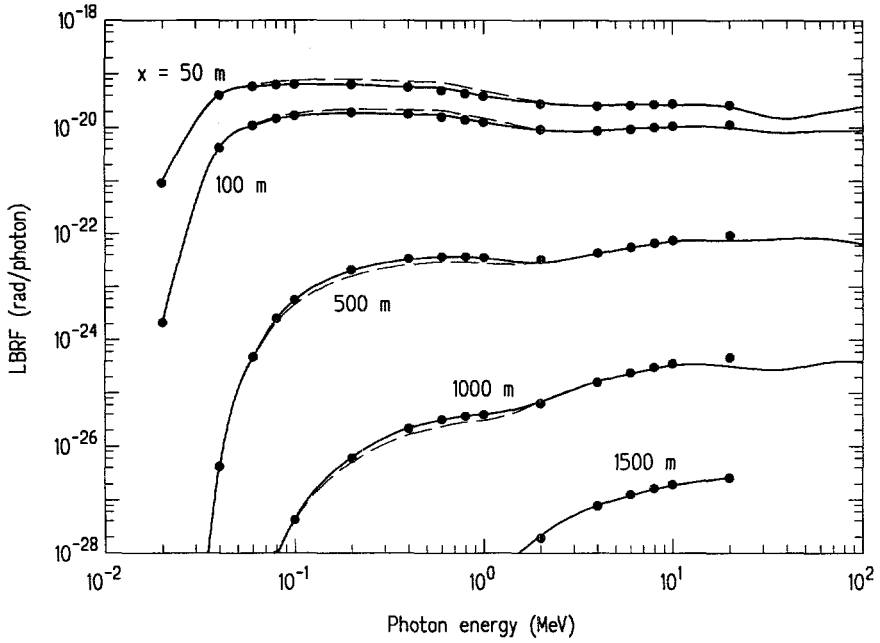

Figure 4.11. Comparison at different source-to-detector distances of the point kernel LBRF (dots) with the three-parameter (dashed lines) and four-parameter (solid lines) LBRF approximations for a beam angle of 150 degrees.

model and most of the points are at energies or angles other than those used to generate the reference LBRF data to which the approximate LBRFs were fit. Both the three parameter approximation (dashed lines) and the four-parameter approximation (solid lines) agree closely with the point kernel data over a wide range of beam angles and directions, As would be expected the four-parameter approximation gives better agreement than the three-parameter approximation.

In Figs. 4.9 through 4.11, which show the LBRF as a function of energy, those portions of the approximate LBRF above 15 MeV were calculated by the three-parameter approximation (obtained by fits to MCNP data). The four-parameter approximation was not developed for these energies, and the four-parameter algorithm used to generate these results reverts automatically to the three-parameter model, thereby causing both approximations to appear to produce identical results. Also the high-energy portion of these results for distances greater than 1000 m are values obtained by extrapolating the three-parameter approximation beyond its maximum fit range, and as will be seen in the next section, such an extrapolation tends to underpredict the LBRF.

Finally, in Fig. 4.12 the LBRF is shown as a function of the source-to-detector distance. Besides results from the point kernel LBRF model and the two approximate LBRFs, this plot also includes Monte Carlo values calculated by Lynch [Ly58]

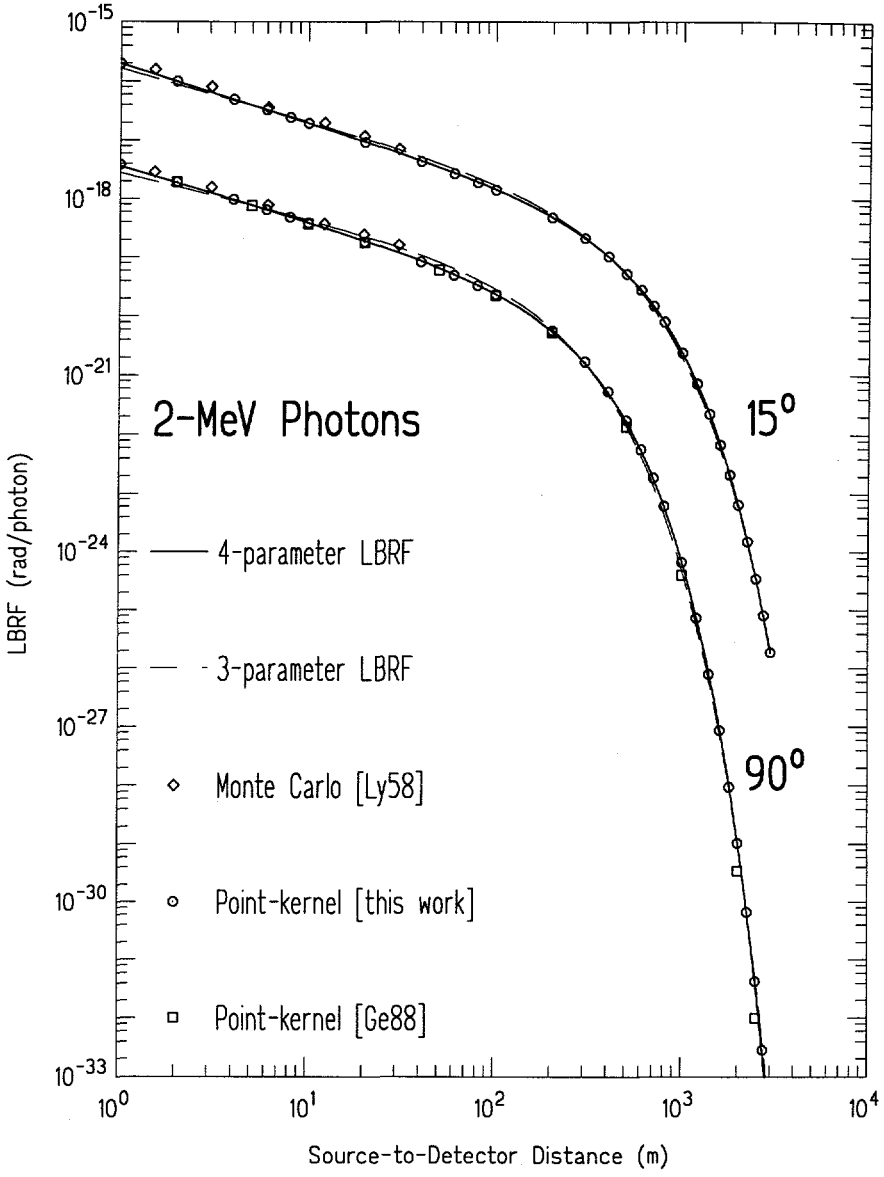

Figure 4.12. Comparison for 2 MeV photons at two beam angles of the point kernel LBRF (circles) with the three-parameter (dashed lines) and four-parameter (solid lines) LBRF approximations. Also shown are Monte Carlo results by Lynch [Ly58] (diamonds) and by an independent point kernel model [Ge88] (squares).

and values from an alternative point kernel model [Ge88]. The excellent agreement between all these results gives confidence in the new approximate LBRFs reported here.

Previous Approximate LBRFs

The three-parameter approximation of Eq. (4.14) has been used in several earlier studies to approximate the LBRF [Pr76, La79, Sh87, Sh92]. The set of approximating parameters used varied with each study, each study improving the accuracy and/or range of the approximate LBRF. The most recent of these earlier sets of approximating parameters [Sh92], although slightly different than that of Appendix A, gives nearly the same results for most skyshine problems and can be used as an alternative to that of Appendix A.

No parameter set for the four-parameter LBRF approximation has previously been reported. The slightly improved accuracy of this approximation generally makes this approximation the preferred choice for the line-beam skyshine method for source energies below 10 MeV.

4.5.2 The High Energy Approximate LBRF

As mentioned earlier, the point kernel model of the LBRF does not give sufficiently accurate results for photon energies above 15 MeV to form the basis for developing a set of approximation parameters (see Figs. 3.15 to 3.16). With future work, the bremsstrahlung component of the present point kernel LBRF model, which is based on the overly simplistic straight-ahead approximation, may be improved by using a better description of the angular distribution of secondary bremsstrahlung. Such an improved model is needed if accurate reference data are to be generated for distances far from the source.

In the present study, MCNP calculations of the LBRF were used to generate the reference LBRF values, and despite large calculational expenditures, values of the LBRF produced were generally restricted to source-to-detector distances of 1000 m or less. Only for the smallest beam angles was it possible to obtain statistically meaningful values at greater distances. Based on these MCNP calculations, the parameters listed in Appendix A were derived for the three-parameter approximate LBRF. The paucity and accuracy of the reference LBRF values above 15 MeV, precluded fitting a four-parameter approximation to the LBRF.

In Figs. 4.13 to 4.15 the resulting three-parameter approximate LBRF is compared to the MCNP results used to generate the approximation. The approximation is seen to faithfully reproduce the MCNP results.

The question arises as to whether the approximate LBRF may be used at source-to-detector distances greater than the 1000 m limit used to generate the fit parame-

ters. With multi-day MCNP runs it was possible to obtain far-field LBRF values for a few small beam angles at distances up to 3000 m. Two examples of these far-field calculations are shown in Figs. 4.16 and 4.17. Also shown on these far-field examples are the three-parameter approximation (dotted line) and the point kernel LBRF (solid line). The point kernel not only underpredicts the LBRF but even has the wrong asymptotic slope. The three-parameter approximate LBRF gives good agreement with the MCNP results up to about 1200 m, but at greater distances increasingly underpredicts the LBRF. Thus use of the three-parameter approximate LBRF for energies greater than 15 MeV must be used cautiously at distances greater than about 1200 m.

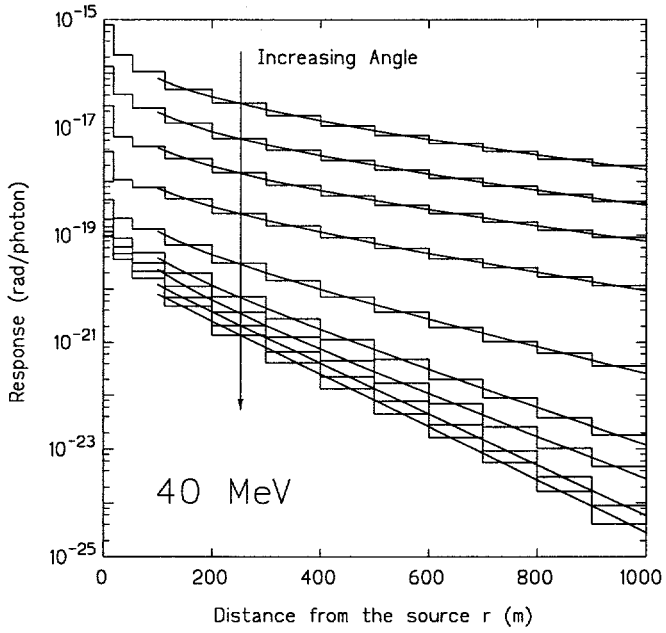

Figure 4.13. Comparison of the three-parameter approximate LBRF (smooth lines) to MCNP calculations (histograms) for 40 MeV photons. The nine LBRF angles are 2, 5, 10, 20, 45, 75, 95, 120, and 150 degrees.

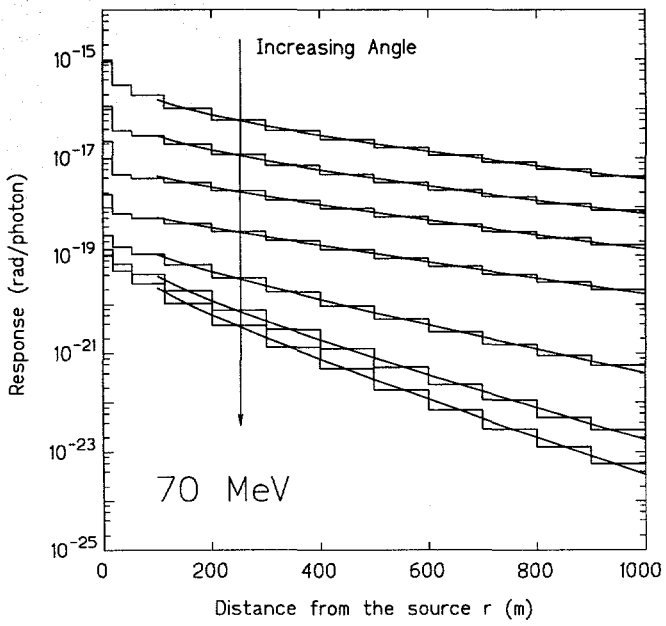

Figure 4.14. Comparison of the three-parameter approximate LBRF (smooth lines) to MCNP calculations (histograms) for 40 MeV photons. The seven LBRF angles are 2, 5, 10, 20, 45, 75, and 95 degrees.

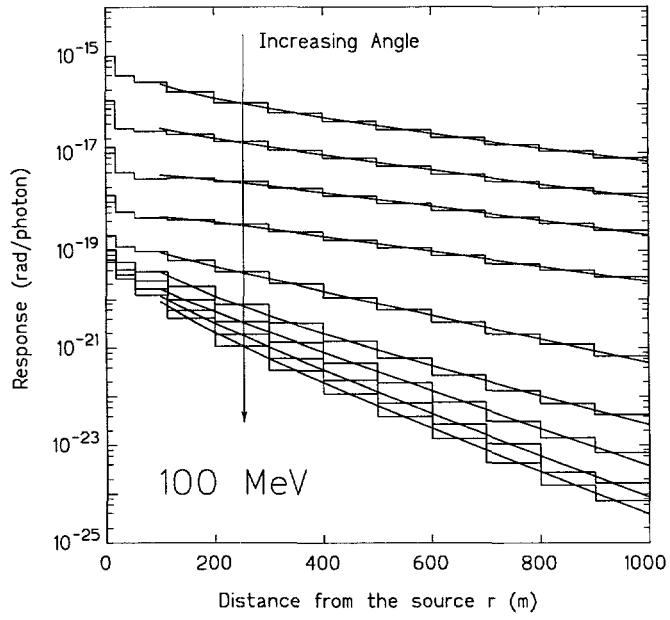

Figure 4.15. Comparison of the three-parameter approximate LBRF (smooth lines) to MCNP calculations (histograms) for 70 MeV photons. The nine LBRF angles are 2, 5, 10, 20, 45, 75, 95, 120, and 150 degrees.

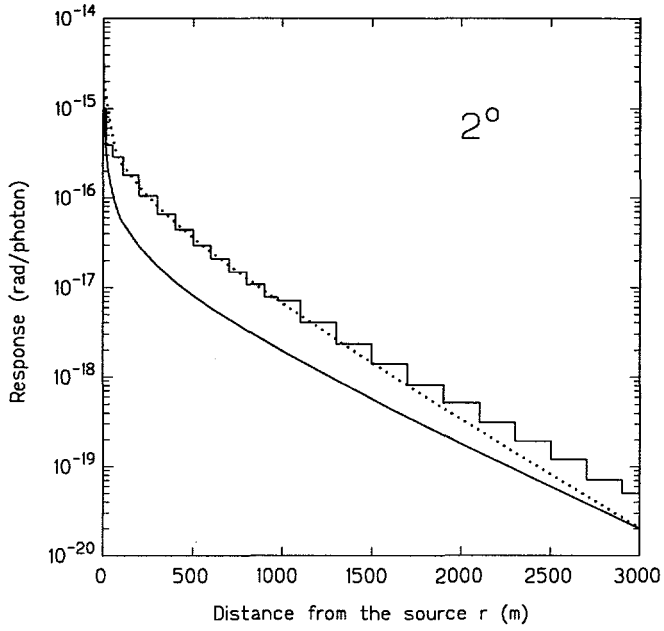

Figure 4.16. Comparison of the point kernel LBRF (solid line), MCNP results (histogram), and the three-parameter approximate LBRF (dotted line) for 100 MeV photons emitted at 2 degrees from the source-detector axis.

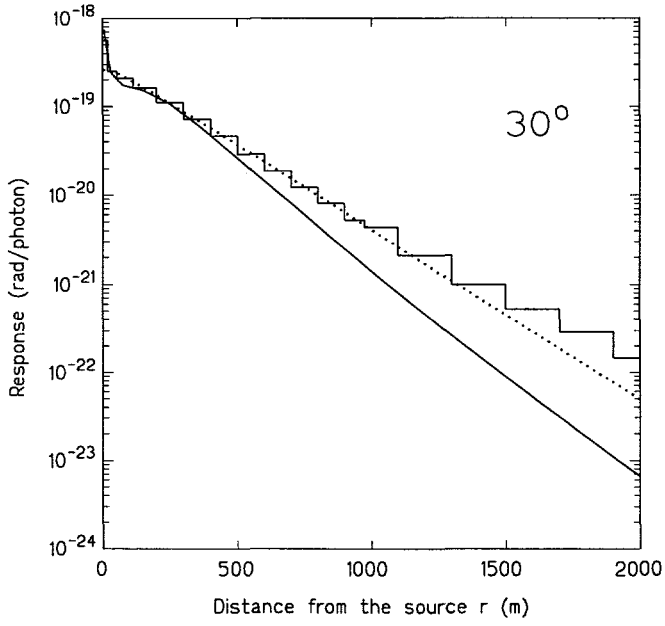

Figure 4.17. Comparison of the point kernel LBRF (solid line), MCNP results (histogram), and the three-parameter approximate LBRF (dotted line) for 100 MeV photons emitted at 30 degrees from the source-detector axis.

Chapter 5

Application to Unshielded Sources

In the previous chapters, the monoenergetic and monodirectional skyshine line-beam response function (LBRF) has been determined by the point kernel method and approximated by a three-parameter empirical formula. With this approximate LBRF, the skyshine dose arising from a point source with any energy and angular distribution can be evaluated easily. In this chapter, explicit results for three basic skyshine geometries are presented.

In the original SKYSHINE method [La79, La88], the LBRF was approximated by the same three-parameter empirical formula used in this study. Tables of the three parameters for the approximating formula were obtained by fitting the formula to Monte Carlo results for 12 energy and 20 angular groups. The SKYSHINE methodology then used a Monte Carlo approach to sample the energy and emission direction of the radiation leaving the skyshine source. The energy and angular group of each source photon was determined and its response function was then used to determine the photon's contribution to the dose at the detector. Such a Monte Carlo approach was still computationally expensive, since it required extensive sampling of source photons to obtain a statistically meaningful estimate of the dose at the detector. Moreover, the relatively broad energy and angular group structure precluded this method from being able to determine the effect of a small change in the energy and/or angular distribution of the skyshine source.

Rather than to use a Monte Carlo approach with the LBRF constrained to fixed energy and angular groups, it is better to use a LBRF which is continuous in energy and direction. The skyshine dose at a remote detector can then be evaluated by integrating the LBRF, weighted by the energy and angular distribution of the source, over all source energies and emission directions. This integral LBRF method has been shown to be a simple, computationally inexpensive, and accurate method for performing routine skyshine analyses [Sh87, Sh91].

The general formulation of the integral LBRF method has already been outlined in Section 1.3. For a bare, monoenergetic, vertically collimated, isotropic source that has no overhead shield, the dose rate at a distance d from the source is given by

Eq. (1.4), namely

$$R(d) = \frac{S_p}{4\pi} \int_0^{2\pi} d\psi \int_{\omega_{min}}^{\omega_{max}} d\omega \, \Re(d, E, \phi), \tag{5.1}$$

where ω is the cosine of the polar angle θ with respect to the zenith, and the azimuthal angle ψ is defined with respect to the projection of the line beam on the horizontal plane. Here ω_{min} and ω_{max} define the permissible range of ω allowed by the source collimation. Generally, these limits are functions of the azimuthal angle ψ.

This formulation can be used to calculate the skyshine dose rate for any point monoenergetic skyshine source.[1] Once the integration limits ω_{min} and ω_{max} are obtained for a particular geometry, either from explicit expressions or numerical procedures, the integrals in Eq. (5.1) can be evaluated readily using standard numerical integration techniques.

In this chapter explicit expressions are given for the integration limits for three frequently encountered skyshine geometries. These are (1) an unshielded source on the axis of a vertical cylindrical-shell shield (open silo), (2) a source behind a infinitely long shield wall, and (3) a source inside a roofless rectangular building.

5.1 Open Silo Geometry

Figure 5.1 shows the geometry of a vertical cylindrical-shell shield with no overhead shielding. The inner radius of the silo is r and the wall is assumed to be black, i.e., all incident source radiation is absorbed by the wall. A monoenergetic point source isotropically emitting photons of energy E is located on the vertical axis of the silo at distance h_s below the horizontal plane of the silo top. A detector (receiver or dose point) is located in air of density ρ at a radial distance x from the silo axis and at a distance h_d below the horizontal top of the silo wall. If the source or the detector is located above the top of the silo, h_s or h_d is taken to be negative. The total detector response for this open silo geometry, with azimuthal symmetry, is explicitly

$$R(d) = \frac{S_p}{2\pi} \int_0^{\pi} d\psi \int_{\omega_o}^{1} d\omega \, \Re(d, E, \phi). \tag{5.2}$$

To evaluate this expression, one must first determine ω_o, ϕ, and the source-to-detector distance d in terms of the problem parameters. The distance from the source to the detector is

$$d = \sqrt{x^2 + (h_s - h_d)^2} \tag{5.3}$$

and the angle ζ between the horizontal and the source-to-detector axis is

$$\zeta = \tan^{-1}[(h_s - h_d)/x]. \tag{5.4}$$

[1]For polyenergetic sources, Eq. (5.1) also needs to be integrated over the source energy distribution, or equivalently, treated as a sum of monoenergetic sources. See Section 1.3.

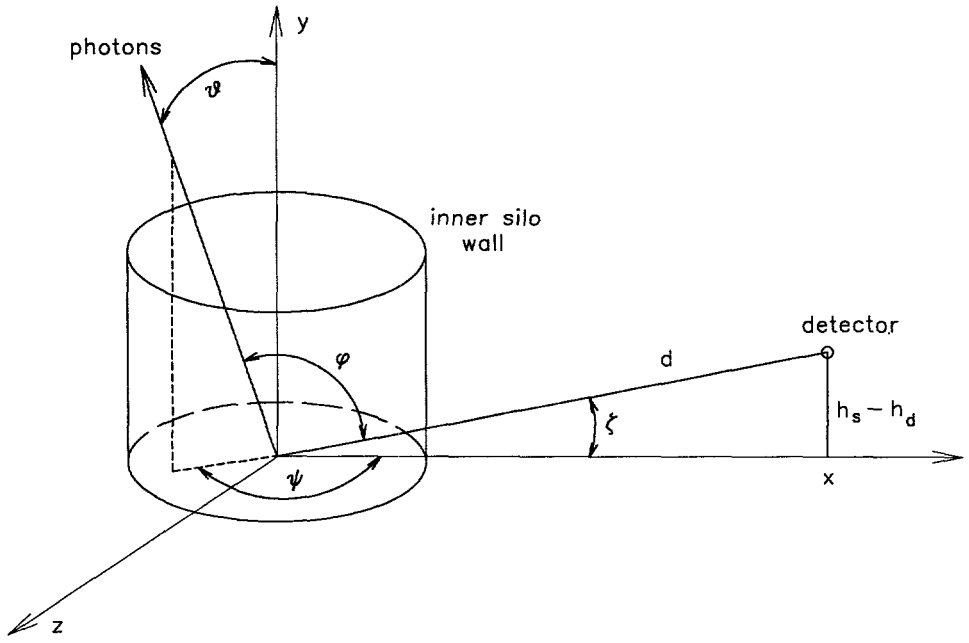

Figure 5.1. Geometry for the open silo skyshine problem. The point source is on the silo axis at the origin of the spherical coordinate system. The silo walls are assumed to be black.

The photons emitted from the point source are collimated by the silo wall into a cone with a polar angle ϑ_{max} given by

$$\omega_o \equiv \cos\vartheta_{max} = h_s/\sqrt{r^2 + h_s^2}. \tag{5.5}$$

The emission angle φ between the direction $\mathbf{\Omega}(\vartheta, \psi)$ of photon emission and the source-to-detector axis is a function of the polar angle ϑ, the azimuthal angle ψ measured from the vertical plane through the source and the detector, and the angle ζ given by Eq. (5.4). For a photon emitted at polar angle ϑ and azimuthal angle ψ, the cosine of the beam angle φ is the dot product of the unit vector along the emission direction (denoted by $\mathbf{e}$) and the unit vector along the source-to-detector axis (denoted by $\mathbf{u}$). Explicitly

$$\mathbf{e} = \mathbf{i}\sin\vartheta\cos\psi + \mathbf{j}\cos\vartheta + \mathbf{k}\sin\vartheta\sin\psi \tag{5.6}$$

and

$$\mathbf{u} = \mathbf{i}\cos\zeta + \mathbf{j}\sin\zeta, \tag{5.7}$$

where the $\mathbf{i}$, $\mathbf{j}$, and $\mathbf{k}$ are the unit vectors along the x-axis, y-axis and z-axis, respectively. Thus, the cosine of emission angle φ is

$$\cos\varphi = \mathbf{e}\bullet\mathbf{u} = \sin\vartheta\cos\psi\cos\zeta + \cos\vartheta sin\zeta. \tag{5.8}$$

The integral over ω from ω_o to 1 in Eq. (5.2) means that only those photons emitted from the source with a polar angle ϑ equal to or less than ϑ_{max}, or $\omega \geq \cos\vartheta_{max}$, defined by the silo wall, make a contribution to the skyshine dose rate at a distance d from the source. The wall does not influence the dose estimate other than to provide source collimation. However, the detector response may be slightly underestimated because of the neglect of contributions from photons that first scatter from the silo wall and then escape the confines of the silo. This underestimate is balanced by the neglect of the shielding provided by the silo walls against photons that scatter in the air inside the silo before proceeding towards the detector. However, both of these contributions are generally small, especially for large source-to-detector distances.

5.1.1 Comparison with Experiment and Previous Results

In a skyshine benchmark experiment [Na81], an isotropic point ^{60}Co source was placed on the axis of a cylindrical concrete silo with a wall sufficiently thick to preclude radiation penetrating it radially. The ratio of the silo radius r to the source depth h_s was designed so as to define an open conical aperture with a full-angle, $2\theta_{max}$, of 150.5 degrees with the source at the apex. Calculations for this geometry were performed using the integral line-beam method over a source-to-detector distance range from 5 m to 700 m, and energy range from 0.05 MeV to 1.25 MeV. The results of these calculations are shown in Fig. 5.2 together with the benchmark experimental data. In this plot, the source-to-detector distance is expressed in units of areal density, the product of the air density and the source-to-detector distance. The dependent variable is the exposure per photon multiplied by the square of the source-to-detector distance and divided by the solid angle of collimation, namely 4.683 sr. In this form, the strong effect of source-to-detector distance on detector response, through the inverse-square law, is suppressed.

There are two sets of calculations illustrated in Fig. 5.2. The solid lines are the results based on the new 3-parameter LBRF approximation obtained in this study. The dashed lines are the results based on a previous LBRF approximation [Sh87]. The differences between the new and old results increase with decreasing photon energy. There are no comparison data for 0.05 MeV photons since the old LBRF could not be used to evaluate skyshine for source photons below 0.1 MeV (the new LBRF can be used for skyshine dose calculations for photons between 10 keV and 15 MeV). It is seen from these results that the improved line-beam response function gives results that are slightly closer to the experimental benchmark results, especially at large detector distance, than are those obtained with the older line-beam response function.

Fig. 5.3 shows the same data in a different format along with very detailed MCNP calculations done for this experiment [Ol93] and with results obtained from the new 3-parameter and 4-parameter approximate LBRFs. Fig. 5.4 shows the same results on a logarithmic scale as well as results from a 39 energy-group discrete-ordinates calculation [Na81]. All these results agree well, although there are noticeable dif-

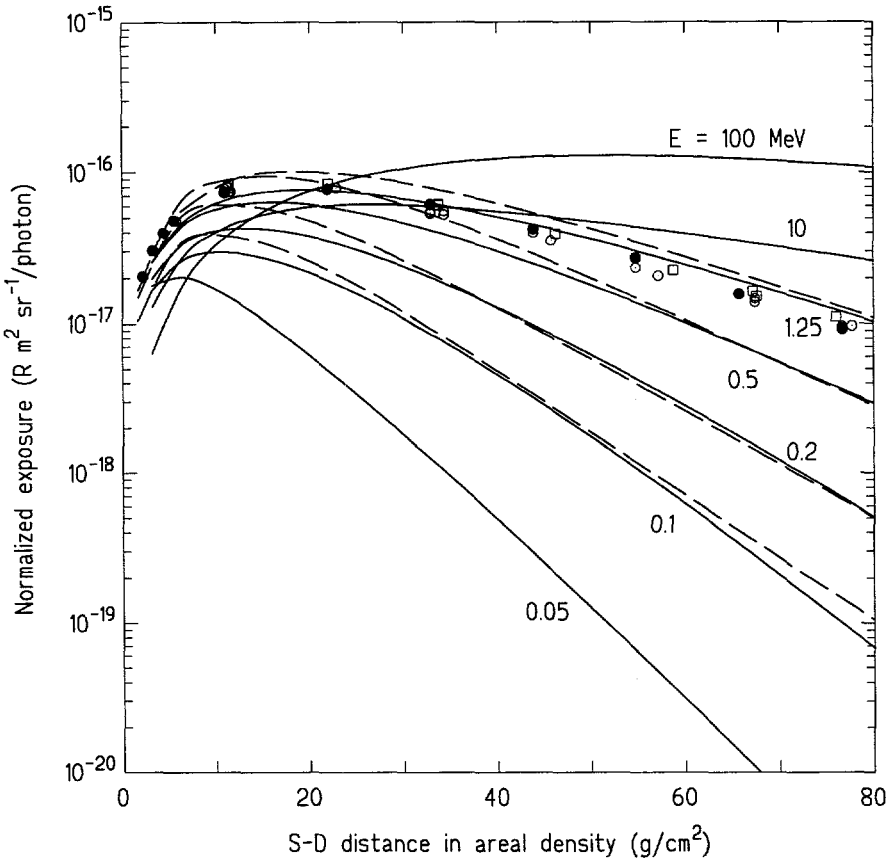

Figure 5.2. Results for a benchmark skyshine experiment. The source is on the axis of a cylindrical silo with 150.5-degree (full conical angle) collimation. Solid lines represent results obtained with the improved LBRF approximation. Dashed lines are results based on an earlier LBRF approximation [Sh91]. Closed circles are results of detailed MCNP calculations [Ol93]. Measured data are from a benchmark skyshine experiment for a ^{60}Co source [Na81]. Open circles represent measurements made using a high pressure ion chamber. Open squares represent measurements made using a NaI scintillation detector.

ferences between the two approximate LBRFs with the 4-parameter LBRF giving slightly better values at large source-to-detector distances.

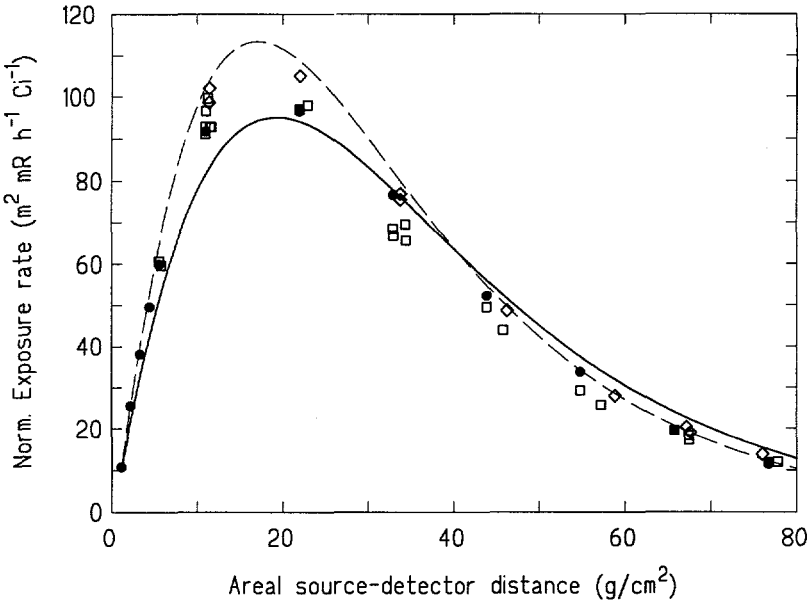

Figure 5.3. Comparison of calculated and experimental results for the open-silo benchmark experiment with a ^{60}Co source [Na81]. Open diamonds represent measurements made with a high pressure ion chamber, and the open squares are measurements made with a NaI scintillation detector. The lines are results obtained from the integral line-beam method, with the solid line based on the four-parameter approximate LBRF, and the dashed line on the three-parameter approximation. Solid circles are from detailed MCNP Monte Carlo calculations [Ol93].

5.1.2 Importance of In-Silo Scattering

In the proceeding analysis for the open silo problem, it was assumed that all photons emitting from the collimated source make a contribution to the skyshine dose (as indicated by the integration along the line beam from zero to infinity in Eq. (2.24)) even though the initial portions of the line beam is occluded from the detector by the silo wall. Photons scattered from the initial portion of the beam are still inside the silo, and, therefore, they cannot make a direct contribution to the skyshine dose. Photons emitted in the backward direction, away from the detector, and that interact in the air just outside the source structure can also be shielded from the detector by the interposing source confinement structure. Generally, inclusion of this in-silo scattering (or occluded) component will not cause a serious overestimation in the skyshine dose except, perhaps, for the case of very low energy photons that travel only a short distance along the beam before interacting. In this section, the importance of the occluded portion of the line beam is discussed.

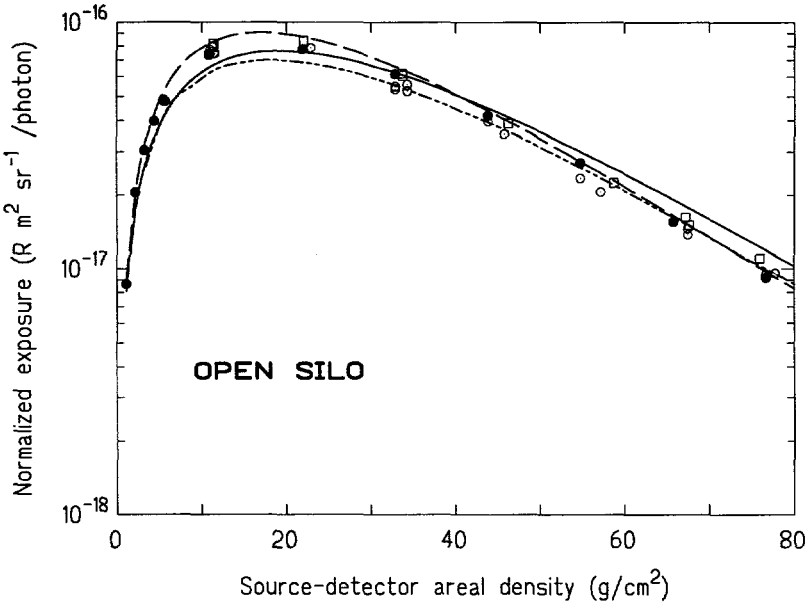

Figure 5.4. Comparison of calculated and experimental results for the open-silo benchmark experiment with a ^{60}Co source [Na81]. Open squares represent measurements made with a high pressure ion chamber, and the open circles are measurements made with a NaI scintillation detector. The lines are results obtained from the integral line-beam method, with the solid line based on the four-parameter approximate LBRF, and the dashed line on the three-parameter approximation. The broken line (with short dashes) is based on DOT 39-group discrete ordinates calculations. Solid circles are from detailed MCNP Monte Carlo calculations [Ol93].

The geometry used to analyze the importance of in-silo scattering is illustrated in Fig. 5.5. Consider an arbitrary photon beam emitted from a monoenergetic point source located at the axis of an open silo. Secondary photons produced along the beam from 0 to y_h cannot make direct contributions to the skyshine dose because of the intervening silo wall. The value of y_h is the length along the beam from the source to the point at which a line from the detector that just grazes the top of the silo wall intersects the beam. Thus the line beam response function, defined by Eq. (2.24), should be modified as

$$\Re(x, E, \phi) = \frac{1}{2\pi} \rho^2(\mu/\rho) \int_{y_h}^{\infty} d\hat{y}\, f(\hat{y}, x, E, \phi), \tag{5.9}$$

where the function $f(\hat{y}, x, E, \phi)$ is the integrand given by Eq. (2.61).

For the special case that the source and the detector are at the same elevation, y_h is found to be [De91]

$$y_h = \frac{h_s x}{x\cos\theta + h_s \sin\theta \cos\psi - r\cos\theta\cos\psi_c}, \tag{5.10}$$

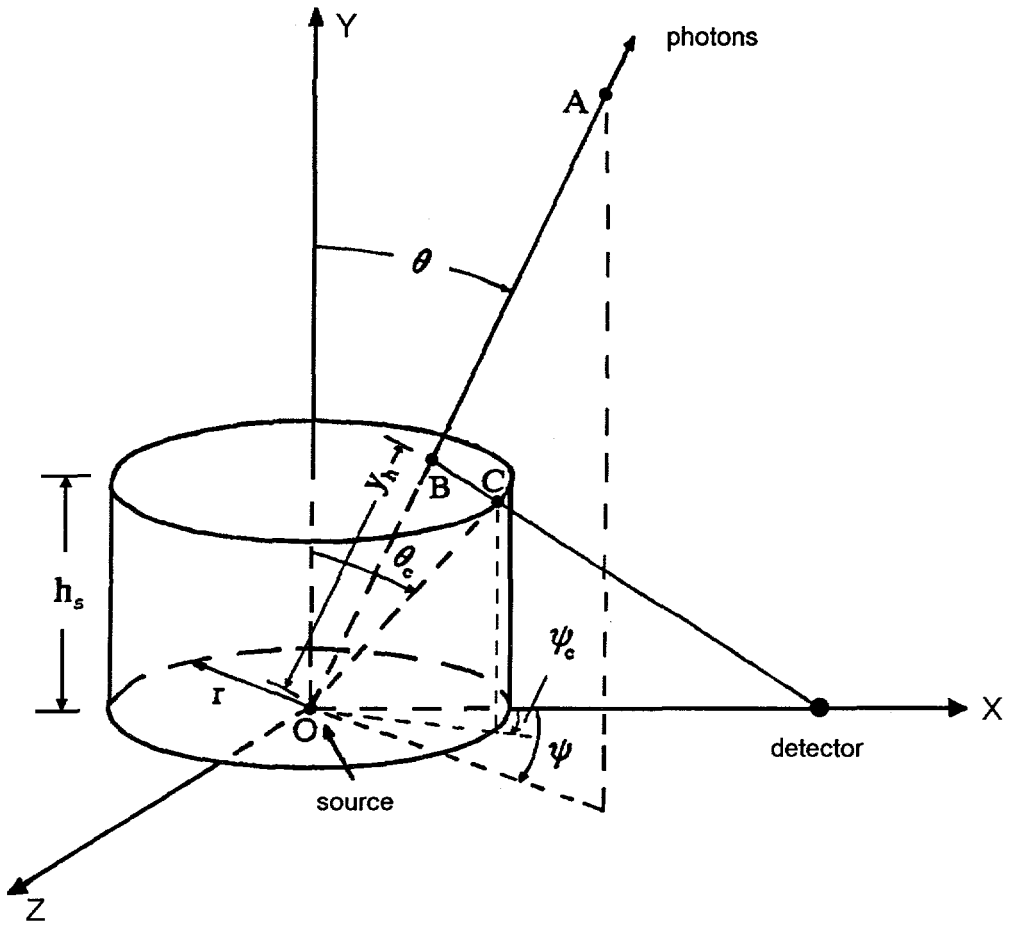

Figure 5.5. Geometry used to analyze the effect of the silo wall occluding the initial portion of the line beam.

with

$$\psi_c = \sin^{-1}\left(\frac{\tan\theta \sin\psi}{\tan\theta_c}\right). \tag{5.11}$$

Skyshine doses calculated from Eq. (2.24) ($y_h = 0$) and from Eq. (5.10) ($y_h > 0$) for the open silo geometry are compared for different source energies in Figs. 5.6 and 5.7. In Fig. 5.6 the source is 5 m below the top of an open silo of 1-m radius. The contribution from the occluded portion of the beam is seen to be significant only for very low energies ($E < 30$ keV) and is greatest when the detector is near the outer wall of the silo. In Fig. 5.7 the source is raised to 1 m from the top of the silo, thereby greatly broadening the conical collimation of the emitted radiation and shortening the beam occlusion lengths. Even for the lowest of the energies shown, the contribution from the occluded portion of the emitted beams is seen to be negligible.

For most practical cases the inclusion of the occluded beam section in the skyshine dose introduces a negligible over estimation. Only for very low source energies and

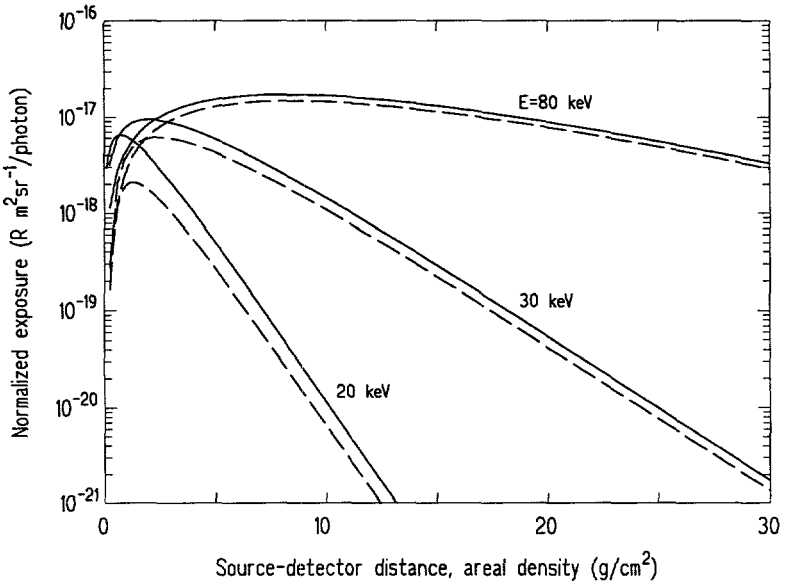

Figure 5.6. Comparison of the skyshine dose with the occluded portion of the source beams excluded (dashed lines) and using the entire length of the source beams (solid lines). Results are for a source on the axis of a 2-m diameter silo 5 m below the silo top.

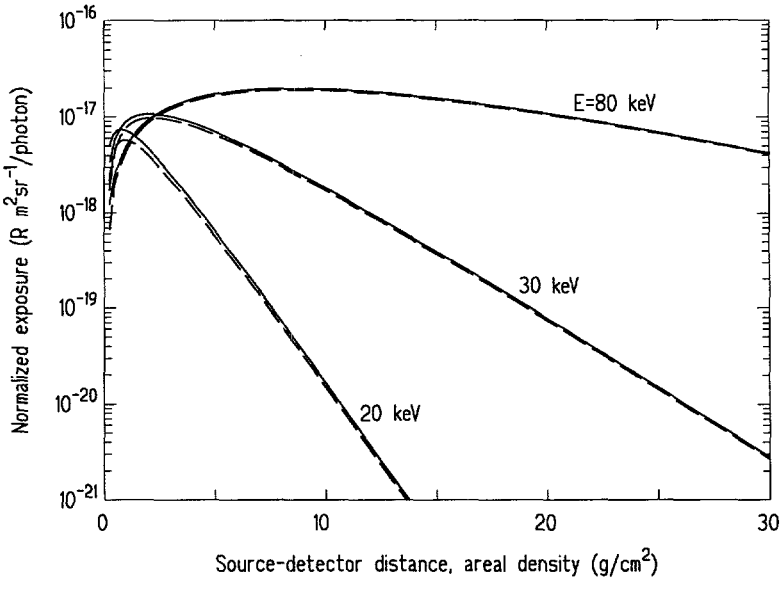

Figure 5.7. Comparison of the skyshine dose with the occluded portion of the source beams excluded (dashed lines) and using the entire length of the source beams (solid lines). Results are for a source on the axis of a 2-m diameter silo 1 m below the silo top.

for sources deep below the top of the confinement walls should the occluded portion of the beam be omitted in the skyshine calculations.

5.2 Infinite Wall Geometry

The geometry of this skyshine problem is illustrated in Fig. 5.8. A point monoenergetic source, shielded by a vertical and infinitely long black wall, isotropically emits photons of energy E. The source is a vertical distance h_s from the horizontal plane through the top of the wall and a perpendicular distance r from the wall. A detector is located in air of density ρ at a distance h_d beneath the same reference plane as used for h_s, at a distance x_d from the source along a normal to the wall, and with a horizontal offset z to the normal axis from the source to the wall.

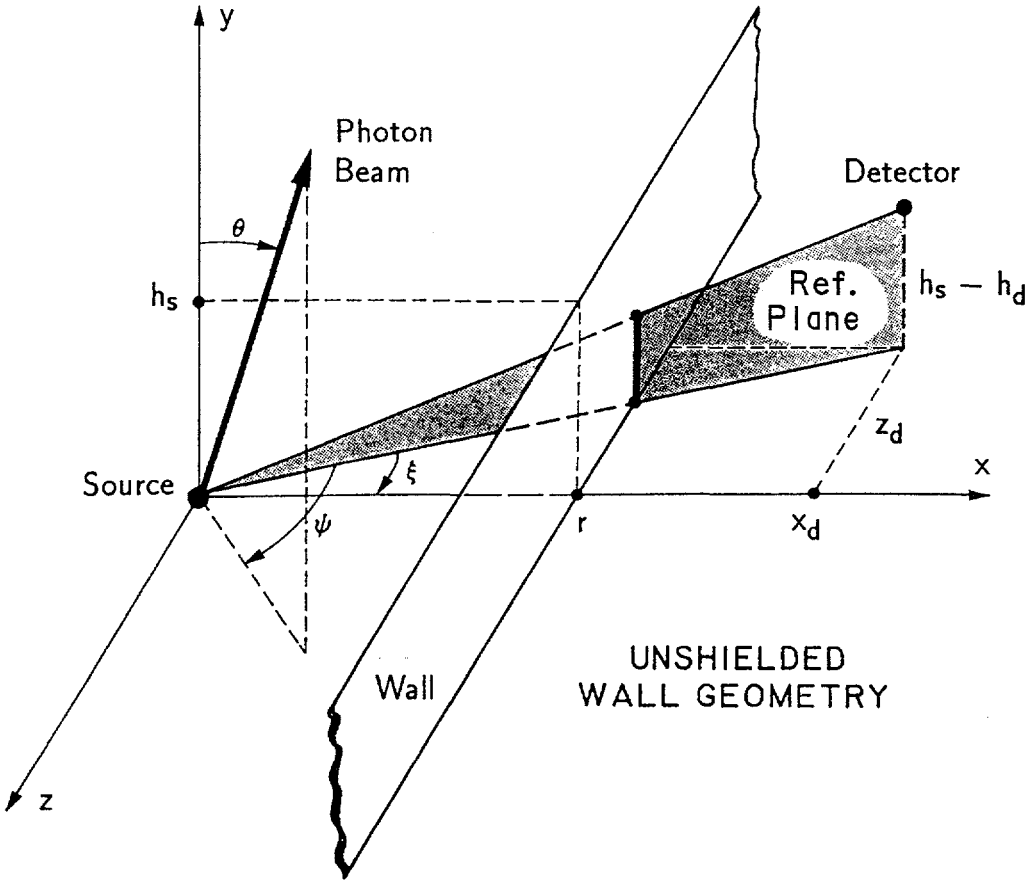

Figure 5.8. Geometry for the infinite wall skyshine problem. A point isotropic source is place a distance h_s below the top and a distance r behind an infinitely long black wall. The detector on the other side of the wall has coordinates $(x_d, h_s - h_d, z_d)$ in a coordinate system with the origin at the source and the horizontal $x-y$ plane parallel to the top of the wall.

The skyshine dose for this infinite-wall geometry is given explicitly by

$$R(d) = \frac{S_p}{4\pi} \int_0^{2\pi} d\psi \int_{\omega_{min}}^{1} d\omega \, \Re(d, \phi). \tag{5.12}$$

To evaluate this expression, one must first determine ω_{min}, the beam angle ϕ, and the source-to-detector distance d. From the geometry of Fig. 5.8, the distance from the source to detector is found to be

$$d = \sqrt{x_d^2 + (h_s - h_d)^2 + z_d^2}, \tag{5.13}$$

and the angle ζ between the horizontal and the source-detector axis is determined by

$$\zeta = \tan^{-1}\left(\frac{h_s - h_d}{\sqrt{x_d^2 + z_d^2}}\right). \tag{5.14}$$

The angle ξ between the source-to-detector axis and the normal from the source to the wall is given by

$$\xi = \tan^{-1}(z_d/x_d), \tag{5.15}$$

The cosine of the angle ϕ between the direction of the photon beam and the source-to-detector axis is the dot product of the unit vector $\mathbf{e}$ along the beam and unit vector $\mathbf{u}$ along the source-detector axis, namely

$$\mathbf{e} = \mathbf{i} \sin\theta \cos(\psi - \xi) + \mathbf{j} \cos\theta + \mathbf{k} \sin\theta \sin(\psi - \xi), \tag{5.16}$$

and

$$\mathbf{u} = \mathbf{i} \cos\xi \cos\zeta + \mathbf{j} \sin\zeta - \mathbf{k} \cos\zeta \sin\xi. \tag{5.17}$$

Thus,

$$\cos\phi = \mathbf{e} \cdot \mathbf{u} = \cos\psi \sin\theta \cos\zeta + \cos\theta \sin\zeta. \tag{5.18}$$

For this infinite wall geometry, the minimum polar angle of rays emitted into the atmosphere θ_{min} is clearly equal to 0. To obtain the maximum polar angle θ_{max}, the $(0, 2\pi)$ range for the angular variable ψ is divided into two ranges. In one range $(0 \leq \psi \leq \pi/2 + \xi)$ and $3/2\pi + \xi \leq \psi \leq 2\pi)$, photon beams are directed towards the wall, and the maximum polar angle $(\omega_{min} = \cos\theta_{max})$ is defined by the photon beam that just clears the top of the wall. In the second range $(\pi/2 + \xi \leq \psi \leq 3\pi/2 + \xi)$, photon beams are directed away from the wall. For this case, all beams directed away from the wall are assumed to contribute to the skyshine dose and hence the maximum polar angle is set to $\pi/2$ (or $\omega_{min} = 0$). This simplified treatment for the backward beams will, in principle, overestimate the skyshine dose because the initial portion of these backward beams will be occluded from the detector by the infinite wall. However, this overestimation will generally not cause a serious error since the contribution made by the shielded portion of the backward beams is several orders

of magnitude less than that made by the beams directed towards the detector. Thus the maximum polar angles for the infinite wall problem are given by [Sh91]

$$\theta_{max} = \begin{cases} \tan^{-1}\left(\dfrac{r}{h_s \cos(\psi - \xi)}\right), & 0 \le \psi \le \pi/2 + \xi, \quad 3/2\pi + \xi \le \psi \le 2\pi, \\ \pi/2, & \pi/2 + \xi \le \psi \le 3\pi/2 + \xi \end{cases} \tag{5.19}$$

Figure 5.9 shows the results of skyshine dose calculations for the infinite-wall geometry problem. A bare, point, isotropic source of ^{16}N gamma photons with energy of 6.2 MeV emits one photon per second. A detector is placed at distances x ranging from 10 to 1600 m, and at an offset $z_o = 0$ m. The skyshine doses are calculated for the source placed at different depths h_s at a perpendicular distance r of 1 m from the black wall. The solid lines are results based on the new approximation for the LBRF, and the data points are results based on the LBRF obtained by Shultis et al. [Sh91]. The excellent agreement between the new and old results at this energy is to be expected since the old LBRF has been shown to be quite accurate in this energy region. The dose rate produced by a bare source near the top of the wall ($h_s = 0$) is much higher than that for a source below the top of the wall. The shielding effect of the wall is very obvious even at an h_s of 0.5 m.

Figure 5.10 compares the skyshine doses for the infinite wall skyshine problem obtained by the new LBRF approximation (solid lines) and a previous LBRF approximation [Sh91] (dashed lines) for different source energies The results obtained from the new and the old LBRF are in good agreement at energies above 1 MeV. The differences between two approximations, however, increase with decreasing energy below 0.2 MeV. There are no comparison data for the 0.05 MeV skyshine dose in Fig. 5.12 since the old LBRF is restricted to an energy range of 0.1 MeV to 10 MeV.

5.3 Open Rectangular Building Geometry

Of considerable practical importance is the skyshine problem in which photons are emitted from a source inside a rectangular building with thick walls but a thin roof. The geometry for this skyshine problem is illustrated in Fig. 5.11. A point monoenergetic source, isotropically emitting photons of energy E, is located on the z-axis at a depth h_s from the horizontal plane defined by the top of the rectangular building. As shown in Fig. 5.11(b), the source is a perpendicular distance x_2 from the front wall, x_1 from the rear wall, y_1 from one side wall, and y_2 from the other side wall. The walls are assumed to be black. A detector is located at coordinates x $(= x_1 + x_d)$ and y $(= y_d)$ in a horizontal plane, with x_d measured from the detector along an axis normal to the front wall and offset a distance y_d from this normal axis. The detector is located at depth h_d below the horizontal plane through the top of the wall. The

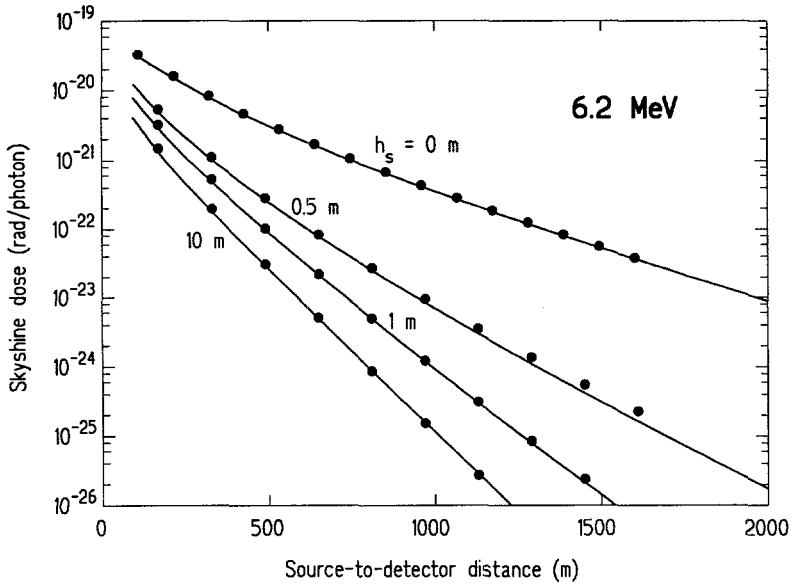

Figure 5.9. Variation of the skyshine dose with source-to-detector distance for a source of 6.2 MeV photons 1 m behind a black wall and at various depths below the top of the wall. The detector is placed 17.4 m below the top of the wall. Data points are based on earlier LBRF approximations [Sh91]. Solid lines are based on the new 4-parameter LBRF approximations.

skyshine dose for the detector is then given explicitly by

$$R(d) = \frac{S_p}{4\pi} \int_0^{2\pi} d\psi \int_{\omega_{min}(\psi)}^{1} d\omega \, \Re(d, E, \phi). \tag{5.20}$$

To evaluate this expression, one must first determine ω_{min}, the beam angle ϕ, and the source-to-detector distance d. The distance from source to detector is found to be

$$d = \sqrt{(x_2 + x_d)^2 + (h_s - h_d)^2 + y_d^2}. \tag{5.21}$$

The angle between the reference plane through both the source and the detector and a plane normal to the wall is given by

$$\xi = \tan^{-1}\left(\frac{y_d}{x_2 + x_d}\right), \tag{5.22}$$

and the angle ζ between the horizontal and the source-to-detector axis is given by

$$\zeta = \tan^{-1}\left(\frac{h_s - h_d}{\sqrt{(x_2 + x_d)^2 + y_d^2}}\right). \tag{5.23}$$

The angle ϕ between the direction of a photon beam and source-detector axis is given by Eq. (5.8) for this rectangular building problem.

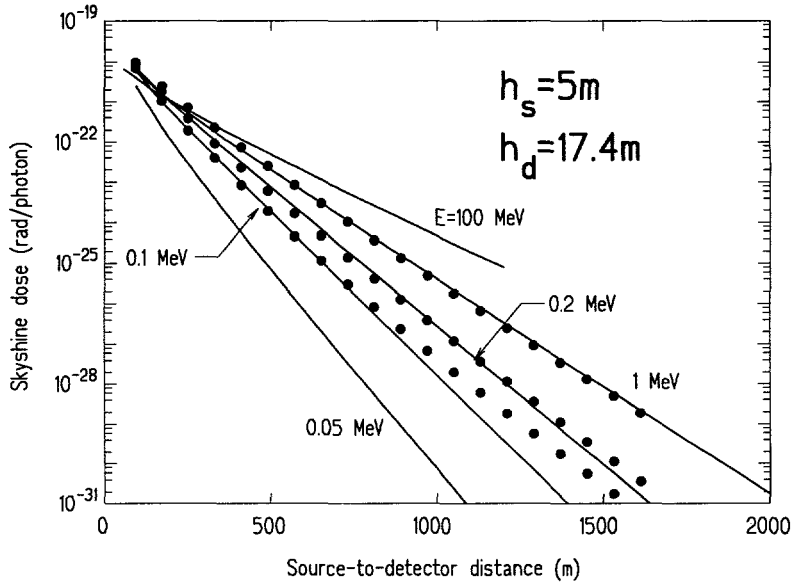

Figure 5.10. Variation of the skyshine dose with source-to-detector distance for different photon energies. The source is located 1 m behind a black wall and 5 m below the top of the wall. The detector is placed 17.4 m below the top of the wall. The solid lines are results obtained with the improved LBRF approximation, and the dashed lines a results based on a previous LBRF approximation [Sh91].

The minimum polar angle θ_{min} equals 0. To obtain the maximum polar angle, the 2π range for ψ was divided into four subranges. As shown in Fig. 2.9(b), ψ is measured in the horizontal plane from a vertical plane through the source-detector axis. Each ψ range is defined by the critical angles ψ_1, ψ_2, ψ_3, and ψ_4 shown in Fig. 5.11(b) that are measured from the reference plane to the corners of the rectangular building. The critical ψ angles are given by

$$\psi_1 = \tan^{-1}(y_1/x_2) - \xi, \tag{5.24}$$

$$\psi_2 = \tan^{-1}(x_1/y_1) + \pi/2 - \xi, \tag{5.25}$$

$$\psi_3 = \tan^{-1}(y_2/x_1) + \pi - \xi, \tag{5.26}$$

$$\psi_4 = \tan^{-1}(x_2/y_2) + 3\pi/2 - \xi, \tag{5.27}$$

In the above formulation, the angle ξ can be either positive (when the detector is offset in the positive ψ direction) or negative (when the detector is offset in the negative ψ direction). Thus the maximum polar angles for this rectangular building

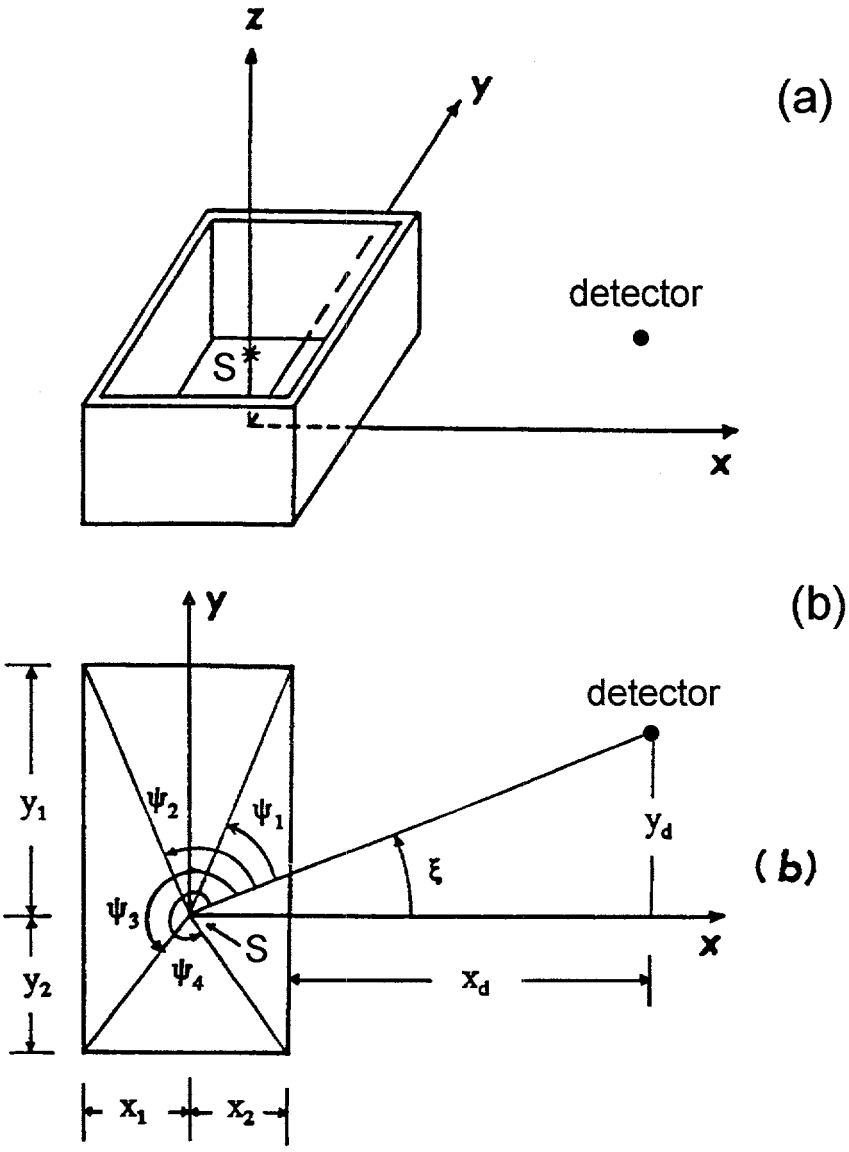

Figure 5.11. (a) Geometry for the rectangular building skyshine problem. A point isotropic source is placed within a roofless rectangular building with black walls. (b) Plan view showing the geometry variables used to calculate the skyshine dose.

problem are found to be

$$\theta_{max} = \begin{cases} \tan^{-1}\left(\dfrac{x_2}{h_s \cos(\psi + \xi)}\right) & \psi_4 - 2\pi \leq \psi \leq \psi_1 \\ \tan^{-1}\left(\dfrac{y_1}{h_s \cos(\psi + \xi - \pi/2)}\right) & \psi_1 \leq \psi \leq \psi_2 \\ \tan^{-1}\left(\dfrac{x_1}{h_s \cos(\psi + \xi - \pi)}\right) & \psi_2 \leq \psi \leq \psi_3 \\ \tan^{-1}\left(\dfrac{y_2}{h_s \cos(\psi + \xi - 3\pi/2)}\right) & \psi_3 \leq \psi \leq \psi_4. \end{cases} \tag{5.28}$$

5.3.1 Results for ANSI Benchmark Skyshine Problems

ANSI/ANS-6.6.1 Reference Problem I-1 involves a 6.12-MeV point isotropic source positioned in air 18.3 m above the earth. Detectors are placed 0.91 m above the earth at distances from 61 to 1500 m from the normal through the source to the ground. The results of skyshine dose calculations based on the new beam response function compared with those of several benchmark calculations are presented in Fig. 5.13. Only the dose rate due to skyshine is shown.

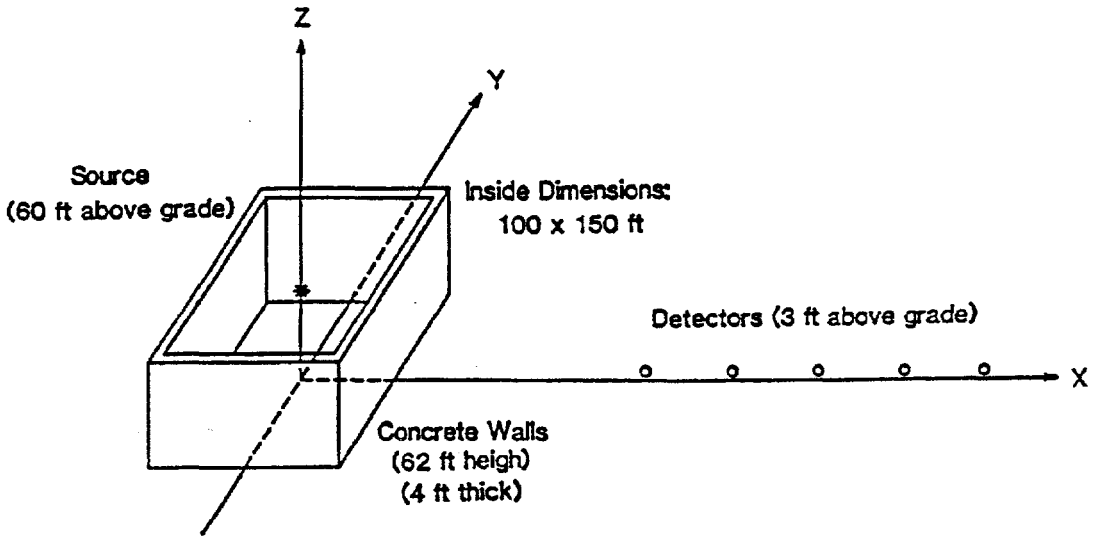

Figure 5.12. Geometry for the ANSI/ANS-6.6.1 Reference Problem No. I.2.

ANSI/ANS-6.6.1 Reference Problem I-2 involves a 6.12-MeV point isotropic source collimated by an open rectangular building [An87]. The source is placed on the vertical axis of the rectangular roofless building which has black walls. The geometry of this benchmark problem is shown in Fig. 5.12. The results of skyshine dose calculations based on the new beam response function compared with those of several

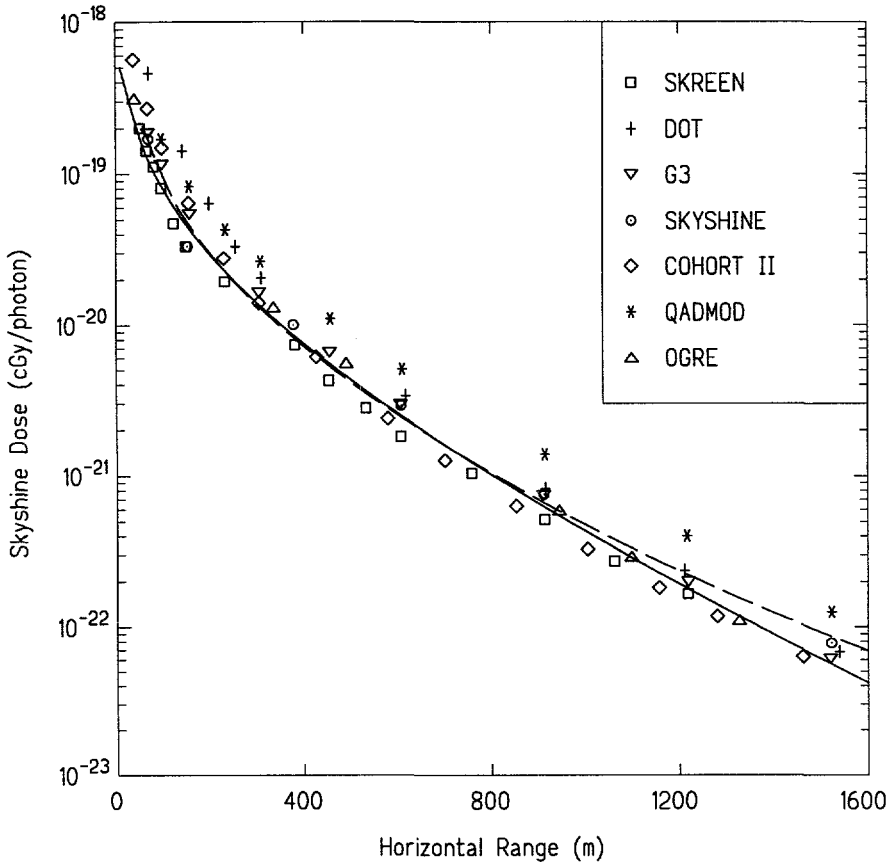

Figure 5.13. Comparison of results obtained by different methods for ANSI/ANS-6.6.1 Reference Problem I1 [An87]. The solid lines are values obtained with the new 4-parameter LBRF approximation. Dashed lines are based on the original 3-parameter LBRF approximation used in the RRA SKYSHINE series of codes [La79].

benchmark calculations are presented in Fig. 5.14. The new LBRF approximation gives results that are in much better agreement with other benchmark calculations than those from the SKYSHINE code which uses an older LBRF approximation.

5.4 Comparison to Moment-Method Results

A special limiting case for the skyshine problem occurs when the point monoenergetic source and detector are at the same horizontal level as the top of the shielding walls, with $\omega_{min} = 0$. The source thus emits photons of energy E isotropically into a hemisphere. The skyshine dose for such a 2π-collimated source is exactly one-half of the dose from a bare point isotropic source in an infinite air medium (less the uncol-

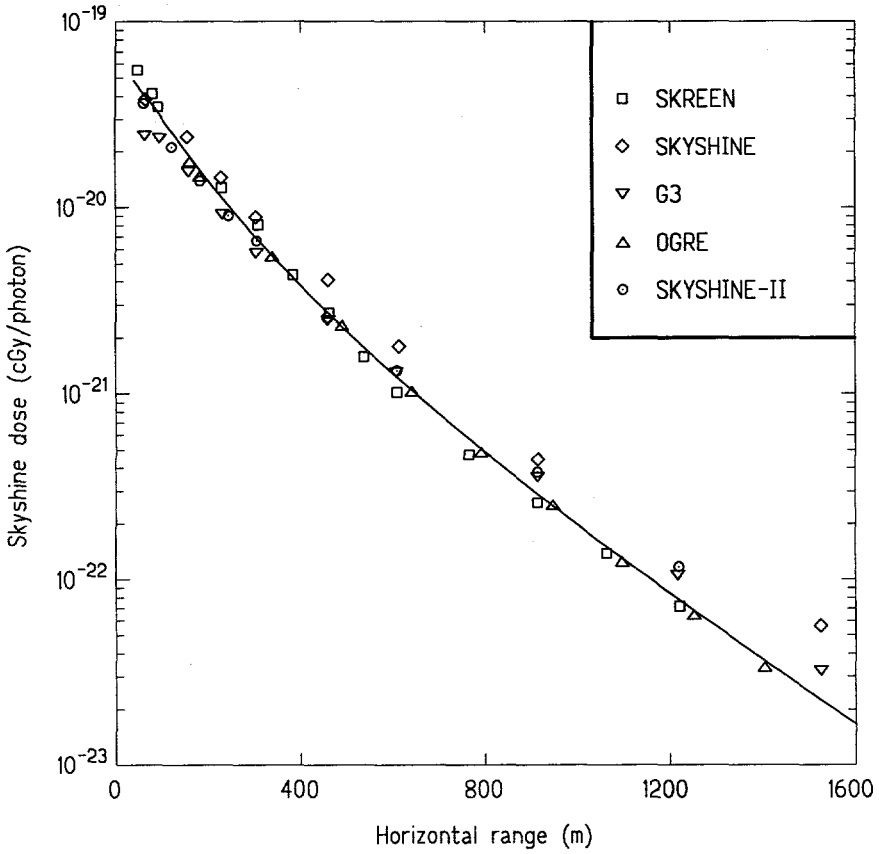

Figure 5.14. Comparison of results obtained by different methods for ANSI/ANS-6.6.1 Reference Problem I2 [An87]. The solid line are values obtained with the new LBRF approximation using the rectangular building skyshine geometry.

lided component). The exposure due to a point isotropic source has been calculated by the moments method by Chilton, Eisenhauer, and Simmons in their calculation of the point-source, infinite-medium, buildup factor [Ch79]. Therefore, one can use these moments calculations to verify the integral line-beam method for the limiting 2π-collimation case.

The moments method results for the 2π-geometry problem can be obtained by taking one-half of the scattered dose component arising from a point source in an infinite air medium. If $\mathcal{R}_K(E)$ is the air kerma rate response function (rad m^2), $B(E,x)$ the kerma buildup factor for photons of energy E at distance x from the source, and $\mu(E)$ the total air attenuation coefficient for photons of energy E, the kerma rate, in units of rad/photon, is given by

$$R(x)/S_p = \frac{\mathcal{R}_K(E)e^{-\mu(E)x}[B(E,x)-1]}{8\pi x^2}. \tag{5.29}$$

Comparison benchmark values were obtained from this expression by using the buildup factors found by the moments method [Ch84] and the attenuation coefficient data from the same source as used in the LBRF calculations [Dl88]. The skyshine dose calculation for this limiting 2π-geometry problem was performed with open silo geometry with the source and detector at the same elevation as the top of the silo wall and with a 1-m silo radius, although the silo radius plays no role in the calculation. Thus the skyshine dose rate reduces to

$$R(d)/S_p = \int_0^{2\pi} d\psi \int_0^1 d\omega \, \Re(E, \phi, d), \tag{5.30}$$

where the LBRF can be approximated by either Eq. (4.14) or (4.15). In the verification calculation, the source-to-detector distance varied from 2 to 2500 m, and the photon energy ranged from 0.1 MeV to 100 MeV. A standard air density of 1.225 mg/cm^3 was used.

The 2π-skyshine results obtained from these two different methods are shown in Fig. 5.15. The solid lines are the results obtained with the integral line-beam method, and the data points are the results based on the moments method. A similar comparison of the two methods was previously given by Faw and Shultis [Fa87, Sh91]. In their plot, there were some inconsistencies at low energies because of the coarseness of the energy structure used in their LBRF below 1 MeV. In this study, using an improved LBRF with better low energy structure, the results of two different methods are in remarkably good agreement.

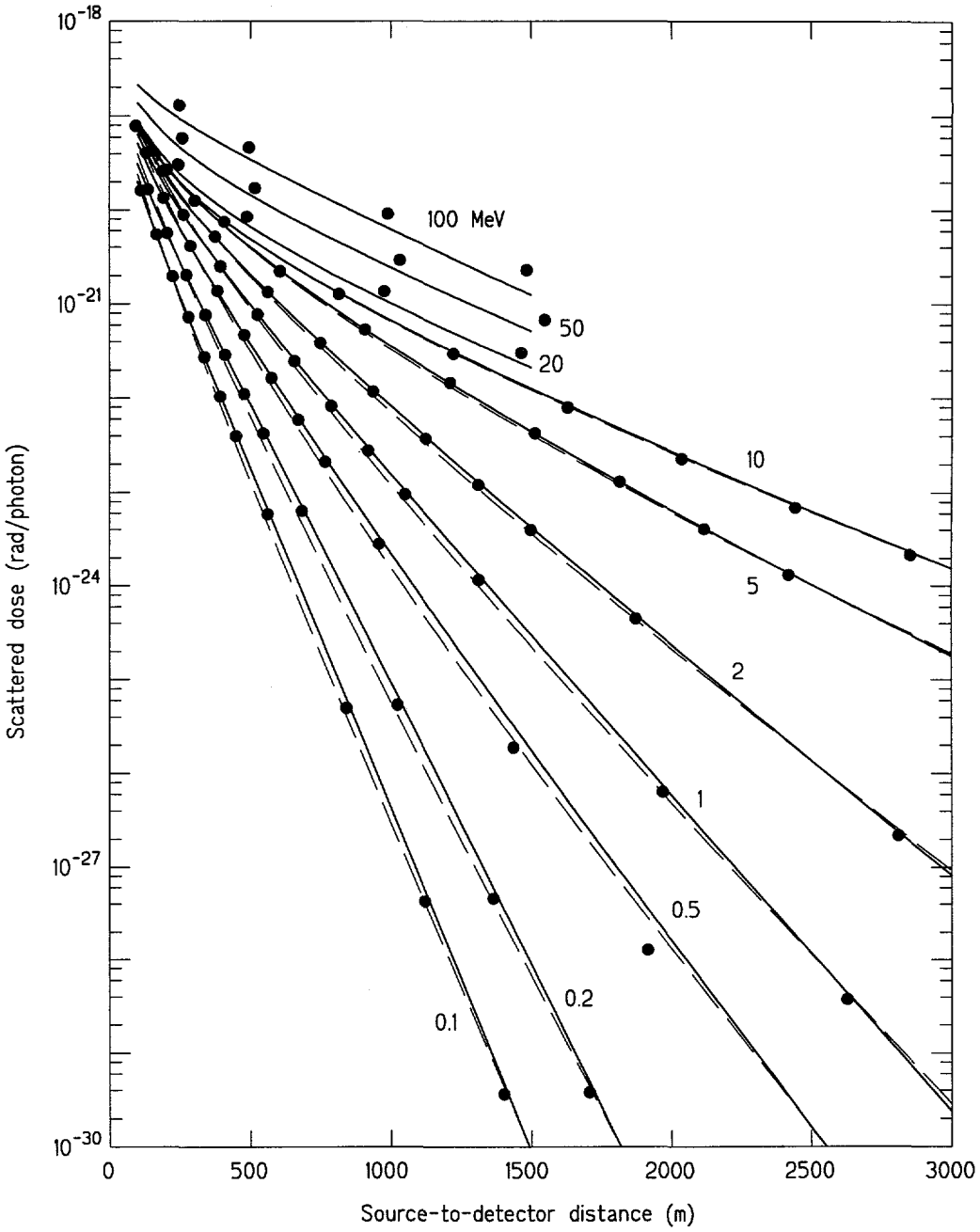

Figure 5.15. Comparison of the integral line-beam method using the 3-parameter approximate LBRF (dashed lines) and the 4-parameter approximate LBRF (solid lines) with results obtained from buildup factors (circles) for different photon energies. In this example a point source emits photons isotropically only into the upward 2π hemisphere.

Chapter 6

Application to Shielded Sources

In many instances, photons from a skyshine source must first pass through some mass of overhead material before escaping into the atmosphere. The overhead material acts as a shield and tends to reduce the skyshine doses. While passing through such overhead material, some photons will be absorbed, others will be scattered into different directions with lower energies, some will create secondary annihilation photons through pair production interactions, and some will pass through the material without interaction and maintain their original energy and direction.

6.1 Previous Approaches

The exact transport treatment of the skyshine doses arising from photons escaping through a source shield and subsequently migrating through the atmosphere is a computationally difficult problem, especially for large source-to-detector distances. For accurate results, particle transport methods such as discrete ordinates or Monte Carlo techniques must be used. However, such methods are expensive for routine or preliminary analyses and, consequently, several approximate and computationally less expensive approaches have been proposed to account for the effect of an overhead shield on the skyshine dose. Four such approximate methods are reviewed below.

6.1.1 Exponential Attenuation With Buildup

The use of simple exponential attenuation combined with a buildup factor has been found effective in describing the skyshine from photon beams passing through horizontal overhead slab concrete shields [Ro82, Ge88] and has been incorporated into the integral line-beam method [Sh91] and the MICROSKYSHINE code [Gr87]. In this approach, the expression for the skyshine dose of Eq. (1.1) is modified as

$$R(d) = \int_0^\infty dE' \int_{\Omega_s} d\Omega\, S(E', \Omega) \Re(d, E', \phi(\Omega)) B(E', \lambda') e^{-\lambda'}. \qquad (6.1)$$

Here $B(E', \lambda')$ is the buildup factor in the shield material for source photons of energy E' emitted in direction $\mathbf{\Omega}$ which must travel λ' mean-free-path lengths through the shield before they reach the atmosphere. In this method the attenuation and buildup of scattered photons in the shield is accounted for, but the change in energy and direction of the secondary photons created in the shield is neglected. Although simple to implement in the integral line-beam method, this method is at best approximate and can result in over- or underprediction of the skyshine dose by factors of 2 to 5 [Ba89].

6.1.2 Transmission Factors

The later versions of the SKYSHINE codes [La88]incorporated empirical "transmission functions" that approximately calculate the energy and angular distribution of photons that pass through a slab of material which is illuminated by photons of a given energy and angle of incidence. Thus energy and angular distributions of source photons incident on interior walls of a confining structure around the source are modified to account for spectral and angular changes as the photons pass through the walls. The modified transmitted energy-angle distribution is then used as a source for a bare skyshine calculation based on the infinite medium LBRF. This approach is computationally simple since it avoids any detailed transport description of the photons passing through a source shield. Its accuracy is determined primarily by the detail contained in the empirical transmission functions and by the Monte Carlo procedure used to integrate over all photon energies and directions. Decoupling of radiation transport in building materials and in the atmosphere is discussed in greater detail in Section 6.1.4.

6.1.3 Modified Line-Beam Response Functions

A recent approach for treating an overhead slab shield is to incorporate the shield's effect directly into the LBRF itself [Ha94]. With this method the shield can be accounted for exactly, provided the LBRF is approximated from data that includes the exact effects of the shield. The skyshine dose a distance d from the source is thus calculated as

$$R(d) = \int_0^\infty dE' \int_{\mathbf{\Omega}_s} d\Omega \, S(E', \mathbf{\Omega}) \Re(d, E', \phi(\mathbf{\Omega}), T). \tag{6.2}$$

where now the LBRF $\Re$ is a function of the shield thickness T and the shield material. This "shielded LBRF" can be approximated well by the four-parameter formula of Eq. (4.12) by fitting this formula to Monte Carlo results that include the overhead shield [Ha94]. At present, parameters for an approximate shielded LBRF are not available. Although this method appears capable of good accuracy, the computational effort required to generate reference LBRF values and to obtain approximation LBRF parameters for all combinations of source energies, beam angles, and shield thicknesses, and shield materials appears to be prohibitive.

6.1.4 Decoupled Calculations

Another approach, which is capable of good accuracy for the case of a horizontal slab shield over a point source, is to decouple the shielded skyshine problem into two independent problems. First the energy and angular distribution of the photon flow rate or z-component of the current density, $j_z(x, y, T, E, \Omega)$, escaping through the plane surface ($z = T$) on the atmospheric side of the shield is computed using a transport method such as discrete ordinates or Monte Carlo. This escaping distribution is then integrated over the entire slab surface and used as an effective bare point skyshine source $S_{eff}(E, \Omega)$ centered on the outer shield surface, namely

$$S_{eff}(E, \Omega) = \int dx \int dy \; j_z(x, y, T, E, \Omega) \tag{6.3}$$

where the integration is over the entire outer shield surface. This effective point source is then used in an unshielded skyshine calculation performed with the integral line-beam method.

One important approximation in this two step hybrid approach is that the lateral spread of the photons escaping the shield is negligibly small compared to the source-detector distances of interest. Further, it is assumed that the dimensions of the shielding structure are much less than the air transport distances, so as to have negligible effect on the subsequent atmospheric transport problem. A key simplification in the transport calculation is achieved if lateral leakage of photons can be ignored as, for example, in a very wide slab shield. In this case a much simpler one-dimensional transport calculation suffices to obtain $S_{eff}(E, \Omega)$ [Ba89]. If, in addition, the angular distribution of the incident photons on the inner shield surface is azimuthally symmetric, such as shield illumination from a point isotropic source, the transport calculation can be performed with a one-dimensional azimuthally-symmetric algorithm.

Keck and Herchenroder [Ke82] were the first to use this two step method. They used the one-dimensional discrete ordinates code ANISN [En67] to estimate the surface-integrated flux density of photons escaping from the shield. Later Bassett [Ba89] used the discrete ordinates code KSLAB [Ry79], which is based on the exact-kernel method [Mi77], to calculate the escaping photon distribution. This later approach is capable of a more detailed evaluation of the angular dependence of the escaping photons than is a discrete ordinates method based on traditional Legendre polynomial expansions. This accurate angular capability is especially needed for source photons that are collimated vertically before reaching the overhead shield, e.g., by the walls of a building or shielding around an experiment. The results of such calculations were shown to give good predictions of shielded benchmark skyshine experiments and were then used as benchmarks themselves to assess the accuracy of the simpler exponential attenuation with buildup method to account for the shield effect [Ba89].

6.2 A Hybrid Monte-Carlo/LBRF Approach

In this study two variants of the two-step hybrid method for shielded skyshine sources were investigated. A specialized analog Monte Carlo code module was written to generate the energies and directions of photons escaping from the outer surface of an infinite horizontal slab shield which is illuminated on the inner surface by monoenergetic photons emitted from a point isotropic source. The source may be collimated so that only a portion of the inner surface is illuminated.

Once the energy and direction of escaping photons are determined by the Monte Carlo procedure, two methods can be used to obtain an estimate of the skyshine dose caused by these escaping photons. In the first method, called the *individual* scoring scheme, the LBRF evaluated at each escaping photon's energy E and direction ϕ with respect to the source-detector axis is factored into the average value contributed by previous photons at the detector where the skyshine dose is to be estimated. This running average will approach the true skyshine dose, per source particle, as the number of escaping particles used to compute the running average becomes large.

If a large number of escaping photons is used to estimate the skyshine dose by the individual scoring method, the LBRF will have to be evaluates many times, once for each photon leaking from the shield. To reduce the computational effort an alternative scoring procedure was investigated. In this second method, called the *binning* scoring method, the Monte Carlo shield simulation is used first to generate the energies and directions of many escaping photons each of which is binned according to its energy E and direction ϕ. Then, after the energy and directional distribution of escaping photons has been built up from many source photon histories, the values of the LBRF evaluated at the centroid of each bin and weighted by the bin's relative number are summed to obtain the dose at the detector location. In this way far fewer evaluations of the LBRF are required.

Although, this second binning approach requires less computation for the same number of source particles, it does introduce a discretization error by restricting photon energies and directions to those of the bin centroids. The relative merits of these two Monte Carlo approaches were investigated in this study.

6.2.1 Simplified Simulation

Monte Carlo simulations usually require considerable computer resources and generally are not attempted on microcomputers. However, the recent increase of computational capability of microcomputers and the simplicity of the one-dimensional simulation needed for the shielded skyshine problem make it possible to incorporate the Monte Carlo hybrid method into a microcomputer program.

Because the geometry for this infinite horizontal slab shield is relatively simple and because only the energy and direction of escaping photons is needed and because

the (x, y) coordinates of where a particle escapes the shield are not needed, the Monte Carlo simulation becomes a simple one-dimensional simulation. Where on the shield's upper surface photons exit is of no interest since the hybrid method assumes all escaping photons do so at the center of the upper shield surface. Consequently, only the energy E, direction $\mathbf{\Omega}$, and z-coordinate (normal to the slab surface) need be computed for each event in constructing the random walk in the shield for a photon.

The Monte Carlo module developed for this study accounts for secondary photons from Compton scattering, based on the Klein-Nishina cross section, and from annihilation of positrons created by pair production. However, no correction for positron transport in the shield is made; positrons are assumed to annihilate in the shield at the point where they were created. No fluorescence or bremsstrahlung is considered. Cross sections for the shield material are approximated by accurate rational approximations similar to those used for air (see Eqs. (2.48) and (2.49)).

To simplify further the Monte Carlo simulation, any photon reflected from the shield is immediately killed, and photons are allowed to migrate laterally to any distance inside the shield. With this simplification, a photon history is continued in the slab shield until the photon is absorbed or crosses a shield surface.

The one complicated aspect of the Monte Carlo algorithm is the capability to allow very general collimation of the incident source photons on the inner surface of the shield. This collimation feature is discussed next.

6.2.2 Collimation of Source Photons Beneath the Shield

The gamma photons incident on the inner surface of an overhead shield will often be effectively collimated by shielding around the source or by building walls. Thus, the shield, modeled as an infinite horizontal slab, will generally not be illuminated at all points. Rather, the area of illumination will be restricted to some finite portion of the surface. To permit analysis of such a restricted area of illumination, the Monte Carlo simulation algorithm used in this study was designed to track only those photons that stream from a point isotropic point source and enter the shield only in the area permitted by the collimation.

The area of the shield surface illuminated by the source is assumed to be in the shape of a polygon defined by N vertices (x_i, y_i), $i = 1, \ldots, N$ on the inner surface of the shield. To determine whether a source photon is to be tracked in the Monte Carlo simulation, it is necessary to determine if the point (x_p, y_p) on the surface at which a source photon enters the shield is within the polygon.

The standard method for determining if a test point (x_p, y_p) lies within a polygon is known as the "far-point algorithm". This method selects a point known *not* to be inside the polygon (usually a point far from the polygon). A straight line is then drawn from this "far" point to the test point and the number of crossings this line makes with the polygon's perimeter is calculated. If the test point is inside the

polygon the number of perimeter crossings will be an odd number.

Unfortunately, this algorithm is computationally inefficient in a Monte Carlo simulation since it must compute the intersection point of the test line with the lines joining each adjacent pair of polygon vertices. Each intersection then must be tested to determine if it occurs between the pair of vertices and thus represents an intersection with the polygon's perimeter.

A New Inside-Point Algorithm

For the present simulation it was decided to restrict the class of all polygons illuminated by the source to convex polygons, i.e., to those polygons whose interior vertex angles are all less than 180 degrees. For these polygons, the far point algorithm is considerably simplified since the line from the far point, which is outside the polygon, to an interior point makes only a single intersection with the polygon's perimeter. If zero or two intersections are found, then the test point lies outside.

However, an even simpler algorithm was developed in this study to determine if a test point is inside the polygon. Consider the general polygon shown in Fig. 6.1.

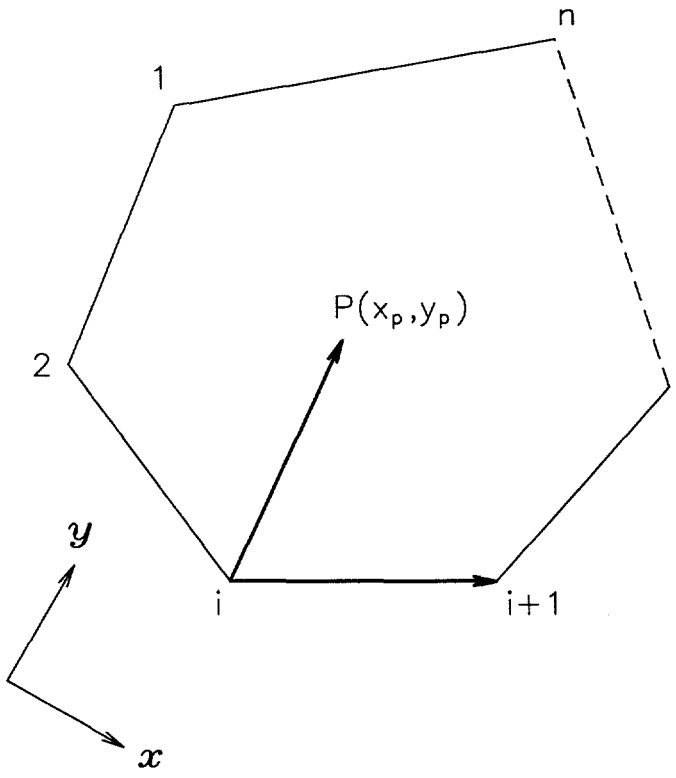

Figure 6.1. General convex polygon with a test point P inside.

If the test point (x_p, y_p) is inside a convex polygon, then the angle ϕ_i between the vector $\mathbf{u_i}$ from node i to the neighboring node $i+1$ (counter-clockwise node ordering is assumed) and the vector $\mathbf{v_i}$ from node i to the test point P will be < 180 degrees for every node i. If P is outside, then at least one ϕ_i will be > 180 degrees. Equivalently, $\sin\phi_i > 0,\ i = 1, \ldots, N$ if the point P is inside the polygon, and at least one $\sin\phi_i$ will be negative if the point is outside. If P should lie exactly on the perimeter of the polygon, then one ϕ_i will vanish.

Rather than evaluate $\sin\phi_i$ (computationally expensive), the following procedure can be used. The vectors $\mathbf{u_i}$ and $\mathbf{v_i}$, which lie in the $x-y$ plane, are given by

$$\mathbf{u}_i = \mathbf{i}(x_{i+1} - x_i) + \mathbf{j}(y_{i+1} - y_i) + \mathbf{k}\ 0 \tag{6.4}$$

$$\mathbf{v}_i = \mathbf{i}(x_p - x_i) + \mathbf{j}(y_p - y_i) + \mathbf{k}\ 0. \tag{6.5}$$

where the nodes are labeled cyclically (counterclockwise) with vertex $N+1 =$ vertex 1. Recall that

$$\begin{aligned}
\mathbf{u}_i \times \mathbf{v}_i &= \mathbf{k}|\mathbf{u}||\mathbf{v}|\sin\varphi_i \\
&= \det \begin{vmatrix} \mathbf{i} & \mathbf{j} & \mathbf{k} \\ (x_{i+1} - x_i) & (y_{i+1} - y_i) & 0 \\ (x_p - x_i) & (y_p - y_i) & 0 \end{vmatrix} \\
&= \mathbf{k}[(x_{i+1} - x_i)(y_p - y_i) - (x_p - x_i)(y_{i+1} - y_i)]. \qquad (6.6)
\end{aligned}$$

Thus for $\sin\phi_i$ to be positive at each node, $\delta_i \equiv (x_{i+1}-x_i)(y_p-y_i)-(x_p-x_i)(y_{i+1}-y_i)$ must also be positive at each node. If P is outside the polygon at least one δ_i will be negative. Notice, that the calculation of the δ_i involves only simple arithmetical operations.

Finally, this algorithm can be generalized to relax the assumption of counterclockwise ordering of the vertices. If P is inside the polygon, all δ_i will have the same sign for either clockwise or counterclockwise ordering, whereas if P is outside, one or more δ_i will have a sign different from the others.

6.2.3 The Monte Carlo Algorithm

The Monte Carlo simulation model described above has been implemented in a shielded skyshine code written for this study. The details of the algorithm are described elsewhere [St94] and are not further discussed here.

6.2.4 Comparison of Binning and Individual Scoring

Computational Times

The reason for proposing the binning method of estimating the skyshine dose was to decrease the computational effort. To test the two scoring methods, three test problems were constructed. All three cases used a ^{60}Co source ($E = 1.25$ MeV) and a concrete overhead shield of density 2.3 g cm^{-3}. The first problem was for a shielded silo in which the silo walls collimated the source photons into a vertical cone with a 30 degree half angle. The second problem was also for a shielded silo but one with a conical collimation half angle of 60 degrees. The third problem was for a source 10 m below the concrete roof shield and on the vertical axis of a rectangular building with interior walls each of 10 m width.

Calculations of the skyshine dose were made using both scoring methods at 20 source-to-detector distances ranging from 50 m to 1000 m. Various thicknesses of the overhead concrete shield, up to a maximum thickness of 7 mean-free-path lengths, were used. For the binning method, 20 equi-spaced energy bins and 20 angular bins were used. For each scoring method the calculations were performed using the same particle histories, i.e., the same sequence of pseudo random numbers were used, so that the difference in execution times is a direct result of the scoring technique used.

In Fig. 6.2 the ratio of the execution times for the two methods is shown as a function of the shield thickness. As is to be expected, the execution times approach each other as the shield becomes very thick since most of the execution time is spent tracking the particles inside the shield. However, for thin shields in which many sources particle penetrate the shield without collisions and for which the Monte Carlo simulation involves very few steps per particle, the computational cost of calculating a LBRF for each particle escaping the shield becomes a major component of the total execution time. For shield thickness greater than a few mean-free-path thickness, there is no appreciable difference between the two methods and the individual scoring method is preferred since it involves no binning errors. For thin shields, by contrast, it is much more efficient to use the binning scoring method.

Accuracy of the Binning Method

Although the binning method is computationally preferred for source shields of less than a few mean-free-path lengths in thickness, this method nevertheless introduces an error from the discretization of the energy and angles of the photons escaping the shield. To assess this error, a test problem was constructed in which the source was on the z-axis 10 m below the bottom of a horizontal laminate shield composed of one mean-free-path thickness each of lead (bottom) and concrete (top). Further, the source was collimated such that only an irregular hexagonal area on the lower shield surface was illuminated. The (x, y) coordinates of the six vertices of this illuminated polygon were chosen as (-5,-5), (-5,5), (-2,10), (5,15), (10,0) and (5,-5). The skyshine

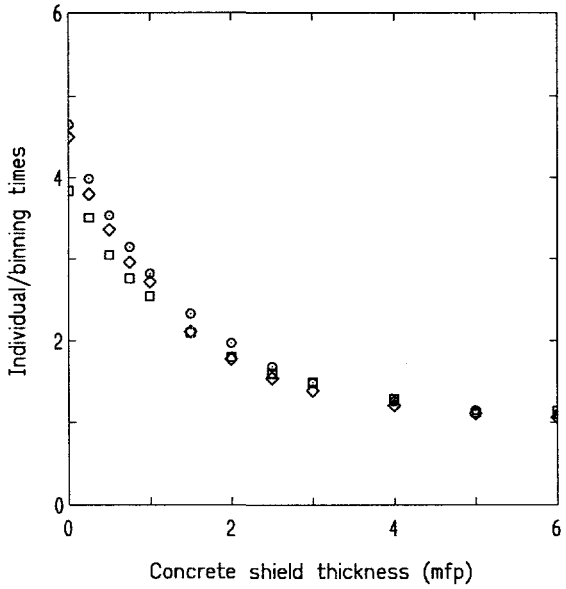

Figure 6.2. Ratio of execution times for the two scoring methods using in Monte Carlo line-beam hybrid method as a function of the concrete shield thickness for three test problems.

detectors were located at an elevation 10 m above the source (bottom shield elevation) along the x-axis. Three different source energies were used, namely 0.5 MeV, 1.25 MeV (^{60}Co), and 6.12 MeV (^{16}N).

To assess the effect of different bin sizes 20 different bin structures were employed. The coarsest structure used 10 energy bins and 20 angular bins. The energy bins were all of equal width equally distributed between 0.02 MeV (the cutoff energy) and the source energy. Energy bin structures using 10, 20, 30, 40 and 50 bins were used. The angular bin structure, by contrast, was not equally distributed between 0 and 180 degrees. The upper limits of the 20 angular-bin case is shown below. To create

Table 6.1. The angular limits, in degrees, for the case of 20 angular bins.

j	ϕ_j	j	ϕ_j	j	ϕ_j	j	ϕ_j
1	1.0	6	10.0	11	50.0	16	100.0
2	2.0	7	15.0	12	60.0	17	120.0
3	3.0	8	20.0	13	70.0	18	140.0
4	5.0	9	30.0	14	80.0	19	160.0
5	7.0	10	40.0	15	90.0	20	180.0

finer angular bin structures, the 20 angular bins were divided into halves, fourths and eights to create 40, 80 and 160 angular bins.

Calculations were made using the same photon histories but with varying numbers of energy and angle bins for sorting the photons that penetrate the shield. The same particle histories were also use in the individual scoring method for this test problem. The detailed results of these calculations are tabulated by Stedry [St94].

To quantify the accuracy of the binning scoring method relative to the individual scoring method, the following procedure was used. The absolute fractional difference in the skyshine dose estimated by the two methods was calculated at 20 source-to-detector distances d_j equally spaced between 50 and 1000 m. These 20 fractional difference were then summed to give a measurement of the differences between the two methods averaged over a range of source-to-detector differences. Explicitly, the following quantity was determined for varying numbers of energy and angle bins for each of the three source energies.

$$\text{Total Absolute Fraction Difference} = \sum_{j=1}^{20} \left| \frac{R_{ind}(d_j) - R_{bin}(d_j)}{R_{ind}(d_j)} \right| \tag{6.7}$$

where R_{ind} and R_{bin} are the skyshine doses calculated by the individual and binning scoring methods, respectively. The results are presented in Table 6.2.

Table 6.2. The sum over 20 source-to-detector distances of the absolute factional differences between the individual and binning scoring methods of calculating the skyshine doses.

	Total Absolute Fractional Difference for 20 Distances											
Energy	0.5 MeV				1.25 MeV				6.12 MeV			
	No. angle bins				No. angle bins				No. angle bins			
No. energy bins	20	40	80	160	20	40	80	160	20	40	80	160
10	.111	.047	.012	.009	.226	.099	.060	.050	.853	.720	.641	.620
20	.108	.052	.013	.003	.190	.071	.023	.012	.315	.178	.101	.080
30	.108	.053	.013	.003	.187	.076	.022	.008	.274	.101	.048	.038
40	.108	.053	.014	.003	.184	.074	.020	.006	.290	.113	.054	.041
50	.108	.053	.013	.003	.184	.075	.020	.006	.282	.109	.045	.030

As expected, the binning results generally agree more closely to the individual scoring results as the number of energy and angle bins increases. The results shown in Table 6.2 show that all the energy and angle bin combinations vary at most by approximately a 4% average percent deviation at any given detector location d_j. The average percent deviation at a detector location d_j is calculated by dividing the total fractional difference by the number of detector locations (in this case 20) and multiplying the result by 100. Thus, for the 6.129 MeV case with 10 energy bins and 20 angle bins (the worst agreement), the average percent deviation at a detector location is just over 4%. One observation from Table 6.2 is that for a given number of energy bins the difference between the results of the two methods decreases as the number of angle bins increases. Also, for a fixed number of angle bins the difference between the results decreases as the number of energy bins increases. For a fixed number of angle

bins there is a maximum number of energy bins past which more energy bins does not improve the calculated skyshine dose. For the 0.5 MeV and the 1.25 MeV cases this is clearly seen, while for the 6.129 MeV case the fractional difference begins to fluctuate around the limiting number of energy bins. This observation means that for a given number of angle bins a limit of the number of energy bins exists past which better accuracy is not achieved. Based on the results in Table 6.2, 20 energy bins and 20 angle bins are recommended for routine calculations using the hybrid Monte Carlo/LBRF method.

6.3 Comparison of Results

6.3.1 Comparisons to Benchmark Experimental Results

In Fig. 6.3 results are shown for the bare skyshine experiment discussed earlier in Section 5.1.1. In this plot, the measured skyshine dose rate D_{meas} has been normalized by (1) multiplying the dose rate by the square of the source-to-detector distance r to remove the $1/r^2$ geometric attenuation effect, and (2) by dividing by the ^{60}Co source activity, S_{act}, i.e., $D_{norm} = r^2 D_{meas}/S_{act}$. The source-to-detector distance is expressed in areal density ρr to correct approximately for the different atmospheric densities which occurred during the measurements. Also shown on Fig. 6.3 are calculations using the hybrid MC-LBRF method and the integral line-beam method. Both of these methods used the 3-parameter approximate LBRF and an air density of 0.001125 g/cm^3. The MC-LBRF hybrid method used binning scoring with 20 energy bins and 20 angular bins. Since the Monte Carlo component consists solely of uncollided radiation, it is not surprising that these results agree well with the integral line-beam calculations.

The KSU benchmark skyshine experiment [Na81], besides providing benchmark skyshine data for an unshielded ^{60}Co source, also included two sets of measurements when the source in the silo was placed beneath a slab concrete shield with two different thicknesses. Specifically, the source photons, which were collimated by the silo walls into a vertically upward cone with a 150.5 degree full angle, were shielded by a concrete shield of density 2.13 g cm^{-3} and of thickness 21.0 cm or 42.8 cm.

In Fig. 6.4 results from the MC-LBRF hybrid method for the two shielded benchmark experiments are compared with experimental and results from an earlier hybrid method by Bassett [Ba89]. It is seen the present MC-LBRF hybrid method agrees closely with Bassett's discrete-ordinates-LBRF hybrid method and with the experimental data.

Although the hybrid method is more computationally expensive than the simpler approach for shielded source of exponential attenuation with buildup (see Section 6.1.1), it is more accurate. Results using exponential attenuation with buildup for the two shielded skyshine experiments are also shown in Fig. 6.4 and, while sufficient for very approximate analyses, are not as accurate as the MC-LBRF hybrid method, particularly at large source-to-detector distances.

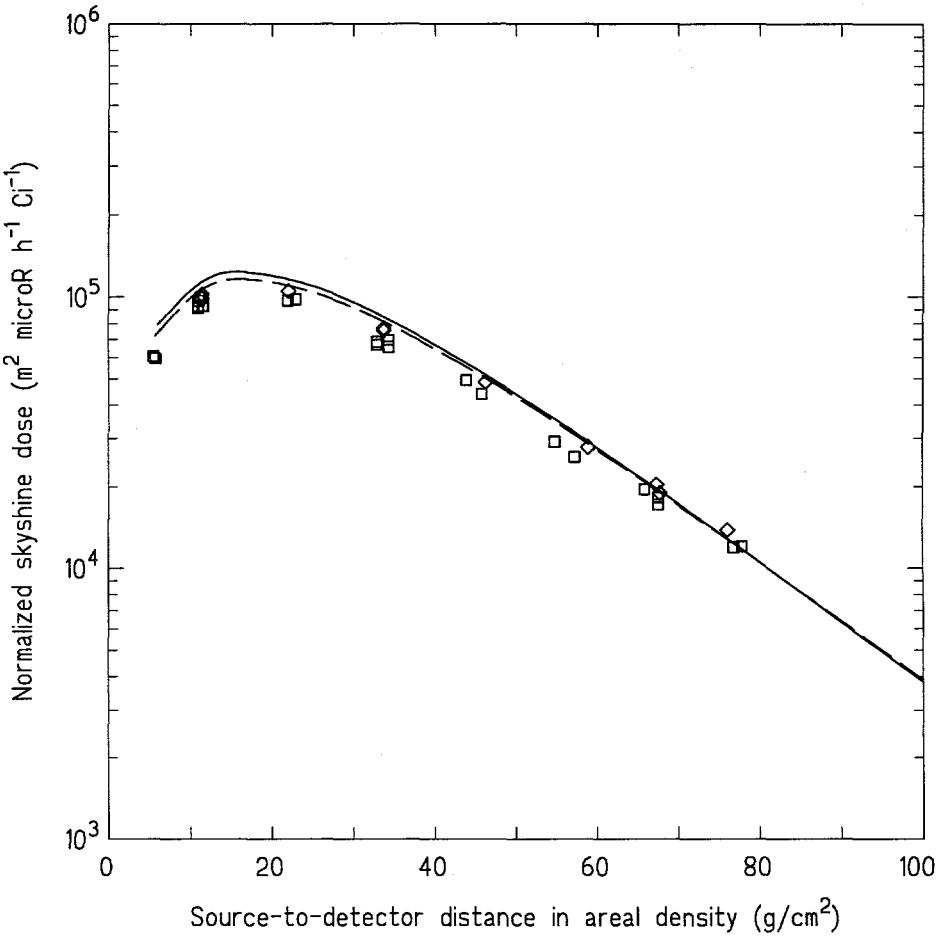

Figure 6.3. Comparison of measurements (squares and diamonds) for the unshielded benchmark skyshine experiment [Na81] with values obtained by the MC-LBRF hybrid method (solid line). Also shown are results (dashed line) from the integral line-beam method presented earlier in Chapter 5.

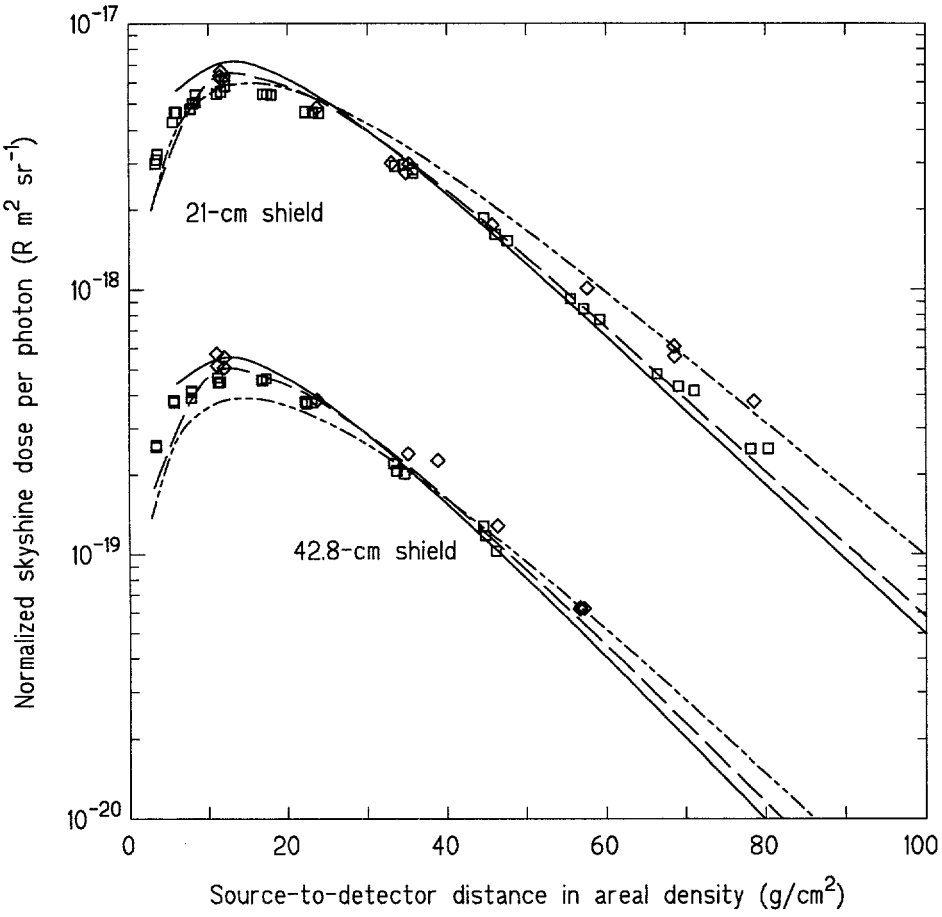

Figure 6.4. Comparison of high-pressure ion chamber measurements (squares) and NaI measurements (diamonds) for the shielded benchmark skyshine experiment [Na81] with values obtained by (1) the MC-LBRF hybrid method (solid lines), (2) Bassett's hybrid method [Ba89] based on discrete ordinates calculations (long-dash lines), and (3) the LBRF method using exponential attenuation with buildup to account for the shield (broken lines).

Comparison to Bassett's Hybrid Method

Bassett [Ba89] used a hybrid method in which transport through the source shield calculated by a specialized energy-multigroup discrete-ordinates algorithm that was capable of giving an accurate description of the angular distribution of the photons escaping through the shield. Although he used a slightly different set of parameters for the three-parameter approximate LBRF than was developed in this study, his results should provide an excellent standard against which the MC-LBRF hybrid method proposed here can be tested.

In Figs. 6.5 to 6.7 a comparison of the two hybrid methods is shown for several shielded silo skyshine problems. Each figure is for a different source energy (6.12, 1.25, and 0.5 MeV) and shows the skyshine dose at a fixed distance from the source as a function of concrete shield thickness for several different source collimation angles. From these figures, it is seen that the two hybrid methods give almost identical results. By contrast, the exponential attenuation with buildup method is seen to underpredict the skyshine dose at high source energies and to overpredict at low energies.

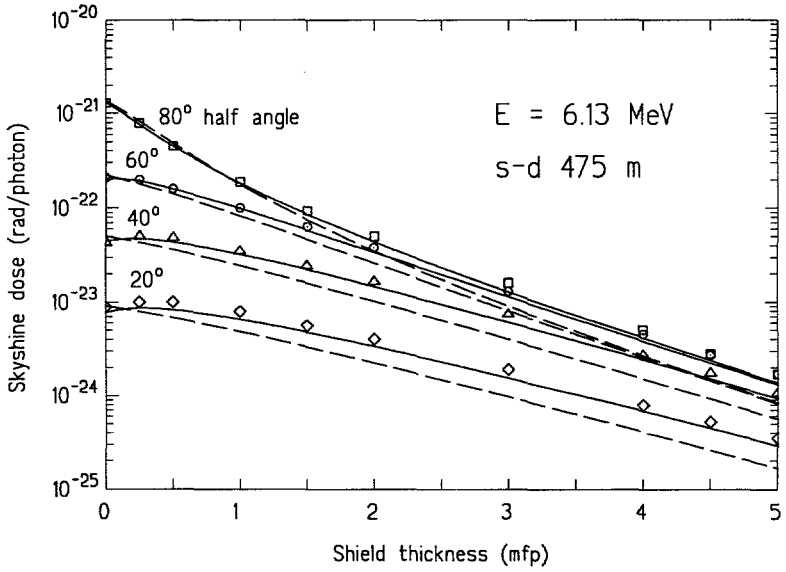

Figure 6.5. The skyshine dose at 475 m from a shielded, collimated, point ^{16}N source (E = 6.13 MeV) in shielded silo geometry as calculated by the discrete-ordinates LBRF hybrid method of Bassett [Ba89] (open symbols), by the MC-LBRF method developed in this study (solid lines), and by the exponential attenuation with buildup method (dashed lines).

Finally, Figs. 6.8 to 6.9 show results from the two hybrid methods for a concrete or iron source shield, both one mean-free-path in thickness. Both methods are seen to give very similar results, the differences resulting primarily from the different approximate LBRFs used by each method. More important, the dose profiles are nearly

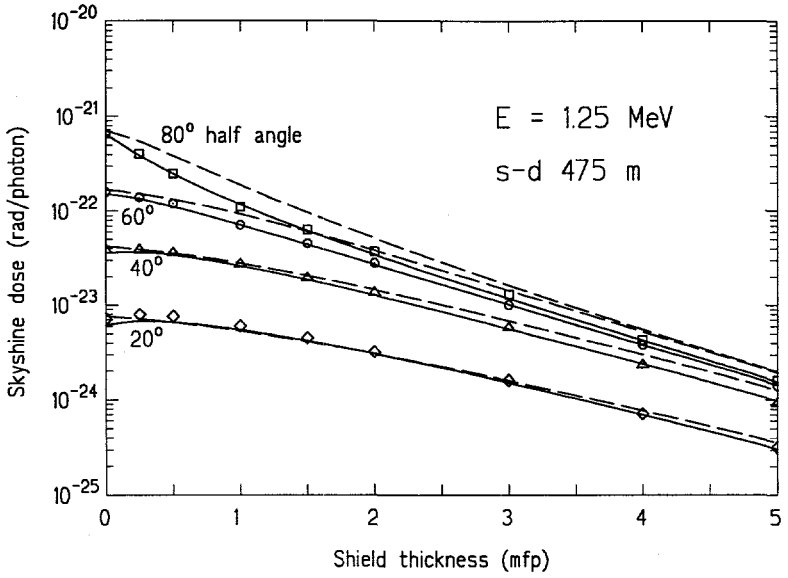

Figure 6.6. The skyshine dose at 475 m from a shielded, collimated, point ^{60}Co source (E = 1.25 MeV) in shielded silo geometry as calculated by the discrete-ordinates LBRF hybrid method of Bassett [Ba89] (open symbols), by the MC-LBRF method developed in this study (solid lines), and by the exponential attenuation with buildup method (dashed lines).

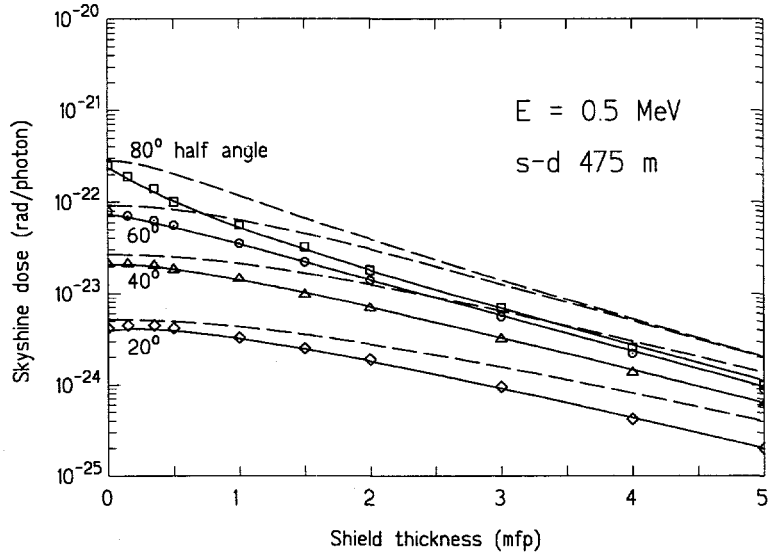

Figure 6.7. The skyshine dose at 475 m from a shielded, collimated, point, monoenergetic (E = 0.5 MeV) in shielded silo geometry as calculated by the discrete-ordinates LBRF hybrid method of Bassett [Ba89] (open symbols), by the MC-LBRF method developed in this study (solid lines), and by the exponential attenuation with buildup method (dashed lines).

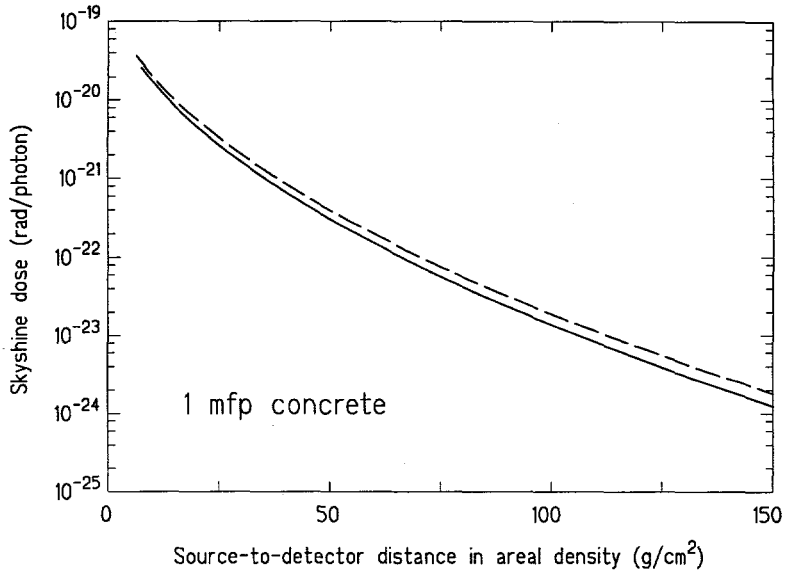

Figure 6.8. The skyshine dose from a point ^{16}N source ($E = 6.12$ MeV) in shielded silo geometry in which the source is collimated to a 80-deg. half angle and shielded by a concrete overhead slab one mean-free-path thick. Results by the MC-LBRF method of this study are shown as a solid line and results by Bassett's [Ba89] discrete-ordinates-LBRF hybrid method by a dashed line.

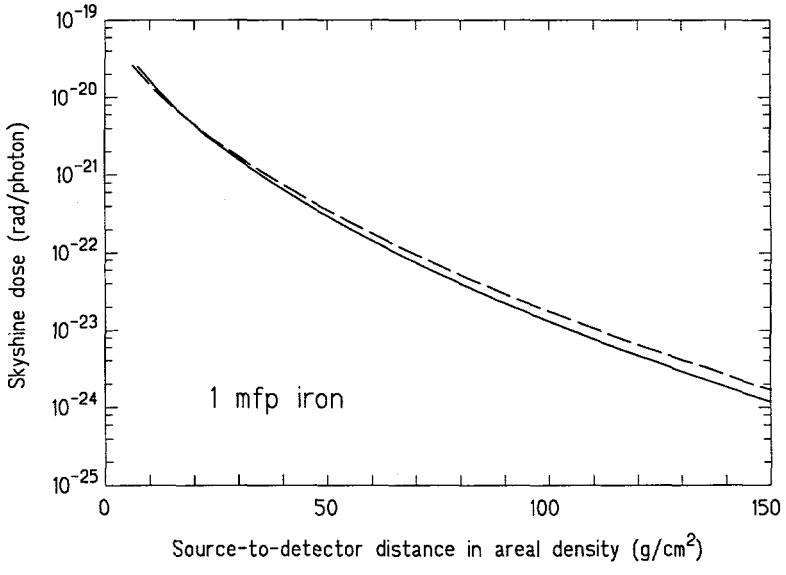

Figure 6.9. The skyshine dose from a point ^{16}N source ($E = 6.12$ MeV) in shielded silo geometry in which the source is collimated to a 80-deg. half angle and shielded by an iron overhead slab one mean-free-path thick. Results by the MC-LBRF method of this study are shown as a solid line and results by Bassett's [Ba89] discrete-ordinates-LBRF hybrid method by a dashed line.

identical for the two different shield materials. This result suggests that the mass thickness of the source shield is the important shield parameter and that skyshine doses are relatively insensitive to the particular material used for the shield. Further justification of this conjecture is presented later.

Comparison to the Exponential Attenuation with Buildup Method

The MC-LBRF may be used to test the range of applicability of the simpler but less accurate method of using exponential attenuation with shield buildup (see Section 6.1.1). In Fig. 6.10 results from the two methods are shown for a shielded silo problem with three different energy sources shielded by a 3 mean-free-path thick concrete shield. For the broad source collimation used in this problem, both methods give comparable results over a wide range of source-to-detector distances. Similarly, both methods are seen in Fig. 6.11 to give similar results for different concrete shield thicknesses, again for a broadly collimated source. However, as the collimation of the sources becomes smaller, i.e., more tightly collimated in the vertical direction, the exponential attenuation with buildup method can be expected to increasingly underpredict the skyshine dose because this method cannot properly account for those photons redirected by the shield into directions with polar angles greater than allowed by the collimation. This collimation angle effect is seen clearly in Fig. 6.12.

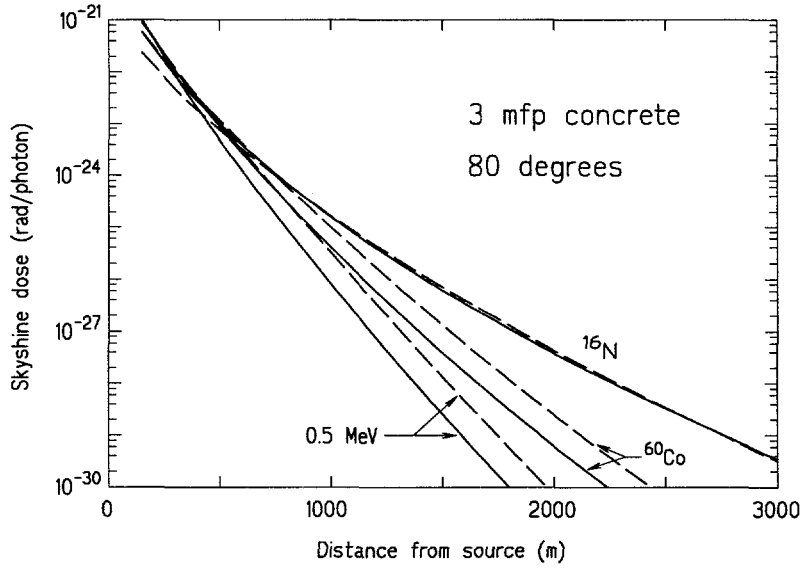

Figure 6.10. The skyshine dose resulting from a shielded source in silo geometry for three different source energies. The concrete shield is 3 mean-free-path lengths thick and the source is collimated into a vertical cone with an 80-degree half angle. Solid line are results from the MC-LBRF method and dashed lines are from the exponential attenuation with buildup method.

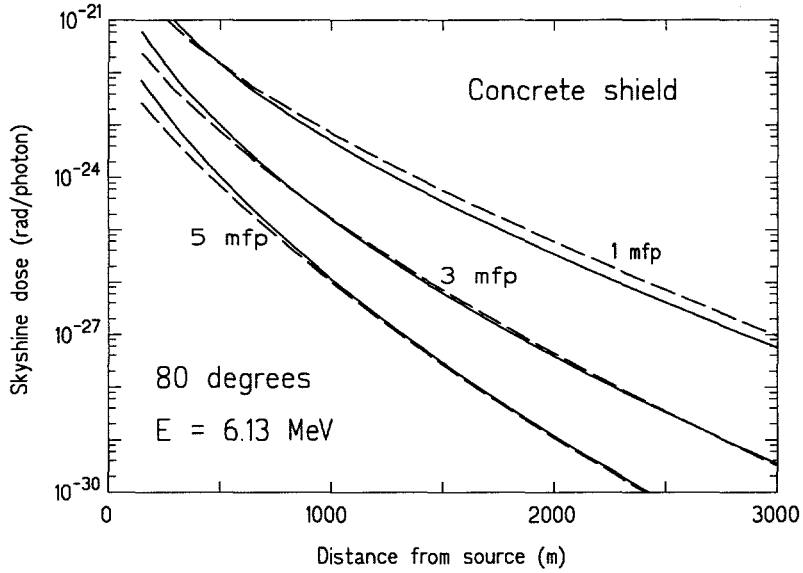

Figure 6.11. The skyshine dose resulting from a shielded source in silo geometry for three different shield thicknesses. The source emits 6.13-MeV photons which are collimated into a vertical cone with an 80-degree half angle. Solid lines are results obtained with the MC-LBRF method and dashed lines are for the exponential attenuation with buildup method.

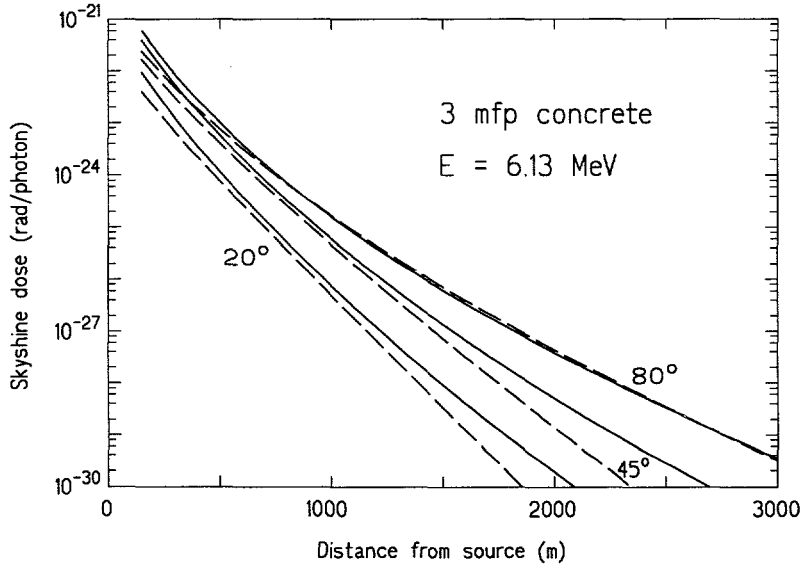

Figure 6.12. The skyshine dose resulting from a shielded source in silo geometry for three different source collimations (denoted by their conical half-angle). The source emits 6.13-MeV photons and has an overhead concrete shield 3 mean-free-path lengths thick. Solid lines are results obtained with the MC-LBRF method and dashed lines are for the exponential attenuation with buildup method.

6.4 Effect of Shield Material

The results for the iron and concrete shields, Figs. 6.8 and 6.9, are almost identical. Further calculations were made with the MC-LBRF method for shields of other material. Results for shields of different thicknesses and of various materials are shown in Fig. 6.13. The results, for a given shield mass thickness, are almost independent of the shield material for the specified source energy and collimation. In Fig. 6.14, it is also seen that the skyshine dose for different source collimation angles is also insensitive to the shield material.

Finally, in Fig. 6.15 which shows the effect of different source energies on the shielded skyshine dose, it is seen that at low source energies a lead shield begins to have a slightly different influence on the dose compared to the other shield materials. This is a result of the quite larger photo-electric absorption cross sections for lead compared to the other materials, which, for low source energies, causes lead to absorb more photons in a given mass thickness of a shield compared to the other materials.

From the results presented in this section, it is seen that for shielded skyshine calculations the composition of the overhead shield is unimportant, for all but the lowest source energies. Rather, the mass thickness of the shield alone determines the skyshine doses.

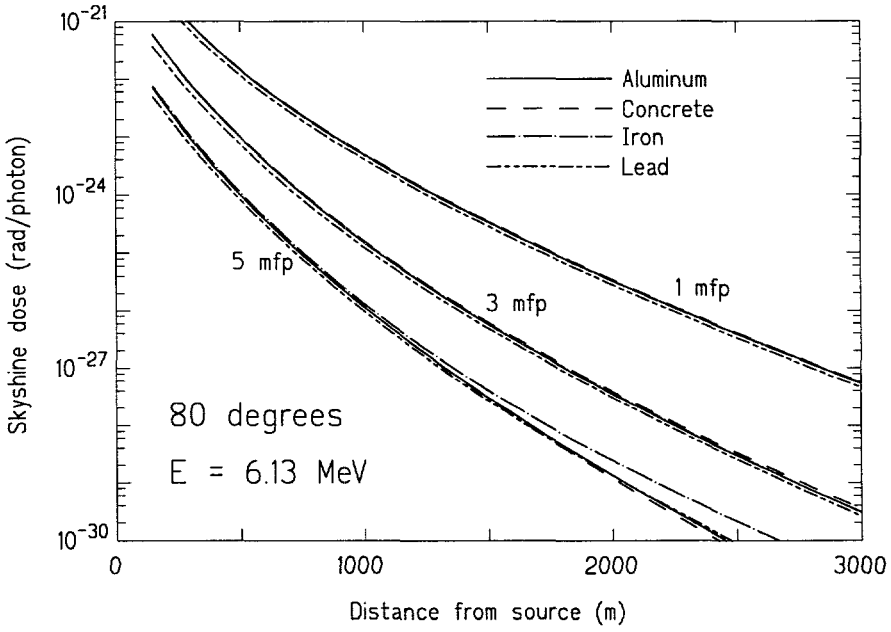

Figure 6.13. The skyshine dose from a collimated point ^{16}N source (E = 6.13 MeV) in shielded silo geometry in which the source is collimated to a 80-deg. half-angle and shielded by different materials of the same mass thickness.

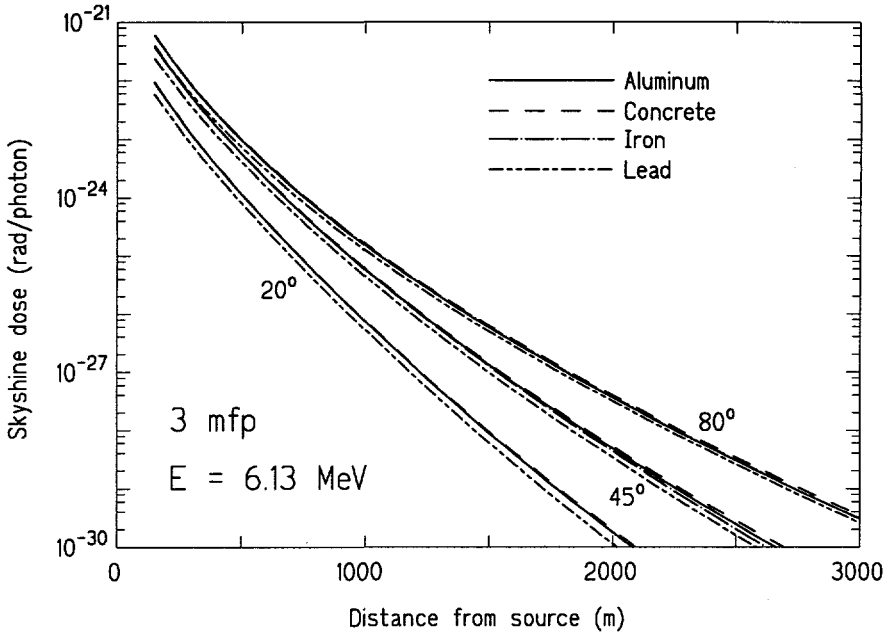

Figure 6.14. The skyshine dose from a collimated point ^{16}N source (E = 6.13 MeV) in shielded silo geometry in which the source has different half-angle collimations and is shielded by different materials each 3 mean-free-paths thick.

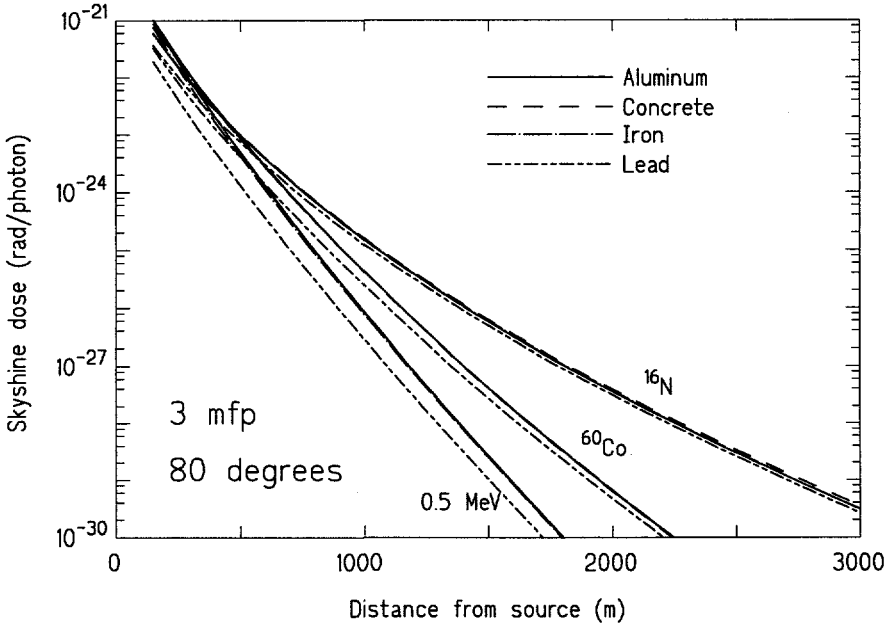

Figure 6.15. The skyshine dose from a collimated point source with three different energies in shielded silo geometry in which the source has an 80-degree half-angle collimations and is shielded by a concrete shield 3 mean-free-paths thick.

Chapter 7

Air-Ground Interface Effect

Conventional wisdom in skyshine analyses is that the air-ground interface is well modeled by using an infinite air medium. This premise is supported by the fact that most soils have an average atomic number close to that of air ($Z_{air} = 7.225$). However, the actual abrupt change in mass density experienced by radiation crossing the interface can be expected to alter the reflective properties at the interface as compared to that of a homogeneous infinite air medium.

At detector positions near the source, radiation scattered from the atmosphere into the ground, will more be more likely to scatter closer to the detector and hence reach the detector than if the ground were replaced by air with its much smaller density. Thus the ground will appear to act near the source as a reflector compared to an air medium below the interface.

By contrast, at distances far from the source, the soil will prevent photons that scatter first in the atmosphere and then in the ground from reaching the detector since these photons must travel through a much greater mass thickness to reach the detector than if the ground were replaced by an air medium. Thus for far detector distances, the ground will appear to act as an absorber compared to the case when air is placed beneath the interface.

However, despite these expectations of the difference between air and soil beneath the interface, the quantification of this difference has not previously been made for the skyshine problems considered in this report. Though the effect is conventionally thought to be small, how small has not been determined. As an ancillary investigation to this study, computations were made for the LBRF both in an infinite air medium and in a medium with soil beneath the air-ground interface. As discussed in this chapter this difference is not always negligible, and, consequently, empirical correction factors were derived to correct skyshine doses computer for infinite air medium to account for the air-ground interface. The results of this investigation are reported in this chapter.

7.1 LBRF Examples with a Ground Interface

To investigate the effect of the air-ground interface, the line-beam skyshine problem was modeled by the MCNP code to obtain the LBRF for both an infinite air medium and a medium with a ground interface. For the case with a ground interface, the soil was assumed to have a composition defined by [Ja86], the point source was placed 1 m above the interface, and the detectors were located 1 m above the air-ground interface[1]. Details of the MCNP models used are reported by Kahn [Ka95].

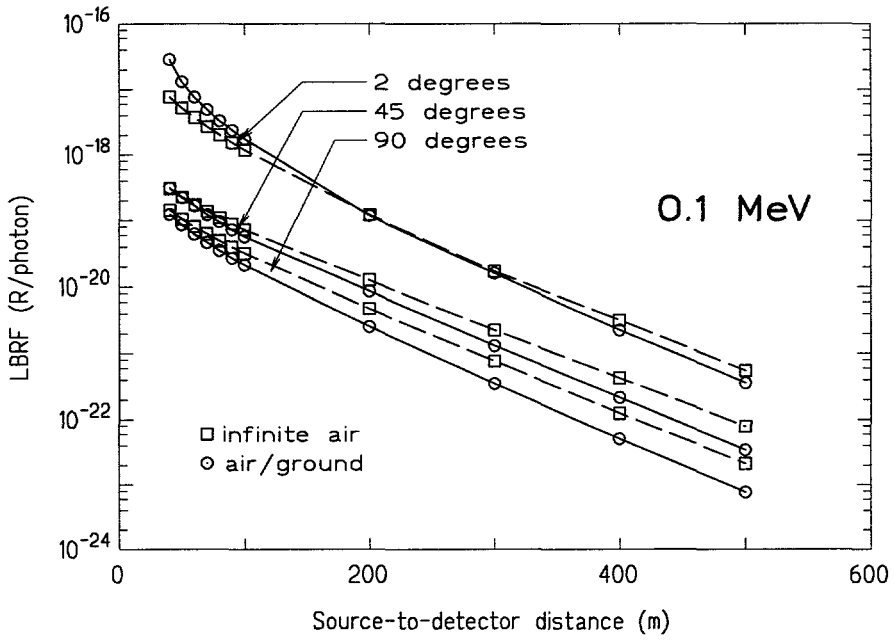

Figure 7.1. The LBRF in an infinite medium (dashed lines and squares) and in a medium with an air-ground interface (solid lines and circles) for a 0.1-MeV source emitting photons at three different angles to the source-detector axis.

The LBRF was calculated by the MCNP models, with and without the air-ground interface, for 15 source energies (0.1, 0.25, 0.5, 1, 1.5, 2, 2.5, 3, 4, 5, 6, 7, 8, 9, and 10 MeV) at 15 beam angles (2, 3.5, 5, 7.5, 10, 15, 20, 30, 45, 60, 80, 85, 90, 110, and 130 degrees) and 16 source-to-detector distances (40, 50, 60, 70, 80, 90, 100, 200, 300, 400, 500, 600, 700, 800, 900, and 1000 m).[2] In all, 3,465 values of the LBRF were computed with the ground interface and an equal number for an infinite air medium. Examples of these calculated LBRFs are shown in Figs. 7.1 to 7.3. From such results, the ground is indeed seen to act as a reflector near the source while far from the source the ground acts as an absorber.

[1]The "detector" was an air volume in which the average fluence, weighted with the air-kerma response function, was computed. These detector volumes were 2 m tall, 15 m wide, and 10 m thick for distances less than 100 m and 100 m thick for greater source-to-detector distances.

[2]For the lowest energies, the maximum distance for the LBRF was less than 1000 m. The maximum distance for energies of 0.1, 0.25, and 0.5 MeV were 500, 700, and 900 m, respectively.

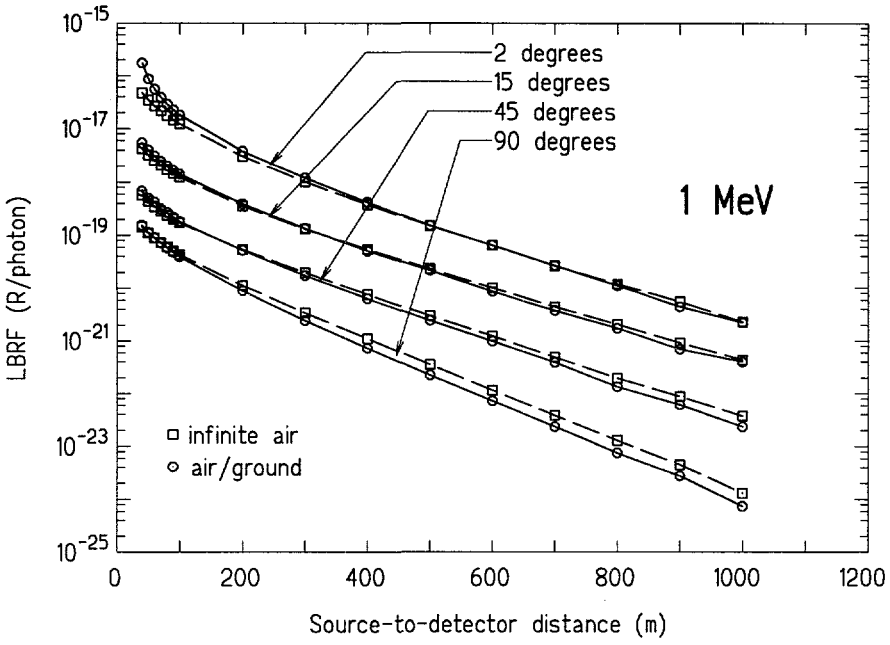

Figure 7.2. The LBRF in an infinite medium (dashed lines and squares) and in a medium with an air-ground interface (solid lines and circles) for a 1-MeV source emitting photons at three different angles to the source-detector axis.

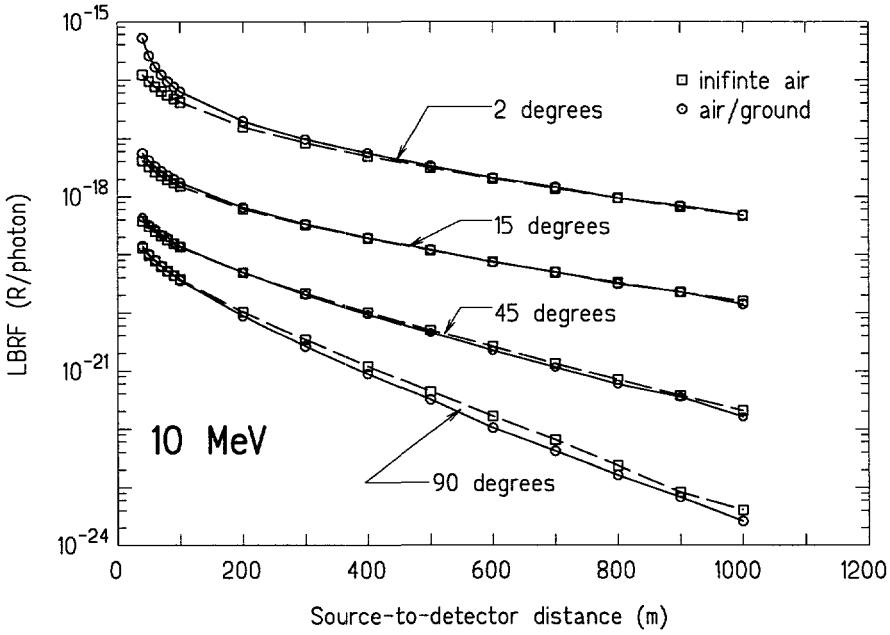

Figure 7.3. The LBRF in an infinite medium (dashed lines and squares) and in a medium with an air-ground interface (solid lines and circles) for a 10-MeV source emitting photons at three different angles to the source-detector axis.

7.2 Ground Correction Factors for LBRF

To avoid the necessity of deriving an approximate LBRF with a ground interface, the infinite medium LBRF was multiplied by a ground correction factor CF. This correction factor is defined as

$$CF(x, E, \phi) \equiv \frac{\Re_{gnd}(x, E, \phi)}{\Re_{\infty}(x, E, \phi)} \tag{7.1}$$

where $\Re_{gnd}$ and $\Re_{\infty}$ is the LBRF with and without the ground interface. The CF also depends on the relation of the source-detector axis to the ground interface. In this study the source-detector axis is positioned 1 m above the ground.

The CF can be evaluated from the MCNP calculations described in the previous section by taking the ratio of the LBRF with the ground interface to that of the infinite air medium at the same values of x, E, and ϕ. The complete set of CF values so calculated are reported by Kahn [Ka95]. Some of these values of CF are shown in Figs. 7.4 through 7.9. In each plot the CF values for a given beam angle are plotted for all energy and source-detector distances used in the MCNP calculations. Only for the smallest angle (2 degrees) is a discernible pattern apparent. For the smallest distance (40 m) the CF is seen to be very large, about 4, for all energies between 0.1 and 10 MeV. As the beam angle or distance increases, the CFs for a given distance, while still displaying a pattern as a function of the mean-free-path distance, the patterns for each distance overlap. Surprisingly, the general trend of these scatter diagrams shows a similar behavior — a monotonic decreasing value of CF with increasing source-to-detector distance expressed in terms of mean-free-path lengths, μx.

7.3 Empirical Formulas

The CF values calculated from the MCNP calculations were used as the basis for deriving an approximate formula for the ground correction factors. To find a function that can accurately represent these data, the program TABLECURVE-3D [Ja93] was used. This program fits many thousands of different two-dimensional (i.e., two independent variables) to any set of data. From such analyses, the two approximating formulas discussed below were developed.

7.3.1 An Energy-Distance Formula

The CF values calculated for each beam angle (such as those shown in each one of Figs. 7.4 to 7.9) were fit by TABLECURVE-3D. For the 15 different beam angles considered, the following formula was found to give the best fit to the data.

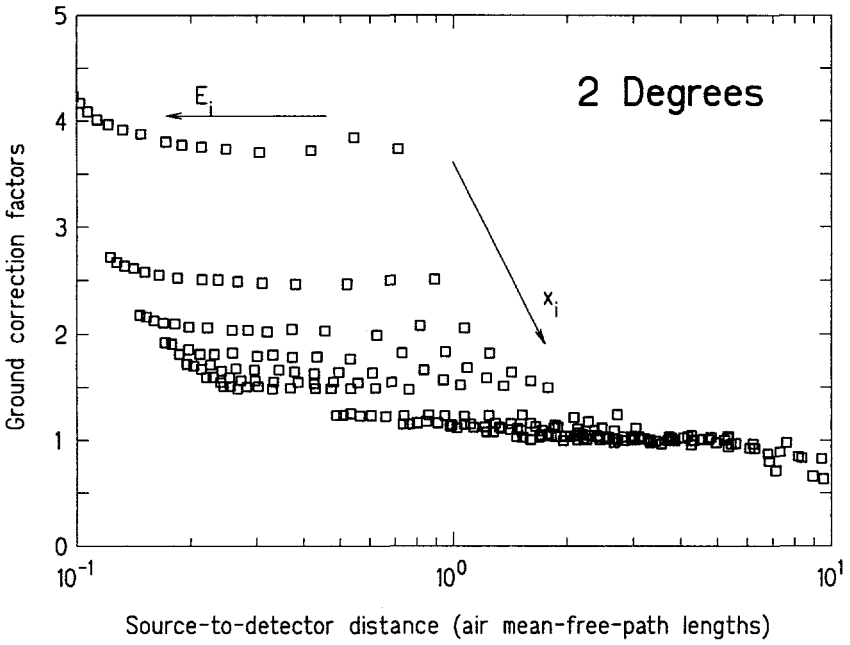

Figure 7.4. Calculated ground correction factors *CF* for a beam angle of 2 degrees. Each circle represents a value of *CF* for a particular energy and source-detector distance in mean-free-path lengths.

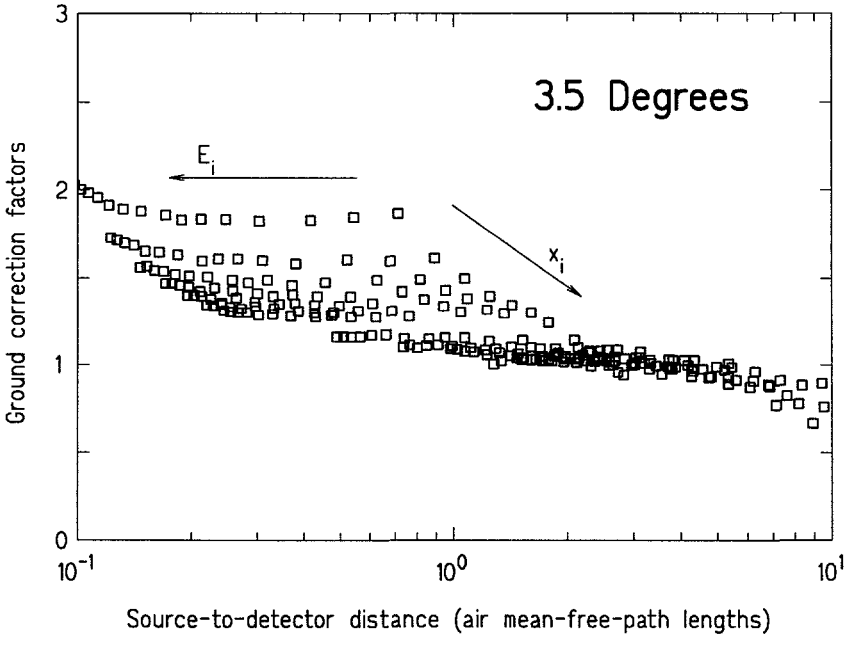

Figure 7.5. Calculated ground correction factors *CF* for a beam angle of 3.5 degrees. Each circle represents a value of *CF* for a particular energy and source-detector distance in mean-free-path lengths.

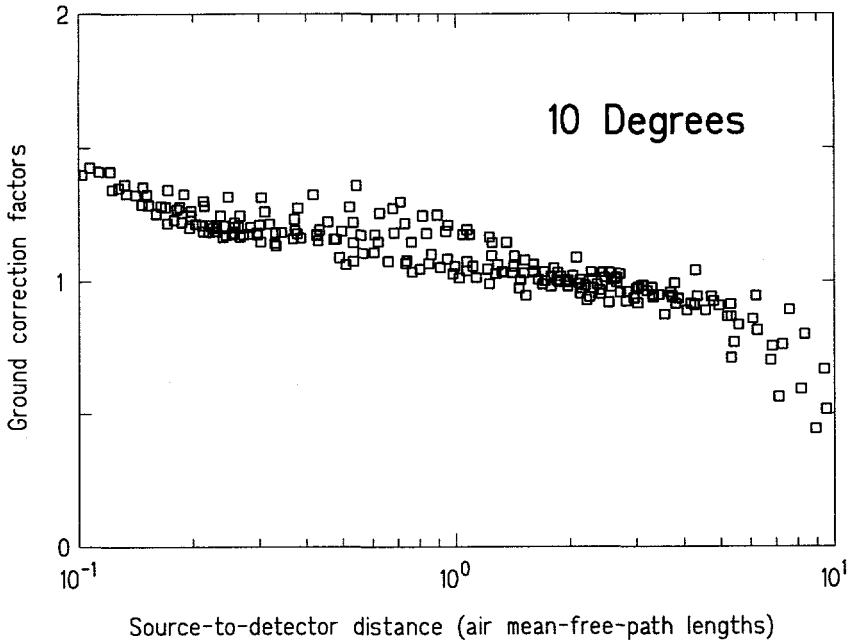

Figure 7.6. Calculated ground correction factors *CF* for a beam angle of 10 degrees. Each circle represents a value of *CF* for a particular energy and source-detector distance in mean-free-path lengths.

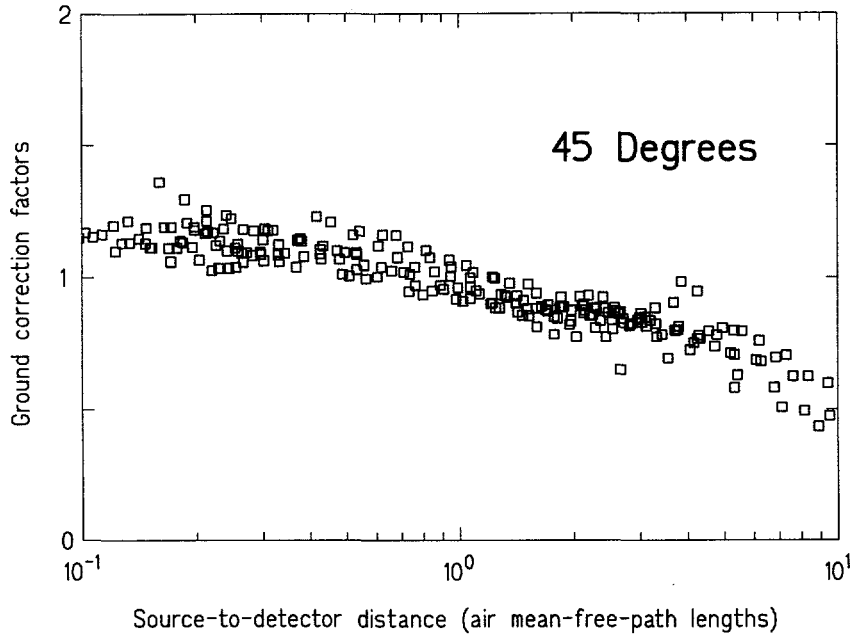

Figure 7.7. Calculated ground correction factors *CF* for a beam angle of 45 degrees. Each circle represents a value of *CF* for a particular energy and source-detector distance in mean-free-path lengths.

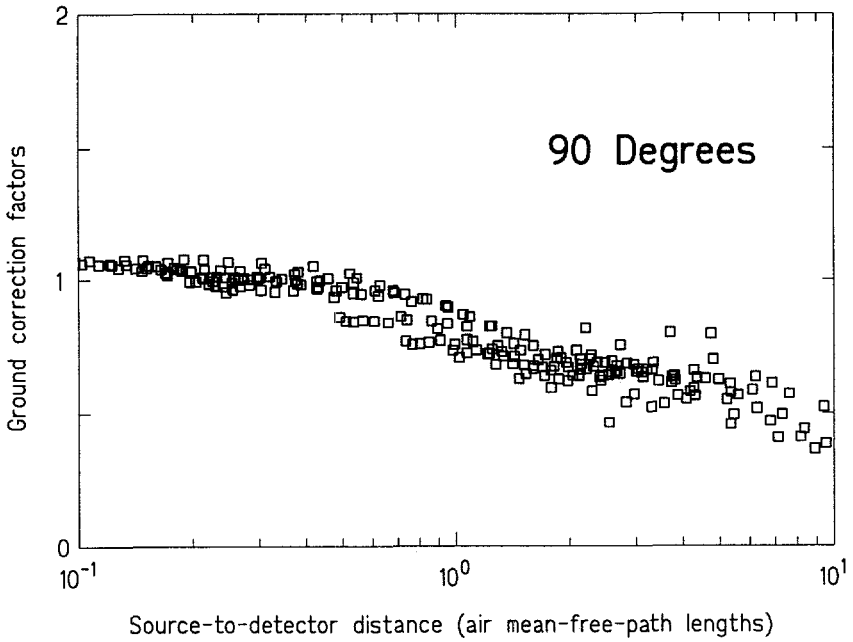

Figure 7.8. Calculated ground correction factors *CF* for a beam angle of 90 degrees. Each circle represents a value of *CF* for a particular energy and source-detector distance in mean-free-path lengths.

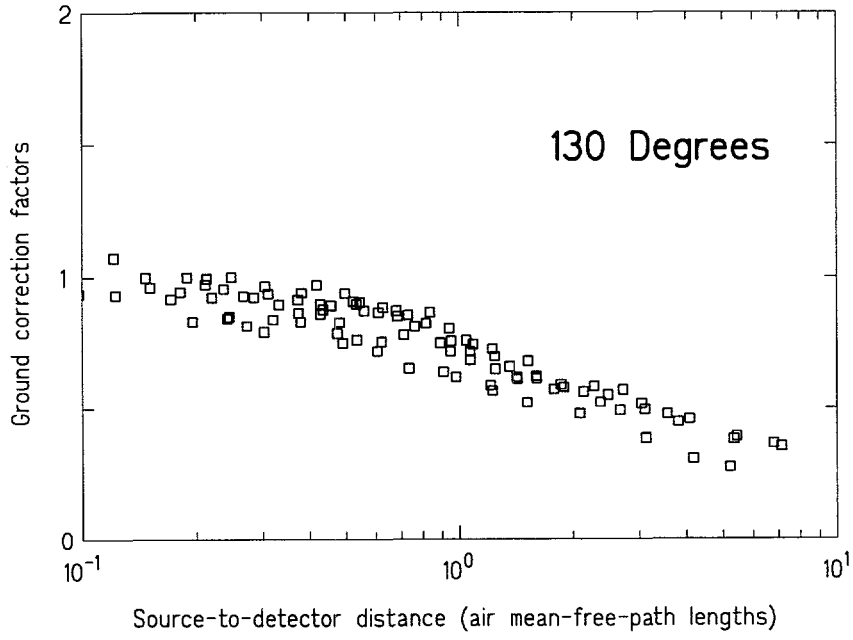

Figure 7.9. Calculated ground correction factors *CF* for a beam angle of 130 degrees. Each circle represents a value of *CF* for a particular energy and source-detector distance in mean-free-path lengths.

$$
\begin{aligned}
CF &= \mu x E \exp[a + b \ln E + c \ln(\mu x) + d(\ln \mu x)^2] \\
&= e^a E^{b+1} (\mu x)^{c + d \ln \mu x + 1} \qquad (7.2)
\end{aligned}
$$

The approximation parameters a, b, c, and d depend only on the beam angle ϕ. The values of these parameters for the different beam angles used are presented in Table 7.1. The formula was obtained for each angle from MCNP CF values for energies $0.1 < E < 10$ MeV, and distances $40 < x < 1000$ m.

The average absolute difference between this fit and the MCNP data is almost always less than 5% and the maximum absolute difference is less than 12% for all but the lowest energies (0.1 and 0.25 MeV) or the smallest beam angle (2 degrees). For a beam angle of 2 degrees, the approximation underpredicts CF by as much as 45% at the nearest distance to the source (40 m). Similarly, at energies below about 0.4 MeV the approximation can produce maximum errors of over 40%. Thus Eq. (7.2) should be use for source energies in the range $0.5 \leq E < 10$ MeV. Similarly, for a beam angle of 2 degrees or less, the approximation is useful only for source-to-detector distances greater than 100 m.

Table 7.1. Parameters for the approximate ground correction factor of Eq. (7.2). Approximation is valid for $0.1 \leq E \leq 10$ MeV and for source-to-detector distances between 0.1 and 10 mean-free-path lengths in air.

Angle ϕ (degrees)	Parameters for Approximate Correction Factor			
	a	b	c	d
2.0	0.36926681	−1.09056278	−1.27822860	0.00664603
3.5	0.21009622	−1.06774858	−1.20246703	0.01527704
5.0	0.16831381	−1.04249133	−1.14460081	0.00017244
7.5	0.12535491	−1.01321668	−1.13753496	−0.02508111
10.0	0.11241432	−1.00809364	−1.13092737	−0.03043949
15.0	0.09071555	−1.00166524	−1.12317594	−0.03227529
20.0	0.07367380	−0.99877595	−1.12284850	−0.03523390
30.0	0.03669662	−1.00143750	−1.12830365	−0.03344318
45.0	−0.00630292	−1.00196498	−1.14871980	−0.03693434
60.0	−0.04900306	−1.00563896	−1.16935065	−0.04659270
80.0	−0.11426299	−1.00959999	−1.22568433	−0.05361156
90.0	−0.19684753	−1.01725920	−1.20003669	−0.02561614
110.0	−0.26018469	−1.02106343	−1.26545276	−0.04098882
130.0	−0.34254488	−1.04104105	−1.31574368	−0.06258089

7.3.2 An Energy-Distance-Angle Formula

A approximation formula depending on all three beam parameters was also sought. The best formula found was

$$\begin{aligned} CF &= (\mu x E/\phi)\exp[a + b\ln(\phi/E) + c\ln(\mu x) \\ &= e^a(\mu x)^{c+1}\left(\frac{\phi}{E}\right)^{b-1}. \end{aligned} \tag{7.3}$$

By a least squares fit of this formula to the CF calculated by MCNP , the approximation parameters were found to be $a = 0.134307854$, $b = 0.936284462$, and $c = -1.13375177$. The range of applicability of this approximate formula is as follows: $0.1 < E < 10$ MeV, $2 < \phi < 150$ degrees, and $50 < x < 1000$ m. While this global formula is considerably simpler than that of Eq. (7.2), it is not as accurate, especially for energies below .5 MeV and beam angles less than 5 degrees, and should be used only if very approximate results are appropriate.

7.4 Comparison of Calculated and Approximate Ground Correction Factors

To assess the accuracy of the approximate CF formula of Eq. (7.2) the ratio of the CF values calculated from the approximation to that determines from the MCNP data were calculated for each energy, distance, and angle used in the MCNP calculations. The better the fit approximation, the closer these ratios will be to unity. Typical results, corresponding to the CF values of Figs. 4.4 to 4.11, are shown in Figs. 4.12 to 4.17.

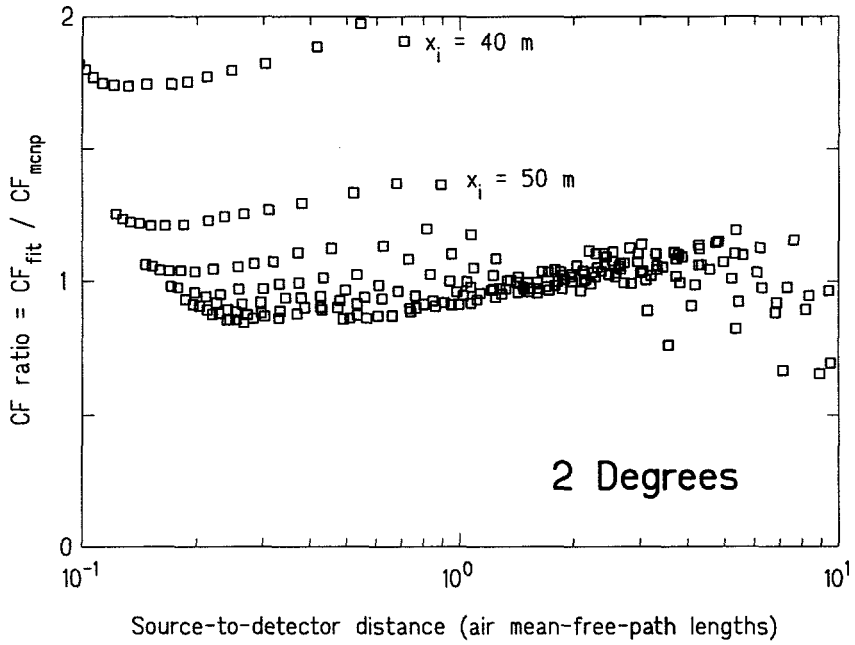

Figure 7.10. Ratio of the approximate *CF* calculated from Eq. (7.3) to that obtained from MCNP calculations for a beam angle of 2 degrees.

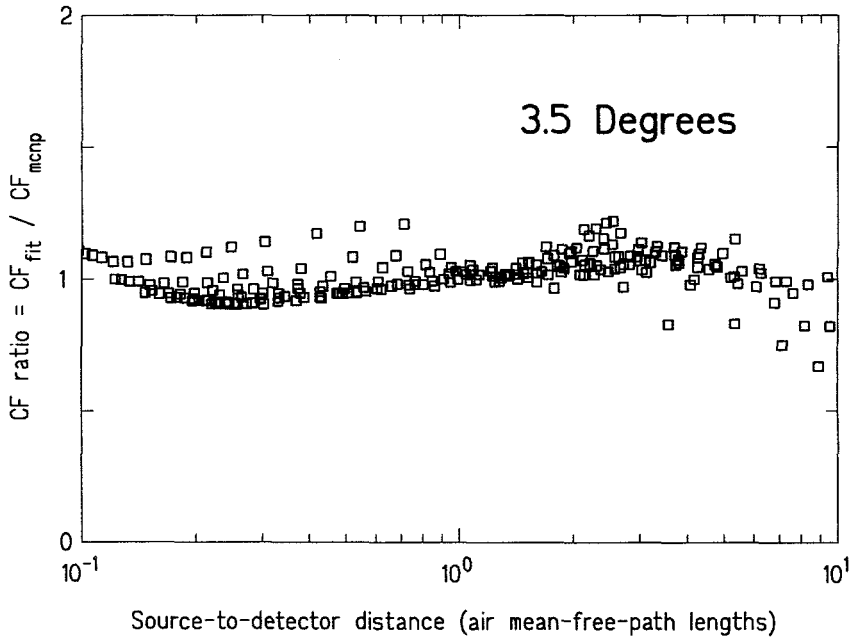

Figure 7.11. Ratio of the approximate *CF* calculated from Eq. (7.3) to that obtained from MCNP calculations for a beam angle of 3.5 degrees.

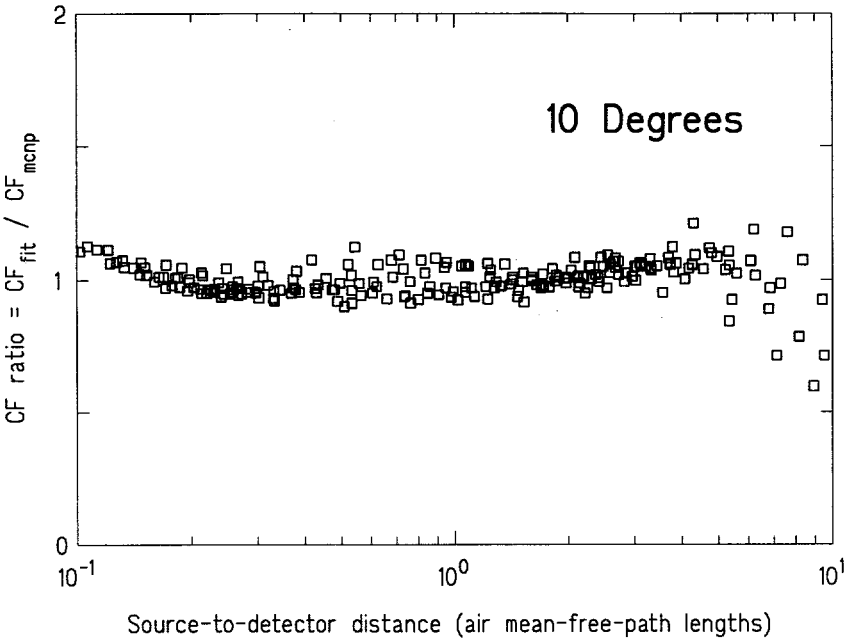

Figure 7.12. Ratio of the approximate *CF* calculated from Eq. (7.3) to that obtained from MCNP calculations for a beam angle of 10 degrees.

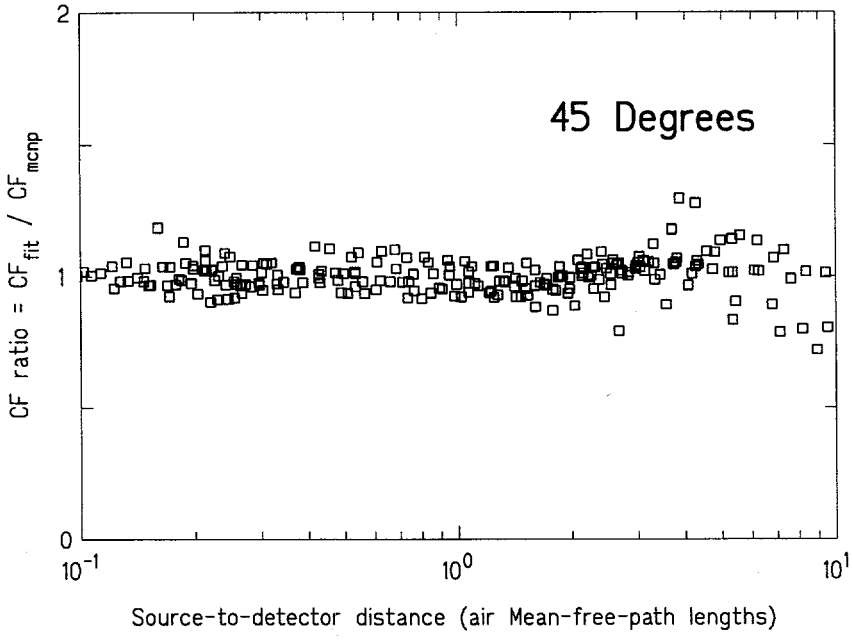

Figure 7.13. Ratio of the approximate *CF* calculated from Eq. (7.3) to that obtained from MCNP calculations for a beam angle of 45 degrees.

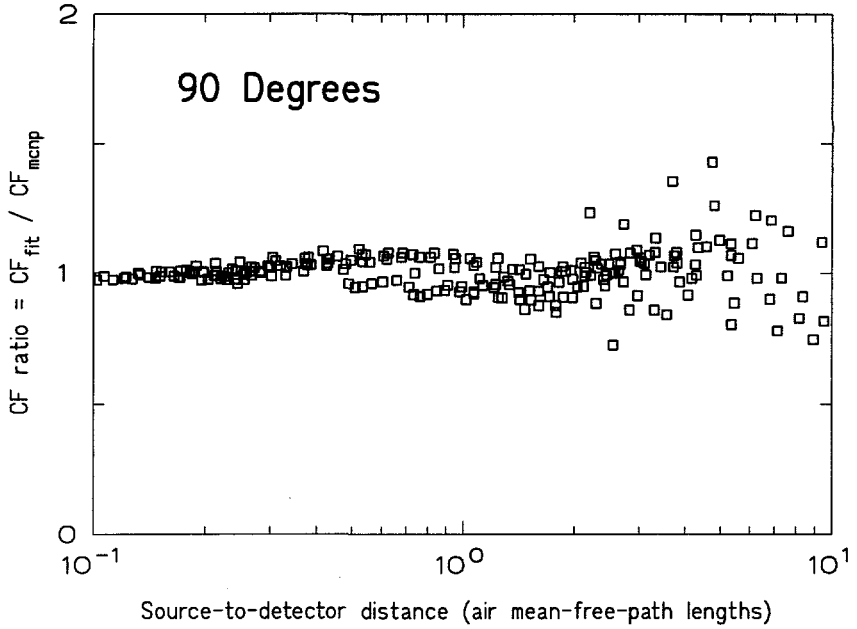

Figure 7.14. Ratio of the approximate *CF* calculated from Eq. (7.3) to that obtained from MCNP calculations for a beam angle of 90 degrees.

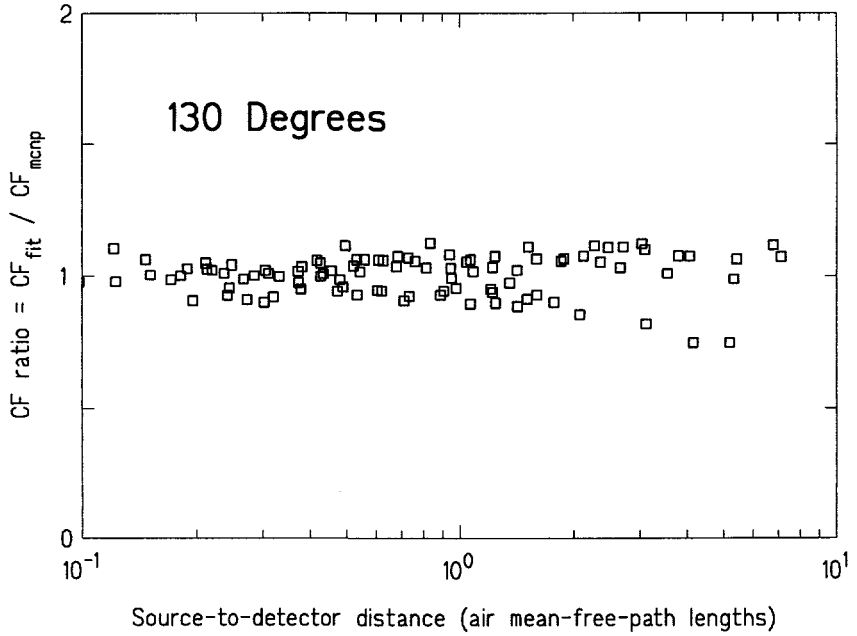

Figure 7.15. Ratio of the approximate *CF* calculated from Eq. (7.3) to that obtained from MCNP calculations for a beam angle of 130 degrees.

Chapter 8

Conclusions

A refined point-kernel model for the gamma-ray LBRF in an infinite air medium has been developed. This model, which extends an earlier model by including secondary bremsstrahlung and the transport of positrons and electrons, was found from comparison to MCNP calculations to give accurate values of the LBRF for energies below 15 MeV. Moreover, unlike MCNP which was able to calculate the LBRF only for source-to-detector distances less than 1000 m, the point kernel model was able to predict the LBRF at distances up to 3000 m from the source.

Values of the LBRF obtained from the point kernel model were then used to obtain two approximations for the LBRF, one based on the same three-parameter formula used in earlier studies, and another on a new four-parameter formula that was found to give a more accurate representation of the point kernel data with little increase in computational effort. Several different fitting criteria were investigated, and the method adopted in this study for generating the coefficients for the approximate LBRFs was based on minimizing the maximum absolute fractional deviation between the LBRF values and the approximation.

For gamma-ray energies above about 20 MeV, the "straight-ahead" approximation used by the point kernel model to describe the angular distribution of bremsstrahlung approximation was found to be too crude to yield accurate values of the LBRF at small beam angles. Thus, to develop an approximate LBRF for gamma-ray energies between 15 and 100 MeV, extensive MCNP calculations were performed. From the results of these calculations, coefficients for a three-parameter LBRF approximation were determined for source-to-detector distances up to 1000 m.

With the new approximations for the LBRF developed in this study, the integral line-beam method was used to analyze several benchmark skyshine problems. From comparison of these results to both experimental measurements and to results obtained by other computational methods, the integral line-beam method was found to give excellent agreement for unshielded skyshine sources.

For shielded skyshine sources, the use of exponential attenuation with buildup to account for photon interactions in the source shield is often an effective and simple way to account for the effect of the shield. This simple approximation has been found to be give results within a factor of two compared to a more accurate skyshine methods for broadly collimated sources [Sh91]. For tightly collimated sources and thick source shields in which significant photon redirection can occur, the exponential attenuation with buildup method, however, is underpredictive sometimes by a factor of four. Nevertheless, for many skyshine analyses, particularly those involving broadly collimated sources with modest overhead shielding, this simple method provides acceptable accuracy.

For thick shields over a tightly collimated source, a more accurate method is needed if highly accurate skyshine results are desired. In this study a hybrid method was developed that used a Monte Carlo simulation to accurately calculate the energy and direction of photons transmitted through the source shield and then used the integral line-beam method to transport these transmitted photons through the atmosphere. The new hybrid method also allows the source to be collimated in almost any manner beneath the shield. While computationally more expensive than the exponential attenuation with buildup method, the hybrid MC-LBRF method gives excellent agreement with benchmark experimental data and with other hybrid calculations.

Finally, the effect of the air-ground interface on the skyshine dose at positions near the interface was investigated. The ground was found to increase the skyshine dose at locations near the source (60 m) by up to a factor of four for small beam angles (2 degrees). By contrast, at large source-to-detector distances (1000 m) the ground interface can depress the skyshine dose by up to a factor of two. An empirical formula was developed for a ground correction factor for all beam angles and for photon energies between 0.02 and 10 MeV.

Future work still is needed to improve the LBRF approximation above 15 MeV. To extend the approximation beyond 1000 m, methods other than MCNP or discrete ordinates must be used. The refined point kernel method described in this report has the capability of predicting the LBRF at large source-to-detector distances, and, with a more rigorous treatment of the directional dependence of bremsstrahlung, this model should be capable of generating values of the LBRF upon which to base a better approximation of the LBRF for high-energy photons.

With the results obtained in the study, the integral line-beam method may be used with confidence for a wide range of source energies at a small fraction of the computational effort required by other skyshine methods.

Bibliography

[Am65] Abramowitz M. and I.A. Stegun (eds.), *Handbook of Mathematical Functions*, Appl. Math. Series 55, U.S. Government Printing Office, Washington, DC, 1965.

[An87] *American National Standard for Calculation and Measurement of Direct and Scattered Gamma Radiation from LWR Nuclear Power Plants*, ANSI/ANS-6.6.1-1987, American Nuclear Society, LaGrange Park, Illinois, 1987.

[An91] *American National Standard for Gamma-Ray Attenuation Coefficients and Buildup Factors for Engineering Materials*, ANSI/ANS-6.4.3, American Nuclear Society, LaGrange Park, Illinois, 1991.

[Ba89] Bassett, M.S., *Gamma Skyshine Calculations for Shielded Source*, M.S. Thesis, Department of Nuclear Engineering, Kansas State University, Manhattan, KS, 1989.

[Bi72] Biggs, F., R. Lighthill, *Analytical Approximations for Photon-Atom Differential Scattering Cross-Sections Including Electron Binding Effects*, SC-RR-72-659, Sandia Laboratories, Albuquerque, NM, 1972.

[Bi86] Bielajew, A.F. and D.W.O. Rogers, "PRESTA: The Parameter Reduced Electron-Step Transport Algorithm for Electron Monte Carlo Transport," Report PIRS-042, National Research Council of Canada, Ottawa (1986).

[Br93] Briesmeister, J.F. (ed.), *MCNP — A General Monte Carlo N-Particle Transport Code*, Version 4A, Los Alamos Laboratory Report LA-12625, Los Alamos, NM, 1993.

[Br94] Brockhoff, R.C, *Calculation of the LBRF for High Energy Gamma Rays*, M.S. Thesis, Kansas State University, Manhattan, KS, 1994.

[Ch79] Chilton, A.B., "Tschebycheff-fitted Berger Coefficients for Eisenhauer-Simmons Gamma-Ray Buildup Factor in Ordinary Concrete," *Nucl. Sci. & Engg.*, **69**, 436-438 (1979).

[Ch80] Chilton, A.B., C.M. Eisenhauer, and G.L. Simmons, "Photon Point Source Buildup Factors for Air, Water, and Iron," *Nucl. Sci. Engg.* **73**, 97-107 (1980).

[Ch83] Chou, Dong-Pao, T.-P. Hsaio, and G.-H. Lai, it SKYSHINE-P, A Point Kernel Computer Program for Calculating Skyshine Exposure Rates, Report INER-0498, Institute for Nuclear Energy Research, Taiwan, Republic of China, 1983.

[Ch84] Chilton, A.B., J.K. Shultis, and R.E. Faw, *Principles of Radiation Shielding*, Prentice-Hall, Englewood Cliffs, NJ, 1984.

[Cu80] J.R. Cunningham and H.E. Johns, "Calculation of the Average Energy Absorbed in Photon Interactions," Med. Phys. 7(1), 51-54, 1980; actual numerical data were obtained from the DLC-139/SIGMA-A Data Library available from RSIC, Oak Ridge National Laboratory, Oak Ridge, TN.

[De91] Deng, X., *Improved Response Functions for Gamma-Ray Skyshine Analyses*, M.S. Thesis, Kansas State Univ., Manhattan, KS, 1991.

[Dl88] *DLC-139/ SIGMA-A Extensive Library of Photon Interaction Coefficients*, Ontario Cancer Institute, Toronto, Canada, 1988.

[Em75] Emmett, M.B., *The MORSE Monte Carlo Radiation Transport System*, ORNL-4972, Oak Ridge National Laboratory, TN (1975).

[En67] Engle, W.W., Jr., *A User's Manual for the ANISN Code*, USAEC K-1963, U.S. Atomic Energy Commission, Washington, DC, 1967.

[Fa87] Faw, R.E. and J.K. Shultis, *The MicroSkyshine Method for Gamma-Ray Skyshine Analysis*, Report 188, Engineering Experiment Station, Kansas State University Manhattan, KS, 1987.

[Fa93] Faw, R.E. and J.K. Shultis, "Absorbed-Dose Buildup Factors in Air for 10- to 100-MeV Photons," *Nucl. Sci. & Engg.*, **114**, 76-80 (1993).

[Ge88] George, D.L., *Computational Techniques in Gamma-Ray Skyshine Analysis*, Report 204, Engineering Experiment Station, Kansas State University, Manhattan, KS, (1988).

[Gi89] Gianakon, T., *Calculation of Neutron Line-Beam Response Function with TWODANT*, M.S. Thesis, Department of Nuclear Engineering, Kansas State University, Manhattan, KS, 1989.

[Gr87] *MicroSkyshine User's Manual*, Grove Engineering, Inc., Rockville, MD, 1987.

[Ha78] Haskell, K.H. and E.J. Rondall, "Brief Instructions for Using the Sandia Mathematical Subroutine Library," (Version 7.3), Sandia Laboratories, Albuquerque, NM, 1978.

[Ha86] Harima, Y., Y. Sakamoto, S. Tanaka, and M. Kawai, "Validity of the Geometric-Progression Formula in Approximating Gamma-Ray Buildup Factors," *Nucl. Sci. Engg.*, **94**, 24-35 (1986).

[Ha78] Haskell, K.H. and E.J. Rondall, "Brief Instructions for Using the Sandia Mathematical Subroutine Library," (Version 7.3), Sandia Laboratories, Albuquerque, NM, 1978.

[Ha86] Harima, Y.Y. Sakamoto, S. Tanaka, and M. Kawai, "Validity of the Geometric-Progression Formula in Approximating Gamma-Ray Buildup Factors," *Nucl. Sci. & Engg.*, **94**, 24-35 (1986).

[Ha94] Harima, Y., H. Hirayama, Y. Sakamoto, and A. Shimazu, "A Simplified Method of Gamma-Ray Skyshine Calculations" Proc. 8th International Conference on Radiation Shielding, Arlington Texas, April 1994, pp. 939-945.

[Ic87] ICRP Publication 51, Annals of the ICRP 17 No. 2/3, *Data for use in protection against external radiation*, 1987.

[IC82] International Commission on Radiological Units, *Stopping Powers for Electrons and Positrons*, ICRU-37, 1982.

[Ja86] "Effective Dose Equivalents for Photon Exposures from Plane Sources on the Ground," *Radiation Protection Dosimetry*, **14**, 299-310, (1986).

[Ja90] *TABLECURVE*, Jandel Scientific, San Rafael, CA, 1990.

[Ja93] *TABLECURVE-3D*, Jandel Scientific, San Rafel, CA, 1993.

[Jo80] Johns, H.E., and J.R. Cunningham, "Calculation of the Average Energy Absorbed in Photon Interactions," *Med. Phys.* **7(1)**, 51-54 (1980).

[Ka62] Kaplan,I., *Nuclear Physics*, Addison-Wesley, New York, NY, 1962.

[Ka95] Kahn, F., *Gamma-Ray Skyshine LBRF Near an Air-Ground Interface*, M.S. Thesis, Kansas State University, Manhattan, KS, 1995.

[Ke82] Keck, B. and P. Herchenroder, "Nachrechneneines Gamma-Skyshine-Benchmark Experiments," *Atomwirtschaft* (1982).

[Ki68] Kitazume, C.M., "A Simple Calculation for Air-Scattered Gamma-Rays," *J. Nucl. Sci. & Tech.*, **5**, 464-471, (1968).

[Kn89] Knoll, G.F. *Radiation Detection and Measurement*, John Wiley & Sons, New York, NY, 1989.

[Kr23] Kramers, H.A., "On the Theory of X-Ray Absorption and of the Continuous X-Ray Spectrum," *Phil. Mag.*, **46**, 836 (1923).

[La79] Lampley, C.M., *The SKYSHINE-II Procedure: Calculation of the Effects of Structure Design on Neutron, Primary Gamma-Ray, and Secondary Gamma-ray Dose Rates in Air*, Report RRA-T7901 (NUREG/CR-0791), Radiation Research Associates, Fort Worth, Texas, 1979.

[La88] Lampley, C.M., M.C. Andrews, and M.B. Wells, *The SKYSHINE-III Procedure: Calculation of the Effects of Structure Design on Neutron, Primary Gamma-Ray and Secondary Gamma-Ray Dose Rates in Air*, RRA T8209A, (RSIC Code Collection CCC-289), Radiation Research Associates, Fort Worth, Texas, 1988.

[Ly58] Lynch, R.E., J.W. Benoit, W.P. Johnson, and C.D. Derby, *A Monte Carlo Calculation of Air-Scattered Gamma-Rays*, Report ORNL 2292, Oak Ridge National Laboratory, Oak Ridge, TN, 1958.

[Ma73] Malefant, R.E., *G3: A General Purpose Gamma-Ray Scattering Program*, Report LA-5176, Los Alamos Scientific Laboratory, Los Alamos, New Mexico, 1973.

[Mi77] Mikols, W.J. and J.K. Shultis, "Selection of Angular Quadrature for Anisotropic Transport Calculations," *Nucl. Sci. Engg.*, **63**, 91-95 (1977).

[My73] Mynatt, F.R. et al., *The DOT II Two-Dimensional Discrete-Ordinates Transport Code*, Report ORNL-TM-4280, Oak Ridge National Laboratory, Oak Ridge, TN, 1973.

[Na81] Nason, R.R., J.K. Shultis, R.E. Faw, and C.E. Clifford, "A Benchmark Skyshine Experiment," *Nucl. Sci. & Engg.*, **79**, 404 (1981).

[Ne85] Nelson, W.R., H. Hirayama, and D.W.O. Rogers, *The EGS4 Code System*, SLAC-265, Stanford Linear Accelerator Center, Stanford, California (1985).

[Ol93] Olsher, R.H., H. Hsu, and W.F. Harvey, "Benchmarking the MCNP Monte Carlo Code with a Photon Skyshine Experiment,", *Nucl. Sci. Engg.*, **114**, 219-227 (1993).

[Pe84] Peng, Wu-Heng, "Skyshine Radiation from a PWR Containment Dome," *Trans. Am. Nucl. Soc.*, **47**, 373-375 (1984).

[Pe65] Penny, S.K., D.K. Trubey, and M.B. Emmett, *OGRE, A Monte Carlo System for Gamma-ray Transport Studies, Including an Example (OGRE-P1) for Transmission Through Laminated Slabs*, Report ORNL-3905, Oak Ridge National Lab., Oak Ridge, TN, 1965.

[Pl75] Plechaty, E.F., D.E. Cullen, and R.J. Howerton, Report UCRL-50400, Vol. 6, Rev. 1, National Technical Information Service, 1975.

[Pr74] Price, J.H., *Utilization Instructions for QAD-MOD*, ORNL-4972, Oak Ridge National Lab., Oak Ridge, TN, 1974.

[Pr76] Price, J.H., D.G. Collins, and M.B. Walls, "Utilization Instructions for SKYSHINE," Research Note RRA-N7608, Radiation Research Associates, Fort Worth, TX (1976).

[Pr92] Press, W.H., S.A. Teukolsky, W.T. Vetterling, and B.P. Flannery, *Numerical Recipes*, Cambridge University Press, Cambridge, 1992.

[Ro80] Roseberry, M.L., *Benchmark Skyshine Exposure Rates*, M.S. Thesis, Dept. of Nuclear Engineering, Kansas State University, Manhattan, KS, 1980.

[Ro82] Roseberry, M.L. and J.K. Shultis, "Point-Kernel Calculations of Skyshine Exposure Rates," *Nucl. Sci. & Engg.*, **80**, 334-338, 1982.

[Rs86] *Documentation for CCC-483B/QAD-CGCP Code Package*, Report CCC-493, Radiation Shielding Information Center, Oak Ridge National Laboratory, Oak Ridge, TN, 1986.

[Rs87] *Geometric Progression Buildup Factors and Attenuation Coefficients*, Code Library Package DLC-129/ANS643, Radiation Shielding Information Center, Oak Ridge National Laboratory, Oak Ridge, Tennessee.

[Rs88] *SIGMA-A: Photon Interaction and Absorption Cross Sections*, RSIC Data Library DLC-139, Radiation Shielding Information Center, Oak Ridge National Laboratory, Oak Ridge, Tennessee (1988).

[Ry79] Ryman, J.C., *On the Application of Discrete Ordinates Methods in Gamma Photon Transport*," Ph.D. Dissertation, Kansas State University, Manhattan, KS, 1979.

[Sa90] Sakamoto, Y. and S. Tanaka, *QAD-CGGP2 and G33-GP2: Revised Versions of QAD-CGGP and G33-GP Codes with Conversion Factors from Exposure to Ambient and Maximum Dose Equivalents,* JAERI-M-110, Japan Atomic Energy Research Institute, 1990.

[Sa94] Sato, O., et al., "Evaluation of Fluence to Dose Equivalent Conversion Factors for High Energy Photons," *Proceedings of the 8th International Conference on Radiation Shielding*, April 1994, Arlington, Texas; published by American Nuclear Society, LaGrange Park, Illinois, 1984.

[Sh87] Shultis, J.K., and R.E. Faw, *Improved Response Functions for the MicroSkyshine Method*, Report 189, Engineering Experiment Station, Kansas State University, Manhattan, KS, 1987.

[Sh91] Shultis, J.K., R.E. Faw, and M.S. Bassett, "The Integral Line-Beam Method for Gamma Skyshine Analysis," *Nucl. Sci. & Engg.*, **107**, 228-245 (1991).

[Sh92] Shultis, J.K., R.E. Faw, and X. Deng, "Improved Response Functions for Gamma-Ray Skyshine Analyses," SAND92-7296, Sandia National Laboratory, Albuquerque, NM, 1992.

[So75] Soffer, L. and L.C. Clemons, Jr., *COHORT-II: A Monte Carlo General Purpose Shielding Computer Code*, Report NASA-D-6170, Lemis Research Center, Cleveland, OH, 1975.

[St67] Storm, E. and H.I. Israel, " Photon Cross Sections from 0.001 to 100 MeV for Elements 1 through 100," Report LA-3753, Los Alamos Scientific Laboratory, Los Alamos, New Mexico, 1967.

[St86] Stephen, M.S. and J.B. Martin, "Bremsstrahlung Energy Spectra from Electrons with Kinetic Energy 1 keV-10 GeV Incident on Screened Nuclei and Orbital Electrons of Neutral Atoms with Z=1-100," *Atomic Data and Nuclear Table*, Vol.35, No 3, Nov. 1986.

[St94] Stedry, M.H., *A Monte-Carlo Line-Beam Calculation of Gamma-Ray Skyshine for Shielded Sources*, M.S. Thesis, Kansas State University, Manhattan, KS, 1994.

[Tr89] Trubey, D.K., M.J. Berger and J.H. Hubbell *Photon Cross Sections for ENDF/B-VI*, American Nuclear Society Topical Meeting , Advances in Nuclear Engineering Computation and Radiation Shielding, Sante Fe, New Mexico, April 1989; actual numerical data were obtained from the DLC-136/PHOTX Data Library available from RSIC, Oak Ridge National Laboratory, Oak Ridge, TN.

[Tr61] Trubey, D.K., "The Single-Scattering Approximation to the Solution of the Gamma-ray Air-Scattering Problem," *Nucl. Sci. & Engg.*, **10**, 102-116 (1961).

[Wh91] Whalen, D.J., D.E. Hollowell, and S.J. Hendricks, *MCNP Photon Benchmark Problems*, LA-12196, Los Alamos National Laboratory, Los Alamos, NM, 1991.

[Wy52] Wyard, S.J., "Intensity Distribution of Bremsstrahlung from Beta Rays," *Proc. Phys. Soc. London*, A65, 377 (1952).

[Ze56] Zerby, C.D., *Radiation Flux Transformation as a Function of an Infinite Medium with Anisotropic Point Sources*, USAEC Report ORNL-2100, Oak Ridge National Laboratory, Oak Ridge, TN, 1956.

Appendix A

Data for the Three-Parameter Approximate LBRF

In Chapter 4, an approximate LBRF was obtained by fitting the following three-parameter empirical formula to calculated LBRF values.

$$\Re(x, E, \phi) = \kappa E(\rho/\rho_o)^2[x\rho/\rho_o]^b e^{a-cx\rho/rho_o}$$

Here ρ_o is the standard air density (= 0.0012 g cm^{-3}), ρ is the actual air density, E is the photon energy in MeV, and, for $\kappa = 1.308 \times 10^{-11}$, the LBRF $\Re$ has units of air-rad/photon.

Values for the parameters a, b, and c, which depend on E and ϕ, were obtained by fitting the above equation calculated values of the LBRF. For energies less than 20 MeV, the approximate LBRF was fit values obtained from the point-kernel LBRF model. For higher energies the fit was based on values calculated by MCNP . The approximation parameters (a, b, c) so obtained are tabulated here for 19 discrete source energies from 0.02 to 100 MeV. For each discrete energy, parameters are tabulated at 20 (for $E < 20$ MeV) or 17 (for $E > 20$ MeV) discrete beam angles.

In these tables the maximum range of the fit and deviations from the point-kernel LBRF value are also given. Parameters were obtained by fits to LBRF values calculated over a limited range of source-to-detector distances. For energies less than 20 MeV, the fit extended from 1 m to a maximum distance x_M which was taken as the smaller of 3000 m or the distance at which the LBRF dose became less than 10^{-30} rad/photon. Although fits over greater ranges are available from the authors, the point-kernel values, upon which the fits depend, are based on buildup factor data extrapolated beyond their tested validity. For energies of 20 MeV or higher, the fits were limited to the maximum range of the MCNP calculations, namely 1000 m. The minimum source-to-detector distance used for the high energy fits was 100 m.

The average deviation of the fitted LBRF to the point-kernel values over all data values and the mazimum deviation and where it occurs are also provided in these tables.

Source Energy 0.02 MeV							
ϕ_j (deg.)	Fit Range[a] x_M (m)	LBRF Fit Parameters			Deviations		
		a	b	c	Aver. (%)	Max. (%)	x_{max} (m)
0.5	400	−3.2260	−1.01008	0.082733	0.5	-0.7	400
1.5	400	−4.3262	−1.02587	0.082972	1.1	1.7	1
2.5	400	−4.8423	−1.03759	0.083122	1.5	-2.2	10
4.0	400	−5.3226	−1.05197	0.083298	1.9	2.8	1
6.0	400	−5.7431	−1.06857	0.083484	2.3	3.4	200
8.5	400	−6.1111	−1.08709	0.083677	2.7	4.1	1
12.5	400	−6.5294	−1.11307	0.083952	3.3	-4.9	8
17.5	400	−6.9077	−1.14100	0.084293	3.8	-5.6	8
25.0	400	−7.3244	−1.17944	0.084817	4.5	6.5	100
35.0	300	−7.7283	−1.23323	0.085354	5.7	8.1	1
45.0	300	−8.0482	−1.26546	0.086869	5.8	-8.0	6
55.0	300	−8.2911	−1.30727	0.088023	6.6	-9.1	6
65.0	300	−8.4674	−1.36460	0.088447	8.6	11.7	100
75.0	300	−8.6262	−1.37644	0.090837	8.2	-11.1	6
85.0	300	−8.7348	−1.39885	0.092420	8.8	11.9	100
95.0	300	−8.7970	−1.43095	0.093787	8.9	14.3	1
110.0	300	−8.8880	−1.41313	0.096396	9.3	-12.6	8
130.0	300	−8.9319	−1.39895	0.099190	9.0	-12.3	8
150.0	300	−8.9420	−1.38270	0.101293	8.7	11.9	100
170.0	300	−8.9415	−1.37327	0.102427	8.5	-11.6	8

[a] Dose beyond this range is less that 10^{-30} rad/photon

Source Energy 0.03 MeV							
ϕ_j (deg.)	Fit Range[a] x_M (m)	LBRF Fit Parameters			Deviations		
		a	b	c	Aver. (%)	Max. (%)	x_{max} (m)
0.5	1000	−4.4477	−0.99217	0.036624	0.6	0.8	20
1.5	800	−5.5594	−0.98604	0.036444	0.9	-1.4	400
2.5	800	−6.0823	−0.98150	0.036389	1.3	1.9	800
4.0	800	−6.5680	−0.97762	0.036372	1.6	-2.4	300
6.0	800	−6.9910	−0.97605	0.036395	1.7	-2.7	1
8.5	800	−7.3574	−0.97780	0.036449	1.6	2.7	20
12.5	800	−7.7683	−0.98477	0.036559	1.3	-2.4	200
17.5	800	−8.1338	−0.99661	0.036719	0.9	1.8	20
25.0	700	−8.5233	−1.02011	0.036967	0.4	-0.7	4
35.0	700	−8.8999	−1.05291	0.037385	1.0	-1.8	6
45.0	700	−9.1820	−1.08656	0.037864	2.2	-3.5	8
55.0	700	−9.3966	−1.12149	0.038408	3.5	5.4	1
65.0	700	−9.5609	−1.15425	0.039022	4.7	7.4	200
75.0	600	−9.6878	−1.17912	0.039772	5.6	8.9	200
85.0	600	−9.7696	−1.21142	0.040168	7.1	-11.5	10
95.0	600	−9.8489	−1.21027	0.041223	7.0	11.2	200
110.0	600	−9.9155	−1.21367	0.042262	7.3	-11.6	10
130.0	600	−9.9499	−1.21375	0.043214	7.3	-12.4	10
150.0	600	−9.9716	−1.19207	0.044380	6.9	-11.0	10
170.0	600	−9.9734	−1.18496	0.044871	6.7	-10.7	600

[a] Dose beyond this range is less that 10^{-30} rad/photon

Source Energy 0.04 MeV							
ϕ_j (deg.)	Fit Range[a] x_M (m)	LBRF Fit Parameters			Deviations		
		a	b	c	Aver. (%)	Max. (%)	x_{max} (m)
0.5	1200	−5.2498	−0.98579	0.025860	1.3	1.9	40
1.5	1200	−6.3942	−0.95719	0.025523	3.6	5.5	40
2.5	1200	−6.9346	−0.93815	0.025393	5.1	7.9	40
4.0	1200	−7.4396	−0.91771	0.025315	6.7	-10.1	500
6.0	1200	−7.8783	−0.90028	0.025291	7.8	-11.9	1
8.5	1200	−8.2567	−0.88736	0.025311	8.6	-13.1	500
12.5	1200	−8.6834	−0.87420	0.025429	9.3	14.3	40
17.5	1200	−9.0456	−0.87587	0.025503	9.1	13.7	1200
25.0	1000	−9.4255	−0.89362	0.025556	7.3	11.6	20
35.0	1000	−9.7973	−0.91429	0.025857	6.2	-10.0	400
45.0	1000	−10.0687	−0.94130	0.026188	5.0	-7.9	400
55.0	1000	−10.2745	−0.97131	0.026551	3.6	5.8	40
65.0	1000	−10.4304	−1.00040	0.026955	2.6	3.6	40
75.0	1000	−10.5230	−1.03221	0.027363	1.6	-2.3	600
85.0	1000	−10.6052	−1.04910	0.027859	2.0	-2.9	8
95.0	1000	−10.6692	−1.05969	0.028324	2.6	4.0	1
110.0	800	−10.7285	−1.06729	0.028968	3.0	-5.2	10
130.0	800	−10.7738	−1.05676	0.029737	3.1	4.8	300
150.0	800	−10.7856	−1.04775	0.030294	3.0	-4.8	20
170.0	800	−10.7870	−1.04235	0.030595	2.9	4.7	300

[a] Dose beyond this range is less that 10^{-30} rad/photon

Source Energy 0.06 MeV							
ϕ_j (deg.)	Fit Range[a] x_M (m)	LBRF Fit Parameters			Deviations		
		a	b	c	Aver. (%)	Max. (%)	x_{max} (m)
0.5	1600	−6.1089	−0.98678	0.019503	2.2	3.7	1600
1.5	1600	−7.2549	−0.93625	0.019074	8.2	-13.4	800
2.5	1600	−7.8889	−0.88471	0.018954	11.2	17.6	1600
4.0	1600	−8.4148	−0.84805	0.018851	14.1	21.9	1600
6.0	1600	−8.8969	−0.80814	0.018849	16.4	-25.9	1
8.5	1400	−9.2540	−0.80177	0.018622	16.4	-25.1	1
12.5	1400	−9.6929	−0.77641	0.018648	17.9	-27.1	600
17.5	1400	−10.0813	−0.75884	0.018724	18.6	27.9	40
25.0	1400	−10.4881	−0.75089	0.018866	18.5	-27.9	500
35.0	1400	−10.8702	−0.75722	0.019078	17.5	-26.5	500
45.0	1400	−11.1412	−0.77559	0.019306	16.0	-24.3	500
55.0	1400	−11.3415	−0.79937	0.019558	14.2	21.6	1400
65.0	1400	−11.4882	−0.82471	0.019831	12.2	-18.6	500
75.0	1200	−11.5798	−0.85583	0.020022	9.4	14.4	1200
85.0	1200	−11.6588	−0.87247	0.020337	7.8	12.0	40
95.0	1200	−11.7158	−0.88280	0.020643	6.7	-10.1	1
110.0	1200	−11.7723	−0.88751	0.021062	5.6	-8.3	500
130.0	1200	−11.8119	−0.88254	0.021527	5.1	-7.4	500
150.0	1200	−11.8275	−0.87607	0.021864	4.9	-7.2	500
170.0	1200	−11.8315	−0.87214	0.022046	4.9	-7.1	400

[a] Dose beyond this range is less that 10^{-30} rad/photon

Source Energy 0.08 MeV							
ϕ_j (deg.)	Fit Range[a] x_M (m)	LBRF Fit Parameters			Deviations		
		a	b	c	Aver. (%)	Max. (%)	x_{max} (m)
0.5	1800	−6.4784	−0.98979	0.017245	3.6	6.0	300
1.5	1800	−7.7109	−0.90971	0.016888	10.4	-17.1	1
2.5	1600	−8.1901	−0.89674	0.016592	12.9	21.1	60
4.0	1600	−8.7769	−0.84483	0.016497	16.1	25.5	60
6.0	1600	−9.2859	−0.79872	0.016450	18.6	-28.8	700
8.5	1600	−9.7153	−0.76011	0.016483	20.5	-32.5	1
12.5	1600	−10.1946	−0.71935	0.016581	22.7	36.2	40
17.5	1600	−10.5639	−0.71142	0.016499	23.2	-35.5	600
25.0	1600	−11.0504	−0.67063	0.016873	24.9	-39.5	1
35.0	1600	−11.3896	−0.69692	0.016802	22.8	-34.8	600
45.0	1600	−11.6705	−0.71134	0.017000	21.5	-32.9	600
55.0	1600	−11.8652	−0.73514	0.017209	19.8	-30.5	600
65.0	1400	−12.0081	−0.76635	0.017321	16.8	25.5	40
75.0	1400	−12.1321	−0.78359	0.017590	14.9	22.6	40
85.0	1400	−12.2156	−0.79878	0.017852	13.3	-20.1	600
95.0	1400	−12.2767	−0.80824	0.018103	12.0	18.1	40
110.0	1400	−12.3394	−0.81253	0.018440	10.9	16.2	40
130.0	1400	−12.3877	−0.80703	0.018807	10.4	-15.2	500
150.0	1400	−12.4124	−0.79980	0.019064	10.2	-15.0	500
170.0	1400	−12.4216	−0.79542	0.019201	10.2	15.0	20

[a] Dose beyond this range is less that 10^{-30} rad/photon

Source Energy 0.1 MeV							
ϕ_j (deg.)	Fit Range[a] x_M (m)	LBRF Fit Parameters			Deviations		
		a	b	c	Aver. (%)	Max. (%)	x_{max} (m)
0.5	1800	−6.6238	−1.00191	0.015962	4.1	-6.0	1000
1.5	1800	−7.8593	−0.91815	0.015607	10.4	-17.2	1000
2.5	1800	−8.4558	−0.87163	0.015468	14.3	-23.2	800
4.0	1800	−9.0119	−0.82592	0.015366	17.8	-28.4	800
6.0	1800	−9.4946	−0.78681	0.015302	20.7	-32.5	800
8.5	1800	−9.8987	−0.75674	0.015271	22.7	-35.5	700
12.5	1800	−10.3808	−0.71966	0.015285	24.4	-38.2	700
17.5	1800	−10.7957	−0.69512	0.015333	25.6	-39.9	700
25.0	1800	−11.2446	−0.67658	0.015442	26.0	-40.4	700
35.0	1600	−11.6866	−0.66391	0.015698	25.6	-40.7	1
45.0	1600	−11.9434	−0.69416	0.015686	23.2	-36.0	1
55.0	1600	−12.2130	−0.69112	0.016098	22.8	-36.4	1
65.0	1600	−12.3357	−0.73070	0.016119	19.9	-30.7	1
75.0	1600	−12.4554	−0.74962	0.016355	18.1	28.0	40
85.0	1600	−12.5359	−0.76577	0.016592	16.6	25.8	40
95.0	1400	−12.5980	−0.78091	0.016716	14.6	22.1	40
110.0	1400	−12.6731	−0.78342	0.017036	13.6	-20.4	600
130.0	1400	−12.7311	−0.77879	0.017387	13.1	-19.3	600
150.0	1400	−12.7490	−0.77592	0.017623	13.1	-19.3	500
170.0	1400	−12.7653	−0.77120	0.017754	13.0	19.1	20

[a] Dose beyond this range is less that 10^{-30} rad/photon

Source Energy 0.2 MeV							
ϕ_j (deg.)	Fit Range[a] x_M (m)	LBRF Fit Parameters			Deviations		
		a	b	c	Aver. (%)	Max. (%)	x_{max} (m)
0.5	2250	−6.6392	−1.02974	0.013119	3.6	-7.1	1400
1.5	2250	−7.8308	−0.96259	0.012803	11.0	-19.3	1200
2.5	2250	−8.4817	−0.91106	0.012692	14.3	-25.1	1000
4.0	2250	−9.1089	−0.85571	0.012619	17.9	30.2	2250
6.0	2250	−9.6651	−0.80532	0.012583	20.9	-34.1	1000
8.5	2250	−10.1427	−0.76164	0.012606	23.3	-38.0	1
12.5	2250	−10.6212	−0.73470	0.012579	25.6	-40.5	1000
17.5	2250	−11.0631	−0.71063	0.012630	27.1	-42.5	1000
25.0	2000	−11.5621	−0.69283	0.012684	26.5	-42.3	1
35.0	2000	−12.0459	−0.68932	0.012828	26.3	41.6	40
45.0	2000	−12.4932	−0.66331	0.013295	28.2	-44.6	1
55.0	2000	−12.6433	−0.72148	0.013248	25.0	-39.7	800
65.0	1800	−12.8772	−0.73884	0.013406	22.4	35.0	40
75.0	1800	−13.0635	−0.74810	0.013687	21.0	-32.7	700
85.0	1800	−13.2075	−0.75519	0.013966	19.7	-30.7	1
95.0	1800	−13.3086	−0.76140	0.014224	18.8	29.3	1800
110.0	1600	−13.4229	−0.76412	0.014553	17.4	27.8	40
130.0	1600	−13.5045	−0.76983	0.014806	16.8	25.7	40
150.0	1600	−13.5545	−0.76633	0.015043	17.1	-25.9	600
170.0	1600	−13.6012	−0.75826	0.015177	16.9	25.7	40

[a] Dose beyond this range is less that 10^{-30} rad/photon

Source Energy 0.4 MeV							
ϕ_j (deg.)	Fit Range[a] x_M (m)	LBRF Fit Parameters			Deviations		
		a	b	c	Aver. (%)	Max. (%)	x_{max} (m)
0.5	2750	−6.8132	−1.01346	0.010558	3.1	-4.9	1800
1.5	2750	−7.9922	−0.96488	0.010291	9.1	15.5	2750
2.5	2750	−8.6244	−0.92355	0.010197	12.1	-21.1	1400
4.0	2750	−9.3021	−0.86517	0.010154	15.3	-25.3	1200
6.0	2750	−9.8097	−0.83151	0.010120	18.1	-29.7	1200
8.5	2750	−10.2779	−0.79695	0.010150	20.8	-34.2	1
12.5	2750	−10.7890	−0.77127	0.010160	22.8	-36.5	1
17.5	2750	−11.2741	−0.74817	0.010247	24.5	-39.0	1000
25.0	2500	−11.8073	−0.73949	0.010333	24.5	-38.7	1000
35.0	2500	−12.3707	−0.73107	0.010621	25.1	-39.7	1000
45.0	2250	−12.7820	−0.74652	0.010847	23.7	-37.3	800
55.0	2250	−13.1706	−0.74506	0.011226	23.0	-36.3	800
65.0	2250	−13.4650	−0.75024	0.011611	22.2	-35.1	800
75.0	2000	−13.6597	−0.77057	0.011874	20.3	-31.9	800
85.0	2000	−13.8378	−0.77498	0.012237	19.7	-31.0	800
95.0	2000	−13.9797	−0.77691	0.012568	19.3	-30.4	800
110.0	1800	−14.1176	−0.78771	0.012900	18.0	28.0	40
130.0	1800	−14.2733	−0.78137	0.013360	17.9	27.8	40
150.0	1800	−14.3687	−0.77600	0.013666	17.9	-27.8	700
170.0	1800	−14.3655	−0.78495	0.013794	18.2	28.6	40

[a] Dose beyond this range is less that 10^{-30} rad/photon

Source Energy 0.7 MeV							
ϕ_j (deg.)	Fit Range[a] x_M (m)	LBRF Fit Parameters			Deviations		
		a	b	c	Aver. (%)	Max. (%)	x_{max} (m)
0.5	3000	−7.0617	−1.00458	0.008475	2.2	-3.1	1800
1.5	3000	−8.2370	−0.96936	0.008252	6.4	-11.1	1600
2.5	3000	−8.9139	−0.92435	0.008189	8.9	-15.0	1400
4.0	3000	−9.4742	−0.89573	0.008133	11.7	-19.7	1400
6.0	3000	−9.9829	−0.86818	0.008115	14.2	-23.6	1400
8.5	3000	−10.4429	−0.84390	0.008131	16.3	-26.9	1200
12.5	3000	−10.9929	−0.81606	0.008204	18.6	-30.2	1200
17.5	3000	−11.5097	−0.79498	0.008338	20.3	-32.7	1200
25.0	3000	−12.1310	−0.77407	0.008599	21.6	-34.7	1200
35.0	2750	−12.7676	−0.76734	0.008966	21.6	34.5	60
45.0	2750	−13.2827	−0.76320	0.009436	22.0	-34.9	1000
55.0	2500	−13.6431	−0.77959	0.009857	21.2	33.7	40
65.0	2500	−14.0201	−0.76938	0.010384	20.7	32.8	40
75.0	2250	−14.2607	−0.78142	0.010785	19.4	30.7	2250
85.0	2250	−14.4720	−0.78166	0.011239	19.3	-30.6	800
95.0	2000	−14.6150	−0.79365	0.011547	18.3	28.8	2000
110.0	2000	−14.8303	−0.78818	0.012084	18.3	28.8	40
130.0	1800	−15.0041	−0.79442	0.012529	17.5	27.2	40
150.0	1800	−15.1166	−0.79293	0.012887	17.7	-27.5	700
170.0	1800	−15.1820	−0.78916	0.013075	17.6	27.4	40

[a] If less than 3000 m, dose beyond this range is less that 10^{-30} rad/photon

Source Energy 1 MeV							
ϕ_j (deg.)	Fit Range[a] x_M (m)	LBRF Fit Parameters			Deviations		
		a	b	c	Aver. (%)	Max. (%)	x_{max} (m)
0.5	3000	−7.3049	−0.99389	0.007225	1.2	-2.0	1800
1.5	3000	−8.4947	−0.96151	0.007041	4.7	7.9	100
2.5	3000	−9.0754	−0.94022	0.006961	6.9	-11.6	1400
4.0	3000	−9.6029	−0.92235	0.006908	9.3	-15.9	1400
6.0	3000	−10.1455	−0.89227	0.006906	11.5	-19.0	1400
8.5	3000	−10.6115	−0.87131	0.006933	13.3	21.9	3000
12.5	3000	−11.1732	−0.84739	0.007025	15.4	-25.1	1200
17.5	3000	−11.7154	−0.82793	0.007190	17.0	-27.5	1200
25.0	3000	−12.4317	−0.78523	0.007637	20.5	33.4	60
35.0	3000	−13.1556	−0.76134	0.008197	22.8	36.1	60
45.0	3000	−13.7157	−0.75288	0.008772	22.8	-36.6	1
55.0	2750	−14.0696	−0.78240	0.009167	20.1	-31.9	1000
65.0	2500	−14.4061	−0.78804	0.009692	19.4	-30.9	1000
75.0	2500	−14.7152	−0.77967	0.010263	19.4	30.8	2500
85.0	2250	−14.8953	−0.79476	0.010682	18.8	-30.0	800
95.0	2250	−15.1262	−0.78274	0.011160	18.7	29.6	40
110.0	2000	−15.3219	−0.79226	0.011650	17.9	-28.2	800
130.0	2000	−15.5065	−0.79610	0.012235	18.3	29.1	2000
150.0	1800	−15.6603	−0.79505	0.012551	17.2	26.8	40
170.0	1800	−15.7254	−0.79419	0.012746	17.3	-26.8	1

[a] If less than 3000 m, dose beyond this range is less that 10^{-30} rad/photon

Source Energy 2 MeV							
ϕ_j (deg.)	Fit Range[a] x_M (m)	LBRF Fit Parameters			Deviations		
		a	b	c	Aver. (%)	Max. (%)	x_{max} (m)
0.5	3000	−7.7503	−0.99299	0.005109	0.8	1.3	3000
1.5	3000	−8.8938	−0.98007	0.004969	2.9	-4.9	1400
2.5	3000	−9.5002	−0.95935	0.004927	4.3	7.2	100
4.0	3000	−10.0600	−0.94313	0.004900	5.9	9.9	100
6.0	3000	−10.5789	−0.92678	0.004912	7.5	-12.4	1
8.5	3000	−11.0630	−0.91192	0.004965	8.8	-14.6	1200
12.5	3000	−11.6801	−0.88817	0.005133	10.8	18.0	80
17.5	3000	−12.2734	−0.87649	0.005340	11.9	-19.2	1200
25.0	3000	−13.0164	−0.85713	0.005791	13.5	21.8	3000
35.0	3000	−13.8161	−0.83421	0.006513	15.3	24.5	3000
45.0	3000	−14.4440	−0.81468	0.007298	16.9	26.9	3000
55.0	3000	−14.9502	−0.79617	0.008086	18.1	-28.7	1000
65.0	2750	−15.3678	−0.78179	0.008797	18.2	28.8	2750
75.0	2500	−15.7255	−0.75839	0.009554	19.7	31.7	60
85.0	2500	−15.9966	−0.74961	0.010153	20.6	32.5	60
95.0	2250	−16.0909	−0.79682	0.010304	16.3	-25.9	800
110.0	2250	−16.2930	−0.82512	0.010598	13.3	-20.1	600
130.0	2250	−16.4711	−0.85865	0.010793	9.4	14.3	40
150.0	2000	−16.4608	−0.91269	0.010806	9.2	14.4	1200
170.0	2000	−16.4096	−0.95593	0.010734	11.4	16.7	1200

[a] If less than 3000 m, dose beyond this range is less that 10^{-30} rad/photon

Source Energy 4 MeV							
ϕ_j (deg.)	Fit Range[a] x_M (m)	LBRF Fit Parameters			Deviations		
		a	b	c	Aver. (%)	Max. (%)	x_{max} (m)
0.5	3000	−8.2758	−0.98923	0.003561	0.6	1.0	6
1.5	3000	−9.4475	−0.97774	0.003475	1.7	-2.9	1400
2.5	3000	−10.0171	−0.97071	0.003444	2.6	4.5	3000
4.0	3000	−10.5948	−0.95890	0.003442	3.6	6.2	3000
6.0	3000	−11.1462	−0.94601	0.003478	4.5	-7.8	1400
8.5	3000	−11.6673	−0.93523	0.003557	5.5	9.3	80
12.5	3000	−12.3366	−0.92036	0.003743	6.6	11.1	3000
17.5	3000	−13.0435	−0.89535	0.004098	8.3	-14.1	1200
25.0	3000	−13.8961	−0.86519	0.004715	10.3	17.1	80
35.0	3000	−14.7437	−0.84347	0.005556	10.9	-17.8	1000
45.0	3000	−15.4316	−0.80780	0.006519	12.5	20.1	3000
55.0	3000	−16.0274	−0.75342	0.007593	16.4	25.9	60
65.0	3000	−16.4891	−0.71579	0.008514	18.9	-29.3	1
75.0	2750	−16.7164	−0.73543	0.009067	16.5	-26.7	1000
85.0	2500	−16.9985	−0.72739	0.009588	15.4	25.1	2500
95.0	2500	−17.1738	−0.74239	0.009874	13.5	-21.5	800
110.0	2250	−17.3938	−0.77161	0.009984	8.3	-13.0	1
130.0	2250	−17.5883	−0.79817	0.010083	5.1	8.0	40
150.0	2250	−17.6928	−0.82578	0.010002	2.2	3.3	40
170.0	2250	−17.7441	−0.83766	0.009993	1.8	-3.0	300

[a] If less than 3000 m, dose beyond this range is less that 10^{-30} rad/photon

Source Energy 7 MeV							
ϕ_j (deg.)	Fit Range[a] x_M (m)	LBRF Fit Parameters			Deviations		
		a	b	c	Aver. (%)	Max. (%)	x_{max} (m)
0.5	3000	−8.7366	−0.98522	0.002731	0.6	-1.6	20
1.5	3000	−9.9111	−0.97908	0.002675	1.2	-2.2	1
2.5	3000	−10.5030	−0.97167	0.002665	1.8	-3.0	1
4.0	3000	−11.0991	−0.96280	0.002679	2.6	4.0	100
6.0	3000	−11.6799	−0.95355	0.002727	3.3	5.1	3000
8.5	3000	−12.2511	−0.94369	0.002825	4.0	-6.1	1200
12.5	3000	−12.9971	−0.92818	0.003046	4.8	7.2	80
17.5	3000	−13.7578	−0.90887	0.003409	5.6	8.4	10
25.0	3000	−14.6649	−0.87832	0.004081	6.9	10.5	10
35.0	3000	−15.6265	−0.80689	0.005259	11.7	-15.1	1
45.0	3000	−16.3092	−0.78085	0.006202	9.7	-14.8	800
55.0	3000	−16.8448	−0.73980	0.007241	11.6	-17.8	800
65.0	3000	−17.3930	−0.65099	0.008440	18.2	23.9	80
75.0	2750	−17.7441	−0.62661	0.009151	15.8	24.0	80
85.0	2500	−17.9783	−0.63045	0.009543	14.1	-20.7	1000
95.0	2500	−18.1721	−0.63762	0.009780	11.9	-17.1	1000
110.0	2500	−18.3791	−0.66374	0.009875	7.8	-11.2	1
130.0	2250	−18.5822	−0.69285	0.009870	4.1	6.9	4
150.0	2250	−18.7128	−0.70699	0.009877	2.9	-4.9	1
170.0	2250	−18.7757	−0.71234	0.009883	2.4	4.1	4

[a] If less than 3000 m, dose beyond this range is less that 10^{-30} rad/photon

Source Energy 10 MeV							
ϕ_j (deg.)	Fit Range[a] x_M (m)	LBRF Fit Parameters			Deviations		
		a	b	c	Aver. (%)	Max. (%)	x_{max} (m)
0.5	3000	−9.0128	−0.98651	0.002360	1.5	2.2	20
1.5	3000	−10.2088	−0.97795	0.002323	1.6	-2.7	1200
2.5	3000	−10.8240	−0.96682	0.002345	2.2	3.9	20
4.0	3000	−11.4369	−0.96433	0.002342	2.2	-3.8	1200
6.0	3000	−12.0593	−0.95128	0.002427	3.2	5.2	10
8.5	3000	−12.6725	−0.94721	0.002505	3.3	-5.5	1
12.5	3000	−13.4995	−0.91818	0.002810	5.7	-8.4	1
17.5	3000	−14.3047	−0.90810	0.003120	5.1	8.9	10
25.0	3000	−15.2699	−0.86862	0.003838	7.1	11.8	10
35.0	3000	−16.2390	−0.80974	0.004940	9.3	-15.3	500
45.0	3000	−16.9695	−0.75096	0.006080	10.9	18.1	10
55.0	3000	−17.5507	−0.69119	0.007189	11.9	19.9	8
65.0	3000	−18.0818	−0.58373	0.008494	17.9	26.9	10
75.0	2750	−18.4452	−0.54038	0.009317	20.1	27.6	10
85.0	2500	−18.6529	−0.56660	0.009519	13.8	-21.6	1000
95.0	2500	−18.8486	−0.57068	0.009738	11.4	-18.5	1
110.0	2500	−19.0804	−0.57172	0.009965	10.0	15.2	6
130.0	2500	−19.2583	−0.61284	0.009876	5.3	9.1	4
150.0	2250	−19.3800	−0.62850	0.009875	4.4	-6.6	1
170.0	2250	−19.4411	−0.63086	0.009897	3.2	5.8	4

[a] If less than 3000 m, dose beyond this range is less that 10^{-30} rad/photon

Source Energy 15 MeV							
ϕ_j (deg.)	Fit Range[a] x_M (m)	LBRF Fit Parameters			Deviations		
		a	b	c	Aver. (%)	Max. (%)	x_{max} (m)
0.5	3000	−9.3204	−0.98134	0.002086	1.8	-2.7	40
1.5	3000	−10.5377	−0.97434	0.002056	2.2	3.4	20
2.5	3000	−11.1842	−0.96023	0.002101	2.9	-5.4	1
4.0	3000	−11.8504	−0.95198	0.002132	3.6	-6.4	1
6.0	3000	−12.5102	−0.95427	0.002134	3.5	-5.9	800
8.5	3000	−13.1987	−0.94400	0.002244	4.3	7.0	20
12.5	3000	−14.0811	−0.92796	0.002492	6.0	-9.3	600
17.5	3000	−15.0360	−0.86111	0.003074	7.6	16.0	20
25.0	3000	−16.0715	−0.79763	0.003897	9.6	20.9	20
35.0	3000	−17.0954	−0.71128	0.005128	11.8	-25.8	1
45.0	3000	−17.7750	−0.69366	0.006045	16.8	-24.4	400
55.0	3000	−18.4651	−0.56180	0.007542	16.4	-32.1	1
65.0	3000	−18.8348	−0.56239	0.008250	17.9	27.3	3000
75.0	2750	−19.3079	−0.43873	0.009487	23.7	34.9	10
85.0	2500	−19.4561	−0.49512	0.009484	15.4	25.1	8
95.0	2500	−19.7029	−0.45011	0.009981	17.4	26.2	10
110.0	2500	−19.8314	−0.51867	0.009792	10.8	16.7	2500
130.0	2500	−20.0569	−0.50219	0.010062	8.1	-13.8	1
150.0	2500	−20.1422	−0.54596	0.009914	6.0	8.5	4
170.0	2250	−20.1998	−0.54699	0.009933	3.9	7.6	4

[a] If less than 3000 m, dose beyond this range is less that 10^{-30} rad/photon

Source Energy 20 MeV							
ϕ_j (deg.)	Fit Range x_M (m)	LBRF Fit Parameters			Deviations		
		a	b	c	Aver. (%)	Max. (%)	x_{max} (m)
2.0	1000	−11.5254	−0.83971	0.002336	1.3	3.6	850
3.5	1000	−12.1040	−0.87880	0.002201	0.6	-1.6	250
5.0	1000	−12.2872	−0.94602	0.002147	0.5	0.8	650
7.5	1000	−13.1321	−0.92409	0.002240	0.8	1.4	850
10.0	1000	−13.7109	−0.92011	0.002360	0.5	-1.1	750
15.0	1000	−14.7587	−0.88616	0.002634	0.9	-1.7	250
20.0	1000	−15.5978	−0.84187	0.003056	1.0	2.5	650
30.0	1000	−16.5634	−0.81272	0.003909	0.8	1.9	650
45.0	1000	−17.4956	−0.77512	0.005232	2.0	-3.2	950
60.0	1000	−17.4157	−0.89453	0.006081	3.7	-7.5	950
75.0	1000	−18.9171	−0.65583	0.007686	2.1	-4.8	950
85.0	1000	−19.0702	−0.67991	0.008210	2.4	4.3	750
95.0	1000	−18.6824	−0.78609	0.008300	3.2	5.3	550
105.0	1000	−20.1047	−0.50890	0.009520	2.9	-6.5	750
120.0	1000	−19.6238	−0.66046	0.009405	1.2	2.0	750
135.0	1000	−19.5357	−0.71284	0.009503	1.2	-2.2	250
150.0	1000	−20.5199	−0.52957	0.010147	4.5	-17.6	850

Source Energy 40 MeV							
ϕ_j (deg.)	Fit Range x_M (m)	LBRF Fit Parameters			Deviations		
		a	b	c	Aver. (%)	Max. (%)	x_{max} (m)
2.0	1000	−11.8173	−0.79296	0.002288	1.1	-2.1	250
3.5	1000	−12.5321	−0.81852	0.002255	0.5	1.5	750
5.0	1000	−13.0204	−0.84391	0.002232	0.8	1.9	550
7.5	1000	−13.9220	−0.82980	0.002272	1.1	-2.3	250
10.0	1000	−14.7938	−0.78470	0.002419	0.9	-2.0	250
15.0	1000	−16.2632	−0.67687	0.002871	1.2	-2.4	950
20.0	1000	−17.0569	−0.65228	0.003186	1.1	3.1	650
30.0	1000	−18.2489	−0.59163	0.004005	1.6	-3.0	250
45.0	1000	−18.5164	−0.69527	0.005024	3.2	6.4	750
60.0	1000	−18.8970	−0.72093	0.006110	3.3	-5.4	250
75.0	1000	−19.7789	−0.61671	0.007384	2.3	5.6	850
85.0	1000	−19.1617	−0.79481	0.007494	4.3	7.4	650
95.0	1000	−19.8258	−0.69570	0.008221	3.1	-6.0	950
105.0	1000	−19.4890	−0.79981	0.008275	4.1	-8.4	950
120.0	1000	−22.8286	−0.13046	0.010713	5.4	11.9	950
135.0	1000	−20.4077	−0.68665	0.009323	2.0	-3.3	950
150.0	1000	−23.4310	−0.07530	0.011202	9.3	22.3	950

Source Energy 70 MeV							
ϕ_j (deg.)	Fit Range x_M (m)	LBRF Fit Parameters			Deviations		
		a	b	c	Aver. (%)	Max. (%)	x_{max} (m)
2.0	1000	−12.2645	−0.66953	0.002439	0.9	-2.4	250
3.5	1000	−13.2846	−0.65430	0.002437	1.7	-3.1	250
5.0	1000	−14.3083	−0.58927	0.002591	1.2	-3.9	250
7.5	1000	−16.0555	−0.43965	0.002768	2.4	-5.4	250
10.0	1000	−17.3921	−0.31804	0.003034	2.4	-5.4	250
15.0	1000	−19.4567	−0.12560	0.003501	2.3	-5.2	250
20.0	1000	−20.0629	−0.15312	0.003647	2.1	-3.4	350
30.0	1000	−20.8303	−0.18181	0.004359	2.4	-4.6	950
45.0	1000	−20.3404	−0.44229	0.005060	3.9	-7.1	950
60.0	1000	−20.2337	−0.57049	0.006019	5.9	-13.1	950
75.0	1000	−20.0056	−0.70464	0.006708	5.6	-10.2	950
85.0	1000	−20.5941	−0.63060	0.007525	3.2	-5.7	850
95.0	1000	−20.5578	−0.67732	0.007969	4.5	7.5	650
105.0	1000	−19.5986	−0.91715	0.007729	8.7	-18.9	950
120.0	1000	−21.5116	−0.56177	0.009139	2.1	-4.0	250
135.0	1000	−20.1149	−0.89330	0.008584	7.1	20.0	850
150.0	1000	−22.0577	−0.51814	0.009751	3.0	6.0	750

Source Energy 100 MeV							
ϕ_j (deg.)	Fit Range x_M (m)	LBRF Fit Parameters			Deviations		
		a	b	c	Aver. (%)	Max. (%)	x_{max} (m)
2.0	1000	−12.4373	−0.59313	0.002566	0.8	-1.8	250
3.5	1000	−14.3007	−0.43470	0.002759	1.9	-3.6	250
5.0	1000	−16.0334	−0.25688	0.003008	3.2	-6.0	250
7.5	1000	−18.0766	−0.06719	0.003232	3.5	-5.4	250
10.0	1000	−20.2588	0.19482	0.003641	3.3	-5.7	250
15.0	1000	−21.8571	0.27787	0.003875	2.2	-3.6	250
20.0	1000	−22.1404	0.18095	0.003888	3.3	6.1	750
30.0	1000	−22.4079	0.05628	0.004467	1.7	2.6	550
45.0	1000	−22.0297	−0.17763	0.005334	3.3	5.7	750
60.0	1000	−22.0498	−0.27341	0.006488	3.0	-5.5	950
75.0	1000	−19.9816	−0.80877	0.005959	7.3	-12.8	950
85.0	1000	−21.8342	−0.46573	0.007794	3.8	-7.1	250
95.0	1000	−22.9422	−0.29019	0.008532	6.8	-16.7	950
105.0	1000	−23.6121	−0.15362	0.009863	4.4	-12.0	850
120.0	1000	−22.1031	−0.52334	0.009245	7.5	33.0	850
135.0	1000	−21.4043	−0.69378	0.009269	1.8	3.8	850
150.0	1000	−21.1517	−0.78965	0.009154	5.4	13.1	850

Appendix B

Data for the Four-Parameter Approximate LBRF

In Chapter 4, an approximate LBRF was obtained by fitting the following four-parameter empirical formula to calculated LBRF values.

$$\Re(x, E, \phi) = \kappa E(\rho/\rho_o)^2[x\rho/\rho_o]^{(b-dx)}e^{a-cx\rho/\rho_o}$$

Here ρ_o is the standard air density ($= 0.0012$ g cm^{-3}), ρ is the actual air density, E is the photon energy in MeV, and, for $\kappa = 1.308 \times 10^{-11}$, the LBRF $\Re$ has units of air-rad/photon.

Values for the parameters a, b, c, and d, which depend on E and ϕ, were obtained by fitting the above equation to values calculated with the point-kernel model of Chapter 2. The approximation parameters so obtained are tabulated here for 15 discrete source energies from 0.02 to 15 MeV. For each discrete energy, parameters are tabulated at 20 discrete beam angles.

In these tables the maximum range of the fit and deviations from the point-kernel LBRF value are also given. Parameters were obtained by fits to LBRF values calculated over a limited range of source-to-detector distances. The fit extended from 1 m to a maximum distance x_M which was taken as the smaller of 3000 m or the distance at which the LBRF dose became less than 10^{-30} rad/photon. Although fits over greater ranges are available from the authors, the point-kernel values, upon which the fits depend, are based on buildup factor data extrapolated beyond their tested validity.

The average deviation of the fitted LBRF to the point-kernel values over all data values and the mazimum deviation and where it occurs are also provided in these tables.

Source Energy 0.02 MeV								
ϕ_j (deg.)	Fit Range[a] x_M (m)	LBRF Fit Parameters				Deviations		
		a	b	c	d	Aver. (%)	Max. (%)	x_{max} (m)
0.5	400	−3.2316	−1.00079	0.084128	−0.000215	0.0	0.0	1
1.5	400	−4.3375	−1.00541	0.086187	−0.000498	0.2	-0.2	300
2.5	400	−4.8561	−1.01139	0.087389	−0.000664	0.3	0.4	1
4.0	400	−5.3388	−1.01947	0.088758	−0.000851	0.5	0.6	400
6.0	400	−5.7619	−1.02912	0.090193	−0.001047	0.7	0.8	60
8.5	400	−6.1323	−1.04083	0.091647	−0.001245	0.8	1.1	1
12.5	400	−6.5541	−1.05790	0.093345	−0.001466	1.1	1.3	1
17.5	400	−6.9340	−1.07967	0.094860	−0.001652	1.4	-1.7	300
25.0	400	−7.3508	−1.10978	0.097000	−0.001908	1.8	-2.5	300
35.0	300	−7.7632	−1.13177	0.103947	−0.002938	1.5	2.5	1
45.0	300	−8.0736	−1.16694	0.107122	−0.003304	2.0	3.2	40
55.0	300	−8.3214	−1.20455	0.109286	−0.003479	2.6	3.6	300
65.0	300	−8.5068	−1.22703	0.114258	−0.004077	2.8	4.7	40
75.0	300	−8.6537	−1.24823	0.118003	−0.004450	3.2	-5.2	200
85.0	300	−8.7640	−1.26187	0.121439	−0.004754	3.4	5.6	1
95.0	300	−8.8437	−1.26810	0.124266	−0.004951	3.6	5.8	40
110.0	300	−8.9198	−1.26807	0.126879	−0.004991	3.6	5.8	1
130.0	300	−8.9638	−1.25697	0.128859	−0.004855	3.5	-5.5	200
150.0	300	−8.9745	−1.24541	0.129826	−0.004667	3.3	5.2	1
170.0	300	−8.9737	−1.23797	0.130477	−0.004587	3.2	-5.1	200

[a] Dose beyond this range is less that 10^{-30} rad/photon

Source Energy 0.03 MeV								
ϕ_j (deg.)	Fit Range[a] x_M (m)	LBRF Fit Parameters				Deviations		
		a	b	c	d	Aver. (%)	Max. (%)	x_{max} (m)
0.5	1000	−4.4406	−0.99970	0.035983	0.000087	0.0	0.1	500
1.5	800	−5.5468	−1.00010	0.035085	0.000191	0.0	0.1	500
2.5	800	−6.0655	−1.00063	0.034525	0.000262	0.1	-0.1	200
4.0	800	−6.5481	−1.00091	0.034063	0.000325	0.1	-0.2	200
6.0	800	−6.9704	−1.00090	0.033873	0.000356	0.2	0.5	500
8.5	800	−7.3389	−1.00109	0.033998	0.000347	0.4	0.7	500
12.5	800	−7.7543	−1.00292	0.034554	0.000286	0.5	-0.8	200
17.5	800	−8.1240	−1.00804	0.035452	0.000182	0.5	0.7	20
25.0	700	−8.5181	−1.02314	0.036664	0.000045	0.4	-0.7	700
35.0	700	−8.9051	−1.03810	0.039434	−0.000299	0.6	1.1	1
45.0	700	−9.1935	−1.05746	0.041712	−0.000560	1.2	-1.9	500
55.0	700	−9.4150	−1.07667	0.044222	−0.000846	1.9	2.9	60
65.0	700	−9.5861	−1.09360	0.046853	−0.001139	2.5	3.9	60
75.0	600	−9.7272	−1.10731	0.049506	−0.001444	2.6	-3.7	6
85.0	600	−9.8276	−1.11459	0.051845	−0.001680	2.9	4.0	1
95.0	600	−9.9011	−1.11694	0.053742	−0.001854	3.1	-4.2	6
110.0	600	−9.9720	−1.11401	0.055549	−0.001969	3.1	-4.1	400
130.0	600	−10.0145	−1.10469	0.056581	−0.001940	2.9	-4.1	400
150.0	600	−10.0326	−1.09326	0.057107	−0.001881	2.7	3.9	600
170.0	600	−10.0364	−1.08647	0.057409	−0.001852	2.7	3.8	100

[a] Dose beyond this range is less that 10^{-30} rad/photon

Source Energy 0.04 MeV								
ϕ_j (deg.)	Fit Range[a] x_M (m)	LBRF Fit Parameters				Deviations		
		a	b	c	d	Aver. (%)	Max. (%)	x_{max} (m)
0.5	1200	−5.2291	−1.00342	0.024663	0.000159	0.2	0.2	200
1.5	1200	−6.3365	−1.00685	0.022000	0.000469	0.3	-0.4	8
2.5	1200	−6.8542	−1.00787	0.020369	0.000669	0.2	-0.4	8
4.0	1200	−7.3450	−1.00404	0.018901	0.000856	0.4	-0.7	300
6.0	1200	−7.7622	−1.00207	0.017717	0.001012	0.6	-1.3	1200
8.5	1200	−8.1310	−0.99753	0.016981	0.001115	0.9	-1.9	1200
12.5	1200	−8.5521	−0.99056	0.016608	0.001177	1.3	-2.6	200
17.5	1200	−8.9257	−0.98609	0.016758	0.001174	1.6	-3.0	200
25.0	1000	−9.3258	−0.99162	0.016807	0.001203	1.4	-2.6	200
35.0	1000	−9.7095	−0.99894	0.018324	0.001036	1.2	-2.2	1000
45.0	1000	−10.0057	−1.00710	0.020242	0.000817	1.0	-1.5	200
55.0	1000	−10.2110	−1.02352	0.022338	0.000574	0.8	-1.1	6
65.0	1000	−10.3787	−1.03599	0.024047	0.000400	1.1	1.8	1
75.0	1000	−10.5083	−1.04378	0.026231	0.000155	1.5	-2.4	8
85.0	1000	−10.6061	−1.04746	0.028086	−0.000033	1.9	2.8	1
95.0	1000	−10.6787	−1.04567	0.029910	−0.000226	1.8	-2.9	8
110.0	800	−10.7540	−1.03153	0.032709	−0.000532	1.5	-2.2	8
130.0	800	−10.7992	−1.01985	0.033834	−0.000584	1.2	-1.8	500
150.0	800	−10.8121	−1.01003	0.034336	−0.000575	1.0	1.6	200
170.0	800	−10.8134	−1.00483	0.034582	−0.000567	0.9	1.6	800

[a] Dose beyond this range is less that 10^{-30} rad/photon

Source Energy 0.06 MeV								
ϕ_j (deg.)	Fit Range[a] x_M (m)	LBRF Fit Parameters				Deviations		
		a	b	c	d	Aver. (%)	Max. (%)	x_{max} (m)
0.5	1600	−6.0522	−1.01717	0.018223	0.000161	1.0	-2.1	1000
1.5	1600	−7.1609	−1.03063	0.013321	0.000738	1.4	2.3	200
2.5	1600	−7.6851	−1.03121	0.010588	0.001073	1.1	-1.9	10
4.0	1600	−8.1837	−1.02323	0.008351	0.001351	1.1	-1.6	1600
6.0	1600	−8.6368	−1.00695	0.006828	0.001544	1.7	-2.7	1600
8.5	1400	−9.0060	−1.00300	0.004946	0.001793	1.5	-2.7	1400
12.5	1400	−9.4350	−0.98923	0.003852	0.001943	1.9	3.8	1000
17.5	1400	−9.8189	−0.97614	0.003439	0.002010	2.4	4.8	1000
25.0	1400	−10.2369	−0.96369	0.003716	0.001994	2.9	5.6	1000
35.0	1400	−10.6385	−0.95602	0.004875	0.001871	3.0	-6.0	1400
45.0	1400	−10.9357	−0.95556	0.006431	0.001696	2.8	5.8	1000
55.0	1400	−11.1629	−0.95840	0.008221	0.001493	2.5	5.2	1000
65.0	1400	−11.3366	−0.96189	0.010121	0.001279	2.1	-4.4	1400
75.0	1200	−11.4390	−0.97818	0.010984	0.001208	0.9	2.3	800
85.0	1200	−11.5563	−0.97107	0.012921	0.000991	1.0	-1.8	300
95.0	1200	−11.6301	−0.96626	0.014401	0.000834	0.8	-1.5	1200
110.0	1200	−11.7000	−0.95740	0.015878	0.000692	0.6	-1.3	300
130.0	1200	−11.7538	−0.94260	0.016944	0.000613	0.9	-1.4	300
150.0	1200	−11.7762	−0.93073	0.017592	0.000573	1.2	1.9	6
170.0	1200	−11.7837	−0.92442	0.017890	0.000558	1.4	2.2	6

[a] Dose beyond this range is less that 10^{-30} rad/photon

Source Energy 0.08 MeV								
ϕ_j (deg.)	Fit Range[a] x_M (m)	LBRF Fit Parameters				Deviations		
		a	b	c	d	Aver. (%)	Max. (%)	x_{max} (m)
0.5	1800	−6.3750	−1.03192	0.015906	0.000164	2.2	4.3	1800
1.5	1800	−7.4895	−1.05013	0.010201	0.000839	2.5	-4.2	1000
2.5	1600	−8.0201	−1.04963	0.007353	0.001185	2.1	-3.4	10
4.0	1600	−8.5176	−1.04470	0.004410	0.001557	1.8	-2.8	10
6.0	1600	−8.9546	−1.03567	0.002394	0.001808	1.4	-2.0	1600
8.5	1600	−9.3656	−1.01583	0.001115	0.001974	2.0	3.0	1200
12.5	1600	−9.8062	−0.99906	−0.000135	0.002140	2.4	4.4	1200
17.5	1600	−10.2011	−0.98288	−0.000750	0.002230	2.8	5.6	1200
25.0	1600	−10.6356	−0.96650	−0.000748	0.002247	3.4	-6.8	1600
35.0	1600	−11.0572	−0.95405	0.000131	0.002159	3.7	-7.5	1600
45.0	1600	−11.3724	−0.94887	0.001494	0.002009	3.7	7.5	1200
55.0	1600	−11.6153	−0.94832	0.003077	0.001832	3.4	7.0	1200
65.0	1400	−11.7841	−0.96186	0.003644	0.001797	2.1	-4.6	1400
75.0	1400	−11.9289	−0.95960	0.005491	0.001588	1.8	-4.0	1400
85.0	1400	−12.0391	−0.95512	0.007139	0.001406	1.6	-3.7	1400
95.0	1400	−12.1214	−0.94883	0.008469	0.001265	1.5	3.4	1000
110.0	1400	−12.2056	−0.93759	0.009826	0.001131	1.6	3.4	1000
130.0	1400	−12.2682	−0.92262	0.010760	0.001058	2.0	3.6	1000
150.0	1400	−12.2975	−0.91076	0.011218	0.001033	2.3	-3.9	300
170.0	1400	−12.3083	−0.90436	0.011432	0.001024	2.5	-4.1	1400

[a] Dose beyond this range is less that 10^{-30} rad/photon

Source Energy 0.1 MeV								
ϕ_j (deg.)	Fit Range[a] x_M (m)	LBRF Fit Parameters				Deviations		
		a	b	c	d	Aver. (%)	Max. (%)	x_{max} (m)
0.5	1800	−6.5300	−1.02988	0.015323	0.000077	2.7	5.4	300
1.5	1800	−7.6241	−1.05962	0.009153	0.000808	3.2	-5.5	1000
2.5	1800	−8.1569	−1.06191	0.006130	0.001174	2.9	4.6	200
4.0	1800	−8.6536	−1.05892	0.003156	0.001547	2.3	-3.7	10
6.0	1800	−9.0950	−1.04978	0.001054	0.001807	1.9	-2.8	600
8.5	1800	−9.5229	−1.02631	−0.000156	0.001962	2.6	3.9	1400
12.5	1800	−9.9812	−1.00559	−0.001330	0.002115	3.3	-5.5	1800
17.5	1800	−10.3461	−1.00016	−0.002216	0.002236	3.4	-7.2	400
25.0	1800	−10.8023	−0.97925	−0.002215	0.002252	4.2	-8.7	1800
35.0	1600	−11.2579	−0.96908	−0.002540	0.002328	3.7	7.4	1200
45.0	1600	−11.5913	−0.96182	−0.001358	0.002202	3.7	7.5	1200
55.0	1600	−11.8500	−0.95878	0.000106	0.002041	3.5	-7.1	1600
65.0	1600	−12.0508	−0.95676	0.001724	0.001862	3.2	6.6	1200
75.0	1600	−12.2063	−0.95392	0.003305	0.001688	2.9	-6.0	1600
85.0	1600	−12.3250	−0.94959	0.004705	0.001538	2.6	5.6	1200
95.0	1400	−12.3976	−0.95522	0.004855	0.001556	1.6	-3.6	400
110.0	1400	−12.4913	−0.94460	0.006060	0.001440	1.7	3.5	1000
130.0	1400	−12.5652	−0.92992	0.006988	0.001365	2.1	-3.7	300
150.0	1400	−12.6026	−0.91861	0.007459	0.001337	2.4	4.0	1000
170.0	1400	−12.6178	−0.91243	0.007690	0.001324	2.6	-4.2	300

[a] Dose beyond this range is less that 10^{-30} rad/photon

Source Energy 0.2 MeV								
ϕ_j (deg.)	Fit Range[a] x_M (m)	LBRF Fit Parameters				Deviations		
		a	b	c	d	Aver. (%)	Max. (%)	x_{max} (m)
0.5	2250	−6.6467	−1.03733	0.012698	0.000051	3.4	-6.4	1400
1.5	2250	−7.7595	−1.06411	0.007745	0.000621	3.9	7.0	300
2.5	2250	−8.2984	−1.06795	0.005191	0.000922	3.5	-5.9	1200
4.0	2250	−8.8025	−1.06721	0.002759	0.001215	2.8	4.9	200
6.0	2250	−9.2497	−1.06249	0.000703	0.001468	2.4	4.0	1
8.5	2250	−9.6491	−1.05414	−0.000753	0.001646	2.0	-3.0	10
12.5	2250	−10.1625	−1.02792	−0.001775	0.001778	3.0	-4.4	600
17.5	2250	−10.6099	−1.00942	−0.002466	0.001873	3.8	-6.0	500
25.0	2000	−11.0881	−1.00591	−0.003744	0.002055	3.4	-5.7	400
35.0	2000	−11.5954	−0.99242	−0.003546	0.002057	3.8	6.9	1400
45.0	2000	−11.9942	−0.98487	−0.002836	0.001998	3.9	7.3	1400
55.0	2000	−12.2762	−0.99118	−0.002023	0.001925	3.7	7.4	1400
65.0	1800	−12.5464	−0.99046	−0.001526	0.001903	2.7	5.1	1400
75.0	1800	−12.7456	−0.98746	−0.000297	0.001781	2.5	4.8	1400
85.0	1800	−12.9016	−0.98286	0.000845	0.001670	2.4	4.6	1400
95.0	1800	−13.0234	−0.97682	0.001774	0.001585	2.4	4.6	1400
110.0	1600	−13.1463	−0.97632	0.001970	0.001610	1.9	-3.6	1600
130.0	1600	−13.2655	−0.96418	0.002593	0.001577	2.3	-4.2	300
150.0	1600	−13.3356	−0.95495	0.002871	0.001574	2.6	-4.8	1600
170.0	1600	−13.3683	−0.95012	0.002986	0.001576	2.8	-5.1	300

[a] Dose beyond this range is less that 10^{-30} rad/photon

Source Energy 0.4 MeV								
ϕ_j (deg.)	Fit Range[a] x_M (m)	LBRF Fit Parameters				Deviations		
		a	b	c	d	Aver. (%)	Max. (%)	x_{max} (m)
0.5	2750	−6.8233	−1.02376	0.010058	0.000059	2.2	3.8	1
1.5	2750	−7.9344	−1.04479	0.006783	0.000421	3.0	4.9	400
2.5	2750	−8.4709	−1.04912	0.004973	0.000628	2.7	-4.5	1400
4.0	2750	−8.9790	−1.04987	0.003153	0.000842	2.2	-3.9	20
6.0	2750	−9.4347	−1.04696	0.001692	0.001015	1.8	-3.2	10
8.5	2750	−9.8442	−1.04230	0.000463	0.001165	1.7	2.5	200
12.5	2750	−10.3746	−1.01930	−0.000342	0.001271	2.6	3.6	2000
17.5	2750	−10.8041	−1.02018	−0.001230	0.001390	2.9	-5.5	2750
25.0	2500	−11.3880	−1.00124	−0.001853	0.001494	3.5	5.5	1800
35.0	2500	−11.9700	−0.99001	−0.001762	0.001520	4.2	-6.9	1
45.0	2250	−12.4253	−0.99667	−0.002115	0.001611	3.6	-6.1	2250
55.0	2250	−12.8062	−0.99358	−0.001410	0.001569	3.7	6.4	1600
65.0	2250	−13.1117	−0.99123	−0.000562	0.001511	3.7	-6.5	2250
75.0	2000	−13.3363	−1.00030	−0.000501	0.001556	2.7	-4.8	400
85.0	2000	−13.5278	−0.99721	0.000280	0.001503	2.6	4.8	1400
95.0	2000	−13.6805	−0.99358	0.000909	0.001466	2.6	4.9	1400
110.0	1800	−13.8405	−0.99554	0.000978	0.001517	1.9	-3.6	1800
130.0	1800	−13.9998	−0.98733	0.001524	0.001506	2.1	3.9	1400
150.0	1800	−14.0970	−0.98132	0.001830	0.001506	2.3	4.2	1400
170.0	1800	−14.1436	−0.97796	0.001987	0.001506	2.3	4.3	1400

[a] Dose beyond this range is less that 10^{-30} rad/photon

Source Energy 0.7 MeV								
ϕ_j (deg.)	Fit Range[a] x_M (m)	LBRF Fit Parameters				Deviations		
		a	b	c	d	Aver. (%)	Max. (%)	x_{max} (m)
0.5	3000	−7.0739	−1.01292	0.008036	0.000052	1.1	1.9	3000
1.5	3000	−8.1891	−1.02770	0.005847	0.000286	1.9	3.0	3000
2.5	3000	−8.7274	−1.03184	0.004513	0.000436	1.8	-2.9	20
4.0	3000	−9.2389	−1.03370	0.003134	0.000596	1.6	-2.7	20
6.0	3000	−9.7031	−1.03240	0.001986	0.000732	1.3	-2.2	10
8.5	3000	−10.1244	−1.02970	0.001033	0.000848	1.2	1.9	200
12.5	3000	−10.6372	−1.02227	0.000175	0.000961	1.6	3.0	2000
17.5	3000	−11.1713	−1.00226	−0.000156	0.001019	2.6	-4.0	600
25.0	3000	−11.7747	−0.99050	−0.000410	0.001083	3.4	5.5	2000
35.0	2750	−12.4150	−0.98742	−0.000760	0.001180	3.6	-5.9	2750
45.0	2750	−12.9193	−0.98818	−0.000508	0.001208	4.0	-7.1	2750
55.0	2500	−13.3565	−0.98593	−0.000374	0.001258	3.5	6.0	1800
65.0	2500	−13.6980	−0.98288	0.000261	0.001243	3.6	6.2	1800
75.0	2250	−13.9590	−0.99048	0.000202	0.001314	2.9	-5.2	1
85.0	2250	−14.1789	−0.98749	0.000781	0.001299	3.0	5.4	1600
95.0	2000	−14.3429	−0.99494	0.000533	0.001386	2.3	4.2	1400
110.0	2000	−14.5517	−0.99157	0.001053	0.001388	2.4	-4.5	2000
130.0	1800	−14.7338	−0.99646	0.000911	0.001478	1.9	-3.5	1
150.0	1800	−14.8547	−0.99361	0.001242	0.001482	2.0	3.7	1400
170.0	1800	−14.9130	−0.99151	0.001434	0.001481	2.0	3.8	1400

[a] If less than 3000 m, dose beyond this range is less that 10^{-30} rad/photon

Source Energy 1 MeV								
ϕ_j (deg.)	Fit Range[a] x_M (m)	LBRF Fit Parameters				Deviations		
		a	b	c	d	Aver. (%)	Max. (%)	x_{max} (m)
0.5	3000	−7.2747	−1.00801	0.006846	0.000044	0.7	1.1	3000
1.5	3000	−8.3949	−1.01891	0.005188	0.000218	1.2	-2.0	1800
2.5	3000	−8.9354	−1.02285	0.004097	0.000340	1.3	-2.0	20
4.0	3000	−9.4519	−1.02493	0.002961	0.000471	1.2	-2.0	20
6.0	3000	−9.9231	−1.02462	0.001985	0.000587	1.0	1.7	200
8.5	3000	−10.3553	−1.02305	0.001169	0.000688	0.9	1.4	200
12.5	3000	−10.9008	−1.01278	0.000490	0.000783	1.4	-2.1	700
17.5	3000	−11.4371	−1.00202	0.000077	0.000853	2.1	-3.1	600
25.0	3000	−12.0549	−0.99997	−0.000320	0.000940	2.6	-4.7	500
35.0	3000	−12.7548	−0.98835	−0.000204	0.000990	3.5	6.1	2000
45.0	3000	−13.3393	−0.97309	0.000306	0.001001	4.1	-6.8	3000
55.0	2750	−13.7822	−0.97548	0.000311	0.001077	3.9	-6.5	500
65.0	2500	−14.1180	−0.98505	0.000176	0.001169	3.3	-5.9	400
75.0	2500	−14.4241	−0.97714	0.000791	0.001163	3.5	-6.0	400
85.0	2250	−14.6487	−0.98414	0.000615	0.001252	2.8	-5.1	2250
95.0	2250	−14.8431	−0.98171	0.001045	0.001257	3.0	5.4	1600
110.0	2000	−15.0579	−0.98864	0.000881	0.001355	2.3	-4.3	2000
130.0	2000	−15.2742	−0.98652	0.001393	0.001366	2.5	4.6	1400
150.0	1800	−15.3956	−0.99357	0.001138	0.001452	1.9	-3.5	1800
170.0	1800	−15.4606	−0.99323	0.001309	0.001455	1.9	3.6	1400

[a] If less than 3000 m, dose beyond this range is less that 10^{-30} rad/photon

Source Energy 2 MeV								
ϕ_j (deg.)	Fit Range[a] x_M (m)	LBRF Fit Parameters				Deviations		
		a	b	c	d	Aver. (%)	Max. (%)	x_{max} (m)
0.5	3000	−7.7335	−1.00194	0.004832	0.000033	0.3	0.5	400
1.5	3000	−8.8667	−1.00741	0.003850	0.000133	0.6	1.0	1
2.5	3000	−9.4163	−1.00997	0.003160	0.000210	0.7	-1.1	20
4.0	3000	−9.9477	−1.01166	0.002405	0.000297	0.7	-1.1	10
6.0	3000	−10.4395	−1.01209	0.001725	0.000381	0.7	-1.1	10
8.5	3000	−10.9014	−1.01131	0.001170	0.000453	0.6	1.0	200
12.5	3000	−11.4922	−1.00421	0.000714	0.000526	1.0	1.5	2000
17.5	3000	−12.0892	−0.99599	0.000446	0.000587	1.6	-2.4	3000
25.0	3000	−12.8199	−0.98695	0.000284	0.000662	2.2	-3.4	500
35.0	3000	−13.6034	−0.97610	0.000327	0.000745	2.9	-4.7	1
45.0	3000	−14.2226	−0.96580	0.000564	0.000812	3.6	-5.7	500
55.0	3000	−14.7154	−0.95632	0.000920	0.000865	4.1	6.5	2000
65.0	2750	−15.1009	−0.95678	0.000822	0.000970	3.8	6.2	1800
75.0	2500	−15.4109	−0.96026	0.000672	0.001074	3.3	-5.6	1
85.0	2500	−15.6764	−0.95400	0.001341	0.001062	3.6	6.2	1800
95.0	2250	−15.8953	−0.95252	0.001895	0.001049	3.6	6.5	1600
110.0	2250	−16.1610	−0.92822	0.005089	0.000693	6.0	11.3	1600
130.0	2250	−16.4428	−0.88763	0.009648	0.000139	8.4	15.6	1400
150.0	2000	−16.6229	−0.87829	0.011137	−0.000037	7.7	-14.4	400
170.0	2000	−16.6997	−0.86991	0.012514	−0.000212	7.9	-14.9	400

[a] If less than 3000 m, dose beyond this range is less that 10^{-30} rad/photon

Source Energy 4 MeV								
ϕ_j (deg.)	Fit Range[a] x_M (m)	LBRF Fit Parameters				Deviations		
		a	b	c	d	Aver. (%)	Max. (%)	x_{max} (m)
0.5	3000	−8.2658	−0.99510	0.003316	0.000029	0.7	1.0	6
1.5	3000	−9.4110	−0.99885	0.002701	0.000092	0.7	-1.1	8
2.5	3000	−9.9743	−1.00051	0.002259	0.000142	0.6	-1.1	10
4.0	3000	−10.5295	−1.00127	0.001781	0.000199	0.7	-1.2	10
6.0	3000	−11.0568	−1.00058	0.001381	0.000251	0.8	1.2	4
8.5	3000	−11.5669	−0.99847	0.001053	0.000300	0.8	-1.2	10
12.5	3000	−12.2243	−0.99281	0.000881	0.000343	0.8	1.2	2000
17.5	3000	−12.9126	−0.98022	0.000844	0.000386	1.1	-1.8	3000
25.0	3000	−13.7403	−0.96514	0.000891	0.000452	1.7	-2.8	1
35.0	3000	−14.6005	−0.94351	0.001123	0.000535	2.3	-4.0	500
45.0	3000	−15.2668	−0.92103	0.001481	0.000608	2.9	4.9	1800
55.0	3000	−15.7925	−0.90010	0.001901	0.000671	3.4	5.8	2000
65.0	3000	−16.2150	−0.88302	0.002254	0.000735	3.7	-6.5	3000
75.0	2750	−16.5400	−0.88111	0.001973	0.000864	2.9	-5.3	500
85.0	2500	−16.8059	−0.87846	0.002118	0.000918	2.2	-4.2	2500
95.0	2500	−17.0421	−0.86112	0.003711	0.000760	2.8	-5.3	500
110.0	2250	−17.3134	−0.84345	0.006029	0.000495	2.8	5.4	1600
130.0	2250	−17.5544	−0.83056	0.008528	0.000187	2.6	-4.7	2250
150.0	2250	−17.6943	−0.83007	0.009693	0.000040	2.0	3.4	1200
170.0	2250	−17.7611	−0.83146	0.010156	−0.000019	1.6	-2.8	300

[a] If less than 3000 m, dose beyond this range is less that 10^{-30} rad/photon

Source Energy 7 MeV								
ϕ_j (deg.)	Fit Range[a] x_M (m)	LBRF Fit Parameters a	b	c	d	Deviations Aver. (%)	Max. (%)	x_{max} (m)
0.5	3000	−8.7366	−0.98590	0.002550	0.000023	0.9	-1.6	20
1.5	3000	−9.8987	−0.98863	0.002095	0.000071	1.0	-1.7	20
2.5	3000	−10.4812	−0.98919	0.001804	0.000105	1.0	-1.8	20
4.0	3000	−11.0677	−0.98865	0.001490	0.000144	1.1	-1.8	20
6.0	3000	−11.6444	−0.98461	0.001265	0.000176	1.3	-1.9	20
8.5	3000	−12.2130	−0.97948	0.001256	0.000189	0.7	-2.1	20
12.5	3000	−12.9519	−0.97026	0.001400	0.000195	1.8	-2.7	1
17.5	3000	−13.7114	−0.95445	0.001560	0.000220	2.5	3.8	8
25.0	3000	−14.6222	−0.92542	0.001962	0.000254	3.0	-5.7	500
35.0	3000	−15.5467	−0.88272	0.002752	0.000283	4.9	7.8	8
45.0	3000	−16.2514	−0.84021	0.003488	0.000324	5.8	-9.5	1
55.0	3000	−16.8006	−0.80510	0.003794	0.000422	5.2	-10.3	1
65.0	3000	−17.2310	−0.78042	0.004028	0.000504	5.9	10.2	6
75.0	2750	−17.5653	−0.77293	0.003500	0.000667	5.6	8.7	6
85.0	2500	−17.8393	−0.76335	0.003714	0.000705	5.2	7.6	4
95.0	2500	−18.0681	−0.74540	0.005045	0.000573	4.8	-7.3	1
110.0	2500	−18.3320	−0.72532	0.007011	0.000350	3.7	6.7	4
130.0	2250	−18.5696	−0.71533	0.008117	0.000219	2.8	5.6	4
150.0	2250	−18.7091	−0.71307	0.009586	0.000036	2.9	4.5	4
170.0	2250	−18.7750	−0.71385	0.009729	0.000020	2.2	-4.0	1

[a] If less than 3000 m, dose beyond this range is less that 10^{-30} rad/photon

Source Energy 10 MeV								
ϕ_j (deg.)	Fit Range[a] x_M (m)	LBRF Fit Parameters a	b	c	d	Deviations Aver. (%)	Max. (%)	x_{max} (m)
0.5	3000	−9.0224	−0.98312	0.002435	−0.000009	1.5	2.2	20
1.5	3000	−10.2037	−0.98361	0.001985	0.000041	0.9	1.9	20
2.5	3000	−10.8046	−0.98286	0.001771	0.000066	0.9	-1.9	40
4.0	3000	−11.4203	−0.98071	0.001640	0.000084	1.1	-2.1	40
6.0	3000	−12.0325	−0.97655	0.001634	0.000090	1.8	2.5	10
8.5	3000	−12.6498	−0.96917	0.001642	0.000102	2.2	3.3	10
12.5	3000	−13.4612	−0.95294	0.001823	0.000109	3.1	4.8	10
17.5	3000	−14.2847	−0.92712	0.002282	0.000100	4.5	7.0	10
25.0	3000	−15.2557	−0.88198	0.003201	0.000076	6.6	10.5	10
35.0	3000	−16.2296	−0.81914	0.004458	0.000058	8.9	14.3	10
45.0	3000	−16.9594	−0.76367	0.005380	0.000084	10.5	-16.5	1
55.0	3000	−17.5226	−0.71814	0.005913	0.000152	11.5	17.5	8
65.0	3000	−17.9529	−0.69083	0.005684	0.000302	11.3	16.6	8
75.0	2750	−18.2807	−0.68498	0.004746	0.000515	9.9	-14.2	1
85.0	2500	−18.5466	−0.67576	0.004818	0.000567	8.7	12.3	6
95.0	2500	−18.7676	−0.65803	0.006026	0.000446	8.0	-11.3	1
110.0	2500	−19.0202	−0.64006	0.007769	0.000248	6.9	-9.8	1
130.0	2500	−19.2465	−0.63079	0.009151	0.000087	5.6	-8.0	1
150.0	2250	−19.3812	−0.62677	0.009944	−0.000008	4.4	6.7	4
170.0	2250	−19.4426	−0.62836	0.010099	−0.000025	3.6	-6.0	1

[a] If less than 3000 m, dose beyond this range is less that 10^{-30} rad/photon

Source Energy 15 MeV								
ϕ_j (deg.)	Fit Range[a] x_M (m)	LBRF Fit Parameters				Deviations		
		a	b	c	d	Aver. (%)	Max. (%)	x_{max} (m)
0.5	3000	−9.3251	−0.97878	0.002190	−0.000012	2.0	-2.9	800
1.5	3000	−10.5340	−0.97729	0.001935	0.000014	2.1	-3.1	1
2.5	3000	−11.1633	−0.97511	0.001807	0.000030	2.2	3.3	20
4.0	3000	−11.8243	−0.97052	0.001740	0.000040	2.6	3.9	20
6.0	3000	−12.4995	−0.96269	0.001780	0.000042	3.2	-4.8	700
8.5	3000	−13.1916	−0.94955	0.002000	0.000029	4.1	6.3	20
12.5	3000	−14.0975	−0.92312	0.002550	−0.000006	5.8	9.0	20
17.5	3000	−14.9973	−0.88267	0.003385	−0.000057	8.2	12.8	20
25.0	3000	−16.0281	−0.81892	0.004684	−0.000120	11.2	17.4	20
35.0	3000	−17.0593	−0.73228	0.006452	−0.000192	14.7	23.2	10
45.0	3000	−17.8278	−0.65713	0.007753	−0.000204	17.0	26.8	10
55.0	3000	−18.3946	−0.60813	0.007938	−0.000088	17.8	-27.2	1
65.0	3000	−18.8089	−0.58597	0.007103	0.000138	17.2	24.8	10
75.0	2750	−19.1139	−0.58865	0.005592	0.000418	14.7	20.7	8
85.0	2500	−19.3656	−0.58085	0.005623	0.000468	12.7	-17.7	600
95.0	2500	−19.5776	−0.56331	0.006811	0.000347	11.6	16.1	6
110.0	2500	−19.8132	−0.54839	0.008331	0.000177	9.8	13.4	6
130.0	2500	−20.0217	−0.54190	0.009488	0.000048	7.6	-10.6	1
150.0	2500	−20.1451	−0.54176	0.010118	−0.000024	6.1	8.8	4
170.0	2250	−20.2039	−0.53975	0.010602	−0.000084	5.3	8.0	4

[a] If less than 3000 m, dose beyond this range is less that 10^{-30} rad/photon

Distribution:

1 Dr. D. V. Rao
Science and Engineering Associates (SEA)
6100 Uptown Blvd. NE
Albuquerque, NM 87110

10 Prof. J. K. Schultis
Dept. of Nuclear Engineering
Ward Hall
Manhattan, KS 66506

1 Radiation Shielding Information Center
Oak Ridge National Laboratory
P.O. Box 2008
Oak Ridge, TN 37831

1 Dr. David K. Trubey
10800 N. Airway Loop
Citrus Springs, FL 32630

1 Dr. Jeffrey C. Ryman
Oak Ridge National Laboratory
Bldg. 6011
P.O. Box 2008
Oak Ridge, TN 37831

1 C. A. Negin, President
Grove Engineering, Inc.
15215 Shady Grove Rd.
Suite 202
Rockville, MD 20850

1 Dr. Norman M. Schaeffner, President
Radiation Research Associates
3815 Lisben, Suite 201
Fort Worth, TX 76107

1 Dr. William C. Hopkins
Bechtel Power Corp.
15740 Shady Grove Rd.
Gaithersburg, MD 20874

1 Dr. Charles Eisenhauer
NIST
Room A106, Bldg. 235
Gaithersburg, MD 20899

1 Dr. Jack Selby
Health Physics Dept.
Battelle Pacific NW Laboratories
P.O. Box 999
Richland, WA 99352

1 MS 1328 H. N. Jow, 6341
1 MS 1145 P. J. Griffin, 6514
1 MS 1137 R. L. Coats, 6500
1 MS 1146 T. F. Luera, 6504
1 MS 0720 C. D. Massey, 6626
1 MS 1175 K. R. Boldt, 6513

20	MS	1095	T. N. Simmons, 7713
1	MS	1095	D. J. Thompson, 7715
1	MS	1095	S. K. Vosburg, 7715
1	MS	9018	Central Technical Files, 8523-2
1	MS	0619	Print Media, 12615
5	MS	0899	Technical Library, 13414
2	MS	0100	Document Processing, 7613-2 For DOE/OSTI